Imperial College of London
Department of Aeronautics

Morphing Integrated Quadrotor Robot for Forest Applications

Peter Jianyi Zheng

Submitted in part fulfilment of the requirements for the degree of
Doctor of Philosophy
Defended 24th November 2022

Copyright Statement

The copyright of this thesis rests with the author. Unless otherwise indicated, its contents are licensed under a Creative Commons Attribution-NonCommercial 4.0 International Licence (CC BY-NC).

Under this licence, you may copy and redistribute the material in any medium or format. You may also create and distribute modified versions of the work. This is on the condition that: you credit the author and do not use it, or any derivative works, for a commercial purpose.

When reusing or sharing this work, ensure you make the licence terms clear to others by naming the licence and linking to the licence text. Where a work has been adapted, you should indicate that the work has been changed and describe those changes.

Please seek permission from the copyright holder for uses of this work that are not included in this licence or permitted under UK Copyright Law.

Acknowledgements

Dear Joel, for sending me on a much grander journey than what has been written in this thesis, thank you brother. To the question of the meaning of life, I can only surmise, "there's joy in living".

Huss, Seth, we made it!

I would like to thank my supervisor, Prof Mirko Kovac, for his support and inspiration. His ideas, often crazier than my own, have pushed me to greater heights both in engineering research and philosophy.

To the greats in the Aerial Robotics Laboratory, Rob Siddall, Zhang Ketao, and Maxime Bouyssou, thank you. It is an honour to follow in the footsteps of true masters of the engineering art.

Thank you my seniors, but more importantly friends, Pisak, Alejo, Raph and Sophie. Your technical and spiritual guidance was critical through the trials and tribulations.

André and Xiao Feng; my team, my men, my brothers. We are awesome. The stories of truly window-shattering, ceiling-breaking events will be passed down and become legends.

To my friends, Bahadir, Berm, Julien, Sylvie, Wenxi, Xinkai, Yifan, and many more who have aided me through this perilous journey by lending a helping hand from time to time - Thank you.

This thesis, like many others, was written on Overleaf[1]. And like many other engineering research projects, much of the prototyping in my studies was conducted with the E3D V6 ecosystem. Thank you both for supporting the field of engineering research.

Finally, I would like to give my utmost gratitude to my true funders, my parents, for whom it has been a multi-million, multi-decade, and multi-faceted project.

[1] www.overleaf.com

Declaration

I hereby declare that this thesis is novel, of my own work during my PhD research, and written by myself. All non-original content is referenced and the source clearly indicated. My PhD research has covered a broad domain and most results would have not been achievable without valuable collaboration with my colleagues. I list here the exact contributions and clarify the involvement of every researcher in all shared work.

The work in Chapter 2 is published in IEEE Robotics and Automation Letters under the title *TiltDrone: A Fully-Actuated Tilting Quadrotor Platform*, Digital Object Identifier (DOI): 10.1109/LRA.2020.3010460, with the authors: Peter Zheng (PZ), Xinkai Tan (XKT), Basaran Bahadir Kocer (BK), Erdeng Yang (EY), and Mirko Kovac (MK). Peter Zheng and Xinkai Tan are co-first authors. PZ conceptualised the research. XKT finalised and built the first prototype, and provided the stability analysis of the platform. EY made mechanical improvements on the first prototype. Based on the lessons learnt from the first prototype, PZ redesigned the platform with the analysis shown in the chapter. BK reviewed and edited the manuscript and provided clarity on the stability analysis. MK supervised the project.

The design of the robot in Chapter 4 is briefly mentioned in the 2021 Aerial Robotic Systems Physically Interacting with the Environment (AIRPHARO) conference under the title *Forest Drones for Environmental Sensing and Nature Conservation*, Digital Object Identifier (DOI): 10.1109/AIRPHARO52252.2021.9571033, with the authors: Basaran Bahadir Kocer, Boon Ho, Xuanhao Zhu, Peter Zheng, André Farinha, Feng Xiao, Brett Stephens, Fabian Wiesemuller, Lachlan Orr, and Mirko Kovac.

The work in Chapter 6 is published in Nature Scientific Reports under the title *Metamorphic Aerial Robot capable of mid-air shape morphing for rapid perching* with the authors: Peter Zheng (PZ), Feng Xiao (FX), Pham Huy Nguyen (PHN), André Farinha (AF), and Mirko Kovac (MK). FX, MK, and PZ conceptualised the research. PHN and PZ contributed to the literature review. PZ developed the robotic hardware. FX developed the servomotor control pipeline. AF conducted the FEM simulations to assess the dynamic behaviours of the morphing robot arm. FX, PHN, and PZ designed the experiments and conducted the experimental data gathering. MK supervised the project.

The work in Chapter 8 is partly included in a manuscript pending submission under the title *Bee-inspired Multi-Sensory Behavior-Based Aerial Robot for Vertical Surface Interaction*, with the authors: Feng Xiao (FX), Peter Zheng (PZ), Ke Ding (KD), Emily Baird (EB), and Mirko Kovac (MK). FX, EB, and MK conceptualised the research. FX and EB contributed to the literature review. PZ developed the robot's structure. FX developed the robot's sensor system and sensor fusion software. KD developed the neural network algorithm. FX and EB designed the experiments and conducted the experimental data gathering. MK supervised the project.

The work in Chapter 8 regarding the offboard autonomous flight controller architecture is, in various configurations and iterations, also used in:

- the 2019 2nd IEEE International Conference on Soft Robotics (RoboSoft) under the title *A Design and Fabrication Approach for Pneumatic Soft Robotic Arms Using 3D Printed Origami Skeletons*, Digital Object Identifier (DOI): 10.1109/ROBOSOFT.2019.8722719, with the authors: Ketao Zhang, Yifan Zhu, Chuqian Lou, Peter Zheng, and Mirko Kovac. Ketao Zhang and Yifan Zhu are co-first authors.

- IEEE Robotics and Automation Letters under the title *TiltDrone: A Fully-Actuated Tilting Quadrotor Platform*

- IEEE Robotics and Automation Letters under the title *Unmanned Aerial Sensor Placement for Cluttered Environments*, Digital Object Identifier (DOI): 10.1109/LRA.2020.3015459, with the authors: André Farinha, Raphael Zufferey, Peter Zheng, Sophie F. Armanini, and Mirko Kovac.

- IEEE Robotics and Automation Letters under the title *Optic Flow-Based Reactive Collision Prevention for MAVs Using the Fictitious Obstacle Hypothesis*, Digital Object Identifier (DOI): 10.1109/LRA.2021.3062317, with the authors: Feng Xiao, Peter Zheng, Julien di Tria, Basaran Bahadir Kocer, Mirko Kovac.

Dedication

To my family.

Abstract

Climate monitoring is a critical step towards understanding and mitigating natural disasters. Needing to monitor sizable spreads of land, ecologists turn to quadrotor robots. Simple and cost-effective to operate, quadrotor remote sensing bridges the gap between manned aerial surveillance and ground-based ecological monitoring methods.

Yet the need for manual sampling remains. This is especially true of densely forested areas; the canopy cover limits the useful data generated with above-canopy sensing. Just as the remote forest understories are treacherous for ecologists to navigate, robots face similar difficulties. Operating in confined spaces and far from the electrical grid, manoeuvrability and endurance become critical performance limiters. Production and maintenance also pose challenges in remote locations with limited logistical support.

For aerial robots to be productive in forests, they must become more compact and adaptable to their environment. This thesis addresses this aim and its challenges through the application of morphing designs on quadrotor robots. I explored the use of conventional morphing designs, using multi-part assemblies with rigid-body joints, such as bearings and ball joints. Utilising this design concept, I created multiple prototype tiltrotor-quadrotor robots. But as I strived to create lighter and more compact robots, conventional morphing designs became limited in their scalability and possible morphologies. Thus, I applied metamorphic designs with compliant mechanisms, creating robots that can fold their body to interact with and perch on trees.

The range of prototype robots demonstrates how morphing aerial robots can adapt to and take advantage of their environment to enhance their capabilities. Each robot showcases a different morphing quadrotor design. These robotic systems are analytically and numerically studied, experimentally characterised, and compared to identify the broader insights of morphing quadrotor design.

The unique shape-shifting abilities of the presented robots created performance trade-offs. But it is evident that a morphing quadrotor integrates capabilities without substantial increases in size or weight. Overall, integrated morphing design is an effective solution towards creating aerial robots for working within confined and changing natural environments.

Contents

Acknowledgements **5**

Declaration **5**

Dedication **9**

Abstract **11**

List of tables **17**

List of figures **27**

Acronyms **29**

1 Morphing Integrated Quadrotor Robots for Forest Operations **38**

1.1 Remote sensing with aerial robots . . . 38

1.1.1 Design challenges in remote sensing with unmanned aerial vehicles . . . 41

1.1.2 Current outlook on using aerial robots in ecology . . . 43

1.2 Design of conventional multirotors . . . 45

1.2.1 Layout . . . 45

1.2.2 Structure . . . 48

1.2.3 Propulsion . . . 48

1.2.4 Conclusion . . . 49

1.3 The role of morphological change . . . 50

1.3.1 Morphing in nature . . . 51

1.3.2 Morphing in robotics . . . 54

1.3.3 Comparing roles . . . 57

1.4 Integrated morphing quadrotor robots . . . 58

1.4.1 The size of the platform and the scaling of a quadrotor arm . . . 60

1.4.2 Perching robots . . . 64

1.4.3 Morphing in flight . . . 66

1.5 Summary . . . 68

2 Design of a multi-directional quadrotor UAV **70**
2.1 Introduction . . . 70
2.2 Design . . . 73
2.2.1 3D modelling methodology . . . 73
2.2.2 Structural sizing . . . 73
2.2.3 The geometrical effects of tilting . . . 75
2.2.4 Rotor gimbal . . . 78
2.2.5 Tilting Mechanism . . . 79
2.3 Control Framework . . . 80
2.3.1 Control Architecture . . . 80
2.3.2 Control Allocation . . . 80
2.4 Results and Discussion . . . 83
2.4.1 Manufacturing . . . 83
2.4.2 Testing . . . 85
2.5 Conclusions . . . 87

3 Analysis of a fully-actuated multi-directional quadrotor **89**
3.1 Introduction . . . 89
3.2 The Flight Dynamics of Tilting . . . 90
3.3 The Structural Dynamics of Tilting . . . 93
3.3.1 Resultant forces due to tilting . . . 95
3.4 Tilting in motion . . . 95
3.4.1 Geodesic path . . . 96
3.4.2 Path of shortest time . . . 97
3.4.3 Rate of Tilt . . . 100
3.4.4 Servomotor specification . . . 100
3.4.5 Servo velocity properties . . . 102
3.5 Tilting Mechanism Design . . . 103
3.6 Summary . . . 104

4 Tiltrotor Measuring Ring **107**
4.1 Introduction . . . 108
4.2 Results . . . 109
4.2.1 Hardware design . . . 109
4.2.2 Measuring ring validation . . . 111
4.3 Discussion . . . 112

5 The Flight Controller Placement on Tiltrotor Quadrotors 114
5.1 Introduction . . . 115
5.2 Results . . . 117
5.2.1 Simulation Physics . . . 117
5.2.2 Control Architecture . . . 118
5.2.3 Simulation Scenario . . . 119
5.2.4 Comparison of the PID Controller Outputs . . . 119
5.2.5 Root Mean Squared Error Analysis . . . 120
5.2.6 Combining position preference identifier logic . . . 124
5.3 Discussion . . . 127

6 Design and Application of a Metamorphic Aerial Robot 140
6.1 Introduction . . . 140
6.2 Results . . . 143
6.2.1 Morphing robot arm design . . . 143
6.2.2 Tendon drive design . . . 144
6.2.3 Energy usage . . . 145
6.2.4 Vehicle mass breakdown . . . 146
6.2.5 Perching . . . 146
6.3 Discussion . . . 148
6.4 Materials and Methods . . . 150
6.4.1 Robot Construction . . . 150
6.4.2 Control System . . . 150
6.4.3 Experimental Setup . . . 151
6.4.4 Perch strength bench test . . . 152
6.5 Deflection of the morphing robotic arm . . . 154
6.6 Parametric numerical study of the tendon actuation . . . 155
6.7 Video analysis . . . 157
6.8 Robot mass breakdown . . . 157
6.9 Outdoor autonomous flight testing . . . 157
6.10 Summary . . . 159

7 Robust aerial platform for long-duration acoustic sensing 166
7.1 Introduction . . . 166
7.2 Results . . . 168
7.2.1 Hardware design . . . 168
7.2.2 Electronics . . . 172
7.2.3 Numerical assessment . . . 175
7.3 Discussion . . . 176

8 Design and Testing of Single-Part Assembly Metamorphic Aerial Robots 178
8.1 Introduction . . . 179
8.2 The Structural Forces of Rotation . . . 180
8.3 Design . . . 183
8.3.1 Materials . . . 183
8.3.2 Methodology . . . 183
8.4 Testing of Lightweight Prototype Robots . . . 187
8.4.1 Autonomous control system architecture . . . 188
8.5 Discussion . . . 191

9 Conclusion 193
9.1 Contributions . . . 193
9.2 Conclusions . . . 194

Bibliography 195

A Design of a single-actuator multi-launch variable-velocity sensor launcher 220
A.1 Introduction . . . 221
A.2 Ballistic computation . . . 221
A.2.1 Adjustable launch speed . . . 223
A.2.2 Adjustable launch angle . . . 223

B Design of the Armadillo: an omni-orientation protective ball cage for miniature multirotors 226

List of Tables

1.1 Examples of morphing aerial-terrestrial robot research, separated by the methods of aerial and terrestrial locomotion. To the author's knowledge, there have yet to be functional fixed-wing robots that morph into wheeled platforms or rotor-wings which morph into legged platforms for terrestrial locomotion. 57

1.2 Comparison between active and passive perching aerial robots. 66

2.1 Prototype robot performance. 83

2.2 Component mass breakdown. 85

2.3 Step response mean absolute error and standard deviation with conventional (Conv) and fully-actuated (FA) flight. 87

4.1 Errors when the measuring ring is hand tested on various trees. 113

6.1 **Prototype robot mass breakdown**. The integrated subsystems for perching and flight are highlighted in blue and red, respectively. 158

8.1 The role of elastic and plastic deformation in the design of the prototype quadrotor 183

9.1 Summary of Contributions - Chapter 1 to 8 196

List of Figures

1.1 **Commercially available multirotor drones**. (A) Image from Pxfuel. (B) Image from Pxfuel (C) Image from Pxfuel. (D) Image by NeONBRAND from Pxfuel. (E) Image by Antonio Jose Cespedes from Pixabay. (F) Photo by Klaus Foehl, CC BY-SA 4.0 https://creativecommons.org/licenses/by-sa/4.0, via Wikimedia Commons. (G) Image by S. Hermann and F. Richter from Pixabay. (H) Image by jotoya from Pixabay. (I) Image from Pxfuel. 47

1.2 **A comparison of conventional vehicle and animal locomotion principles** on land, sea, and air. (**A**) wheels on cars, (**B**) water propellers, and (**C**) turbofan engines on a plane all use rotary motion to move their respective vehicle. They can only change their rotational speed but not their geometry. Animals use a system of mobile limbs, enabling them to achieve incredible feats of agility, exemplified by (**D**) a cat balancing on a pole. (**E**) Fish, and (**F**) birds move using reciprocal motion with a number of articulated joints. 51

1.3 **The versatility of animals in action**. (**A**) Cats play fighting and (**B**) hugging to stay upright. (**C**) A cameraman holding a camera at ground level filming a basketball player dribbling a ball behind his back. While robots have accomplished singular tasks to greater accuracy, to date, none have mastered the breadth of skills shown by animals. 52

1.4 **Concept** drawing of morphing quadrotors in the forest 59

1.5 **Function Analysis System Technique (FAST) diagram of the tiltrotor-quadrotors in the forest robot**. 60

1.6 **Function Analysis System Technique (FAST) diagram of the metamorphic perching drone and the low-power idle electronics**. While sensor deployment and pickup is a viable option, it is not considered in this thesis. . . . 60

1.7 **Function Analysis System Technique (FAST) diagram of the single-part assembly metamorphic quadrotor**. 61

1.8 **Prototype robots in flight**. The aerial robots shown in this figure are tested to be airworthy. (**A**) Active morphing autonomous perching robot approaching a branch (Chapter 6). (**B**) Multi-directional synchronised tiltrotor (Chapter 2). (**C**) A $100g$ robot built from a single-piece folded structure with a flexible antenna attachment, photographed by Feng Xiao. (**D**) A sub-$250g$ quadrotor with an active tilting protective ring/measuring wheel stably contacting the wall, photographed by Pham Huy Nguyen (Chapter 4). All photographs are edited for clarity. 62

2.1 **The TiltDrone prototype** in (**A**) tilted horizontal, (**B**) level, and (**C**) tilted hovering flight. The prototype TiltDrone can tilt its rotors up to 30 degrees. The backgrounds of the photographs are altered for clarity. 71

2.2 **The design and the prototype**. (A) A photo of the prototype platform. (B) A diagram of the synchronised rotor tilting mechanism. (C) The volume swept by the rotor axis of rotation (red) with linear servomotor axes s_1, s_2 rotated -45° from rotor axes XY. (D) The attitude and polar coordinate presentation of the thrust vector, and (E) side view of the rotor and the compound joint. 72

2.3 **Tilting mechanism diagrams**. (**A**) An illustration of the control allocator. (**B**) Geometrical diagram of the tilting platform and a comparison of the prototype design level and tilted. The rotor workspaces are shaded in yellow. The workspaces can overlap as the rotors are tilted synchronously. 74

2.4 **Height reduction ratio** graphs comparing the vertical profile of the fully-actuated platform with a conventional quadrotor, with (**A**) $\alpha_{\max} \leq \alpha_r$ and (**B**) $\alpha_{\max} > \alpha_r$. Sections in greyscale and colour denote the various heights for fully-actuated (numerator) and conventional (denominator) quadrotors respectively. (**C**) The various tilting scenarios, the border colour of each diagram corresponds to the colour of the lines in (**A**) and (**B**). 77

2.5 **Control architecture of the fully-actuated platform**. (**A**) The servomotor output limiter with trim control. (**B**) The robot control schematics. 81

2.6 **Step response** of conventional and fully-actuated flight at 0° tilt. 86

2.7 **Comparing pitch response due to step position command** of conventional and fully-actuated flight at 0° tilt. The pitch responses are synchronised by the change in position command. 86

2.8 **Static hovering fully-actuated flight** at various roll axis tilt. 87

3.1 **Tilting drone force diagram**. The two rotors are mounted on a four-bar linkage to ensure that T_1 and T_2 are pointing in the same direction. The pitch angle α is measured from the horizon, and the tilt angle ϕ is measured from the vertical. 93

3.2 **Frame of reference to calculate actuator forces due to precession**. (**A**) Spinning top model of a tilting rotor with a massless rod precessing about the pivot point (orange) with the non-stationary tilting-frame (blue). (**B**) The arm frames of reference are static relative to the bodyframe and are orientated at ψ_i, measured from the x-axis, about the z-axis. (**C**) The forces experienced by the mechanism due to a rotation about the axis through rotor 1 and 3 94

3.3 **Coordinate systems** on the rotor unit sphere and servo plane 97

3.4 Top: Heat map showing the maximum time metric T_{cheb} from the current servo position $[s_{1i}, s_{2i}]$ (white spot), the target servo position $[s_{1f}, s_{2f}]$ (red spot) and the boundary of possible servo position paths which achieves minimum travel time. This is more useful than Euclidean distance as the rate of movement is limited by a single servo's maximum rpm. Middle: The variation of servo velocity on a geodesic path under constant rate of tilt. Bottom: Plotting the servo velocities shows that the geodesic path is a straight line. 105

3.5 **Biaxial rack and pinion mechanism** top view (left) and enlarged (right) . . 106

4.1 **The prototype tilting ring robot**. (**A**) A photograph of the Ring-Beatle robot and (**B**) a rendered drawing of the tilting mechanism. 110

4.2 **Hand held measurement percentage accuracy vs tree circumference**. The ground truth is determined manually with a measuring tape. 112

4.3 **A subset of the trees** used in validation. (**A**) A smooth tree. (**B**) A medium coarse tree. (**C**) A coarse tree. 112

4.4 **The prototype flying** (**A**) in free flight, (**B**) at approach, (**C**) and contacting the wall. 113

5.1 **The simulated tiltrotor design**. The payload Centre of Mass (CoM) coincides with the rotor body CoM. The payload body is free to rotate about its CoM and is rotated by the torque from a servomotor. 116

5.2 **Cascaded cascaded PID controller** diagram of the simulated tiltrotor drone with (**A**) the IMU on the rotor body and (**B**) on the payload body. 119

5.3 **Simulation** of the tiltrotor with a cascaded position-Proportional Integral Derivative Controller (PID). The tiltrotor has an inertia ratio of 0.01, corresponding to the rotor body having a 100 times larger inertia than the payload. The Flight Controller (FC) is running at $4000Hz$ and outputs servomotor commands at $50Hz$. The light blue background denotes $T < 5s$, where we commanded a varying position setpoint with a constant zero tilt, and orange encloses $T \geq 5s$, where we commanded a constant position with a varying tilt setpoint. 121

5.4 **Simulation** of the tiltrotor with a cascaded position-Proportional Integral Derivative Controller (PID). The tiltrotor has an inertia ratio of 100, corresponding to the payload body having a 100 times larger inertia than the rotor. The Flight Controller (FC) is running at $4000Hz$ and outputs servomotor commands at $50Hz$. The light blue background denotes $T < 5s$, where we commanded a varying position setpoint with a constant zero tilt, and orange encloses $T \geq 5s$, where we commanded a constant position with a varying tilt setpoint. Note that the tiltrotor becomes unstable in the vertical axis z when the FC is mounted to the rotor body. 122

5.5 **Position root mean squared error** at $0 \leq T < 5s$, where the robot is commanded to follow a position setpoint trajectory at 0° tilt. The servomotor frequency is $50Hz$ while a range of Flight Controller (FC) frequencies was simulated. (**A**) The FC is mounted on the rotor body. The embedded plot shows the full error range when the FC runs at $50Hz$. (**B**) The FC is mounted on the payload body. (**C**) The comparison of the difference in errors as a fraction of the scenario with the larger error reviews which mounting position has a better performance. Note the clear shift in the preferred mounting position as the payload-rotor inertia change at low FC frequencies. And the shift in the preferred position as the FC frequency varies at high payload-rotor inertia ratios. 129

5.6 **Position root mean squared error** from $5 \leq T < 10s$ where the robot is commanded to follow a tilt setpoint trajectory at a static position. The servomotor frequency is $50Hz$ while a range of Flight Controller (FC) frequencies was simulated. (**A**) The FC is mounted on the rotor body. The embedded plot shows the full error range when the FC runs at $50Hz$. (**B**) The FC is mounted on the payload body. (**C**) The comparison between the two mounting positions shows a bifurcation of results occurring at lower FC frequencies. 130

5.7 **Payload angle root mean squared error** at $0 \leq T < 5s$ where the robot is commanded to follow a position setpoint trajectory at 0° tilt. The servomotor frequency is $50Hz$ while a range of Flight Controller (FC) frequencies was simulated. (**A**) The FC is mounted on the rotor body. (**B**) The FC is mounted on the payload body. (**C**) The percentage improvement. 131

5.8 **Payload angle root mean squared error** from $5 \leq T < 10s$ where the robot is commanded to follow a tilt setpoint trajectory at a static position. Servomotor frequency is set at $50Hz$ while a range of Flight Controller (FC) frequencies was simulated. The FC is (**A**) mounted on the rotor body, and (**B**) on the payload body. (**C**) The percentage improvement. 132

5.9 **Position root mean squared error** from $0 \leq T < 5s$ where the robot is commanded to follow a position setpoint trajectory at 0° tilt. The Flight Controller frequency is set at $4000Hz$ while a series of servomotor frequencies are tested. The FC is (**A**) mounted on the rotor body, and (**B**) on the payload body. (**C**) The percentage improvement. 133

5.10 **Position root mean squared error** from $5 \leq T < 10s$ where the robot is commanded to follow a tilt setpoint trajectory at a static position. The Flight Controller frequency is set at $4000Hz$ while a series of servomotor frequencies are tested. The FC is (**A**) mounted on the rotor body, and (**B**) on the payload body. (**C**) The percentage improvement. 134

5.11 **Payload angle root mean squared error** from $0 \leq T < 5s$ where the robot is commanded to follow a position setpoint trajectory at 0° tilt. The Flight Controller frequency is set at $4000Hz$ while a series of servomotor frequencies are tested. The payload tilt angle error when the FC is (**A**) mounted on the rotor body, and (**B**) on the payload body. (**C**) The payload angle RMSE is lower when the FC is mounted to the payload body for most drone setups. But the difference in performance becomes marginal at higher servomotor frequencies and when the rotor body has significantly more inertia. 135

5.12 **Payload angle root mean squared error** from $5 \leq T < 10s$ where the robot is commanded to follow a tilt setpoint trajectory at a static position. The Flight Controller frequency is set at $4000Hz$ while a series of servomotor frequencies are tested. The payload tilt angle error when the FC is (**A**) mounted on the rotor body, and (**B**) on the payload body. (**C**) The percentage improvement. . . 136

5.13 **Position root mean squared error** from $0 \leq T < 5s$. The robot is commanded to follow a position setpoint trajectory at a static payload tilt angle with the payload-rotor body inertia ratios of (**A**) $R_i = 0.01$, (**B**) $R_i = 1$, and (**C**) $R_i = 100$. 136

5.14 **Position root mean squared error** from $5 \leq T < 10s$. The robot is commanded to follow a tilt setpoint trajectory at a static position with the payload-rotor body inertia ratios of (**A**) $R_i = 0.01$, (**B**) $R_i = 1$, and (**C**) $R_i = 100$. 137

5.15 **Payload angle root mean squared error** from $0 \leq T < 5s$. The robot is commanded to follow a position setpoint trajectory at a static payload tilt angle with the payload-rotor body inertia ratios of (**A**) $R_i = 0.01$, (**B**) $R_i = 1$, and (**C**) $R_i = 100$. 137

5.16 **Payload angle root mean squared error** from $5 \leq T < 10s$. The robot is commanded to follow a tilt setpoint trajectory at a static position with the payload-rotor body inertia ratios of (**A**) $R_i = 0.01$, (**B**) $R_i = 1$, and (**C**) $R_i = 100$.137

5.17 **Combined position and payload angle Root Mean Squared Error (RMSE) preferred Flight Controller (FC) mounting position indicator** with the red and blue spots showing where it is definitely preferable to mount the FC in various scenarios. The grey spots indicate that the preferred mounting position is situational. The black-and-yellow dots signifies where, within a ±20% RMSE error difference, there is no preferred mounting position. (**C**) is the combination of the identifiers from (**A**) the payload at a constant angle case and (**B**) payload rotation with no rotor tilt. Similarly (**D**)+(**E**)→(**F**),(**G**)+(**H**)→(**I**), and (**C**)+(**F**)+(**I**)→(**L**) the combination across different flight conditions and inertia ratios. (**J**) and (**K**) shows the preference from the combination of various inertia ratios, ie. (**A**)+(**D**)+(**G**)→(**J**) and (**B**)+(**E**)+(**H**)→(**K**). 138

5.18 **The combination of the position preference identifiers**. The diagram visualises the algorithm or the function that combines multiple position preferences and returns an identifier that follows the same logic as the original. 139

6.1 **The bioinspired perching quadrotor robot.** The top half of the figure diagrams the perching process. (**A**) A photograph of the prototype robot perching upside down on tree branches. The bottom half of the figure diagrams the manufacturing of the morphing arm. The layers are laid on jigs with the elastic membranes pre-stretched before being pressed to form a single panel. The actuation process of the tri-tendon spool mechanism to unlock the arm. 160

6.2 **Performance study of the prototype robot.** The arm morphing process has three stages: 1. locked for flight, 2. transition to unlocked, and 3. fully unlocked to grasp. The photographs of the arm at each stage are displayed. (**A**) The relationship between the tip deflection and thrust loading is plotted against the analytical models and finite element analysis when the arm is locked. (**B**) The time needed for the arm to open and grasp, is determined with a high-speed camera. (**C**) The drop-perch successful rate in relation to the arm position. After landing, the robot must grasp the branch (approximated by a cylindrical pipe) to remain perched. (**D**) The holding current of the servomotor with varying perching angles and branch diameters. 161

6.3 **The morphing robot perching indoors and outdoors.** (**A**) The robot taking off from a perch (bottom to top). (**B**) The robot performing a land-perch (top to bottom). (**C**) The robot performing a drop-perch. 162

6.4 **Statistical analysis of the flight and perching data.** Dynamic finite element simulation of the effect of thrust on the morphing arm's locking behaviour. 163

6.5 **The control flow chart and electronics system.** (**A**) The finite state machine of the land-perch procedure, the drop-perch controller, and the deperch process. (**B**) The electronics architecture of the robot with an additional N-channel MOSFET to switch on and off the servomotor. 164

6.6 **Diagram of the morphing arm** with the dimension variables used to (**A**) model the structural stiffness and the unlocking dynamics, and (**B**) the position of the arm at perch. 165

7.1 **Prototype passive perching platform**. The top view of the robot shows the front arms (teal) in a perched state, and the back arms (red) in the flying configuration. 169

7.2 **Rendered drawings of the prototype platform**. (**A**) Side view of the robot in flight configuration. (**B**) Side view of the robot perched. (**C**) Side view of the perched robot deploying the pod. (**D**) The assembled robot with the far side set of arms in perching configuration. (**E**) Exploded view of the robot. 170

7.3 **Electronics diagrams** of (**A**) the novel 3-stage circuit compared to (**B**) a conventional approach. The proposed circuit design switches on the FC, ESC, and the pod release hot-wire in a hierarchical sequence. This design ensures that Stage III (red) cannot be triggered without Stage II (blue) and Stage I (grey) turned on, and Stage II without Stage I on. This prevents the operator from accidentally turning on increasingly more dangerous components on the robot. . 172

7.4 **A simulation of the Op-Amp signal comparator booster circuit in MATLAB-Simulink**. (**A**) displays the filtered PWM signals from the TBS Tracer RC receiver. The comparator compares a user-controlled channel (purple) to a constant low PWM (yellow). (**B**) shows the output from the Op-Amp (orange) successfully switching the flight controller on/off MOSFET (blue). . . . 174

7.5 **Estimated probability of free-falling through a canopy opening**. (**A**) The most significant differences in probabilities are obtained between $0.4 < r' < 0.7$. (**B**) The radius of canopy opening is non-dimensionalised relative to the distance from the centre of the rigid platform to its rotor. 176

8.1 **Rotor frame of reference** with the rotor centre of mass in yellow, the multi-rotor centre of mass in blue. 182

8.2 **Finite element analysis of the quadrotor arm** when under maximum thrust (left) and torque (right). Common PETG properties were used. This shows that the motor will be secure under all flight conditions. The finalised prototype used a chopped carbon-fibre-filled nylon composite which is stiffer and stronger. . . . 184

8.3 **The assembly drawings of the single-part assembly metamorphic quadrotor**. (**A**) The flat-pack 3D printed drone frame. (**B**) The parallel cross beams are bent into their final positions with plastic deformation. (**C**) The arms are then slotted into the vertical posts. (**D**) the Flight Controller (FC) is pressed into the posts, the springs will index and keep the FC secure. (**E**) The frame with the rotors clipped onto the arms, and the surface interaction antenna module. (**F**) Photographs of the assembled drone. 186

8.4 Side view diagrams of the four-bar linkage compliant mechanism as printed (left) and folded (right). The two parallel members are blue and shaded grey. 187

8.5 **The ROS-RC control architecture**. The blue paths denote onboard sensors and onboard computed odometry. The blue-filled circles are onboard controllers, and red denotes offboard. The grey block indicates the ROS-RC system—angle and angular rate control are handled by the Flight Controller (FC). The user can choose between using motion capture or onboard Visual Inertial Odometry (VIO) for position/velocity control. The user can also send the position odometry to an offboard controller. Note that the total thrust is controlled by the ROS-RC but it is not shown in this figure. 189

8.6 **The internal architecture of the ROS-RC** offboard autonomous flight system. The Functions block is free for the user to modify without hindering safety as the Geofence can shut down the robot or take over control. 190

8.7 **The prototype "BeeMAV" quadrotor platform flying** close to the forest floor with the whisker attachment to allow safe and stable contact with trees. . . 192

A.1 **The available flight paths for a constant exit speed launcher**. (**A**) The firing solutions for a point target are bounded by a parabola, within which there are two available firing solution. On the parabola there is only one solution, beyond the boundary parabola, as indicated by the red arrow, there are no solutions. (**B**) If the impact angle is specified, the firing solutions are further limited to an ellipse. 224

A.2 **Design of the multi-launch launcher**. (**A**) A sectioned view of the sensor pod magazine and feed system. (**B**) Outline sketch of the single-actuator variable launch speed mechanism. 225

B.1 **Rendered picture of the Armadillo drone** (**A**) assembled and (**B**) in exploded view. 227

Acronyms

3D Three dimensional. 26, 40, 41, 73, 176, 178, 179, 186

BLDC Brushless Direct Current. 48, 49, 55, 111

CFRP Carbon-Fibre-Reinforced Polymers. 48, 159

CoM Centre of Mass. 21, 67, 90, 91, 116, 117

CPPM Combined Pulse Position Modulation. 190

DBH Diameter at Breast Height. 67, 108, 109, 111, 113

DC Direct Current. 39

DoF Degrees of Freedom. 51, 53, 66, 110, 111

ESC Electronic Speed Controller. 25, 172

FC Flight Controller. 22, 23, 24, 25, 26, 59, 63, 67, 68, 115, 116, 118, 120, 121, 122, 123, 124, 125, 127, 129, 130, 131, 132, 133, 134, 135, 136, 138, 172, 185, 186, 189, 195

FFF Fused Filament Fabrication. 178, 179, 185, 191

FoV Field of View. 46, 158

GNSS Global navigation satellite system. 41, 65

IMU Inertial Measurement Unit. 40, 63, 68, 195

LiDAR Light Detection And Ranging. 40

LiPo lithium polymer battery. 49

MAV Micro Aerial Vehicle. 48

MIQRo Morphing Integrated Quadrotor Robots. 60

MPC Model Predictive Controller. 190

MTOW Maximum Takeoff Weight. 83

NN Neural Networks. 41

PD Proportional Derivative Controller. 117

PID Proportional Integral Derivative Controller. 21, 22, 68, 118, 119, 120, 121, 122, 127, 151, 189

PWM Pulse Width Modulation. 68, 176

RC Radio Controlled. 48, 59

RL Reinforcement Learning. 41

RMSE Root Mean Squared Error. 24, 120, 123, 124, 138

RTK Real Time Kinematic Positioning. 65

SLAM Simultaneous Localisation And Mapping. 40, 190

SPA Single-Part Assembly. 179, 180

T/W Thrust-to-Weight ratio. 39

UAV Unmanned Aerial Vehicle. 39, 40, 41, 42, 43, 45, 46, 48, 49

VIO Visual Inertial Odometry. 26, 41, 65, 157, 189, 190

Nomenclature

Chapter 1

ΔL_{arm} Difference between the scaled arm L_1 and the nominal arm L_0

ω_z Drone arm vibration natural frequency

ρ_{air} Air density

A_{prop} Area of the rotor/propeller

E Drone arm Young's modulus

I_{arm} Drone arm second moment of area

L_{arm} Drone arm length

m_{arm} Mass of the circular drone arm

P Rotor power

r Radius of the cylindrical drone arm

R_{prop} Rotor radius

T Thrust

Chapter 2

α_P Drone body pitch angle relative to the inertial frame

α_R Drone body roll angle relative to the inertial frame

$\alpha_{\max}$ Maximum tilt angle

β_{s_1} Angle swept by the full travel of rotor tilt due to Servomotor 1

β_{s_2} Angle swept by the full travel of rotor tilt due to Servomotor 2

ϕ_D Drone body azimuthal tilt angle

θ_D Drone body azimuthal tilt direction angle

D_{prop} Propeller diameter

h_b Minimum height of the tiltrotor quadrotor body

H_r Rotor height measured from the top of the rotor to the tilting pivot point

h_{conv} Vertical height of a conventional quadrotor

h_{tilt} Vertical height of a TiltDrone quadrotor

l_{b} Minimum length of the tiltrotor quadrotor body

L_{s_1} The length of travel of Servomotor 1

L_{s_2} The length of travel of Servomotor 2

s_1 The axis of travel of Servomotor 1

s_2 The axis of travel of Servomotor 2

$s_{1,2_{\text{trim}}}$ Servomotor travel trim

T_{prop} Propeller cylinder thickness

w_{conv} Horizontal width of a conventional quadrotor

w_{tilt} Horizontal width of a TiltDrone quadrotor

Z_0 Height offset of the servomotor plane of actuation from the centre of tilt rotation

Chapter 3

$[x_u, y_u, z_u]$ Rotor spin axis direction unit vector

α_P Tiltrotor drone body pitch angle

Δx Difference between the final and initial position x

Δy Difference between the final and initial position y

Δz Difference between the final and initial position z

$\dot{s}_{1\max}$ Fastest travel velocity of servomotor 1

$\dot{s}_{2\max}$ Fastest travel velocity of servomotor 2

$\hat{b}_u$ Intermediate rotor spin axis direction unit vector

$\hat{c}_u$ Final rotor spin axis direction unit vector

$\hat{L}_r$ Total angular momentum of a rotor

$\hat{L}_{\text{spin}}$ Angular momentum of a spinning rotor

$\hat{L}_{\text{tilt}}$ Angular momentum of a tilting rotor

$\hat{p}$ Rotor precession unit vector

$\hat{r}$ Rotor spin axis unit vector

$\hat{t}$ Rotor tilting force unit vector

ω Rotor rotational velocity

Ω_t Tilt angular velocity

ϕ, ϕ_t Rotor azimuthal tilt angle

a, b, c Initial, intermediate, and endpoints of rotor tilt and the equivalent servomotor travel

$D_{\text{Chebyshev}}$ Chebyshev distance of the tiltrotor servomotor travel

h_b Perpendicular height offset of the body from the midpoint between the two centres of rotor tilt rotation

h_r Height offset of the rotor centre of mass from the rotor tilt pivot point

I_b Moment of inertia of the tiltrotor drone body in the pitch axis

I_r Rotor assembly moment of inertia of about its thrust/spin axis

I_t Moment of inertia of a single rotor in the axis of tilt rotation

m_b Mass of the tiltrotor drone body

m_r Mass of a single rotor

n Normalised distance unit where when $n = 0$, $[x, y, z] = [x_i, y_i, z_i]$, and when $n = 1$, $[x, y, z] = [x_f, y_f, z_f]$

R_{prec} Reaction force from the tiltrotor structure to resist precession when tilting

R_{servo} Reaction force from the tiltrotor structure to transmit servomotor actuation when tilting

T_{Cheb} Chebyshev time of the tiltrotor servomotor travel

$w_{\frac{1}{2}}$ Half-width of the tiltrotor drone body

$x_{i,f}$ Initial and final Cartesian x position of the rotor centre of mass relative to the tilt pivot point

$y_{i,f}$ Initial and final Cartesian y position of the rotor centre of mass relative to the tilt pivot point

Z_0 Distance between the tilt pivot point and the servomotor plane of actuation

$z_{i,f}$ Initial and final Cartesian z position of the rotor centre of mass relative to the tilt pivot point

Chapter 5

ω_{s} Servomotor rotational velocity

τ_{s} Servomotor torque

θ_1 Pitch angle of the tiltrotor payload body

θ_2 Pitch angle of the tiltrotor rotor body

θ_{s} Servomotor rotational position

D_{servo} Servomotor voltage controller derivative gain

$f_\sigma\left(\sum_{k=1}^{m} N_{\mathrm{pref,k}}\right)$ Function to find the combined flight controller position preference identifier

k_{s} Servomotor constant

N_{pref} Flight controller mounting position preference identifier

P_{improve} Percentage improvement gained between the better and the worse flight controller mounting position

P_{servo} Servomotor voltage controller proportional gain

R_i Payload-rotor body inertia ratio

R_{s} Servomotor internal resistance

V_{s} Servomotor drive voltage

Chapter 6

α_s Internal angle between the links

λ Membrane stretch ratio (current/unstretched)

λ_0 Initial stretch ratio (at manufacturing)

σ Stress of elastic membrane

τ Servo torque

θ	Servo angle of rotation
θ_{ext}	Arm angle when perching assuming that only the root joint moves
θ_{a1}	Root folding joint angle
θ_{a2}	Mid-arm folding joint angle
θ_{a3}	Tip folding joint angle
a	Distance of tendon anchor to the hinge
b	Distance of tendon edge to hinge
C_{01}	Elastic constant of latex membrane
C_{10}	Elastic constant of latex membrane
d	Distance of membrane attachment to the hinge
E_k	Elastic modulus of polyimide hinge
L_{arm}	Length of a single arm
m_0	Gradient of the tangent to the tree surface, approximated by a circle
$m_\perp$	Gradient of the normal to the tangent
P	tendon tension
R	Radius of spool
r_b	Radius of the branch
T	Thrust of a single rotor
t_k	Thickness of polyimide hinge
t_m	Thickness of membrane
w_m	Width of membrane

x_0 Distance between rigid links (hinge gap)

x_{cont} Horizontal position of where the morphing arm first contacts the circular branch

x_{root} Horizontal position of the morphing arm root

y_{cont} Vertical position of where the morphing arm first contacts the circular branch

y_{root} Vertical position of the morphing arm root

z_{arm} vertical deflection of the morphing arm

Chapter 7

μ Coefficient of friction between the Cam-follower and the cam-track

F Friction between the cam and the cam tracks

n_{rotor} Total number of rotors

T Thrust of a single rotor

y_{rot} Height of the cam-follower position where the arms are free to rotate, relative to the folding hinge

y_{top} Initial height of the cam-track's vertical section relative to the folding hinge

Chapter 1

Morphing Integrated Quadrotor Robots for Forest Operations

"*It is no longer difficult to imagine a world where human-made robots work in harmony with us humans to safeguard our planet. The question is when and how will we get there.*"

Working in the forest, be it for forestry or conservation projects, is an arduous task. Traversing unpaved terrain to reach deep into cluttered environments with tools and equipment is undeniably physically demanding, especially with tasks such as ecological data collection where the researcher has to travel deep into the forest mostly on foot. Like other manual tasks, we look to automation and technology as aids to reduce the physical effort and increase efficiency. While some mechanised solutions are available, there remain many scenarios where they are unsuitable. Most of all, there has yet to be an autonomous system that has the physical capabilities and characteristics to access such treacherous regions. Here lies the frontier of remote sensing technology and research.

1.1 Remote sensing with aerial robots

Remote sensing, the act of gathering information from afar, is notably associated with World War I. Although the observation of enemy entrenchments from balloons and aeroplanes soon

turned into dogfights and aerial warfare, the usefulness of remote sensing remains evident.

Today, remote sensing has expanded onto a broad range of platforms. In order of scale, the height of observation, and cost: satellites are capable of imaging entire regions of the globe; high-flying manned aerial vehicles can scan areas in the scale of kilometres; static sensors map the surrounding area within their line of sight. The newest addition to the remote sensing toolbox, small Unmanned Aerial Vehicle (UAV)s, can be operated by a single user to map areas within a radius of hundreds of meters.

Drones are no longer novelties in the consumer market. Increasingly smaller, more autonomous, and more capable drone platforms have given individual users a much greater ability to view their surroundings from the air. The remote sensing and ecological science community have also embraced the use of drones, especially multirotors, for data collection [1]. Compared to the more traditional means of remote sensing, drone platforms offer a combination of low cost, high mission flexibility, high spatial fidelity, and ease of maintenance.

A key differentiator in consumer-size drone designs is their means of providing the lifting force for flight. Traditionally, fixed-wing platforms, similar to a scaled-down propeller-driven manned aircraft, utilise internal combustion engines or Direct Current (DC) electric motors with fixed pitch propellers to provide the forward thrust. The lift is provided by the wings on the drone and the craft is controlled aerodynamically by movable surfaces interacting with the oncoming airflow. Fixed-wing platforms are often able to cover a long range at speed. Trialled in various conditions and on multiple continents, the fixed wing design has been shown to be robust and lower in cost to set up than equivalent multirotor platforms [2, 3, 4].

Multirotor and helicopter platforms, on the other hand, use motor-driven propellers as the lifting mechanism; variations in the rotor speeds provide the steering control. This enables these drones to maintain a stable level hover. The slower flight speed can be beneficial when the fidelity of the data is paramount [4]. This propulsive method is also less limiting on the form factor of the platform. Therefore, the drone can accept a greater range of payload modules, simplifying the payload design and logistics. However, the flexibility and the ability to hover are penalised by rotorcrafts' low flight endurance. Unlike their fixed-wing or lifting-gas counterparts, rotorcrafts need to maintain a Thrust-to-Weight ratio (T/W) of 1 to hover.

In practice, for practical designs, the drone's design maximum T/W is nearer to 2 to ensure a reasonable rate of ascend and manoeuvrability (rotational angular rate). This high thrust requirement results in low endurance. But with the current regulatory standards of needing to fly within the visual line-of-sight (LOS) [2], we can overlook the issues of short flight time and range.

A less widely used class of drones is the airship. Airships, also known as blimps, are vehicles filled with lighter-than-air gases or hot air to provide most to all of the lifting force. They are often fitted with propellers for steering. This gives them the combination of long endurance and the ability to hover [5]. The volume-to-weight ratio limits the craft to operations in open spaces. Owning to their benefits and drawbacks, airships are mostly used as high-altitude weather stations.

The other key factor of remote sensing with UAVs is the sensor. Various sensors and methods of data acquisition have been applied to great effect. A unique set of methods, associated and driven by the use of UAVs, is computer vision. Within this group of software technologies are Simultaneous Localisation And Mapping (SLAM) and structure-from-motion [6, 7]. High-resolution point clouds can be generated with the use of Light Detection And Ranging (LiDAR) scanners, depth cameras, and RGB cameras. By combining continuously streamed image data from these sensors with the sensor's attitude from an onboard Inertial Measurement Unit (IMU), a 3D map of the area can be constructed during or post-flight.

The post-processing of UAV acquired data has advanced alongside sensing technology. First, the spatial data need to be georeferenced. Similar to satellite and airborne laser data, the common approach was to establish ground control points, with which the data can be calibrated during post-processing [8, 9]. While this is a widely accepted practice, the use of ground control points is contradictory to the reasoning for UAV remote sensing. Ground control points often have to be manually set up. Therefore, accurately mapping an area with current techniques requires manual labour. The intent of using UAV remote sensing is to automate the data-gathering process and reduce human workload. The increasing use and decreasing cost of real-time kinetic global positioning systems onboard the UAV are significant steps towards automated remote sensing [10].

1.1.1 Design challenges in remote sensing with unmanned aerial vehicles

As alluded to above, the use of aerial platforms for remote sensing is not without concerns. As a tool for ecological monitoring, the issues with drone use stem from a combination of three stakeholders: technology, human, and the environment.

Limiting technologies

Operations in unconstrained environments have always been challenging for machines; this is no different for robots. While robots have become ubiquitous in this decade, they predominantly take the form of interconnected and digitised machinery, networked information sharing, and the use of artificial intelligence in predictive maintenance [11]. These improvements are mostly made in industries with stationary machines or specially designed factories [12, 13]. Away from such ideal conditions, robotic operations become exponentially more difficult. This is evident by the low predicted scope of automation for industries with less structured and non-standardised infrastructure [14, 15].

Great strides have been made in robotics research to embed aerial systems with sensing and perception, decision making and intelligence. Visual Inertial Odometry (VIO) algorithms have enabled robots to both localise in Global navigation satellite system (GNSS) denied environment and, with the 3D map, recognise and avoid obstacles [16]. The use of Reinforcement Learning (RL) on Neural Networks (NN) gives robots adaptive capabilities. They can use this capability to match their behaviours to their environment and plan better routes through traffic [17, 18]. Further integration on the micro-controller level enables UAV controllers to reach optimal performance without heavily experience-based manual tuning [19, 20].

Despite these advancements in software, the physical limitations of mobile robots have remained unchanged. Endurance is a bottleneck for battery-powered robots. The complexities of other power sources, such as internal combustion, negates their higher energy density. As a result, the chemical battery remains the most practical power source for robots. The increasing use of batteries, for electric vehicles and as buffers for renewable energy, continues to drive their

research [21].

Complex environment

Nature presents the most demanding environment for mobile robots. Beyond the need to function outdoors in everchanging weather, the rugged terrain and chaotic landscape are challenging to traverse and/or interact with. By using aerial robots, the difficulty of moving across land and water is mitigated. However, confined areas such as forest understories offer limited space to manoeuvre and have moving obstacles [22]. Also, the dense bio-matter can be a hindrance to telecommunication thus is difficult to establish functional ground control points. With such an abundance of life and micro-climates, yet difficult to access for both humans and robots, the forest understory is the most interesting and challenging case to study the potential aerial robotic solutions.

Of the various forest remote sensing platforms, most are imaging drones. These remote sensing UAVs take advantage of the open air space by flying at a standoff distance away from any obstacles. In forest environments, they are often flown above the tree crown level with the sensors scanning below the drone. Due to the canopy covering and scattering, data, such as the land surface temperature, on the forest floor is difficult to directly obtain [23].

Human factors

Ultimately, how we use drones will determine their usefulness to us. These human-controlled factors are often, and understandably, overlooked during early-stage robotics research. Nevertheless, human factors are critical when considering mass deployment in the field. With the ubiquitous use of drone imagining, ethics, safety, and regulations are becoming the foremost issues for UAV remote sensing.

A number of reasonable but conservative legal limits have been placed to ensure the safety of humans, the environment, and infrastructure when operating drones [24]. The noise and prop wash from the spinning propeller blades can disturb wildlife. The exposed blades can also cause physical damage if collisions occur. This is especially true when flying near birds. As

a consequence, UAV ecology operations can be constrained to a limited area, during limited seasons [2].

Furthermore, drone operations are largely limited to within visual line of sight. This is mostly due to the low level of autonomy and safety during autonomous operations. The issue with the level of autonomy has been mitigated rather quickly. Newly on-market consumer UAVs have demonstrated situational awareness and the ability to autonomously navigate safely. Operational safety, on the other hand, is currently qualitatively based on ad hoc judgements. Though UAVs are widely used, the social structure, command and control system, and physical infrastructure to support full UAV autonomy are in their infancy. In a similar light to autonomous cars [25], the governing legal procedures for automated drone use are still to be completed. Therefore, there is limited quantitative data to evaluate the risks of various procedures or benchmark the capability of the hardware.

1.1.2 Current outlook on using aerial robots in ecology

Mobilising aerial robots to conduct remote sensing is a multi-faceted problem. The complex environments, the limiting technologies, and the human-placed restrictions are equally challenging hurdles. We cannot fully automate remote sensing without a solution to address these three issues. Understandably, the scope of this solution is too broad to be covered within this thesis, nor is the solution entirely within the field of robotics. But we can break down the problem further to find its root.

The complexity of an environment is subjective to the robot, thus it will be solved with better designs. The confined forest understory is difficult for large ground vehicles to access. By making our robots flight-capable and compact, we mitigate the difficulties of traversing foliage. As hinted above, since most current robots need well-prepared infrastructures, the adaptability of the robot to its environment is a welcomed trait. Like forest-residing animals which interact with their environment by adapting their morphology, we should design robots that can morph to adapt to various scenarios.

Technological advancements can directly mitigate some human factor limitations. Should a

small robot crash, the damages caused would be much less significant than with larger platforms. Lighter robots are also less noisy when flying as less air is disturbed to generate the needed lift. For multirotor robots which operate in forests, the noise from the spinning propellers could be eliminated by perching the robot in the tree canopy and shutting off the motors.

However, there remains a circular problem of needing to prove the safety and reliability of new technologies and needing data from real-life flights to develop the said technology. We have limited data to assess the difficulties of autonomous task planning deep within forests. Often, the development of these control algorithms can be partially completed in simulated environments. The simulation can ensure that the general functionality is met before deploying the robot for real-life flights. In live flights, the algorithms can be fine-tuned for performance. The control algorithms for flying robots at the forest edges, where the trees are sparse and there is minimal aerodynamic interference, can be simulated in software. However, the uncategorised real-life complexities of the forest understory, where the micro-climates exist, amounts to a large simulation-to-reality gap. This gap is sufficiently large enough that most initial live flights within the forest understory would fail. The risk of crashes and failures further drives the fear of the safety of humans and the environment. Hence there arise various regulations to ensure that the level of risk becomes manageable. These regulations are perfectly reasonable, but nevertheless, they can be hurdles to the more challenging experimentation, where risks are inherently high. Therefore, just like other autonomous vehicles, the rate at which autonomous aerial robots develop remains heavily influenced by laws and regulations.

Ultimately, the root of these problems stems from the readiness of the technology. Drones that are designed for working within the forest understory will be more robust in operation. This will allow for more data to be gathered. With a better understanding of flying in the understory and quantifiable metrics to evaluate the robot's performance, more directed regulations can be adopted to ensure the safety of humans and the environment. As such, this thesis, here on, will focus on the design and development of multirotor robots for use within the confines of the forest understory.

1.2 Design of conventional multirotors

Much has been said about the use of drones, specifically multirotors, as platforms to carry sensors. Although multirotors will continue to improve in range/endurance [26], miniaturisation, autonomy, and sensor capability, they are inherently constrained by their design. To understand how to improve the design of multirotors, we must deconstruct their design to the core subsystem level, namely their layout, structure, and propulsion.

1.2.1 Layout

Current commercial multirotors have similar design layouts. Arms, or booms, extend from the central drone body outwards (Fig. 1.1). Motors and propellers are mounted on the end of the arms. The arms are often distanced such that the propellers will not interfere with each other, reducing aerodynamic efficiency. Most multirotors would use four rotors, making them quadrotors. This configuration utilises the least amount of rotors as possible without resorting to tilting the rotors for stability. It also maximises the available propeller area, gaining improved efficiency over platforms with more rotors.

The drone body would typically contain the flight control unit, electronics, and battery. By concentrating all the heavy components into a single location on the drone, namely the body, the drone's moment of inertia is at a minimum. This increases the agility, thus the controllability, of the UAV given the same propulsion setup. Positioning the propellers at equal distances from the body, the main component of the platform's centre of mass, the motors are able to share the workload evenly when at hover or at cruise. Assuming motors from the same batch are used, the even wear rate prolongs the time between overhauls.

Following this design methodology, the mission payload is also mounted to the centre body. For videography drones, the camera unit would be mounted on the bow or the underside of the body; the camera can be gimballed on one or two axes to provide mechanical stabilisation in flight. Interestingly, front-mounted cameras, to the author's best knowledge, have thus far been specially designed units, designed in concordance with their respective drone platforms.

Larger platforms are usually more customisable in payload arrangements. The higher payload capacity of a bigger platform allows the user to mount the more capable conventional camera instead of its lightweight counterpart. While the camera unit can be mounted on the top side of the body, aerial videography is often used to give a downward view. Therefore the camera is mounted on the underside. To avoid landing on the camera, landing gears are required. For gimballed camera units, retractable landing gears are commonly deployed to ensure a clear Field of View (FoV). The DJI Inspire series of quadrotors are unique in the professional videography multirotor UAV world in that it morphs its arms. The arms are held in the anhedral position for takeoff and landing (Fig. 1.1D). At cruise, the arms are configured in a dihedral to provide clearance from the camera's FoV (Fig. 1.1C).



Figure 1.1: **Commercially available multirotor drones**. (A) Image from Pxfuel. (B) Image from Pxfuel (C) Image from Pxfuel. (D) Image by NeONBRAND from Pxfuel. (E) Image by Antonio Jose Cespedes from Pixabay. (F) Photo by Klaus Foehl, CC BY-SA 4.0 https://creativecommons.org/licenses/by-sa/4.0, via Wikimedia Commons. (G) Image by S. Hermann and F. Richter from Pixabay. (H) Image by jotoya from Pixabay. (I) Image from Pxfuel.

1.2.2 Structure

The construction of multirotors follows the trends set by other appliances. As the target user moves from consumers, a mass market that attracts its target audience by producing good user experiences, to hobbyists (prosumers) and professionals, a smaller group of expert pilots which needs a broad spectrum of functions, the style of construction also changes.

Entry and mid-level consumers, often new to Radio Controlled (RC) MAVs, are enticed with products that are "highly convenient, easy-to-use", "convenient to carry, easy to fly", and have "greater flight safety" [27]. These requirements translate to compact, lightweight structures with limited access for user maintenance or modification. Thus, most multirotors of this class employ an exoskeleton design. The exoskeleton is formed with thin injection moulded polymer shells. The rigidity is provided by the high second moment of area. This allows the frame to be light yet strong. Internal mounting points for the electronics are integrated within the shells. This encloses and protects the sensitive components from accidental damage and access from untrained users. Furthermore, to ensure flight safety, both software and hardware protective solutions, such as crash avoidance and propeller guards respectively, are built into the drone. These design approaches result in a highly integrated product, albeit constrained in function.

Hobbyists and professional UAV pilots gravitate towards open platforms (Fig. 1.1B). This class of MAVs, while can vary in size, uses an open-skeleton design. They are designed with multiple decks, spaced with metallic standoffs, upon which the arms are mounted to. The modular design and exposed mounting points allow for easy interchange of payloads, are more accommodating of oversized components, such as larger battery packs, and can be readily modified to suit the pilot's needs. To achieve the stiffness required while minimising weight and structural volume, Carbon-Fibre-Reinforced Polymers (CFRP) are used extensively and the use of plastics is mostly confined to non-structural components.

1.2.3 Propulsion

Currently, most multirotors are Brushless Direct Current (BLDC) motor and propeller-driven aircraft. BLDCs are advantageous due to their efficiency at high rotational speed and good dy-

namic performance [28], respective requirements for prolonged and stable flights. When paired with lithium polymer battery (LiPo), the aircraft can be fully electrified with sufficient power density and acceptable energy density. LiPos can be recharged from any domestic electricity network with ease, hence the BLDC-LiPo architecture is popular in the consumer and commercial market. However, alternative multirotor propulsion systems have been trialled with various degrees of technological and commercial success.

Given the prevalent use of BLDC motors, electric-hybrid setups are commonly explored by researchers and commercial enterprises as a means to provide long-endurance flight. In fact, both petrol-electric and hydrogen fuel cell technologies have been successfully commercialised [29, 30, 31, 32, 33, 34]. However, to the author's knowledge, all current electric-hybrid multirotor manufacturers are small and medium-sized enterprises; multirotor UAV market leaders have remained focused on delivering battery technology.

Petrol-only propulsion mechanically links the engine to the propellers. Due to the need for variation of propeller rotational speeds and the difference of speeds between the propellers during flight, the transmission of a single-engine drone can become overly complex. An alternative solution is to employ collective-pitch control on each propeller [35]. Both designs have vastly higher part counts than their electricity-powered counterparts. Given the complexity of the design, which runs contrary to the current doctrine of viewing multirotors as simple and robust aerial platforms, these internal combustion engine-driven machines are only built as hobbyist and research projects.

1.2.4 Conclusion

It is clear that for the foreseeable future, battery-powered, BLDC motor-driven quadrotors with a centre body and outwards extending arms will be the most common form of UAV used for remote sensing in cluttered environments. At its core, a quadrotor is a simple machine. To augment its capabilities, we can target its rotors, arms, and body.

1.3 The role of morphological change

Viewing the spectrum of unmanned aerial vehicles in detail, one would note that most platforms satisfy the definition of a robot [36]. One can argue that all multirotors, by needing to self-balance to remain stable in flight, are indeed robots. However, such lenient interpretation may trivialise the potential of aerial robots as active entities in their ecosystems. For example, a conventional multirotor platform with an imaging sensor, though can be intelligent by path planning to avoid obstacles, is limited to a passive observer role in its environment due to its payload and prescribed task. Therefore, a multirotor can often be considered a passive actor, aiding its sensor while refraining from any interaction with its surrounding. Naturally, significant research efforts are placed on producing active robots which can physically interact with their ecosystems. This field of research is termed aerial manipulation.

Another significant means of interaction for mobile robots and their ecosystem is their method and medium of movement. Most drones are propeller-driven and move within our atmosphere. Birds, like drones, fly in the air. However, all flying animals also have alternative modes of locomotion; swans can swim, eagles can walk, and fruit bats can climb. By using different modes of locomotion, animals can gain better access to food or nurture their young amongst many other purposes. This multimodal locomotion capability is also an active front of aerial robotics research [37, 38, 39, 40]. By diversifying their medium of movement, robots can access previously inaccessible locations.

Manipulation and multimodal locomotion are accomplished by animals through morphing their body. Morphing, the change of one's form or shape, has been the principal paradigm for nature, both plant and animal life, to move. This is fundamentally different from the approach of locomotion taken by humans since the invention of the wheel. It is unsurprising to find that all man-made self-powered vehicles, from turbofan-powered airliners to steam-driven paddle wheels, use rotary motion to provide movement (Fig. 1.2A-C). With the driving component designed with radial symmetry and having an infinite range of circular motion, a smooth and continuous force can be applied to the medium of locomotion. Undoubtedly efficient and powerful when in their prescribed element, they do not offer the adaptability shown by animals.

Animals move by reciprocal motion (Fig. 1.2D-F). They manipulate their body by contracting and relaxing various muscle groups which are hinged between ball or pin joints and connected to the bones on either side via tendons. When comparing by the cost of transport, the energy expenditure per unit weight and distance travelled, most animals are less efficient than their mechanical counterparts [41, 42]. However, this musculoskeletal system design, while limited in the degree of motion, offers a greater Degrees of Freedom (DoF) per joint. Animals harness the changing of their morphology, gained through the higher DoF per joint, to be adaptive in the wild.

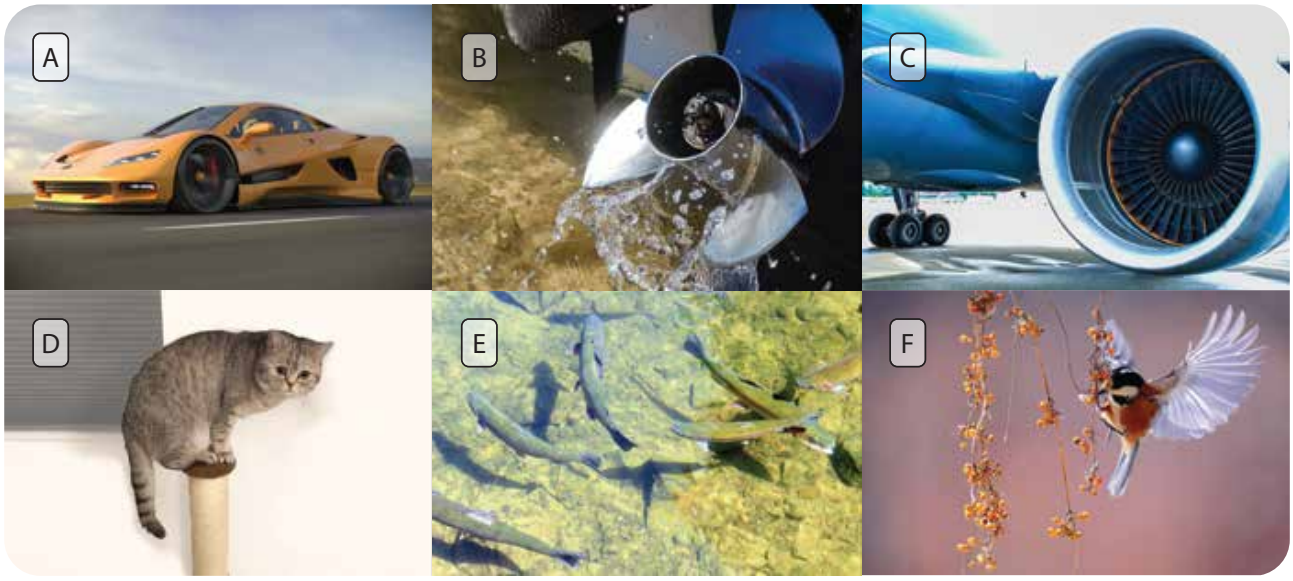


Figure 1.2: **A comparison of conventional vehicle and animal locomotion principles** on land, sea, and air. (**A**) wheels on cars, (**B**) water propellers, and (**C**) turbofan engines on a plane all use rotary motion to move their respective vehicle. They can only change their rotational speed but not their geometry. Animals use a system of mobile limbs, enabling them to achieve incredible feats of agility, exemplified by (**D**) a cat balancing on a pole. (**E**) Fish, and (**F**) birds move using reciprocal motion with a number of articulated joints.

1.3.1 Morphing in nature

Morphing in animals can take many forms, and for different functions. With most jawed vertebrates, their bodies are laid out such that their torso contains all the organs required for homeostasis; the limbs are exclusively used for interactive tasks such as locomotion [43], tool use, active protection and combat, and stabilisation (Fig. 1.3). In their case, the bones, joints,

muscles, and skin work in synergy to create movement. As such, it is imperative to analyse animals' limb use.

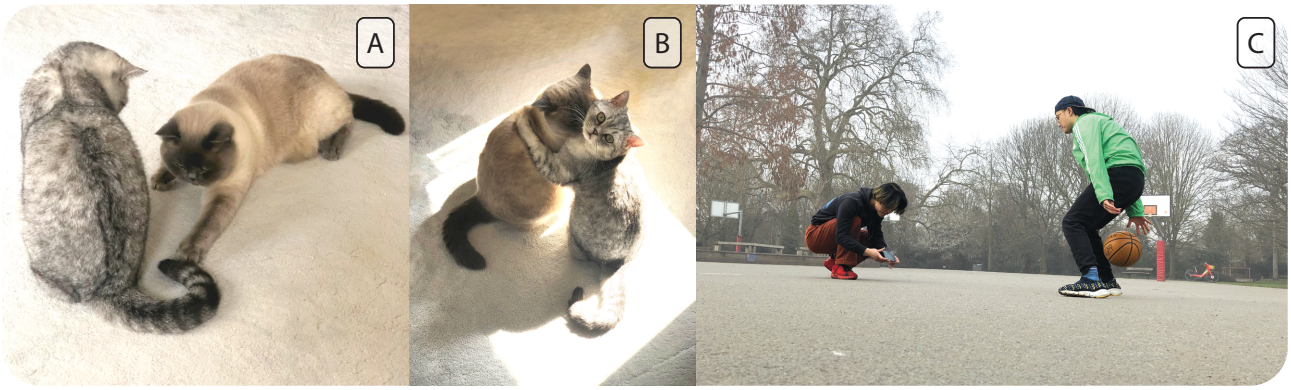


Figure 1.3: **The versatility of animals in action**. (**A**) Cats play fighting and (**B**) hugging to stay upright. (**C**) A cameraman holding a camera at ground level filming a basketball player dribbling a ball behind his back. While robots have accomplished singular tasks to greater accuracy, to date, none have mastered the breadth of skills shown by animals.

Birds' wings extend for flight and fold in to dive or to rest when landed. When folding, the wing is hinged at the bird's shoulder and at both ends of the forewing. All the joints rotate on the plane of the wing. This simple change of morphology enables a peregrine falcon to both cruise at approximately 65 km/h to 97 km/h and perform 390 km/h dives [44]; a speed ratio between cruise and maximum rated speed that most modern aircraft cannot sustain. In addition, to generate thrust, birds flap their wings. This requires rotating the whole wing about multiple axes [45]. This rotation is achieved with a ball-and-socket joint at the shoulder. The ball-and-socket is the most mobile joint found in animals, thus it is understandable that most joints connecting limb roots to the core body are of this nature as it maximises the workspace of the limb.

Birds use their wings to fly, and legs to perch. But animals can also use the same limbs, but apply different movement patterns to achieve different forms of locomotion. Bats, for example, use their arms and legs both to fly and climb. And some mammals would apply the same approach to achieve terrestrial-aquatic locomotion. This exemplifies the adaptability that is inherent in systems that can change their form.

The limbs of quadrupeds are highly adaptive. Quadruped mammals, while varying in stature,

move in similar ways [46]. Animals, such as cats, will select the specific gait depending on their needs at given speeds [47]. These gaits differ in the timing of the strides as well as the stride length. Compounding further is the ability of some of these animals to swim with a specialised aquatic gait [48]. Alternative gaits are also employed ad hoc when the use of a hind limb is lost [49]. These abilities demonstrate intelligent behaviours which are achieved with the combination of high DoF adaptive mechanisms and control methodologies.

Discrete attention should be paid towards the more unique adaptations specific to certain species, such as the human's arms and the spider monkey's prehensile tail. The human arm, in particular, is unparalleled in its ability to generate fast, powerful, and precise motions simultaneously when throwing projectiles [50]. The external rotation of the shoulder joint stores elastic energy within muscles which is then released during the internal rotation phase to launch the projectile further. The ability to throw can be attributed to the human's plasticity, allowing humans to better adapt their body towards specialised tasks. The New World monkeys, a group of primates to which the spider monkey belongs, have prehensile tails [51]. Their prehensile tails are a defining feature that differentiates them from the Old World monkeys. This adaptation functions in conjunction with the New World monkeys' predominately arboreal lifestyle. While the Old World monkeys, from Africa and Asia, have tails, the muscular structure limits their flexibility and controllability. With tendons crossing fewer joints, the New World monkeys' tails are able to flex sufficiently to wrap and grip onto branches when traversing tree canopies. Incidentally, Old World monkeys spend more time on the ground, with a few species being primarily ground-dwelling.

Beyond the movement of joints, morphing also extends to the change of rigid skeletons. Arthropods, animals with hard exoskeletons, will morph and grow their body by undergoing a moulting process. During moulting, crustaceans, such as the fiddler crab, will also regenerate lost limbs and shed the harmful metals accumulated in its body [52].

While crustaceans moult to grow and perform therapeutic treatments, insects undergo a much more drastic transformation called metamorphosis. This is a process where an animal would change its form; for example, dragonfly larvae growing wings. In doing so the animal will often be able to access new environments through its new body composition. Both the adult dragonfly

and its larvae are carnivorous. However, larvae live and hunt underwater, only emerging from the water when they can breathe in air and are ready to metamorphose. Adult dragonflies are known to be rather aggressive flyers, often engaging in aerial combat and cannibalising smaller dragonflies. The division of habitats between dragonfly adults and larvae reduces the competition for food, increasing the survivability of the species. Having two distinct body plans for each stage of an insect's life also allows for more opportunities to evolve the species as a whole [53].

The mechanics of metamorphosis is worth noting. Although substantial programmed cell death and stem cell growth occur, some organs within the insect would be tasked with revised requirements [54]. The material in some of the dying cells is also recycled. This mechanism seems to maximise the use of the bio-material available to the body and be an efficient form of metamorphosis.

1.3.2 Morphing in robotics

Morphing in robotics encompasses a multitude of terms and sub-genres. Morphing robots are often referred to as reconfigurable, transformable, foldable, deployable, adaptive, or origami-like. While the various terminology is not strictly interchangeable, they are fundamentally used to describe the change of the robot's geometry to access different abilities.

Like in nature, morphing robots, too, take many forms. The most trivial solution in morphing hardware design is to mount robotic arms on existing mobile platforms, such as vehicles and drones. The benefits of this method are the simplicity of assembly and robustness. These designs are often seen on research platforms focusing on the interaction behaviours and the control of the vehicle where the emphasis of the research is on the task and not the capability of the robot as a whole.

It is more useful to define morphing platforms as a monolithic system which augments its geometrical shape. Fitting this description of morphing platforms are a breadth of land, sea, air, and multimodal vehicles. We examine the design of these platforms, gaining insights into the methods and ways with which robots morph to accomplish their prescribed task.

Inspired by our own image, humanoid robots are amongst the first attempts at constructing morphing robotic systems. These robots, exemplified by ASIMO, mimic the joints on human legs. With the difficulties of achieving stable bipedal mobility, robotic quadrupeds are the next to appear. These four-legged robots are designed to closely follow the gaits of quadrupedal animals. Using legs increases the adaptability of the platform, allowing them to traverse more varied terrains [55], and even in water [56]. However, legged transport comes at the cost of speed and energy efficiency, the two characteristics at which wheels were designed to be better. To combine the benefits of legged and wheeled transport, newer platforms utilise both [57]. On the other hand, it was also shown to be viable to reinvent the wheel. Passive mechanisms within the wheel can extend to form legs to climb over vertical surfaces [58]. Whereas integrating active origami folding to wheels can expose and retract aggressive tread patterns for different terrains [59].

Being a dense fluid medium, morphing in water brings its own challenges not seen on land. Water-based morphing platforms are broadly involved with reciprocal motions of their body to generate thrust. The unique interplay between the flexibility of the body and the fluid interactions can result in highly efficient means of thrust generation [60].

Locomotion in the air offers the most freedom in motion. Thus it is reasonable to see a wide array of designs. A number of vertical take-off and landing aircraft do so by orientating their thrusters [61]. The use of tilting rotors has also expanded the abilities of quadrotor platforms. The decoupling allows the rotors to counteract the disturbances whiles keeping the body stable. Tiltrotor robots can better generate forces and torques when performing surface inspection [62, 63, 64]. Depending on the direction of flight, tiltrotors can also have reduced cross-sectional area which aids in traversing narrow openings between obstacles [65].

Alternatively, inspired by insects, flapping drones use high voltage and piezoelectrics to reach high wing-flapping frequencies. Flapping has the benefit of being simple to miniaturise as the oscillatory motion can be created by a monolithic actuator driven with solid state electronics [66]. Flapping can also be scaled to larger drones using longer stroke length and lower frequency dielectric elastomer actuators [67], and even larger with multi-linkage mechanisms [68]. These larger platforms are driven by BLDCs to produce a greater range of motion, compensating for

the lower flapping frequency [69]. Despite being more mechanically complicated than fixed-wing propeller-driven drones, large flapping-wing drones avoid the dangers of exposed fast-spinning sharp propellers and can be safer when flying near humans and animals.

Multimodal or multi-terrain robots most exemplify the use of morphing mechanisms. Similar to many animals, diversifying the robot's mode of locomotion produces a more robust machine. Robots with two or more modes of locomotion can actively select the medium that best suits their current situation.

Sailing and flying both utilise aerodynamic surfaces, albeit with the surfaces in different orientations. Thus, aerial-aquatic (surface) platforms could morph their wings between vertical and horizontal to sail and fly respectively [70]. The morphing of a fixed-wing robot can also aid in diving beneath the water's surface. Diving beneath the water surface from height poses both a fluid dynamic and structural engineering challenge. Higher speed dive means the robot can reach a deeper depth, but it increases the impact stresses on the robot's structure; the greater the frontal surface area, the larger the impact force. Yet, operating in a marine environment, these robotic platforms need to use large and slender wings to increase flight endurance, thus increasing the robot's frontal surface area. The common diving strategy for animals is to reduce their frontal area by retracting their limbs before the imminent impact. Robots have used this strategy to great effect [37, 71]. By retracting and streamlining their wings prior to impact, these flying-diving robots can retain the aerodynamic benefits of a long and slender wing whiles reducing the structural stresses from diving into water [72].

The commonality of air and water both being fluids can be taken advantage of by aerial-aquatic multirotors with tilting rotors [73]. By rotating the rotors onto the horizontal plane, they can act as thrusters whiles the robot's buoyancy system controls the depth.

Aerial-terrestrial locomotion is the ability to move in the air and on land. This subset of multimodality differs from aerial-aquatic locomotion as it encompasses two vastly different media. While some robots can borrow underground [74], terrestrial locomotion broadly refers to moving on land. Current morphing aerial-terrestrial robot designs choose between two modes of flight, fixed-wing or rotor-wing, and two modes of terrestrial locomotion, using wheels or legs. This creates four possible combinations of aerial-terrestrial locomotion as shown in Tab. 1.1.

In fact, there are limited examples of using morphing to create robots that can adapt between aerial and terrestrial locomotion, most would use separate mechanisms for air and ground mobility [75].

Table 1.1: Examples of morphing aerial-terrestrial robot research, separated by the methods of aerial and terrestrial locomotion. To the author's knowledge, there have yet to be functional fixed-wing robots that morph into wheeled platforms or rotor-wings which morph into legged platforms for terrestrial locomotion.

	Fixed-wing	Rotor-wing
Wheeled	...	[76]
Legged	[77]	...

Some robots can use morphing as a means of assembly [78]. Either by pre-embedded mechanisms or external inputs, the robots fold into their functional form [79]. This is beneficial in simplifying the manufacturing and assembly process and can aid in transporting the robot when not in use.

1.3.3 Comparing roles

Broadly speaking, morphing in nature and robotics play similar roles. Morphing increases the adaptability of the agent to various environments or tasks. Most morphological aspects identified in Section 1.3.1 have their respective robotic counterparts. However, the similarity in roles does not imply similarity in function.

Current robots can replicate similar motions shown by animals. But the method of actuation forms a large divide between animals and robots. The ability to store elastic energy and generate force within the same muscle group can be mimicked with feedback-controlled motors [80, 81]. With a sole motor, the energy can be recuperated but not stored as elastic potential energy. Robots can use electric motors alongside systems of springs to provide compliance, thereby aiding in their stability when stepping down a step [82], or dynamic capabilities such as eccentrically loaded vertical jumps [83].

Despite these advancements, robots are still outmatched by animals in system performance. So far, the best throwing robots could not match humans in their dexterity of capable tasks.

Flapping-wing robots cannot structurally sustain the number of motion cycles and lack the endurance of bees and hummingbirds [84, 67]. It is also fascinating that animals, even with the many generations of evolution, retain the same structural layout despite operating in vastly different environments; a trait not shown with man-made machines.

While animals have been shown to be highly adaptable and robust, they are not without flaws. The albatross spend long periods in flight so its wings are optimised for high-speed cruise [85]. Thus, they encounter difficulties when executing low wind speed manoeuvres, such as landing without a headwind [86]. This showcases that there are physical limitations despite nature's best efforts in creating robust and adaptable animals. The lesson drawn is that, while the usefulness of nature-inspired morphing designs is undoubted, roboticists must carefully consider the trade-offs when using said designs to increase adaptability. In other words, we should expect similar shortcomings of nature to manifest in bio-inspired robots.

1.4 Integrated morphing quadrotor robots

The need for remote sensing in the forest understory, the lack of capable aerial platforms for this role, and the advantages of morphing design have coalesced to form the aim and hypothesis of this thesis:

Can integrated morphing quadrotor designs benefit aerial robots for remote sensing in the forest understory? If so, how and where do they benefit? And what are the penalties and limitations?

I conceptualised numerous integrated morphing quadrotor designs to examine this hypothesis (Fig. 1.4). Of these novel designs, five are prototyped and of these, four are airworthy platforms. In this thesis, a design is considered "integrated" if both conditions hold true:

- the subsystem cannot perform its primary function when isolated from the system
- the system cannot perform its primary function with the subsystem removed

The platforms differ in their tasks and the subsystem upon which the morphing design is applied. In Chapter 2, I explore multi-directional thrust vectoring by synchronised rotor tilting

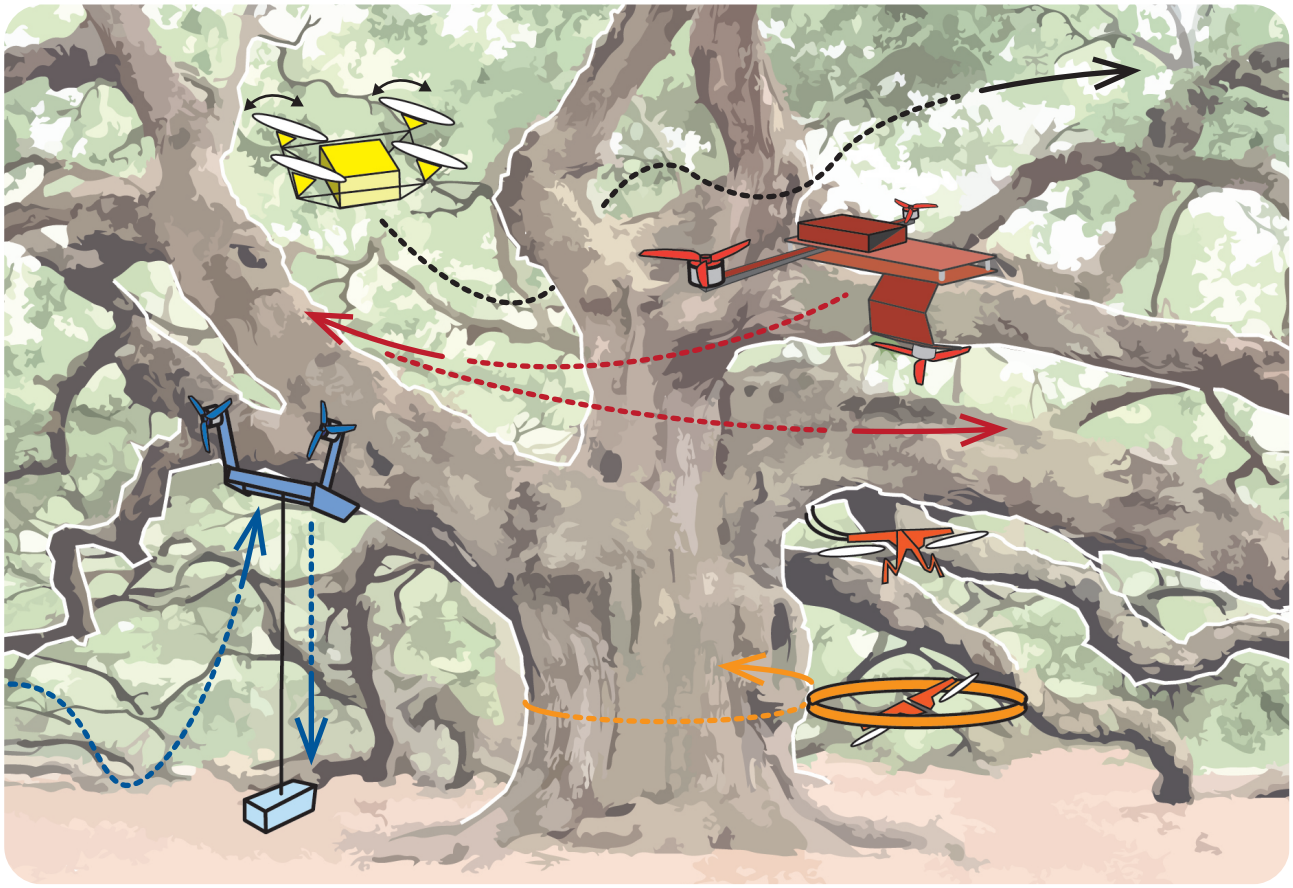


Figure 1.4: **Concept** drawing of morphing quadrotors in the forest

(Fig. 1.5). Chapter 3 continues on to derive the dynamics and properties of the biaxial tilting mechanism and considers possible design improvements. The scaling of the design architecture also is explored in detail. The tiltrotor is further explored in Chapter 4. I designed a quadrotor with an integrated tilting measuring wheel to examine the effects of morphing on lightweight platforms. In conjunction, I studied the effects of the Flight Controller placement on tiltrotors with numerical simulation in Chapter 5. Given the option of placing the FC on the rotor body and the payload body, I simulate how variations in the ratio of inertia between the two bodies and the controller frequency affect flight performance. In Chapter 6, I explore the use of active morphing on the quadrotor structure to achieve autonomous perching (Fig. 1.6). Chapter 7 also examines perching but focuses on the post-perch data recovery process. I designed a passive perching robot with an RC controlled low-power idle electronic system to ensure the robot can be recovered after gathering data for an extended duration (Fig. 1.6). Chapter 8 examines the

use of compliant structures to create lightweight, single-part assembly quadrotors and presents the offboard autonomous flight system that I designed to test all the prototype robots in this thesis (Fig. 1.7).

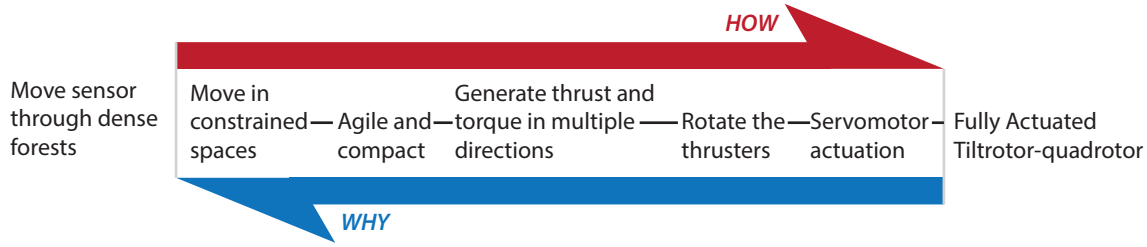


Figure 1.5: **Function Analysis System Technique (FAST) diagram of the tiltrotor-quadrotors in the forest robot**.

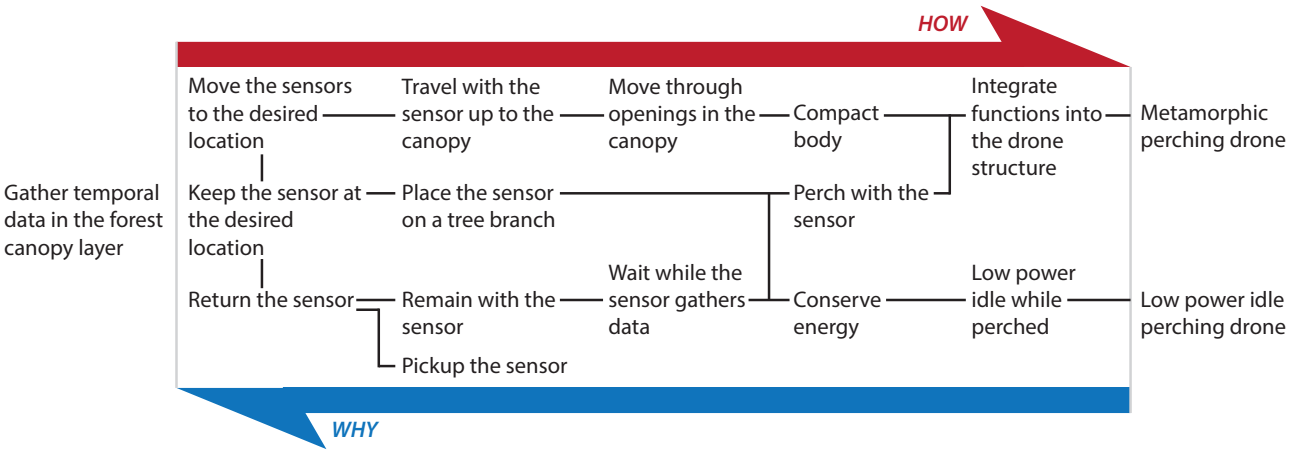


Figure 1.6: **Function Analysis System Technique (FAST) diagram of the metamorphic perching drone and the low-power idle electronics**. While sensor deployment and pickup is a viable option, it is not considered in this thesis.

The rest of this chapter will introduce some of these robots and highlight the insights gained when considering them as a collective. Chapter 9 will offer a broader perspective on Morphing Integrated Quadrotor Robots (MIQRo).

1.4.1 The size of the platform and the scaling of a quadrotor arm

An obvious but significant observation across the range of robots was the impact of vibrations induced by the morphing components. These vibrations are mitigated by different means on

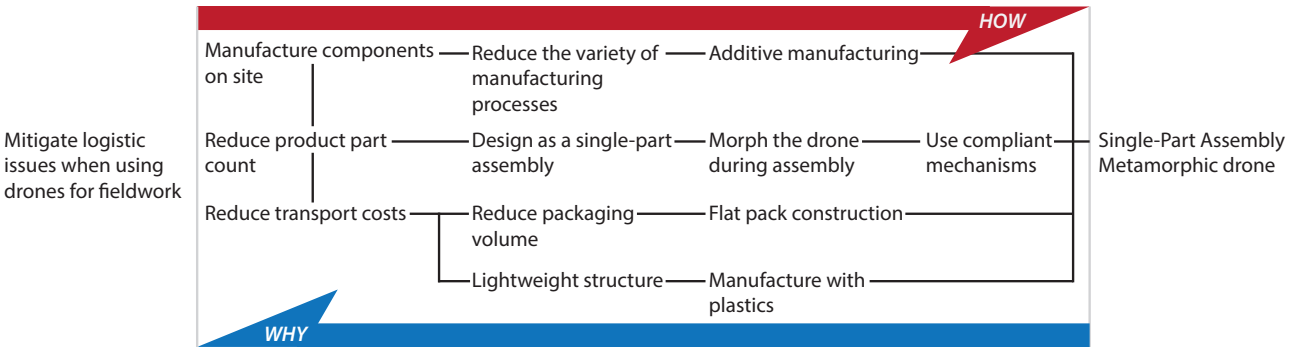


Figure 1.7: **Function Analysis System Technique (FAST) diagram of the single-part assembly metamorphic quadrotor**.

the robots. However, I noted, through subsequent generations of the same robot, that the size of the robot directly impacts the significance of the vibrations.

Thus, let us first consider the size of the robot. As mentioned above, multirotors have arms extending from a central body. Much of the quadrotor size is determined by the arm length, which is set by the size of the propeller. Although this is a rudimentary rule of thumb, most conventional multirotor designs follow this rule to offer a balance between aerodynamics and structural weight [87].

The viability of scaling the quadrotor arms can be examined by applying the disk actuator theory to the drone rotor. A stationary rotor draws power (P) as a function of thrust (T), air density (ρ_{air}), and the area of the rotor ($A_{\text{prop}} = \pi R_{\text{prop}}^2$) as shown below,

$$P = \sqrt{\frac{T^3}{2\rho_{\text{air}} A_{\text{prop}}}} \tag{1.1}$$

which can be rearranged as

$$T = C_0 P^{\frac{2}{3}} R_{\text{prop}}^{\frac{2}{3}} \tag{1.2}$$

where C_0 is a constant given that a stationary rotor means the air density does not change, and R_{prop} represents the rotor radius. We can simplify the morphing perching arm model as a beam hinged at the arm root with the rotor at the free end. The arm is equated to a cantilever beam when locked into its rigid configuration for flight. A number of scale factors are considered, foremost the material limits.

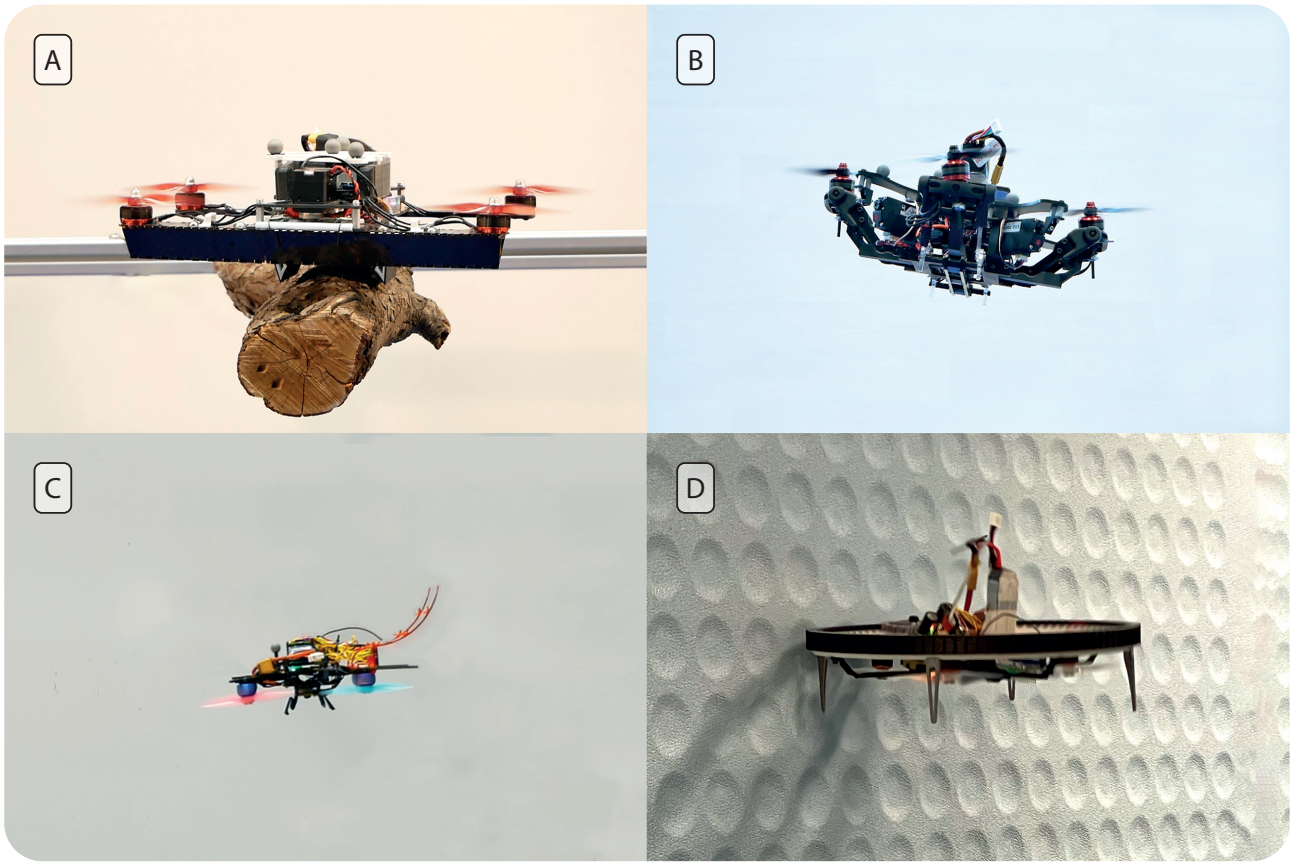


Figure 1.8: **Prototype robots in flight**. The aerial robots shown in this figure are tested to be airworthy. (**A**) Active morphing autonomous perching robot approaching a branch (Chapter 6). (**B**) Multi-directional synchronised tiltrotor (Chapter 2). (**C**) A $100g$ robot built from a single-piece folded structure with a flexible antenna attachment, photographed by Feng Xiao. (**D**) A sub-$250g$ quadrotor with an active tilting protective ring/measuring wheel stably contacting the wall, photographed by Pham Huy Nguyen (Chapter 4). All photographs are edited for clarity.

Rigid structures, such as a quadrotor arm, must operate under the ceiling set by the material yield strength. A quadrotor arm, idealised as a hollow circular Euler–Bernoulli beam with a radius r, thickness t, length L_{arm}, second moment of area $I_{\text{arm}} = \pi r^3 t$, and a mass of $m_{\text{arm}} = 2\rho\pi r t L_{\text{arm}}$, has a maximum stress of

$$\sigma_{\max} = \frac{m_{\text{arm}} R_{\text{prop}}}{I_{\text{arm}}} = \frac{T L_{\text{arm}}}{\pi r^2 t} \tag{1.3}$$

As $L_{\text{arm}} \propto R_{\text{prop}}$ due to the propeller clearance and the proportion is a trivial number for the

purpose of this derivation, I assume $R_{\text{prop}} = L_{\text{arm}}$. Substituting (1.2) into (1.3),

$$P^{\frac{2}{3}} R_{\text{prop}}^{\frac{5}{3}} \propto r^2 t \sigma_{\max} \tag{1.4}$$

$$R_{\text{prop}}^5 \propto \frac{r^6 t^3 \sigma_{\max}^3}{P^2} \tag{1.5}$$

we see that the radius of the arm, needed to withstand the thrust loading, scales almost linearly against the increasing rotor radius.

However, the airworthiness of the drone is also dictated by whether it can be controlled by the Flight Controller (FC), which houses the IMU. As the FC operates on low-pass filtered IMU data, any unfiltered low-frequency vibrations will be acted on by the controller and degrade the flight performance. For this analysis, I simplified the quadrotor arm as a simple spring-mass system with a natural frequency

$$\omega_z = \sqrt{\frac{k}{m_{\text{arm}}}} = \sqrt{\frac{T}{m_{\text{arm}} z}} \tag{1.6}$$

And with the beam tip deflection $z = \frac{T {L_{\text{arm}}}^3}{3 E I_{\text{arm}}}$, the natural frequency can be formulated as

$$\omega_z = \sqrt{\frac{3 E I_{\text{arm}}}{m_{\text{arm}} {L_{\text{arm}}}^3}} = \sqrt{\frac{3E}{2\rho}} \frac{r}{{L_{\text{arm}}}^2} \tag{1.7}$$

$$\omega_z \propto \frac{r}{{L_{\text{arm}}}^2} \tag{1.8}$$

Therefore, for a given minimum natural frequency that the drone arm must achieve, the radius

of the arm varies by

$$r_0 = C_1 \omega_z {L_0}^2 \tag{1.9}$$

$$r_1 = C_1 \omega_z (L_0 + \Delta L_{\text{arm}})^2 \tag{1.10}$$

$$\Delta r = C_1 \omega_z (2 L_0 \Delta L_{\text{arm}} + {\Delta L_{\text{arm}}}^2) = C_1 \omega_z {L_0}^2 \left(2 \frac{\Delta L_{\text{arm}}}{L_0} + \left(\frac{\Delta L_{\text{arm}}}{L_0} \right)^2 \right) \tag{1.11}$$

$$\Delta r = r_0 \left(2 \frac{\Delta L_{\text{arm}}}{L_0} + \left(\frac{\Delta L_{\text{arm}}}{L_0} \right)^2 \right) \tag{1.12}$$

$$r_1 = r_0 \left(\frac{\Delta L_{\text{arm}}}{L_0} + 1 \right)^2 = r_0 \left(\frac{L_1}{L_0} \right)^2 \tag{1.13}$$

where C_1 represents the proportional scale factor of (1.8). (1.13) shows that the arm radius would have to increase by the square of the arm length to achieve the same natural frequency. Thus the drone arm would not scale favourably when considering flight control.

Given that the cross-sectional dimensions of a quadrotor arm and its length do not scale linearly, larger platforms would likely suffer from unproportionally increasing aerodynamic drag. Alternatively, the software low-pass filter can be tuned, but to the detriment of the platform's flight agility. Viable complete solutions to scaling up would be to adopt stiffer structural designs or add vibration-damping elements to the platform. However, both solutions will result in significant design changes which may not be possible given the complex geometries of morphing designs. This simplistic analysis hints towards an intrinsic benefit of smaller, or scaled-down drones needing fewer considerations towards the ratio between their structural stiffness and mass; they are simpler to design.

1.4.2 Perching robots

The two platforms designed for perching shared the approach of using the rotors to aid the transition process of the morphing arms. This is where the similarities end.

The Sloth (Chapter 6) was conceived as an all-purpose, fully-autonomous platform that is capable of perching between flights to various locations. The need to conduct autonomous missions necessitates an onboard computer to manage high-level tasks such as localisation and

trajectory planning. While this penalises the overall weight, the availability of an onboard computer gives the designer, me, the greater freedom to add complex componentry and control them to a greater depth. In this case, the onboard computer can control a smart servomotor via ROS, feeding back its telemetry to the operator. The greater level of control enables the use of active perching. With active perching, the sequence of actions that the platform takes to perch and return to flight is precisely controlled by tunable software parameters. Thus, the perching behaviour of the platform can be changed, depending on the size of the perch target, or take mitigating actions if perch failure is detected.

However, the realities of operating in complex outdoor terrains cannot be ignored. The complexity of outdoor terrains often produces scenarios and behaviours beyond what could be planned for at the design stage of the robot. Whiles the Sloth robot is shown to be able to perch on various tree branches in the forest, its full automation for identifying viable perch locations in outdoor environments is, to date, an ongoing area of research. This drew me towards exploring its antithetical approach. So I developed the Breakaway Drone to explore the following question: "If autonomously avoiding tree branches is so difficult, what is the difficulty of manually crashing head-on into one of them?" (Tab. 1.2).

The Breakaway Drone (BreaDe), presented in Chapter 7, is developed in conjunction with ecologists for the explicit aim of gathering eco-acoustic data in the forest canopy, recording audio data across several days. Having noted the difficulties of GNSS and VIO localisation in leafy forests both from experimentation and literature [88, 89], and seeing the impracticalities of setting up mobile Real Time Kinematic Positioning (RTK) base stations whiles deploying sensors in multiple locations, BreaDe offers a practical short term tool for ecologists in the field. The Breakaway Drone gives the operator, likely an ecologist with no prior knowledge of field robotics, the sole task of flying the robot into a tree branch.

BreaDe perches automatically upon impact; the arms of the robot, aided by the thrust of the propellers, fold around the tree branch. The perch is held by passive mechanisms. To retrieve BreaDe to access its eco-acoustic data the robot self-separates into two parts, the quadrotor structure with the morphing perching mechanism and the motors, and the robot's core, containing the acoustic sensor and the electronics. The quadrotor structure remains

Table 1.2: Comparison between active and passive perching aerial robots.

Categories	**Active perching**	**Passive perching**
Platform size (mm)	300x180	250x165
Platform mass (g)	750	600
Perching direction	Top-down	Bottom-up
Perching actuation	servomotor	impact, rotors
Deperch actuation	rotors, servomotor	manual
Perch holding mechanism	gearbox friction, servomotor	ratchet, spring

perched on the tree as an anchor while the core of the robot is lowered slowly via an onboard crane. With the vital parts of the robot recovered safely, pulling on the cord will bring down the rest of the robot.

1.4.3 Morphing in flight

Multi-directional quadrotors can fly in almost any orientation and direction, manoeuvring in ways that conventional quadrotors cannot. Fully-actuated multirotors possess much greater freedom of movement than conventional multirotor drones, allowing them to perform complex sensing and manipulation tasks. The synchronised tiltrotor drone (Chapter 2) achieves multi-directional flight by a planar mechanism joining all the rotors on the robot. The addition of two servomotors on the quadrotor perfectly achieves fully-actuated flight.

The planar mechanism decouples the roll and pitch of the robot body from its translation in the horizontal plane ($X - Y$). The rotors are mounted on 2-DoF gimbals, allowing pitching and rolling relative to the drone body. The prototype was demonstrated to be able to track trajectories with minimal rotation on the robot body. The quadrotor can also hold a stationary hover at 30° incline. A video, shown in `https://youtu.be/8HOQl_77CVg`, demonstrates the flight. The synchronised tiltrotor has the potential to orientate heavy sensor payloads and fly nimbly through the dense forest canopy.

Beyond proving the feasibility of 6-DoF fully-actuated quadrotor flight with six total actuators, theoretical analysis shows that morphing the rotors reduces the frontal area of the robot for lateral and vertical fight, but only when it is above a threshold tilt angle. However, I observed that while frontal area reduction exists in functional robots, it is heavily compromised by the

form factor of the robot's payload. Furthermore, as derived in Chapter 3, if the rotors' Centre of Mass (CoM) is offset above the CoM of body, the platform body exhibits parasitic motions opposite to the direction of rotor tilt.

The flying measuring ring, in Chapter 4, is designed as a semi-autonomous tool to aid the measuring of the tree Diameter at Breast Height (DBH). The tree DBH is a fundamental index in ecology and forestry. DBH is used to model and extrapolate important data such as tree growth and volume. Measuring DBH largely remains a manual process of using tools such as a tape measurer. Ecologists are increasingly using drones with imagining technologies such as lidar scanning and depth mapping to aid in measuring DBH. However, these sensors are heavy and expensive. Flying near trees in a forest poses a significant danger of collisions. I present a lightweight, low-cost system that can measure DBH and protect the drone from accidental collisions. By utilising a morphing design approach, I built a morphing sub-250g quadrotor drone. The drone uses its protective ring to measure the circumference of the tree trunk and protect itself from damage.

At first glance, the synchronised tiltrotor and the tilting measuring ring seem rather unrelated. Yet upon further consideration, they are rather similar. In fact, when they move forward with the rotors tilted but the tiltrotor body and the ring at level, they are, in the dynamics and mechanical sense, the same. The two robots have been shown to be stable in this flight condition. Both robots have lightweight rotors and components tilting about a non-rotating body of a higher mass and moment of inertia; both have position-controlled tilting actuators.

The difference lies in the positioning of the two robots' FC. Having tilting rotors means we can consider the drone body and the rotors as separate masses. The synchronised tiltrotor FC is mounted to its body, its main mass. The tilting ring FC is mounted with its rotors, which constitute the robot's minor mass. As for these robots, their inertia approximately correlates to their mass, we can assume that the synchronised tiltrotor FC is mounted to the body with the larger inertia, and the tilting ring FC is mounted to the body with the smaller inertia.

The numerical study, presented in Chapter 5, would suggest mounting the FC to the body with the larger inertia to maximise pose tracking performance. However, in practice, I observed that while the body of the synchronised tiltrotor drone remained stable in flight, the

position tracking was comparatively poor. Both PID and PD position controllers were tested with negligible differences in performance. By elimination, this leaves the issue to be with the hardware. The open-loop servo position control means the robot cannot correct for any geometrical imperfections of the tilting mechanism.

The tilting ring does not suffer from this problem. With the rotors and the FC mounted to the same rigid structure, the stability of the drone in flight is evidence of the rotors accurately tracking the command. However, as the ring tilting actuator is in open-loop control, precise control gains must be found to keep the ring level. Too high a gain mapping servo angles to Pulse Width Modulation (PWM) input will cause instabilities upon takeoff. Flying with a low gain is stable, but it results in the ring not being perfectly horizontal.

A comparison of the robots would suggest the opposite approach to FC placement for both. Tilting the FC in synchronisation with the rotors would allow more accurate control over the rotor position, leading to better position tracking but at the detriment of less accurate body orientation control. In direct contrast, placing the FC on the main mass rather than the rotor tilting structure would allow for more accurate body orientation control, desired for the tilting ring robot. While one could argue for adding IMU on all moving bodies to improve control, there may be space, weight, or electronics capability constraints. Thus, as a rule of thumb, keep the feedback sensor as close as possible on the kinematic chain to the part that most needed to be accurately controlled.

1.5 Summary

In this chapter, I analysed how aerial robots are currently being used in ecological monitoring. We see that while quadrotor robot use is viewed positively by the ecological research community, there are limitations. I analysed these issues and noted that technological advances can remove the barriers to the broader use of robots for ecology.

Under the conventional design paradigm, quadrotor robots are limited in the variety of their capabilities. To expand their capabilities, I explore how animals and other types of mobile robots use morphing as a way to acquire new skills. I further describe how I can advance

quadrotor robot design by incorporating morphing as a core design principle. Comparing and contrasting the robot design that I have produced, I draw out insights into the best practices of designing integrated morphing quadrotor robots.

Chapter 2

Design of a multi-directional quadrotor UAV

2.1 Introduction

Unmanned Aerial Vehicles (UAVs) with multirotor configurations have gained popularity in aerial robotics research [90], enabling a variety of applications, from close proximity infrastructure maintenance to ecological monitoring [91, 92, 93, 94, 95]. Conventionally, rotors are fixed perpendicularly to the plane of the platform with steering achieved by differential thrust. Such a simple and effective design gave rise to the use of multirotor systems in applications that require robustness and high thrust-to-weight ratios.

Fixing the rotors in the same orientation on the platform couples the multirotor's rotational and translational degrees of freedom (DOFs). As a result, it is difficult to achieve the desired dexterity to conduct physical interactions, such as sensor installation and surface inspection, and aerial filming. Naturally, there is active interest in decoupling the DOFs, allowing the multirotor to fully actuate its 6-DOF [96].

"Multi-directional" can be defined as the ability to accelerate in any direction and orientation without coupling within the designed workspace. Multi-directional multirotor designs could broadly be grouped into three categories: fixed-tilt, uniaxial-tilt, and biaxial-tilt.

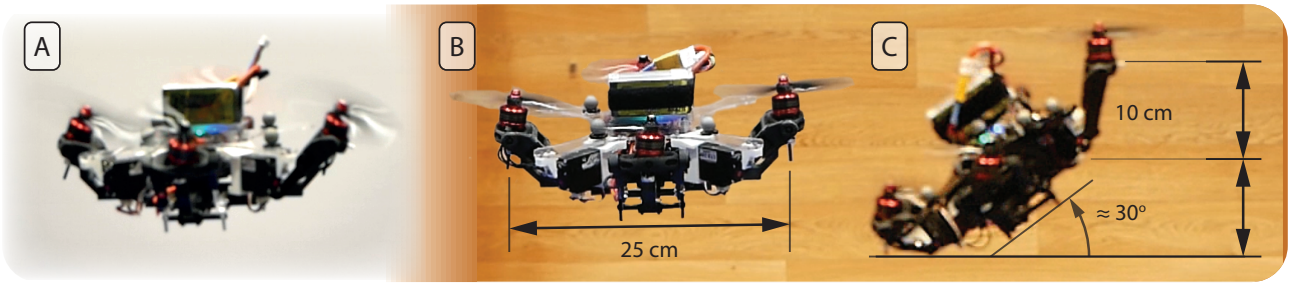


Figure 2.1: **The TiltDrone prototype** in (**A**) tilted horizontal, (**B**) level, and (**C**) tilted hovering flight. The prototype TiltDrone can tilt its rotors up to 30 degrees. The backgrounds of the photographs are altered for clarity.

Multirotors with the motors fixed at various prescribed angles [97, 98, 99, 100, 101, 102] can achieve full range multi-directional motion without any morphological change. They are simple to manufacture and are structurally more robust [96]. However, this reduces the flight time due to the partial cancellation of the non-parallel thrust vectors.

Uniaxial-tilt multirotors actively rotate their rotors about the axis of the individual multirotor arm [62, 103, 104, 105, 106, 107]. Although a full range of motion in 6-DOF is possible, all designs within this category will create opposing thrust vectors.

Biaxial-tilt multirotors [108, 109, 110] successfully avoid the inefficiencies from cross-cancelling rotor thrusts. Tilting can be synchronized such that the thrust axes remain parallel to each other. However, these designs will incur the weight penalty of the tilting mechanism.

To further assess the efficiency of multi-directional designs, we can regroup the drones by the level of mechanical actuation achieved. Although over-actuated systems are beneficial in handling component failures [104], the redundancies result in significant weight penalties.

Underactuated multi-directional flight can be achieved through torque modulation [111]. By installing flexible hinges at an angle, only two counter-rotating rotors are needed to generate directional and/or torsional forces. The aerial vehicle could tilt up to 8°, albeit with friction losses at the swashplate-less hinge [112]. The relatively high frequency of throttle modulation also produces significant heating of the motor.

Fully-actuated designs can be both cost-effective and simple to implement. Control allocation is direct as the input (actuator command) to output (position-orientation) mapping is unique, thus optimisation-based control is not required. Currently, fully-actuated biaxial tilt-rotors with four

propellers have been proven to be feasible and stable [110, 113]. However, the aforementioned evaluations are limited to simulation environments.

I invented the hardware design architecture for the TiltDrone (Fig. 2.1). The TiltDrone design enables multi-directional motion on a fully-actuated quadrotor platform. The quadrotor design comprises a biaxial rotor tilting mechanism, driven by twin linear servomotors in parallel (Fig. 2.2A). The kinematic chain features spherical-cylindrical compound joints, allowing the upper and lower structure to remain a constant distance apart during actuation. The mechanism retains the quadrotor form at all tilt angles. This greatly reduces the complexity of the control. Section 2.2 sets out the geometrical constraints and design feasibility considerations. The control framework is discussed in Section 2.3. The validation of the proposed design architecture and the control framework are presented in Section 2.4 and the conclusions are drawn in Section 2.5.

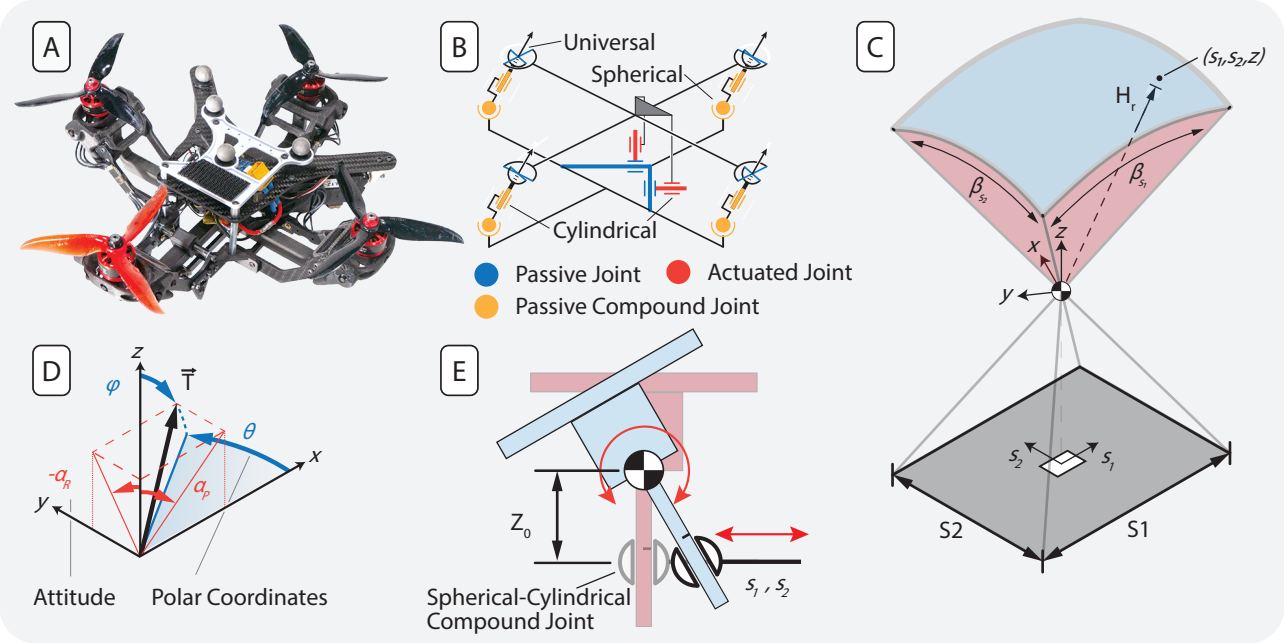


Figure 2.2: **The design and the prototype**. (A) A photo of the prototype platform. (B) A diagram of the synchronised rotor tilting mechanism. (C) The volume swept by the rotor axis of rotation (red) with linear servomotor axes s_1, s_2 rotated $-45°$ from rotor axes XY. (D) The attitude and polar coordinate presentation of the thrust vector, and (E) side view of the rotor and the compound joint.

2.2 Design

Translating the kinematics to a viable mechanism poses challenges in the designing of biaxial-tilting quadrotors. The most critical consideration is the clearance requirements of the platform structure, which may not be immediately obvious when modelling with static drawings. The following design margins were derived with variables shown in Fig. 2.3. It is useful to note that the rotor workspaces can overlap as rotor tilts are synchronised.

2.2.1 3D modelling methodology

To achieve the most compact design and ensure clearance requirements are met, I applied a subtractive modelling strategy (Al. 1). By sculpting out the obstructed areas on the part, the available design volume can then be clearly defined. Given that the maximum tilt angle is the primary design requirement, the order of part design cascades from the rotor mount to the static structures.

Algorithm 1: Subtractive 3D modelling methodology

```
for part i from 1 to N do
    create solid volume to the specified platform size;
    for part j from 1 to i-1 do
        rotate part 1 to j collectively about their respective maximum range of motion;
        for part k from 1 to i-1 do
            if part k interferes with part i then
                remove the interfering volume from part i;
            end
        end
    end
end
```

2.2.2 Structural sizing

The most compact form of the design can be derived from a predefined rotor height H_r, propeller diameter D_{prop}, and tilt angle $\alpha_{\max}$ (Fig. 2.3B). Approximating the propeller as a cylindrical

disk with a cross-section thickness T_{prop}, one could obtain the minimum length l_{b} and height h_b of the quadrotor body. For propeller-propeller clearance when tilting

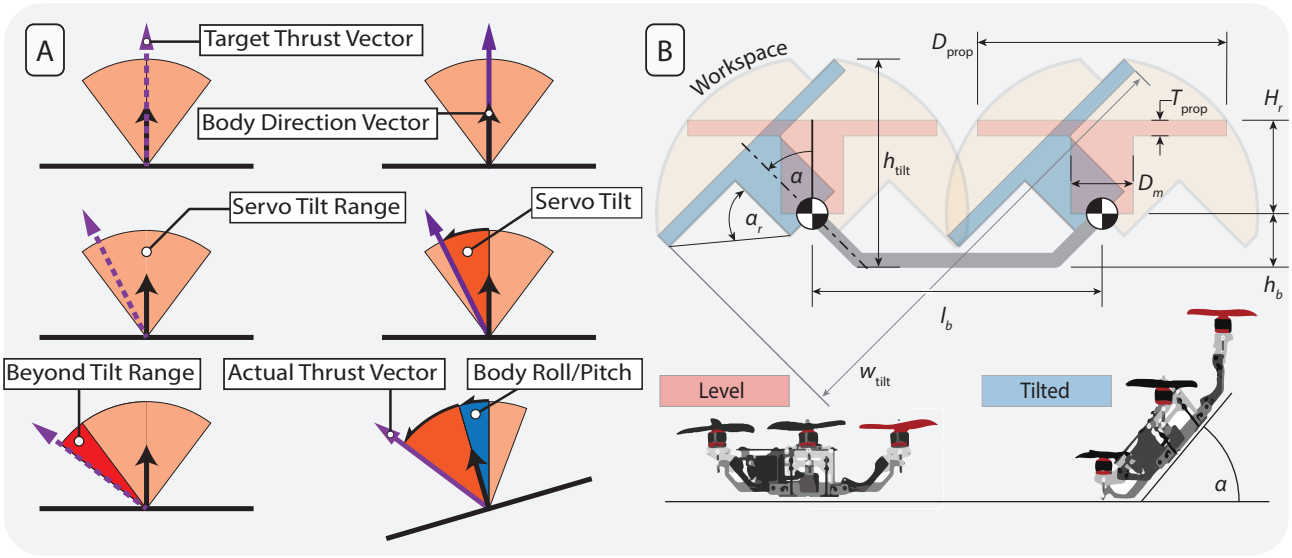


Figure 2.3: **Tilting mechanism diagrams**. (**A**) An illustration of the control allocator. (**B**) Geometrical diagram of the tilting platform and a comparison of the prototype design level and tilted. The rotor workspaces are shaded in yellow. The workspaces can overlap as the rotors are tilted synchronously.

$$l_{\text{b}} > \sqrt{{D_{\text{prop}}}^2 + {T_{\text{prop}}}^2} \tag{2.1}$$

However, if the designed tilt angle is small, as defined by

$$\alpha_{\max} \leq \arctan\left(\frac{T_{\text{prop}}}{D_{\text{prop}}/2}\right), \quad \forall\ -\frac{\pi}{2} < \alpha_{\max} < \frac{\pi}{2} \tag{2.2}$$

such that only propeller-propeller abrasion can occur, the alternative constraint (2.3) is applied.

$$l_{\text{b}} > \frac{D_{\text{prop}}}{\cos(\alpha_{\max})} \tag{2.3}$$

The propeller-motor clearance is also considered in tandem with (2.1). The motor is approxi-

mated as a cylinder with a diameter D_m. The body length is constrained such that

$$\text{if} \quad \alpha_{\max} \geq \arctan\left(\frac{2H_r}{D_{\text{prop}} + D_m}\right) \tag{2.4}$$

$$l_{\text{b}} > \sqrt{{H_r}^2 + \left(\frac{D_{prop} + D_m}{2}\right)^2} \tag{2.5}$$

$$\text{else} \quad l_{\text{b}} > \frac{D_{\text{prop}} + D_m}{2\cos\alpha_{\max}} \tag{2.6}$$

To derive the body height, h_b, it is useful to define a rotor slant angle

$$\alpha_r = \arctan\left(\frac{2(H_r - T_{\text{prop}})}{D_{\text{prop}} - D_m}\right) \tag{2.7}$$

above which the propeller will be the lowest point of a tilted rotor. Therefore, when $\alpha_{\max} \leq \alpha_r$

$$h_b > \frac{D_m}{2}\sin\alpha_{\max} \tag{2.8}$$

$$\text{else} \quad h_b > \frac{D_{\text{prop}}}{2}\sin\alpha_{\max} + (T_{\text{prop}} - H_r)\cos\alpha_{\max} \tag{2.9}$$

2.2.3 The geometrical effects of tilting

A benefit often attributed to morphing multirotors is the ability to shrink their body to traverse narrow openings [114, 115, 116, 117]. This effect of tilting was examined for crossing horizontal and vertical gaps; the TiltDrone design was compared to a conventional quadrotor, with the same rotor dimensions $D_{\text{prop}}, T_{\text{prop}}, D_m$ and H_r.

The width w_{tilt} of the fully-actuated platform relative to the plane of the tilted rotors is

$$w_{\text{tilt}} = D_{\text{prop}} + l_{\text{b}}\cos\alpha \tag{2.10}$$

Assuming that the rotors point vertically upwards when traversing a horizontal gap. We can derive a width reduction ratio (2.11) as compared to a conventional quadrotor with a propeller

tip-to-tip width of $w_{conv} = 2D_{\text{prop}}$.

$$\frac{w_{\text{tilt}}}{w_{\text{conv}}} = \frac{D_{\text{prop}} + l_{\text{b}} \cos\alpha}{2D_{\text{prop}}} = \frac{1}{2} + (\frac{l_{\text{b}}/2}{D_{\text{prop}}}) \cos\alpha \tag{2.11}$$

For the more plausible designs where (2.1) holds with $D_{\text{prop}} \gg H_r, D_m$ and a negligible T_{prop}, the width reduction ratio will be $\cos^2(\alpha/2)$.

Traversing obstacles without pitching the body may also reduce the cross-section height of the platform. In this case, the platform's geometry changes with horizontal acceleration. Due to the discrete geometric transitions with the tilt angle, there are five permutations of the height reduction ratio $h_{\text{tilt}}/h_{\text{conv}}$. They are dependent on the design, $\alpha_{\max}$ and α_r, and the command α. For designs where $\alpha_{\max} \leq \alpha_r$, there are three distinct formulations of the vertical height of the tilted drone, h_{tilt}, as displayed in Fig. 2.4A. If $\alpha \leq \alpha_r$ & $\alpha \leq \alpha_{\max}$, the rotor tilts without needing to pitch. Thus

$$h_{\text{tilt}} = h_b + H_r \cos\alpha + \frac{D_{\text{prop}}}{2} \sin\alpha \tag{2.12}$$

When $\alpha_{\max} < \alpha \leq \alpha_r$, the height hinges on the bottom edge of the motor and the opposing rotor's propeller edge

$$\begin{aligned} h_{\text{tilt}} = &\left(l_{\text{b}} + \frac{D_{\text{prop}} + D_m}{2} \cos\alpha_{\max} - H_r \sin\alpha_{\max} \right) \sin(\alpha - \alpha_{\max}) \\ &+ \left(H_r \cos\alpha_{\max} + \frac{D_{\text{prop}} + D_m}{2} \sin\alpha_{\max} \right) \cos(\alpha - \alpha_{\max}) \end{aligned} \tag{2.13}$$

At $\alpha_{\max} < \alpha_r < \alpha$ the propellers are the upper and lower bounds of the tilted height

$$\begin{aligned} h_{\text{tilt}} = &(l_{\text{b}} \cos(\alpha_r - \alpha_{\max}) + D_{\text{prop}} \cos\alpha_r - T_{\text{prop}} \sin\alpha_r) \sin(\alpha - \alpha_r) \\ &+ (l_{\text{b}} \sin(\alpha_r - \alpha_{\max}) + T_{\text{prop}} \cos\alpha_r + D_{\text{prop}} \sin\alpha_r) \cos(\alpha - \alpha_r) \end{aligned} \tag{2.14}$$

For platforms where $\alpha_{\max} > \alpha_r$ there are two formulas for h_{tilt}. (2.12) is valid when $\alpha \leq \alpha_{\max}$. Otherwise, the fully-actuated platform must combine tilt and pitch to reach the desired angle,

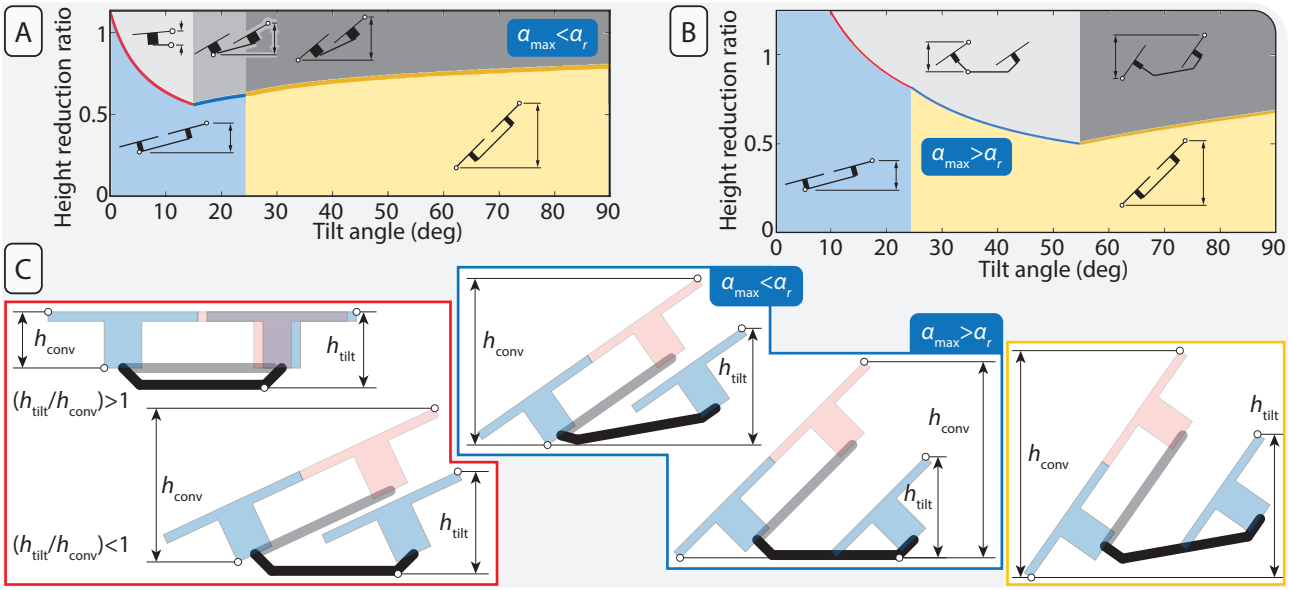


Figure 2.4: **Height reduction ratio** graphs comparing the vertical profile of the fully-actuated platform with a conventional quadrotor, with (**A**) $\alpha_{\max} \leq \alpha_r$ and (**B**) $\alpha_{\max} > \alpha_r$. Sections in greyscale and colour denote the various heights for fully-actuated (numerator) and conventional (denominator) quadrotors respectively. (**C**) The various tilting scenarios, the border colour of each diagram corresponds to the colour of the lines in (**A**) and (**B**).

thus

$$\begin{aligned} h_{\text{tilt}} = (l_{\text{b}} + D_{\text{prop}} \cos\alpha_{\max} - T_{\text{prop}} \sin\alpha_{\max}) \sin(\alpha - \alpha_{\max}) \\ +(T_{\text{prop}} \cos\alpha_{\max} + D_{\text{prop}} \sin\alpha_{\max}) \cos(\alpha - \alpha_{\max}) \end{aligned} \tag{2.15}$$

On the denominator side of the height reduction ratio, the height of the conventional quadrotor during pitch, h_{conv}, is dependent on α. When $\alpha \leq \alpha_r$,

$$h_{\text{conv}} = \left(D_{\text{prop}} + \frac{D_{\text{prop}} + D_m}{2} \right) \sin\alpha + H_r \cos\alpha \tag{2.16}$$

else,

$$h_{\text{conv}} = 2D_{\text{prop}} \sin\alpha + T_{\text{prop}} \cos\alpha \tag{2.17}$$

The minimum height reduction ratio of the prototype platform is approximately 0.5, but with a ratio larger than 1 when operating below 16° tilt angle (Fig. 2.4B). This is due to the body height required to accommodate a higher design tilt angle of 45°.

2.2.4 Rotor gimbal

The rotors are gimballed to allow tilting on the roll and pitch planes, restricting translation and yaw. The control rod extends down from the gimbal platform and slides through the swivel head ball joint. The four ball-joint sockets are interconnected to form the planar mechanism.

It is critical to account for the area swept by the tilting rotor (i.e. the workspace). As the linear servomotors (servos) are mounted perpendicularly, the parallel mechanism sweeps out a square. The rotor axis with a radius of the rotor's height is confined within the plane defined by

$$H_r^2 = s_1^2 + s_2^2 + z^2 \tag{2.18}$$

$$z \geq \pm \tan\Big(\alpha_{s_2,\max} - \frac{\pi}{2}\Big) s_1 \tag{2.19}$$

$$z \geq \pm \tan\Big(\alpha_{s_1,\max} - \frac{\pi}{2}\Big) s_2 \tag{2.20}$$

where H_r is the height of the rotor, measured from the centre of tilt rotation, orthogonal axes s_1, s_2, and z denotes the travel of Servo 1, Servo 2, and the vertical axis respectively (Fig. 2.2A). $\alpha_{s_1,\max}$ and $\alpha_{s_2,\max}$ are the maximum tilt relative to the servo planes. They are calculated by $\alpha_{s_i,\max} = \arctan L_{s_i}/(2Z_0)$ with L_{s_1} and L_{s_2} denoting the maximum length of servo travel, and Z_0 the perpendicular distance of the origin (centre of rotation) to the servo plane (Fig. 2.2E).

Tracing the boundaries set by (2.19) and (2.20), the quadrotor structure and the gimbal mechanism must remain clear of the volumetric sweep by a full rotor tilt. This equates to a rotation of the rotor through an angle of

$$\beta_{s_1} = 2 \arctan \frac{L_{s_1}}{\sqrt{4Z_0^2 + L_{s_2}^2}} \tag{2.21}$$

about centerlines

$$\begin{bmatrix} s_1 \\ s_2 \\ z \end{bmatrix} = \begin{bmatrix} 0 \\ s_2 \\ \pm \cot\big(\alpha - \frac{\pi}{2}\big) s_2 \end{bmatrix} \tag{2.22}$$

and angle

$$\beta_{s_2} = 2 \arctan \frac{L_{s_2}}{\sqrt{4Z_0^2 + L_{s_1}^2}} \tag{2.23}$$

about

$$\begin{bmatrix} s_1 \\ s_2 \\ z \end{bmatrix} = \begin{bmatrix} s_1 \\ 0 \\ \pm \cot\left(\alpha - \frac{\pi}{2}\right) s_1 \end{bmatrix} \tag{2.24}$$

2.2.5 Tilting Mechanism

The quadrotor platform is configured in a "+" formation with the servomotors offset at -45° to the XY axes (Fig. 2.5B). The rotor gimbals are linked via the ball joint housings with a cross-shaped strut. This cancels out the gyroscopic precession of the rotors when actuated in flight [109]. Driven by the two servos, the planar mechanism tilts the rotors opposite the direction of actuation.

The planar mechanism is inherently susceptible to twisting. Although the mechanism is constrained by the servos, small unintended twists can occur due to manufacturing defects and unbalanced actuating forces. In such events, the rotors are vectored to induce yaw. The flight controller attempts to correct for yaw by accelerating one of the diagonal rotor pairs to generate torque. However, this is insufficient as brushless DC motors have low moments of inertia and the propellers are optimised for a high lift-to-drag ratio. Thus, the thrust vector-induced yaw remains the dominant term, resulting in an irrecoverable spin.

This design flaw occurs within the small-angle approximation regime. Therefore the resultant rotor angle is approximately $l_\mathrm{b}/(2Z_0)$ times the twist of the mechanism. A more compact platform will reduce the effect of the twist. However, the more general solution is to use rigid and tight tolerance sliding components to restrict the twist angle.

2.3 Control Framework

This section sets out the conversion of attitude commands into the position of the servomotors, and the combination of thrust vectoring and body rotation when servo travel is exceeded. The parallel mechanism allows straightforward inversion of the kinematic equations. Therefore, although the results presented are of a simple PD-based position controller, it is reasonable to assume that most types of high-level control schemes can function on this platform due to having decoupled translational and attitude channels.

2.3.1 Control Architecture

Our system is autonomously controlled by an offboard RC signal, commanding roll and pitch angles, thrust, yaw rate, and servo positions (Fig. 2.5B). The high-level command inputs are given in the form of position XYZ, Yaw (γ), and body vector $\overrightarrow{T}$ in global frame spherical coordinates (Fig. 2.2B). The position-orientation commands are sent to the high-level controller, where the feedback control loop is formed with odometry provided by a motion capture system.

The body vector commands feed into the *limiter* where they are saturated to prevent unattainable commands from entering the *control allocator*. The *control allocator* takes the output from the high-level controller and maps the attitude commands to servo positions. Pitch and roll are used for compensation when the desired polar angle is beyond the servo limit (Fig. 2.3A). The commands are then sent to the quadrotor via an RC transmitter.

2.3.2 Control Allocation

As the quadrotor receives attitude command and position for servos, the control allocation fundamentally resolves to a conversion between polar, attitude, and Cartesian (servomotor) coordinates, as shown in Fig 2.2B. Although not strictly necessary for control allocation, the body vector command was used in spherical form. This is a more intuitive way to command tilt as we can prioritise the drone body's azimuth (tilt direction θ_D) over the polar angle (tilt

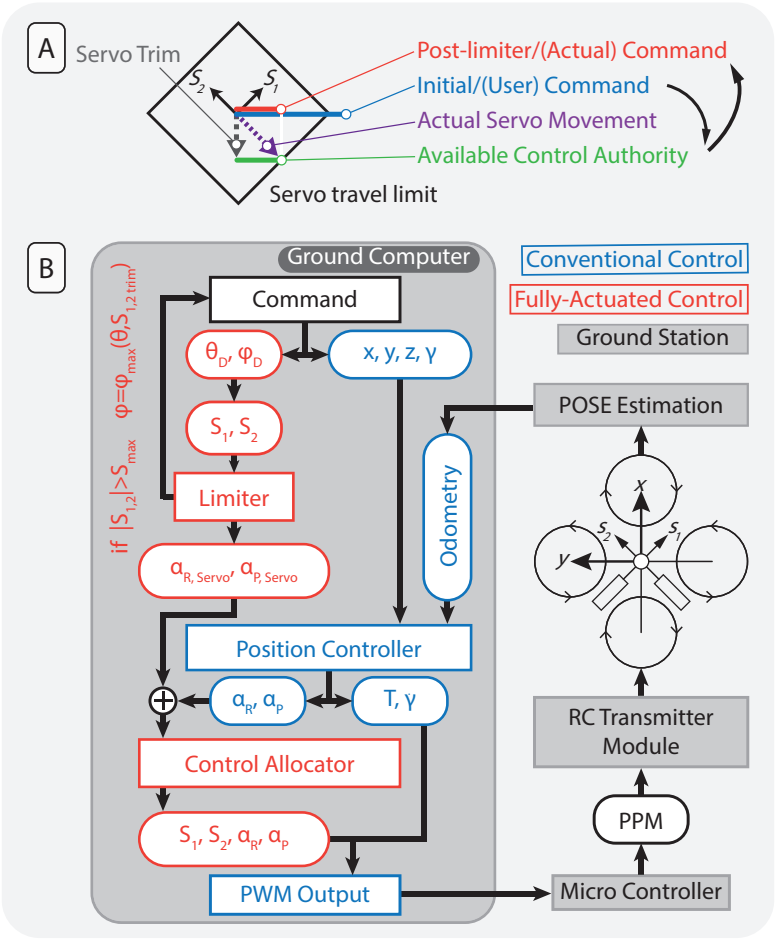


Figure 2.5: **Control architecture of the fully-actuated platform**. (**A**) The servomotor output limiter with trim control. (**B**) The robot control schematics.

angle ϕ_D). Roll α_R and pitch attitude α_P are given as

$$\alpha_R = -\arctan(\sin\theta_D \tan\phi_D) \tag{2.25}$$

$$\alpha_P = \arctan(\cos\theta_D \tan\phi_D) \tag{2.26}$$

They are further converted to servo positions by

$$s_1 = -\frac{\sqrt{2}}{2} Z_0(\tan\alpha_R + \tan\alpha_P) \tag{2.27}$$

$$s_2 = -\frac{\sqrt{2}}{2} Z_0(\tan\alpha_R - \tan\alpha_P) \tag{2.28}$$

Solving the geometrical conversion from the servo position to the polar orientation we get

$$\theta_D = \arctan\left(\frac{s_1 + s_2}{-s_1 + s_2}\right) + \pi \tag{2.29}$$

$$\phi_D = \arctan\left(\sqrt{s_1^2 + s_2^2}\right) \tag{2.30}$$

The prototype platform was designed with $L_{s_1} = L_{s_2} = 2Z_0$. Solving for the tilt limits with $-Si/2 \leq s_i \leq Si/2$ and (2.25)-(2.28), the positive polar angle must satisfy

$$\phi_D \leq \arctan\sqrt{\frac{1 \pm \sin 2\theta_D}{1 \mp \sin 2\theta_D} + 1} \tag{2.31}$$

for Servo 1 and Servo 2 respectively. However, incorporating servo trimming is inconvenient in spherical coordinates due to the non-linear mapping of attitude vector addition in spherical space. The *limiter* maps the commands onto the Cartesian servo coordinate frame. We then solve for the maximum possible magnitude of the command vector given an offset from the origin and the servo travel limits (Fig. 2.5A). This gives the constraint equations

$$if\ s_{1,2} > 1$$

$$\begin{bmatrix} s_{1,2} \\ s_{2,1} \end{bmatrix} = \begin{bmatrix} 1 \\ \frac{(1-s_{1,2})(s_{2,1}-s_{2,1_{\text{trim}}})}{s_{1,2}-s_{1,2_{\text{trim}}}} + s_{2,1_{\text{trim}}} \end{bmatrix} \tag{2.32}$$

$$if\ s_{1,2} < -1$$

$$\begin{bmatrix} s_{1,2} \\ s_{2,1} \end{bmatrix} = \begin{bmatrix} -1 \\ \frac{(-1-s_{1,2})(s_{2,1}-s_{2,1_{\text{trim}}})}{s_{1,2}-s_{1,2_{\text{trim}}}} + s_{2,1_{\text{trim}}} \end{bmatrix} \tag{2.33}$$

With the saturated output given, the *limiter* remaps the control output to give the feasible command input (Fig. 2.5A). Accounting for the servo trims, (2.29) and (2.30) are modified to

give

$$\theta_{D,\text{command}} = \arctan\left(\frac{s_1 - s_{1_{\text{trim}}} + s_2 - s_{2_{\text{trim}}}}{-s_1 - s_{1_{\text{trim}}} + s_2 - s_{2_{\text{trim}}}}\right) + \pi \tag{2.34}$$

$$\phi_{D,\text{command}} = \arctan\left(\sqrt{(s_1 - s_{1_{\text{trim}}})^2 + (s_2 - s_{2_{\text{trim}}})^2}\right) \tag{2.35}$$

the actual (post-*limiter*) commands.

2.4 Results and Discussion

A 5-inch propeller prototype platform was manufactured to validate the design. The gimbals and the planar mechanism were 3D-printed on the Markforged Mark 2 with *Onyx* filament. Continuous carbon fibre (CF) was added where possible for stiffness. An Omnibus F4 V3 flight controller was used with an unmodified version of the *Betaflight* 4.1 firmware[118]. The servomotors are controlled through pulse width modulation (PWM) commands sent from the flight controller at 50Hz with the *Servo Tilt* feature. Though initially designed with $\alpha_{\max} = 45^\circ$ in all directions, issues noted during manufacturing and testing limited the stable hovering tilt angle to 30° (Tab. 2.1).

Table 2.1: Prototype robot performance.

Flight time	$\approx$ 5 minutes at $899g$
Empty weight (without battery)	$737.3g$
Estimated MTOW	$1600g$
Maximum design tilt	40°
Maximum stable tilt command	30°
Maximum tilt command achieved	40°

2.4.1 Manufacturing

Other than the tilting mechanism and the structure of the prototype platform, the components listed in Tab. 2.2 were sourced from consumer-grade suppliers. During the modelling stage, physical considerations caused deviations from the idealized design. They were:

- the need to house the linear servos between the rotors resulted in an approximately 40% increase from the minimum structural length
- the drone structure and mechanism height dimensions were enlarged to increase stiffness and toughness
- the rotor height was increased to give sufficient space to design the gimbal

There were also a number of limitations due to component availability and manufacturing techniques such as:

- the ball bearings, which form the passive compound joints, were approximately limited to a $\pm 40^{\circ}$ cone
- the radial bearings, which form the passive universal joints, limited the minimum size of the gimbal - this resulted in an increased rotor height
- complex geometries limited the use of continuous CF-reinforced plates and tubes in the structure

Asymmetric component alignments were considered. For example, one could offset the linear servos pistons out of the horizontal plane. This reduces the size of the platform by allowing the servos to be placed closer to the drone centre. However, it would create unbalanced sliding friction in the mechanism which must be accounted for in the control system, if significantly large.

The tilt limit due to the ball bearings can be circumvented by employing an "H" configuration. Allowing the opposing bearing socket pairs to rotate with additional revolute joints at the junctions of the mechanism, similar to [93], increases the tilt angle of a single axis. However, owing to parallel linear actuation, the design imposes a tilt limit of 90°.

A rough design performance evaluation can be conducted. The biaxial-tilting mechanism account for all the 3D-printed parts. The rule of mixtures with an approximate continuous CF ratio of 15% gives a tensile modulus of 10.2 GPa [119]. A like-for-like exchange with quasi-isotropic CF-Epoxy material (35.3 GPa) may reduce its weight by 71% [120]. The peripheral

Table 2.2: Component mass breakdown.

Item name	**Unit(s)**	**Per unit weight** (g)	**Subtotal** (g)	**% Total weight**
DYS SE2008	4	33.0	132.0	14.7
DAl T5040C	4	4.2	16.8	1.9
mightyZap L12-20PT3	2	51.0	101.0	11.2
Airbot Typhoon32 4in1	1	16.8	16.8	1.9
Airbot Omnibus F4 SD	1	7.2	7.2	1.3
Biaxial-tilting mechanism	1	307.0	307.0	34.1
4-Cell LiPo Battery	1	162.0	162.0	18.0
Peripherals			156.5	17.4
Total			899.3	

stack (inc. CF mounting plate, minor electronics) can be optimised by a 50% weight reduction. Under such optimistic projections, the frame weight of 167 g is somewhat comparable to an open-sourced 5-inch propeller frame (149.1 g)[121]. I, therefore, conclude that, for future development, the weight and size of the linear servomotor is the main bottleneck of flight endurance.

2.4.2 Testing

Flight tests, using a PD position controller, were conducted to compare the cases with and without fully-actuated motion (i.e. conventional flight) (Fig. 2.6). The aspect of the comparison study is to explore full-actuation, where the system can follow a trajectory while keeping commanded attitude angles. Accordingly, our design provides the decoupled control property and the results show that position tracking errors in the two flight modes are comparable (Tab. 2.3).

In all flight tests, sudden z deviations occur when discontinuous servo position commands were given. As the servo positions were not fed back into the controller, it could not account for the rotor angle during the transition. The short-duration oscillations in x due to y commands are not reciprocated in y when a step command is given in x. This is likely due to a slight structural defect, skewing the geometry of the mechanism. Since the platform did not deviate away from the target position when initially responding to a step command, we conclude that the inertia

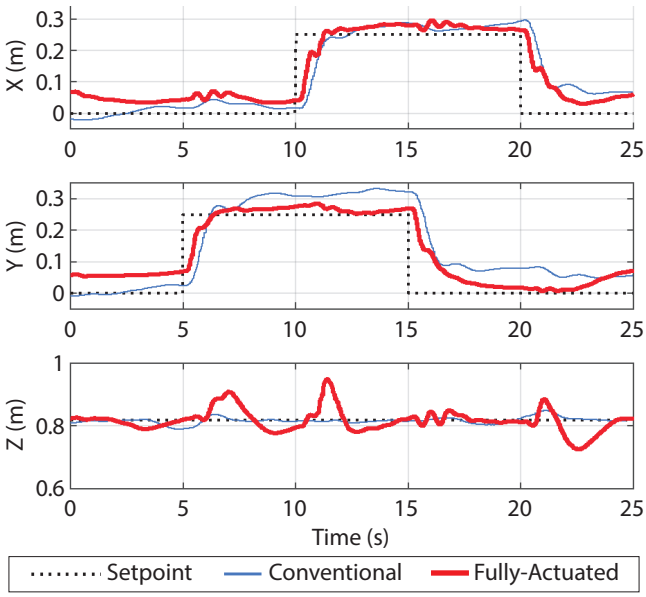


Figure 2.6: **Step response** of conventional and fully-actuated flight at 0° tilt.

of the mechanism is insignificant. Evidently, with aggressive manoeuvres, the fully-actuated platform showed a noticeable reduction in rolling and pitching (Fig. 2.7).

At static hover, the prototype reached a maximum stable tilt of 30° (Fig. 2.8). The changes in the static offset when tilting is likely due to the backlash in the servo and the mechanism.

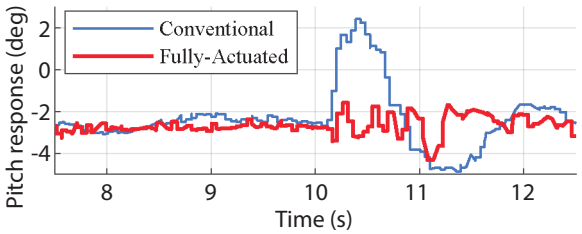


Figure 2.7: **Comparing pitch response due to step position command** of conventional and fully-actuated flight at 0° tilt. The pitch responses are synchronised by the change in position command.

I noted that the prototype tilting mechanism was prone to uncontrollable yaw spins if manufactured with loose tolerance. The prototype uses its servomechanisms as both actuators and twist constraints. This is not ideal as the servo pistons are not sufficiently rigid. Ideally, the servo pistons are not required to constrain the twisting of the planar mechanism. This small angle-induced issue was partially resolved by adding a passive, twist-restricting, linear rail. Alternatively, a third servomotor could be added as active yaw control. Although the plat-

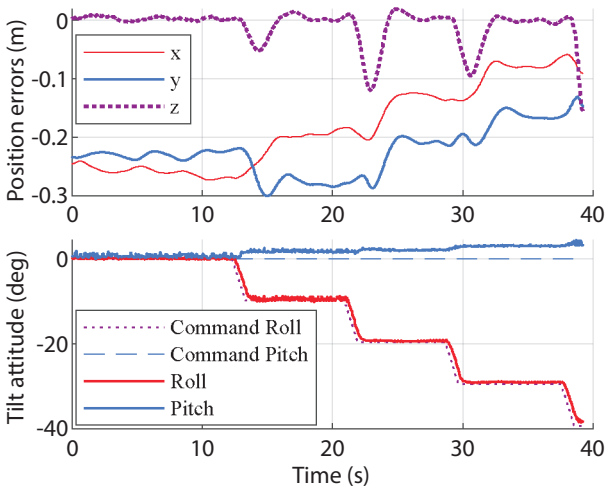


Figure 2.8: **Static hovering fully-actuated flight** at various roll axis tilt.

Table 2.3: Step response mean absolute error and standard deviation with conventional (Conv) and fully-actuated (FA) flight.

	$\mathbf{MAE}_{\text{Conv}}$	$\mathbf{MAE}_{\text{FA}}$	$\mathbf{STD}_{\text{Conv}}$	$\mathbf{STD}_{\text{FA}}$
x (m)	0.0463	0.0477	0.0691	0.0513
y (m)	0.0664	0.0415	0.0706	0.0508
z (m)	0.0074	0.0250	0.0102	0.0364
Roll (deg)	NA	4.0400	NA	0.2839
Pitch (deg)	NA	2.6304	NA	0.3639

form becomes over-actuated with the redundant servomotor, it will gain greater yaw authority through thrust vectoring.

2.5 Conclusions

A fully-actuated, biaxial-tilting, quadrotor hardware design architecture has been presented. A prototype was built to validate the proposed design approach. By placing the rotors on a two-axis gimbal and tilting them in unison with a parallel mechanism driven by two linear servomotors, a simple control allocator is able to decouple the platform's rotation and translation. The prototype platform reached a stable 30° tilt in flight (Tab. 2.1). By leveraging this system, it may be possible to fly through narrow openings or exert forces on different surfaces with reduced effort on the control design. In particular, the ability to tilt while hovering can be exploited to place sensors on previously inaccessible locations.

In future works, greater manoeuvrability can be attained by combining tilting and pitching. This may require advancements in trajectory planning and optimisation-based control. The subsequent prototype platform will feature a gimbaled flight controller, tilting with the rotors. I suspect this may be more intuitive for a human pilot. It also further simplifies the control allocation as the flight controller will always remain parallel to the rotor plane. In addition, the scalability and optimisation of the design warrant further studies.

Chapter 3

Analysis of a fully-actuated multi-directional quadrotor

3.1 Introduction

With the rapid growth of automation in non-industrial domains, robots are becoming ubiquitous. Within the field of robotic research, there has also been an increasing focus on robots in dynamic environments. Obvious examples of this branch are autonomous cars and drones, of which multirotor micro aerial vehicles (MAVs) are the most accessible to researchers.

With the end goal of propagating research into the public domain, the scaling of these MAV systems is critical. While most software, such as Simultaneous Localisation And Mapping (SLAM) and path planning, can be readily applied on most UAVs, most hardware designs require further considerations. Understandably, the majority of these works focused on the sizing of the multirotor powertrain [122, 123, 124, 125].

An intriguing area that is often overlooked is the sizing of prototype multirotors, for which their novel mechanisms are significant features in both structural and powertrain design. This is certainly true of multi-directional fully-actuated biaxial tilting quadrotors; their morphing mechanisms result in added weight and design geometries of greater complexity.

Although the kinematics and spatial concerns of fully-actuated biaxial tilting were addressed

with the previous work, the mechanical analysis remains incomplete [65]. Linear servomotors, though functional, are comparatively too large to be practical. Also, critical flaws noted in the design of the mechanism warrant a revisit.

While Chapter 2 studies the practical aspects of the tiltrotor-quadrotor system and focuses on the tilting of the central drone body with a static rotor orientation, this chapter studies the tilting of the rotor in detail with the drone body frame of reference. In this chapter, the scaling effects of various fully-actuated biaxial-tilting quadrotor designs are explored. Expanding upon the previous work, the TiltDrone, I propose alternative designs with twin radial servomotor actuation. The designs are then compared with consideration of the system mechanics and scaling.

3.2 The Flight Dynamics of Tilting

Following the tilt-rotor design set out in Chapter 2, tilting the rotors involves moving masses on the robot. As the rotor tilting involves internal forces, unlike conventional quadrotors which have to apply differential thrust to rotate, the total Centre of Mass (CoM) of the robot remains stationary. This also implies that the CoM of the robot's body, the structure to which payloads will be mounted, will experience a 'parasitic' reaction force caused by rotor tilting.

Using the generalised tilt-rotor design and force diagram shown in Fig. 3.1, limiting our problem to two-dimensional motion only, we first derive the Lagrangian

$$\begin{aligned} L =& \frac{1}{2} I_b \dot{\alpha}^2 + (I_t + m_r h_r^2)\dot{\phi}^2 + \frac{1}{2}(m_b + 2m_r)(\dot{x}^2 + \dot{z}^2) - (m_b + 2m_r) g z - 2 m_r g h_r \cos(\phi) \\ &+ m_r {w_{\frac{1}{2}}}^2 \dot{\alpha}^2 + 2 m_r h_r \cos(\phi)\dot{\phi}\dot{x} - 2 m_r h_r \sin(\phi)\dot{\phi}\dot{z} \\ &+ m_r h_b^2 \dot{\alpha}^2 - m_r h_b w_{\frac{1}{2}} \sin(2\alpha)\dot{\alpha}^2 - 2 m_r h_b \sin(\alpha)\dot{\alpha}\dot{z} + 2 m_r h_b h_r \sin(\alpha)\sin(\phi)\dot{\alpha}\dot{\phi} \end{aligned} \tag{3.1}$$

where I_b is the inertia of the drone body in its pitch axis, I_t is the inertia of a single rotor in the axis of tilt rotation, m_b and m_r are the mass of the drone body and a single rotor respectively. h_r is the height offset of the rotor from the point of tilt rotation, h_b the height offset of the body from the midpoint between the two centres of rotor tilt rotation, $w_{\frac{1}{2}}$ is the

half-width of the drone body, as defined by the distance between the two centres of rotor tilt rotation. α is the drone body pitch angle measured from the horizon in the inertial frame of reference, ϕ is the rotor tilt in an arbitrary direction from the vertical axis of the inertial frame, x and z are the positions of the robot body relative to a static frame of reference. Note here that x and z are not on the tilt-rotor's CoM. Next, we define the external forces and torque

$$\bar{T} = \frac{T_1 + T_2}{2} \qquad F_x = 2\bar{T}\sin\phi \qquad F_z = 2\bar{T}\cos\phi \qquad \tau_{rotor} = (T_2 - T_1)w_{\frac{1}{2}} \tag{3.2}$$

where F_x and F_z are the total forces acting on the body, and $\bar{T}$ is the average thrust from the back and front rotor pair with thrusts T_1 and T_2, τ_{rotor} the torque applied by the rotor differential thrust. The torque which tilts the rotors, τ_{tilt}, is an internal torque.

From the Lagrangian, we derive the equations of motion

$$F_x = m_b\ddot{x} + 2m_r\ddot{x} \; -2m_r h_r \sin(\phi)\dot{\phi}^2 + 2m_r h_r \cos(\phi)\ddot{\phi} \tag{3.3}$$

$$\begin{aligned} F_z =& m_b(\ddot{z} + g) + 2m_r(\ddot{z} + g) - 2m_r h_b \sin(\alpha)\ddot{\alpha} - 2m_r h_b \cos(\alpha)\dot{\alpha}^2 \\ & -2m_r h_r \sin(\phi)\ddot{\phi} - 2m_r h_r \cos(\phi)\dot{\phi}^2 \end{aligned} \tag{3.4}$$

$$\begin{aligned} \tau_{\text{rotor}} + \tau_{\text{tilt}} =& I_b\ddot{\alpha} + 2m_r({w_{\frac{1}{2}}}^2 + h_b^2)\ddot{\alpha} - 2m_r h_b w_{\frac{1}{2}} \sin(2\alpha)\ddot{\alpha} - 2m_r h_b w_{\frac{1}{2}} \cos(2\alpha)\dot{\alpha}^2 \\ & +2m_r h_b h_r \cos(\phi)\sin(\alpha)\dot{\phi}^2 + 2m_r h_b h_r \sin(\alpha)\sin(\phi)\ddot{\phi} - 2m_r h_b \sin(\alpha)\ddot{z} \end{aligned} \tag{3.5}$$

$$\begin{aligned} \tau_{\text{tilt}} =& 2(I_t + m_r h_r^2)\ddot{\phi} \; +2m_r h_r \cos(\phi)\ddot{x} - 2m_r h_r \sin(\phi)\ddot{z} - 2m_r h_r \sin(\phi)g \\ & +2m_r h_b h_r \cos(\alpha)\sin(\phi)\dot{\alpha}^2 + 2m_r h_b h_r \sin(\alpha)\sin(\phi)\ddot{\alpha} \end{aligned} \tag{3.6}$$

The parts of the equations (3.3)-(3.6) which contain the h_r offset-influenced parasitic motion are shadowed in light blue (e.g. $\cdots$). However, it is not clear whether they are beneficial or harmful to the tilt-rotor's flight dynamics.

Further simplifying the analysis, if we command a setpoint target in x with z remaining con-

stant, and only analyse the initial state of $\alpha = \dot{\alpha} = \phi = \dot{\phi} = \dot{x} = \dot{z} = 0$, we have

$$0 = (m_b + 2m_r)\ddot{x} + 2m_r h_r \ddot{\phi} \tag{3.7}$$

$$T_2 + T_1 = m_b(\ddot{z} + g) + 2m_r(\ddot{z} + g) \tag{3.8}$$

$$(T_2 - T_1)w_{\frac{1}{2}} + \tau_{\text{tilt}} = I_b\ddot{\alpha} + 2m_r({w_{\frac{1}{2}}}^2 + h_b^2)\ddot{\alpha} \tag{3.9}$$

$$\tau_{\text{tilt}} = 2(I_t + m_r h_r^2)\ddot{\phi} + 2m_r h_r \ddot{x} \tag{3.10}$$

Tilting exhibits no effect on vertical motion and only the reaction torque of tilting the rotor, which can be countered by varying the rotor thrust differential. But (3.7) shows a parasitic effect of tilting on the tilt-rotor drone body. Tilting the rotor towards the setpoint target causes an instantaneous linear acceleration of the drone body in the opposite direction. Equally, by substituting (3.7) into (3.10), we get

$$\tau_{\text{tilt}} = -\left(\frac{m_b}{m_r}I + 2I_t + m_b h_r^2\right)\frac{\ddot{x}}{h_r} \tag{3.11}$$

$$\because\ m_b > 0,\ m_r > 0,\ I_t > 0, \text{ and assuming } h_r > 0 \tag{3.12}$$

$$\therefore\ \tau_{\text{tilt}} \propto -\ddot{x} \tag{3.13}$$

relating the force of tilting the rotor to an instantaneous linear acceleration of the drone body in the opposite direction. Thus, I make the argument: "*The tilt angular acceleration of the rotors to correct for a lateral error creates a lateral perturbation of the robot's body in the opposite direction as the error, proportional to the angular acceleration. This, in effect, increases the error. Therefore, rotor tilting with the rotors offset above the tilting origin has, partially, a destabilising effect.*" The simple solution to avoid this parasitic motion is to remove the offset, or flip the design upside down and make the offset a negative value. In the case of the inverted design, the tilting aids the lateral movement by providing an initial acceleration.

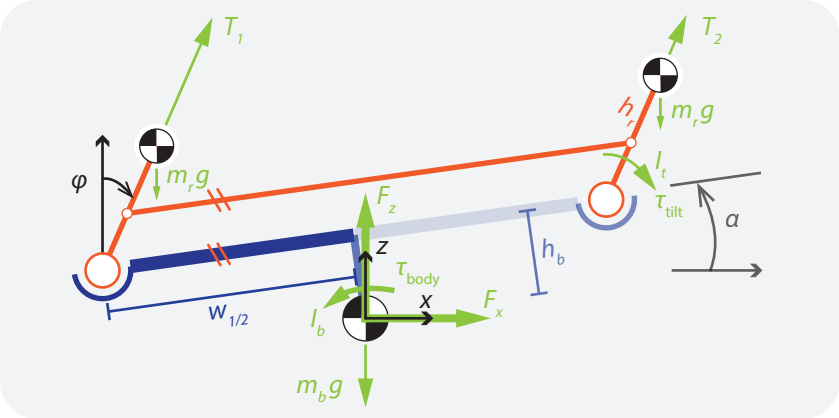


Figure 3.1: **Tilting drone force diagram**. The two rotors are mounted on a four-bar linkage to ensure that T_1 and T_2 are pointing in the same direction. The pitch angle α is measured from the horizon, and the tilt angle ϕ is measured from the vertical.

3.3 The Structural Dynamics of Tilting

Under a rigid body assumption, interconnecting the tilting propellers allows the forces of precession to cancel. However, these forces are transmitted to the mechanism's structure and will cause deformation. To derive the control forces, we model the rotor and gimbal mechanism as an augmented heavy top flywheel with a lever arm on the opposite side of the support where the control forces are applied.

With this model, the command rate of tilt is equivalent to the rate of precession (Fig.3.2A). Thus the force of actuation is perpendicular to the direction of actuation. This results in a somewhat counter-intuitive conclusion - while in flight, no force is required by the actuator. In other words, the rate of tilt is limited by the friction within the mechanism and the actuator's zero-load speed if the rotors are spinning significantly fast. The reaction force from the structure is therefore

$$R_{\text{prec}} = -\frac{Z_0}{h_r \cos\phi}\frac{I_r \omega \Omega_t}{h_r} \tag{3.14}$$

where I_r is the moment of inertia of the rotor assembly about its thrust/spin axis, ω the rotor rotational velocity, Ω_t the tilt angular velocity, ϕ tilt angle, h_r is the distance of the rotor centre of mass to the tilt pivot point, and Z_0 is the distance between the tilt pivot point and

the servomotor plane of actuation.

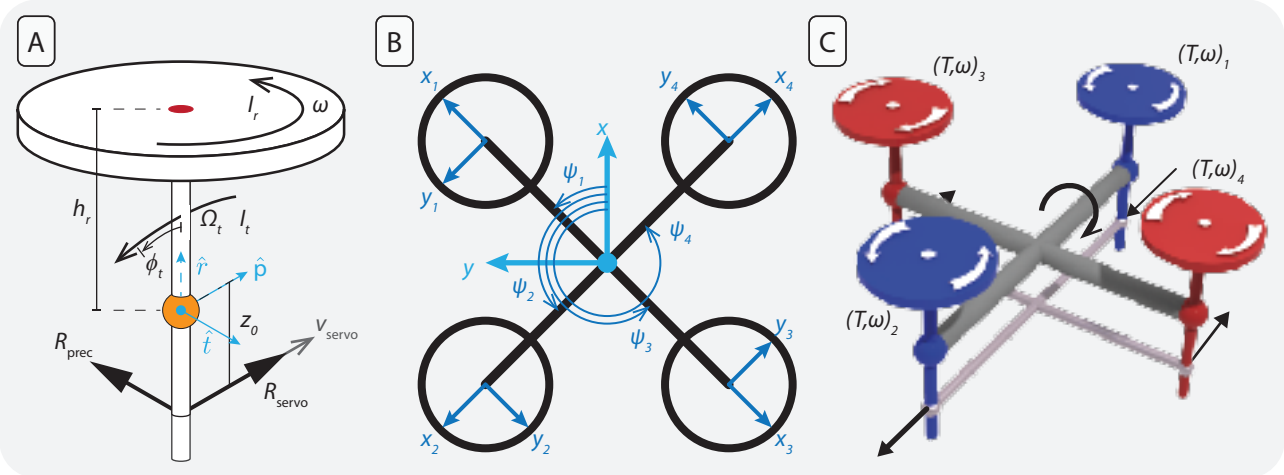


Figure 3.2: **Frame of reference to calculate actuator forces due to precession**. (**A**) Spinning top model of a tilting rotor with a massless rod precessing about the pivot point (orange) with the non-stationary tilting-frame (blue). (**B**) The arm frames of reference are static relative to the bodyframe and are orientated at ψ_i, measured from the x-axis, about the z-axis. (**C**) The forces experienced by the mechanism due to a rotation about the axis through rotor 1 and 3

The analysis is limited to the assumption that $\omega \gg \Omega_t$, which is true for the majority of the flight envelope. Nevertheless, when conducting zero-thrust manoeuvres, the actuators directly impart the force to tilt the rotors. The Force of actuation would then be

$$R_{\text{servo}} = \frac{(I + m_r h_r^2)\dot{\Omega}_t}{Z_0} \tag{3.15}$$

with the rotor's mass denoted as m_r, and I is the rotor's moment of inertia about an axis normal to the spin. As $R_{\text{prec}} \perp R_{\text{servo}}$, $R_{\text{prec,max}}$ and $R_{\text{servo,max}}$ are therefore the design limits for the mechanism's structure and actuator respectively.

3.3.1 Resultant forces due to tilting

For completeness, again by adapting established theories, tilting forces are derived as a function of the tilt rate [126]. The total angular momentum of the rotor is therefore

$$\hat{L}_r = \hat{L}_{\text{tilt}} + \hat{L}_{\text{spin}} \tag{3.16}$$

$$= (I + m_r h_r^2)\Omega_t \hat{t} + I_r \omega \hat{r} \tag{3.17}$$

where $[\hat{r}, \hat{t}, \hat{p}]$ are the Cartesian unit vectors with $\hat{r}$ denoting the rotor spin axis which, when viewed from the drone's frame of reference, varies in orientation over time. $\hat{t}$ represents the unit vector in the opposite direction of the force applied on the rotor and is therefore stationary. The third unit vector $\hat{p}$ lies on the plane of precession and is orthogonal to $\hat{r}$ and $\hat{p}$.

Assuming constant ω and initial $\Omega_t = 0$, a torque τ_{servo} applied to the system will yield

$$\hat{\tau} = \begin{bmatrix} \tau_{\text{rotor}} \\ \tau_{\text{servo}} \\ \tau_{\text{struc}} \end{bmatrix} = \frac{dL_r}{dt} \tag{3.18}$$

$$= (I + m_r h_r^2)\Big(\frac{d\Omega_t}{t}\hat{t} + \Omega_t \frac{d\hat{t}}{dt}\Big) + I_r\Big(\frac{d\omega}{dt}\hat{r} + \omega\frac{d\hat{r}}{dt}\Big) \tag{3.19}$$

and as $\hat{t}$ is held constant by the torque, thus $\frac{d\hat{t}}{dt} = 0$. The change of spin axis orientation $d\hat{r}$ is equal to the change of tilt angle about $\hat{t}$ but in the direction of $\hat{p}$ such that $\frac{d\hat{r}}{dt} = \frac{d\phi_t}{dt}\hat{p} = \Omega_t\hat{p}$. (3.19) simplifies to

$$\hat{\tau} = (I + m_r h_r^2)\dot{\Omega}_t \hat{t} + I_r \omega \Omega_t \hat{p} \tag{3.20}$$

3.4 Tilting in motion

The rudimentary position-controlled servomotors are sufficient in keeping the robot controlled in the air. But commanding position setpoints without a well-defined path, or better yet, a timed trajectory, the abrupt rotor tilts generated by position setpoints can yield jittery motions on the robot. It is therefore necessary to study the properties of the servomotor paths.

3.4.1 Geodesic path

The projection of the rotor orientation to servo positions can be re-imagined as an inverted polar azimuthal projection of the rotor sphere of rotation onto the servo plane [127]. The geodesic path between $[h_r, \theta, \phi]_i$ and $[h_r, \theta, \phi]_f$ lies on a great circle of the rotor sphere (Fig.3.3). Therefore, this path is on a flat plane defined by $[0, 0, 0], [h_r, \theta, \phi]_i, [h_r, \theta, \phi]_f$. As the intersection of two planes forms a straight line, so is the geodesic path on the servo plane. The geodesic path on the servo unit sphere is derived by first converting the spherical coordinates of the initial and final points on the sphere to their Cartesian form.

$$x_{i,f} = \cos\theta_{i,f} \sin\phi_{i,f} \quad y_{i,f} = \sin\theta_{i,f} \sin\phi_{i,f} \tag{3.21}$$

$$z_{i,f} = \cos\phi_{i,f} \tag{3.22}$$

The positions x, y, z are then normalised such that

$$x = x_f + (n-1)\Delta x,\ y = y_f + (n-1)\Delta y,\ z = z_f + (n-1)\Delta z, \text{ where } 0 \leq n \leq 1 \tag{3.23}$$

and the servomotor positions can be calculated by

$$s_1 = -\frac{Z_0}{z}x, \qquad s_2 = \frac{Z_0}{z}y \tag{3.24}$$

$$\frac{ds_1}{dt} = \left(-\frac{Z_0\Delta x}{z} + \frac{Z_0 x \Delta z}{z^2}\right)\frac{dn}{dt}, \qquad \frac{ds_2}{dt} = \left(\frac{Z_0\Delta y}{z} - \frac{Z_0 y \Delta z}{z^2}\right)\frac{dn}{dt} \tag{3.25}$$

To prove that the geodesic path on the servo plane is indeed a straight line

$$\frac{ds_1}{ds_2} = \frac{ds_1}{dt}\left(\frac{ds_2}{dt}\right)^{-1} \tag{3.26}$$

$$= \frac{(x_f + (n-1)\Delta x)\Delta z - (z_f + (n-1)\Delta z)\Delta x}{(z_f + (n-1)\Delta z)\Delta y - (y_f + (n-1)\Delta y)\Delta z} \tag{3.27}$$

$$= \frac{x_f\Delta z - z_f\Delta x}{z_f\Delta y - y_f\Delta z} = \frac{x_i z_f - x_f z_i}{y_f z_i - y_i z_f} = \textbf{constant} \quad \square \tag{3.28}$$

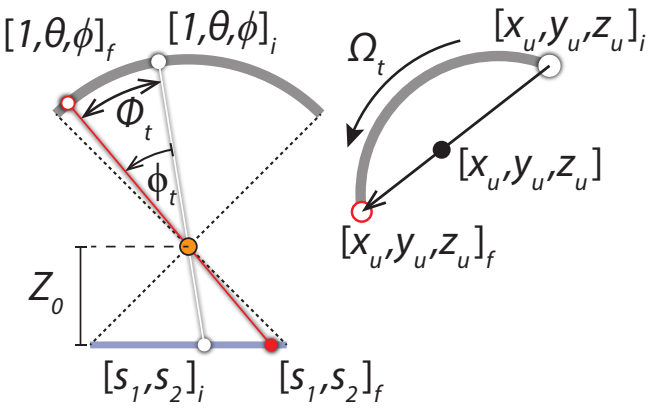


Figure 3.3: **Coordinate systems** on the rotor unit sphere and servo plane

As by the triangle inequality axiom

$$\Delta(a,c) \leq \Delta(a,b) + \Delta(b,c) \tag{3.29}$$

and extending the triangle inequality further such that

$$\Delta(a,c) \leq \Delta(a,b_n) + \Delta(b_n,c) \tag{3.30}$$

$$\Delta(a,b_n) \leq \Delta(a,b_{n-1}) + \Delta(b_{n-1},b_n) \tag{3.31}$$

$$\Delta(a,c) \leq \Delta(a,b_0) + \Delta(b_0,b_1) + ... + \Delta(b_{n-1},b_n) + \Delta(b_n,c) \tag{3.32}$$

where a, b, and c are respectively the initial, intermediate, and endpoints on a plane, we can conclude that the geodesic path is both the non-exclusive shortest path of rotor and servomotor travel.

3.4.2 Path of shortest time

For stepped setpoint rotor tilt angle inputs, the servomotors must reach the desired position in the shortest time. Although the direct geodesic distance represents the shortest path between the current and desired tilt vector, the rate at which this can be achieved is determined by the longest time required for the servomotors to reach their final positions. The difference between the shortest path and the shortest trajectory can be observed by calculating the Chebyshev

distance on the servo plane

$$D_{\text{Chebyshev}} = \max(|c_1 - a_1|, |c_2 - a_2|) = \max(|\Delta s_1|, |\Delta s_2|) \tag{3.33}$$

where a and c are the initial and final servo positions respectively, subscripts denoting the servo axes. Assuming $D_{\text{Chebyshev}} = |\Delta s_1|$, Servo 2's trajectory becomes non-singular. As such, it is necessary to ensure that the servomotors remain within the range of the fastest paths. Given that the timespan of the travel is more critical than the distance travelled, we define and use a temporal metric, the Chebyshev time, as the time required to complete a travel from location a to c using the fastest speed

$$T_{\text{Cheb}} = \max\left(\frac{|\Delta s_1|}{\dot{s}_{1\text{max}}}, \frac{|\Delta s_2|}{\dot{s}_{2\text{max}}}\right) \tag{3.34}$$

Assuming again that Servo 1 is the limiting factor such that

$$|\dot{s}_1(t)| = \dot{s}_{1\text{max}} \quad \textbf{and} \quad \frac{|\Delta s_1|}{\dot{s}_{1\text{max}}} > \frac{|\Delta s_2|}{\dot{s}_{2\text{max}}} \tag{3.35}$$

one can equate the Chebyshev time of both servomotor movements as

$$T_{\text{Cheb}} = \frac{|\Delta s_1|}{\dot{s}_{1\text{max}}} \geq \int_{s_{2i}}^{s_{2f}} \frac{1}{\dot{s}_2(t)} ds_2 \tag{3.36}$$

While (3.36) is by which to determine if the trajectory of Servo 2 is the fastest trajectory, the right-hand side is not solvable as the servomotor velocity is a function of time. But knowing the servomotor trajectory is self-serving as the time at which Servo 2 would reach its target would be known. However, the range of fastest paths is bounded by the paths by which servomotors operate at maximum absolute velocity with minimal changes of direction such that

$$T_{\text{Cheb}} = \sum \frac{\delta s_2}{\mathbf{sgn}(\delta s_2) \cdot \dot{s}_{2\text{max}}} \qquad \text{where} \qquad \Delta s_2 = \sum \delta s_2 \tag{3.37}$$

$$T_{\text{Cheb}} = \sum \frac{\delta s_2(\delta s_2 > 0)}{\dot{s}_{2\text{max}}} + \sum -\frac{\delta s_2(\delta s_2 < 0)}{\dot{s}_{2\text{max}}} \tag{3.38}$$

$$= t_{ab} + t_{bc} \tag{3.39}$$

with t_{ab} denoting the time to an intermediate point b whiles moving constantly at the maximum absolute velocity. Being interchangeable in the order of the direction of travel

$$t_{ab} = \sum \frac{\delta s_2(\delta s_2 > 0)}{\dot{s}_{2\max}} \qquad \text{or} \qquad \sum -\frac{\delta s_2(\delta s_2 < 0)}{\dot{s}_{2\max}} \tag{3.40}$$

$$t_{bc} = \sum -\frac{\delta s_2(\delta s_2 < 0)}{\dot{s}_{2\max}} \qquad \sum \frac{\delta s_2(\delta s_2 > 0)}{\dot{s}_{2\max}} \tag{3.41}$$

Alternatively, we can derive t_{ab} from the difference between the initial and final Servo 2 position

$$\Delta s_2 = \pm \dot{s}_{2\max} t_{ab} \mp \dot{s}_{2\max}(T_{\text{Cheb}} - t_{ab}) \tag{3.42}$$

$$= \pm \dot{s}_{2\max}(2t_{ab} - T_{\text{Cheb}}) \tag{3.43}$$

$$\frac{\Delta s_2}{\dot{s}_{2\max}} = \pm 2t_{ab} \mp T_{\text{Cheb}} \tag{3.44}$$

$$\frac{\Delta s_2}{\dot{s}_{2\max}} \pm T_{\text{Cheb}} = \pm 2t_{ab} \tag{3.45}$$

$$t_{ab} = \frac{1}{2}\Big(T_{\text{Cheb}} \pm \frac{\Delta s_2}{\dot{s}_{2\max}}\Big) \tag{3.46}$$

thus the maximum and minimum Servo 2 positions are

$$s_{2\max} = \frac{1}{2}(\Delta s_2 + \dot{s}_{2\max} T_{\text{Cheb}}) \tag{3.47}$$

$$s_{2\min} = \frac{1}{2}(\Delta s_2 - \dot{s}_{2\max} T_{\text{Cheb}}) \tag{3.48}$$

As shown in Figure 3.4A, if both servomotors operate at maximum absolute velocity, in the same timespan, the longest possible paths would enclose a parallelogram.

3.4.3 Rate of Tilt

It is helpful to derive the total angle Φ_t and the angular rate of tilt Ω_t between set points in terms of the rotor and servomotor positions. Following (3.23), we can derive

$$n = \frac{1}{2}\left(1 - \frac{\tan\left(\frac{\Phi_t}{2} - \phi_t\right)}{\tan\frac{\Phi_t}{2}}\right) \tag{3.49}$$

$$\frac{dn}{dt} = \frac{\Omega_t}{2\tan\frac{\Phi_t}{2}}\left(\frac{1}{\cos^2\left(\frac{\Phi_t}{2} - \phi_t\right)}\right) \tag{3.50}$$

$$\phi_t = \arccos\frac{[x,y,z]_i \cdot [x,y,z]}{\|[x,y,z]\|} \tag{3.51}$$

$$= \arccos\frac{[s_i, Z_0] \cdot [s, Z_0]}{\|[s_i, Z_0]\| \cdot \|[s, Z_0]\|} \tag{3.52}$$

$$\Phi_t = \arccos\frac{[x,y,z]_i \cdot [x,y,z]_f}{\|[x,y,z]_f\|} \tag{3.53}$$

3.4.4 Servomotor specification

As it is impractical to calculate (3.50) at every timestep, the equation can be simplified by assuming $\phi_t = 0$. This implies that the intermediate position $\hat{b}$ is always the initial position of each timestep. Thus we get

$$\frac{dn}{dt} = \frac{\Omega_t}{2\tan\frac{\Phi_t}{2}\cos^2\frac{\Phi_t}{2}} = \frac{\Omega_t}{2\sin\frac{\Phi_t}{2}\cos\frac{\Phi_t}{2}} = \frac{\Omega_t}{\sin\Phi_t} \tag{3.54}$$

To solve for the servomotor velocity as a function of the required rate of tilt, we first represent the vector $[x, y, z]$ with

$$[x,y,z] = \hat{b} = \|\hat{b}\|[b_x, b_y, b_z] \tag{3.55}$$

therefore, on the unit sphere we get

$$[x_u, y_u, z_u]_i = [x_u, y_u, z_u] = \hat{b}_u = |1|[b_x, b_y, b_z] \tag{3.56}$$

$$[x_u, y_u, z_u]_f = \hat{c}_u \ = |1|[c_x, c_y, c_z] \tag{3.57}$$

Substituting the equations above in (3.25) yields

$$\frac{ds_{1,2}}{dt} = \pm \left[\frac{(c_z - b_z)b_{x,y}}{b_z^2} - \frac{c_{x,y} - b_{x,y}}{b_z} \right] \frac{Z_0 \Omega_t}{\sin \Phi_t} \tag{3.58}$$

$$= \pm \left[\frac{(c_z - b_z)b_{x,y}}{b_z^2} - \frac{c_{x,y} - b_{x,y}}{b_z} \right] \frac{Z_0 \Omega_t}{\sqrt{1 - \left(\hat{b} \cdot \hat{c}\right)^2}} \tag{3.59}$$

$$\frac{ds_{1,2}}{dt} = \pm \left[\frac{\left(\frac{Z_0}{\sqrt{s_{1f}^2 + s_{2f}^2 + Z_0^2}} - \frac{Z_0}{\sqrt{s_1^2 + s_2^2 + Z_0^2}} \right) \frac{\mp s_{1,2}}{\sqrt{s_1^2 + s_2^2 + Z_0^2}}}{\frac{{Z_0}^2}{s_1^2 + s_2^2 + Z_0^2}} - \frac{\frac{\mp s_{1,2f}}{\sqrt{s_{1f}^2 + s_{2f}^2 + Z_0^2}} - \frac{\mp s_{1,2}}{\sqrt{s_1^2 + s_2^2 + Z_0^2}}}{\frac{Z_0}{\sqrt{s_1^2 + s_2^2 + Z_0^2}}} \right] \cdot \frac{Z_0 \Omega_t}{\sqrt{1 - \frac{(-s_1 \cdot -s_{1f} + s_2 \cdot s_{2f} + Z_0^2)^2}{(s_1^2 + s_2^2 + Z_0^2)(s_{1f}^2 + s_{2f}^2 + Z_0^2)}}} \tag{3.60}$$

$$\frac{ds_{1,2}}{dt} = \frac{\Omega_t (s_{1,2f} - s_{1,2})({s_1}^2 + {s_2}^2 + {Z_0}^2)}{\sqrt{{Z_0}^2[(s_1 - s_{1f})^2 + (s_2 - s_{2f})^2] + (s_1 s_{2f} - s_2 s_{1f})^2}} \tag{3.61}$$

To further simplify the servo velocity equations for an arbitrary trajectory can satisfy $\Phi_t \to 0$

$$\frac{ds_{1,2}}{dt} \approx \left(\pm \frac{\Delta b_z \hat{b}_{ix,iy}}{\hat{b}_{iz}^2} \mp \frac{\Delta b_{x,y}}{\hat{b}_{iz}} \right) \frac{Z_0 \Omega_t}{\Phi_t} \tag{3.62}$$

$$\Phi_t \approx \sqrt{\Delta b_x^2 + \Delta b_y^2 + \Delta b_z^2} \tag{3.63}$$

To determine the maximum mechanism speed, hence the servos required, we further examine (3.62). As $[\Delta b_x, \Delta b_y, \Delta b_z]$ forms a small circle approximately about $\hat{b}_i$, we can formulate (3.62)

as

$$\Delta b_x = \Phi_t \sin\theta \sin\beta \qquad \Delta b_y = \Phi_t \cos\theta \sin\beta \tag{3.64}$$

$$\Delta b_z = \Phi_t \sin\phi \cos\beta \tag{3.65}$$

$$\frac{ds_1}{dt} = \left(\frac{\sin^2\phi\cos\beta\cos\theta}{\cos^2\phi} - \frac{\sin\theta\sin\beta}{\cos\phi}\right) Z_0\Omega_t \tag{3.66}$$

$$\frac{ds_2}{dt} = \left(\frac{\sin^2\phi\cos\beta\sin\theta}{\cos^2\phi} - \frac{\cos\theta\sin\beta}{\cos\phi}\right) Z_0\Omega_t \tag{3.67}$$

As the servo velocities are inversely correlated with $\hat{b}_z$, maximum servo speed occurs at the highest tilt angle $\phi_{\max}$. Thus,

$$\dot{s}_{1,2\max} = \mathbf{max}\left(\frac{ds_{1,2}}{dt}(\beta, \theta, f(\theta), Z_0, \Omega_{t\max})\right) \tag{3.68}$$

where $0 < \beta \leq \pi$, $-\pi < \theta \leq \pi$, $\phi_{\max} = f(\theta)$, Z_0 is a structural property, and $\Omega_{t\max}$ is the design maximum tilt angular velocity.

$$\frac{d^2s_1}{dt^2} = \left(\frac{Z_0(x_i + n\Delta x)\Delta z}{(z_i + n\Delta z)^2} - \frac{Z_0\Delta x}{z_i + n\Delta z}\right)\frac{d^2n}{dt^2} \tag{3.69}$$

$$- \left(\frac{2Z_0(x_i + n\Delta x)\Delta z^2}{(z_i + n\Delta z)^3}\right)\left(\frac{dn}{dt}\right)^2 \tag{3.70}$$

3.4.5 Servo velocity properties

Though the analysis of the servo motion through time-variant means aids in visualising the possible paths of the shortest time, the position-variant servo velocity functions are more applicable for control.

In plotting the servo velocity as a function of the position (see Fig.3.4), we see that this relation is parabolic, which is not obviously notable given (3.61).

As

$$s_2 = s_{2f} - \frac{ds_2}{ds_1}(s_{1f} - s_1) \tag{3.71}$$

let

$$C = \frac{ds_2}{ds_1} = \frac{s_{2f} - s_2}{s_{1f} - s_1} \tag{3.72}$$

thus by (3.61)

$$\frac{ds_{1,2}}{dt} = \pm \frac{\Omega_t({s_1}^2 + {s_2}^2 + {Z_0}^2)}{\sqrt{{Z_0}^2(1 + C^{\pm 2}) + (C^{\pm 1}s_{1,2f} - s_{2,1f})^2}} \tag{3.73}$$

which expands to

$$\frac{ds_1}{dt} = \begin{bmatrix} (1 + C^2){s_1}^2 \\ \quad +2C(s_{2f} - Cs_{1f})s_1 \\ \quad\quad +(s_{2f} - Cs_{1f})^2 + {Z_0}^2 \end{bmatrix} \quad \square \tag{3.74}$$
$$\cdot\, \Omega_t \left({Z_0}^2(1 + C^2) + (Cs_{1f} - s_{2f})^2\right)^{-\frac{1}{2}}$$

$$\frac{ds_2}{dt} = \begin{bmatrix} (1 + C^{-2}){s_2}^2 \\ \quad +2C^{-1}(s_{1f} - C^{-1}s_{2f})s_2 \\ \quad\quad +(s_{1f} - C^{-1}s_{2f})^2 + {Z_0}^2 \end{bmatrix} \quad \square \tag{3.75}$$
$$\cdot\, -\Omega_t \left({Z_0}^2(1 + C^{-2}) + (C^{-1}s_{2f} - s_{1f})^2\right)^{-\frac{1}{2}}$$

from which we can see the second-degree polynomial relationship. Therefore, for a constant rate of tilt, the servomotors must move parabolically faster when further away from $s_i = 0$.

3.5 Tilting Mechanism Design

The rotors are mounted on universal joint type gimbals. A control rod extends down from the gimbal, connecting to a ball joint by sliding contact. By controlling the planar location of the ball joints in unison, the tilting of the rotors are synchronised. I propose a novel method of actuation to address the shortcomings of the previous twin linear servomotor design in Chapter 2.

The novel design features twin radial servos mounted perpendicularly, above and below a biaxial rack-and-pinion mechanism (see Fig.3.5). This is akin to two widened rack-and-pinion with the

racks joint back-to-back and oriented 90° apart. The proposed mechanism allows independent planar movement while the elongated pinion gears act as rotation constraints.

3.6 Summary

The work presented underpins the theory of the TiltDrone's structural dynamics when tilting with a spinning rotor. The kinematics of the tilting mechanism was presented in Chapter 2, this chapter extends the work to the mechanism's dynamics. I noted the potential benefits of improved transient behaviour if the mechanism is inverted, with the rotors working in a pusher configuration. This would have allowed the reaction on the body due to tilting to act in the same direction as the horizontal thrust. I also noted the distinction between the shortest tilt path by distance and time. This highlights the necessity of controlling the servomotors' velocity.

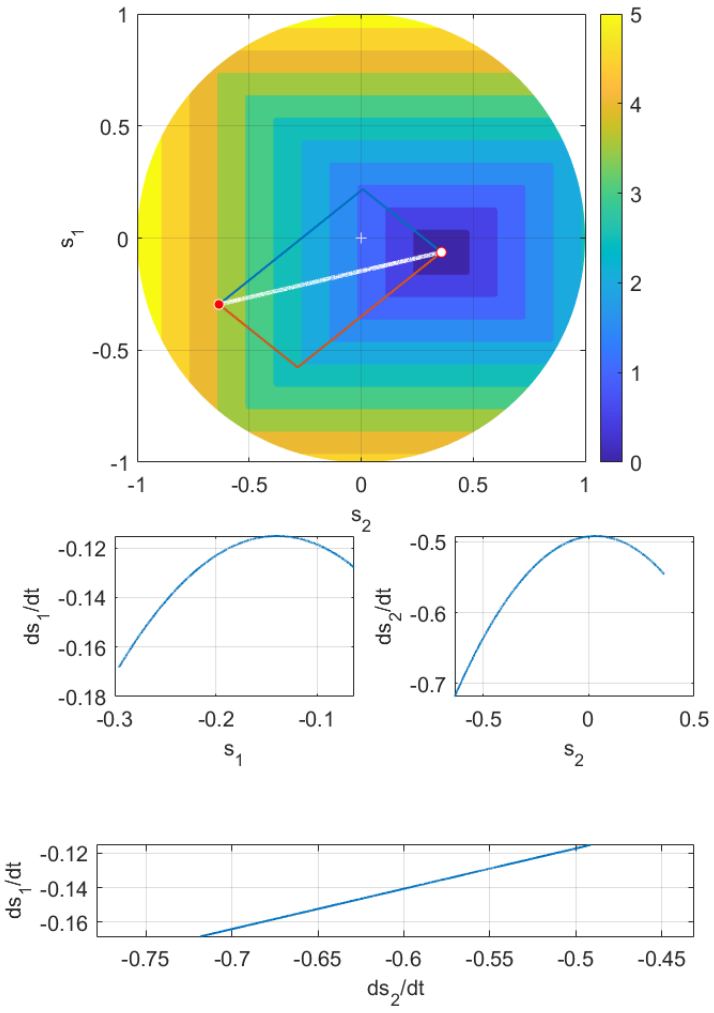


Figure 3.4: Top: Heat map showing the maximum time metric T_{cheb} from the current servo position $[s_{1i}, s_{2i}]$ (white spot), the target servo position $[s_{1f}, s_{2f}]$ (red spot) and the boundary of possible servo position paths which achieves minimum travel time. This is more useful than Euclidean distance as the rate of movement is limited by a single servo's maximum rpm. Middle: The variation of servo velocity on a geodesic path under constant rate of tilt. Bottom: Plotting the servo velocities shows that the geodesic path is a straight line.

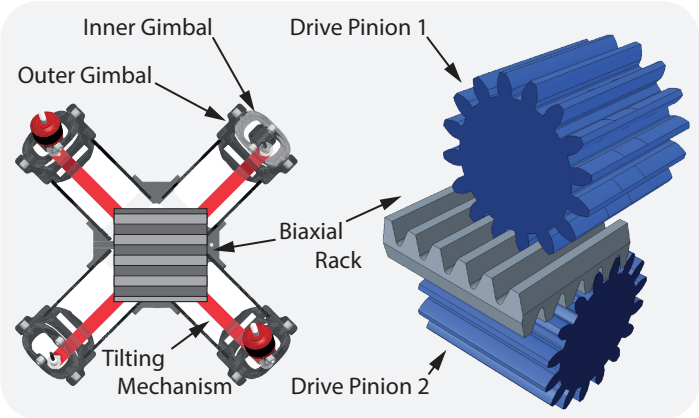


Figure 3.5: **Biaxial rack and pinion mechanism** top view (left) and enlarged (right)

Chapter 4

Tiltrotor Measuring Ring

Quadrotors are well suited to conduct ecological fieldwork. They are simple to maintain, easy to pilot, and can hover in the air. Though quadrotors are in common use as remote sensing platforms, their use as physical tools in the field is limited. To operate quadrotors as tools, they must be in proximity or in contact with their surroundings. But in such scenarios, quadrotor use is limited by the dangers of fast-spinning propellers near animal and plant life, flight stability when in contact with other objects, and spatial constraints in spaces such as forests. This chapter presents a solution; a lightweight tiltrotor system with an externally mounted, ring-shaped, tilting measuring wheel. The tilting ring remains level while the rotors tilt to provide forward and backward thrust. As the drone slides against a tree, its enclosed encoder measures the distance travelled. Thus, with the measured circumference, we can calculate the tree diameter, specifically the diameter at breast height. The sub-250g prototype is capable of stable flight and can maintain stable contact with vertical surfaces. The measuring ring, when accounted for the tree surface texture, can accurately measure the tree circumference. By using quadrotors as tools for ecological fieldwork, researchers can gather vital ecological data at greater rates.

4.1 Introduction

Sampling is a core component of ecology. The empirical data, upon which theories and models are validated, can only be obtained by sampling. With increasing climate change, the need to know and track the state of nature has become more important than ever before. Despite the urgent need for action, funding is still insufficient [128, 129]. Therefore, we need cost- and time-efficient sampling methods to mitigate the funding limitations.

Increasingly, technology has greatly expanded the capabilities of researchers at conducting fieldwork. With a broad range of terrestrial sensors, ecologists can construct three-dimensional maps of the research site at fine temporal and spatial scales [130]. Aerial vehicles, manned and unmanned, with imaging devices further increase productivity by enabling automated data gathering [131]. For regional and global data, satellite imagining is used [132].

Of these technologies, unmanned drones have seen a major uptick in applications. From the more traditional role of aerial imagining, drones have expanded to be used in the deployment of remote sensor networks and collection of biomass samples [133].

While these tools are excellent additions for field researchers, the method of measuring DBH remains fundamentally unchanged. Compounding this problem, trees of interest are often clumped in a forest; satellite and over-canopy imagining may not penetrate the canopy; camera-equipped drones are too large to fly safely under the canopy and are too expensive to replace if damaged; terrestrial sensors are cumbersome to transport. Thus, measuring DBH broadly remains an unautomated, labour-intensive process.

From an aerial robotics perspective, the process of measuring DBH involves two aspects: first is localisation, the need to position the measuring tool at the desired position and height; and surface interaction, making contact with the tree and wrapping the tool around the trunk. Neither are trivial tasks for a drone in a forested environment. Full localisation of a drone requires an array of cameras and onboard image processing, adding significant cost to the platform. However, lightweight optical flow and time-of-flight sensors can provide sufficient information to hover at a set distance away from a vertical surface [134]. On the other hand, there are numerous lightweight solutions for aerial surface interaction.

Flying in dense forests, surface interaction performs a dual role of measuring DBH and protecting the drone from damage. Although single-point interaction mechanisms for data collection have been researched to a greater depth [92], this class of design is not suitable for a protective role. On the contrary, these mechanisms, if not well designed, can cause flight instability in certain situations.

Designs which focus on protection range from rigid crash protection cages to compliant damage-resistant bodies. Here, a distinction can be made between the design intentions. The first kind of design solely ensures the survival of the platform. A second class of design attempts to divert the vehicle to a stable flight path upon impact. By rotating a protective ring, the drone can remain stable in yaw and remain controllable through multiple impacts [135]. However, due to the lack of decoupling on the pitch axis, and to a lesser extent the roll axis, the drone was uncontrollable post-impact at high tilt angles.

I propose an improvement to the rotating protective ring. The design embeds an encoder to measure the rotation of a freely rotating outer ring. This is coupled with an active gimbal mechanism to tilt the rotors. By actively tilting the ring on the pitch axis, the protective ring will remain horizontal at all times; the roll axis will be kept level and not used for steering. At contact with the tree trunk, a slight yaw angle away from the normal will impart a horizontal rotation on the ring. This enables a sub-250 g quadrotor drone, name the "Ring-Beatle", to measure tree circumference by physical contact (Fig.4.1A). The DBH is then calculated from the circumference.

4.2 Results

4.2.1 Hardware design

The 3D-printed platform comprises a drone and an outer ring running on an inner circular track. The ring and the track are gimballed in the pitch axis via a servomotor on the drone. The ring-track unit is mounted on the drone via a connecting beam which also houses the encoder. To reduce the part count and assembly time, the driven gear is integrated into the connecting

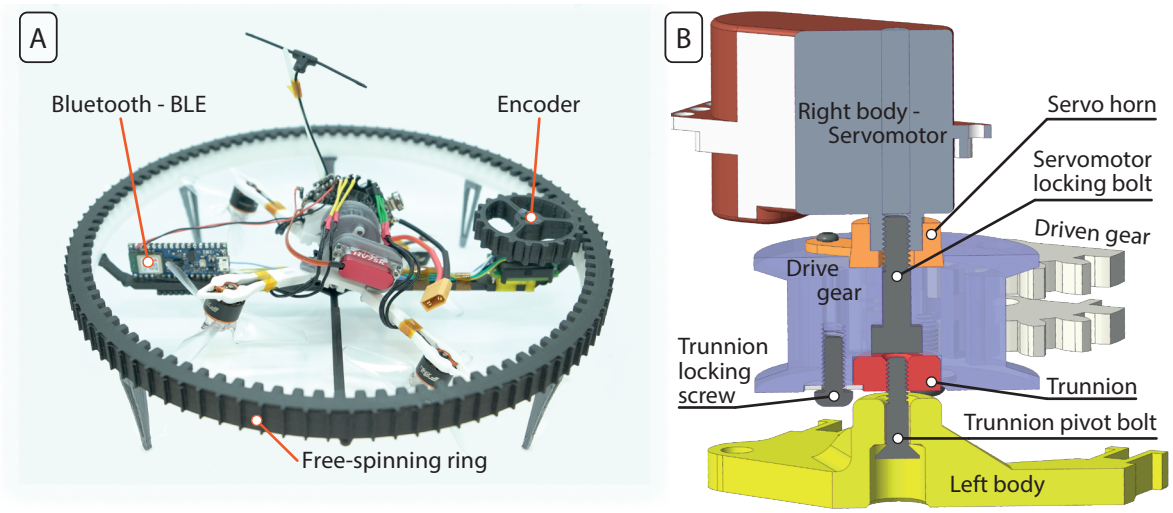


Figure 4.1: **The prototype tilting ring robot**. (**A**) A photograph of the Ring-Beatle robot and (**B**) a rendered drawing of the tilting mechanism.

beam via two parallel halved lamina emergent torsion (h-LET) joints. The connecting beam is 3D printed as a flat part and is bent to form the final configuration. The driven gear is folded perpendicularly during assembly. The h-LET joint was analysed with finite element modelling and deemed to be able to sustain the deformation.

The drone employs a split body design, the two halves join through the servo motor shaft and the gimbal ring pivot shaft. This split body design is necessary to maintain a compact form factor whiles ensuring clearance from the propellers. The four rotors are clipped into the arms and held by the material's spring tension.

While a through bolt joining the two half-bodies through the PTFE ring pivot secures the relative distance between the two halves, it does not sufficiently constrain the twist and torsional movements. Therefore, a second point of connection between the two half-bodies is required. To avoid interference with the tilting ring, the connector can be positioned high above the servomotor drive gear, but joining the bodies through the servomotor presents a compact solution. However, joining the split bodies through the output axis of an HV75K servomotor presented a unique challenge. The servo shaft must freely rotate about its axis whiles restricting movement in all other DoF. Furthermore, the HV75K servomotor does not provide a static concentric shaft to which the two bodies can be rigidly mounted to. All the while, the mechanism must be assemblable.

I designed a nested trunnion that allowed the servo-driven gear to rotate the ring freely whiles providing movement constraints on the other five DoF (Fig.4.1B). To assemble the nested trunnion, the servo horn is first mounted to the drive gear; the servo horn is necessary to transmit torque to the gears without slippage. The drive gear is then meshed with the driven gear and mounted onto the servomotor with a centre locking bolt. The trunnion is press-fitted to the side of the drive gear, opposite to the servo horn. The trunnion is secured with three overlapping screws to ensure stability under bending. Finally, the trunnion pivot bolt is threaded through the left body and screwed into the trunnion, forming a pin joint.

The pusher-propeller design is both aerodynamically and structurally beneficial [87]. Limited by the design of the BLDC motors, the clip-on motor mounts have insufficient material to sustain the peeling load of a puller design. Using a pusher design, the clip-on mounts simply have to be strong enough to withstand the torque from the rotor and its weight when not providing thrust.

Data collection

An encoder is mounted on the ring structure to measure the amount the free-spinning ring had turned. This is recorded by Arduino Nano 33 BLE Sense which disseminates the data via Bluetooth BLE. While testing outdoors, it was noted that Bluetooth BLE cannot penetrate thick tree trunks.

4.2.2 Measuring ring validation

The measuring ring is validated with hand-held tests, measuring tree circumferences (Fig. 4.2). The ground truth is provided by manual measurements using a measuring tape. Both measurements are conducted at breast height. The smaller branches had noticeably more scatter, but the larger branches produced a higher error. This could be because the tree surface roughness correlates with its DBH. Arranging the data in approximate categories of tree surface coarseness (Fig. 4.3), we get a similar trend as above (Tab. 4.1). While an undercount is due to slippages of the ring on the tree, overcounts are due to the ring tracking the concave surfaces,

unlike the measuring tape that bridges across it.

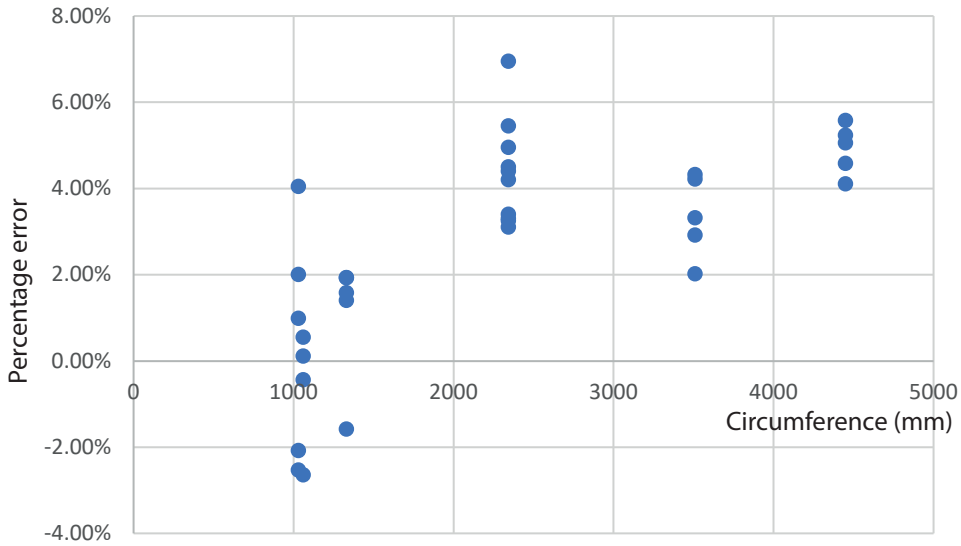


Figure 4.2: **Hand held measurement percentage accuracy vs tree circumference**. The ground truth is determined manually with a measuring tape.



Figure 4.3: **A subset of the trees** used in validation. (**A**) A smooth tree. (**B**) A medium coarse tree. (**C**) A coarse tree.

4.3 Discussion

I have designed and built a prototype tiltrotor platform. The tiltrotor comprises a quadrotor thrust unit tilting within a larger measuring ring. By sliding along a tree, with the measuring ring horizontally level and the thrust unit tilted to provide the contact force, the measuring ring

Table 4.1: Errors when the measuring ring is hand tested on various trees.

Coarseness	Mean	Standard Deviation
Coarse	4.14%	1.10%
Medium	0.32%	1.62%
Smooth	0.49%	2.78%

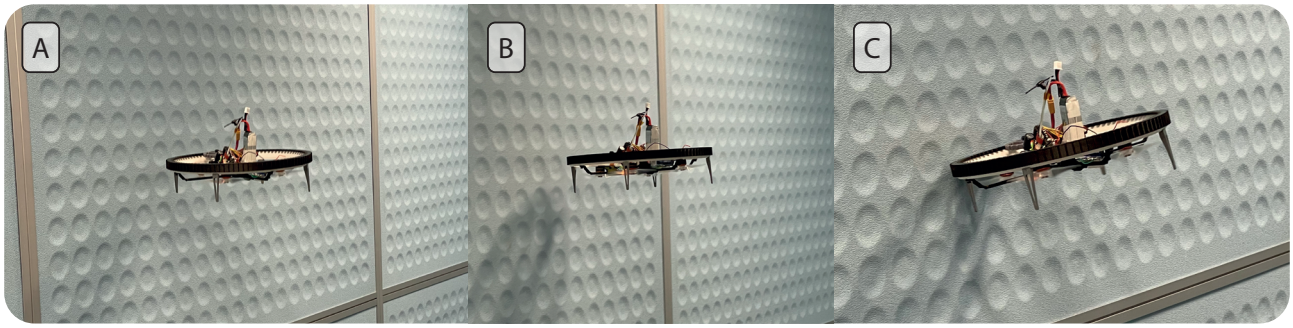


Figure 4.4: **The prototype flying** (**A**) in free flight, (**B**) at approach, (**C**) and contacting the wall.

will rotate independently from the platform. Thus, with an encoder attached, the prototype can measure tree circumferences.

The prototype is airworthy and has shown to be capable of sustaining impacts and continuous contact with vertical surfaces (Fig. 4.4). However, the lack of mechanical damping can cause unstable impacts leading to a coupled oscillation of the ring and the rotors ending in a crash. The much larger inertia relative to the moment arm of the rotors means while the robot is well capable of flight, it has a lower margin of stability. The coupled oscillation was observed when the robot was commanded aggressive manoeuvres.

The measuring is manually tested, and with ground-truth data, we can correct for variables such as tree bark coarseness. To fully realise the platform's use, the measuring ring drone needs a simplistic form of external perception to reduce the workload of the pilot [134]. With the aid of an optical flow sensor to hold a constant relative incidence angle, below the tangential angle, 90 degrees in most cases, the drone will maintain contact with the trunk. The operator intervention is only required to begin and end the measurement. Overall, this novel use of micro-drones greatly enhances the efficiency of ecological fieldwork and increases the rate of measuring tree DBH.

Chapter 5

The Flight Controller Placement on Tiltrotor Quadrotors

The quadrotor is well regarded as a user-friendly class of unmanned aerial vehicles. But, with fixed rotors, a significant limitation of the quadrotor is that it needs to pitch and/or roll its body to move laterally. A significant area of development to mitigate this limitation is the tiltrotor-quadrotor concept, whereby the platform can tilt its rotors to generate thrust at various angles. The quadrotor requires electronic stabilization to fly stably. With at least two moving bodies on the tiltrotor-quadrotor, it begs the question: "where should we mount the flight controller?". While many tiltrotor-quadrotor designs have been successfully trialled, none have explored the interaction between the control system electronics, the actuators, and the platform's inertia. I modelled and simulated an ideal quadrotor with a tilting body in two-dimensional space. I examined the effects of the flight controller placement, flight controller control loop frequency, servomotor control frequency, the tiltrotor body and rotor inertias, and the commanded trajectory on flight stability. The results show that flight performance is heavily influenced by the aforementioned variables. The placement of the flight controller is dependent on which aspect of performance the designer wants to optimise for. But, at high flight controller and servomotor control frequencies, it is preferable to mount the flight controller on the body with the larger inertia.

5.1 Introduction

Having completed the design of the tiltrotors in Chapter 2 and 4, I noted that, due to the presence of the servomotor, the Flight Controller (FC) placement affects the control system architecture. Similar to all quadrotors, the tiltrotor-quadrotor needs onboard sensors and controllers to maintain flight stability. These sensors and controllers are often integrated into a single electronics component, the FC. But with two bodies, there are two locations where the FC can be mounted. Conventionally, the FC would be placed within the larger of the two bodies because it is easier to package components within the larger body. But as flight stability and component packaging are mutually exclusive problems, the relationship between FC placement and flight stability is still unexplored.

I categorise tiltrotor designs with respect to the volumetric size difference between the "rotor body" and the drone's "payload body". I define the "rotor body" to be the rotors and the structures that are static relative to the rotors. Similarly, the "payload body" are the structures that are static relative to the mission-critical components. Using the tiltrotors in Chapter 2 and 4 as examples, the rotor body would refer to the rotors and the rotor mount in Chapter 2, and in Chapter 4 it is the quadrotor thrust unit. Conversely, the payload body comprises the majority of the robot's structure in Chapter 2, including the linear servomotors and the battery; in Chapter 4 it comprises the measuring ring.

We see that there are drone platforms with a large payload body and small rotor body that have interlinked rotors which tilt in the same direction [110, 65]. The platforms with independently actuated rotors can be included in this group in certain flight conditions [136, 93, 108, 109, 137]. There are also drones with roll-stabilising robotic arms that will often work outside their wheelbase [138]. In this group, the size of the payload body and rotor body is approximately equivalent. Examples of drones with a small payload body and a large rotor body would be conventional quadrotors, such as the DJI Mavic series, Parrot Anafi, and Skydio, which use gimbals to rotate a payload, such as a camera. While this is visually distinctive from the other groups of tiltrotors, they are kinematically equivalent.

There is a mild correlation between the volume of the drones' bodies and their inertia. This

is due to the shared requirement of quadrotors needing to be lightweight and manoeuvrable, and most quadrotors use similar propulsion technology—this is usually the only component of significant weight at the extremities of the quadrotor. Applying this correlation, we see that the group with the higher payload inertia mounts the FC on the payload body; the group with the lower payload inertia mounts the FC on the rotor body.

In theory, the FC measures the orientation of the body it is mounted to, and with kinematic equations, we can perfectly calculate the orientation of all the bodies on the platform. But, in practice the FC operates in discrete time, creating issues such as aliasing and limited fidelity. These discrete-time issues can cause a difference between the measured orientation values between the two FC mounting positions. Therefore, it is also plausible that the ratio of the inertias in conjunction with the FC placement can affect tiltrotor flight stability.

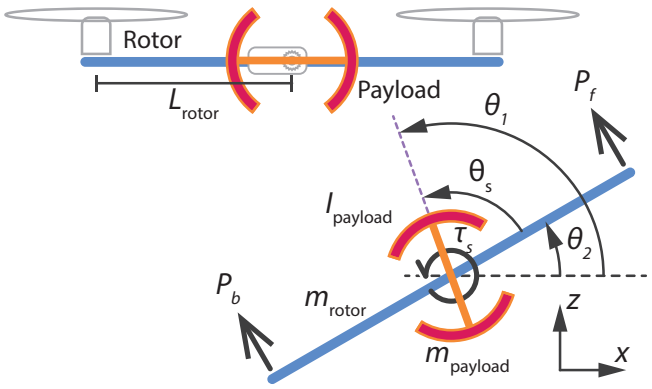


Figure 5.1: **The simulated tiltrotor design**. The payload Centre of Mass (CoM) coincides with the rotor body CoM. The payload body is free to rotate about its CoM and is rotated by the torque from a servomotor.

Physical test beds would most closely replicate our problem. However, limited by design and manufacturing constraints, physical test beds can introduce uncontrolled variables which may skew our analysis. To remove such constraints from influencing our analysis, which would invalidate our results, we simulated a generalised 2-dimensional tiltrotor (Fig. 5.1). A simulation would also allow us to isolate the variables that we would like to study.

5.2 Results

5.2.1 Simulation Physics

The tiltrotor design featured in the simulation is a quadrotor with a rotatable payload body; the rotor body and the payload body are connected via a servomotor. The payload body has a mass m_{payload} and inertia I_{payload}; its Centre of Mass (CoM) coincides with the rotor body's CoM. The servomotor is simulated as a DC motor with a linear torque speed curve. The voltage, hence its torque, is controlled with an angle-Proportional Derivative Controller (PD).

$$V_{\text{s}} = P_{\text{servo}} \cdot (\theta_{\text{s,final}} - \theta_{\text{s}}) - D_{\text{servo}} \cdot \omega_{\text{s}} \tag{5.1}$$

$$\tau_{\text{s}} = \frac{V_{\text{s}} - k_{\text{s}} \cdot \omega_{\text{s}}}{R_{\text{s}}} \cdot k_s \tag{5.2}$$

$$k_{\text{s}} = \frac{V_{\text{s,max}}}{\omega_{\text{s,no-load}}} \quad , \qquad R_s = \frac{k_{\text{s}} \cdot V_{\text{s,max}}}{\tau_{\text{s,max}}} \tag{5.3}$$

Where $\tau_{\text{s,max}}$ and $\omega_{\text{s,no-load}}$ are the stall torque and the no-load speed for the servomotor, k is the motor constant, and R the internal resistance. The voltage supplied to the DC motor is limited to $-V_{\text{s,max}} \leq V_{\text{s}} \leq V_{\text{s,max}}$.

The accelerations are calculated as follows:

$$\tau_{\text{r}_\text{i}} = L_{rotor}(P_{\text{f}_\text{i}} - P_{\text{b}_\text{i}}) \tag{5.4}$$

$$\frac{\text{d}^2\theta_1}{\text{d}t^2}_{i+1} = \frac{\tau_{\text{s}_\text{i}}}{I_{\text{payload}}} \tag{5.5}$$

$$\frac{\text{d}^2\theta_2}{\text{d}t^2}_{i+1} = \frac{\tau_{\text{r}_\text{i}} - \tau_{\text{s}_\text{i}}}{I_{\text{rotor}}} \tag{5.6}$$

$$\frac{\text{d}^2x}{\text{d}t^2}_{i+1} = -\frac{(P_{\text{f}_\text{i}} + P_{\text{b}_\text{i}})\sin(b2_i)}{(m_{\text{payload}} + m_{\text{rotor}})} \tag{5.7}$$

$$\frac{\text{d}^2z}{\text{d}t^2}_{i+1} = \frac{(P_{\text{f}_\text{i}} + P_{\text{b}_\text{i}})\cos(b2_i)}{(m_{\text{payload}} + m_{\text{rotor}})} - 9.81 \tag{5.8}$$

where θ_1 and θ_2 are the pitch angle of the payload and the rotor, respectively, in the world frame. The front and back rotors, providing thrusts P_f and P_b, are mounted a wheelbase half-width L_{rotor} away from the rotor body's CoM. The velocity and displacement use a forward

Euler numerical scheme

$$\frac{\mathrm{d}\theta_n}{\mathrm{d}t}_{i+1} = \frac{\mathrm{d}\theta_n}{\mathrm{d}t}_{i} + \frac{\mathrm{d}^2\theta_n}{\mathrm{d}t^2}_{i+1} dt \tag{5.9}$$

$$\theta_{n_{i+1}} = \theta_{n_i} + \Big(\frac{\mathrm{d}\theta_n}{\mathrm{d}t}_{i} + \frac{\mathrm{d}\theta_n}{\mathrm{d}t}_{i+1}\Big)\frac{dt}{2} \tag{5.10}$$

where $\theta_3 = x$ and $\theta_4 = z$.

5.2.2 Control Architecture

The drone is position controlled with a cascaded PID controller (Fig. 5.2). This is similar to the architectures used in PX4 and iNAV flight controller firmware. When the FC is mounted on the rotor, the tilt angle command is combined with the measured angle from the FC to output the desired servomotor position. The position controller takes in the position command and outputs the desired angle and total thrust. The desired angle is converted to a desired angular rate by the angle controller, and then to the thrust differential by the angular rate controller. The differential thrust and the total thrust are combined to give the front and back rotor thrusts.

When the FC is on the payload body, the desired servomotor angle is the commanded tilt angle, and the output from the position controller is combined with the commanded tilt angle to give the desired rotor angle. The lower-level flight controllers remain the same.

Discrete time PID controller

A delay mechanism is implemented to approximate the effects of having a non-zero control loop time, equivalent to a finite loop frequency (Algorithm 2). The cascaded PID controller returns the previous output until the delay time is reached. For an infinite frequency, the time delay is set to 0 and a new output will be generated every timestep.

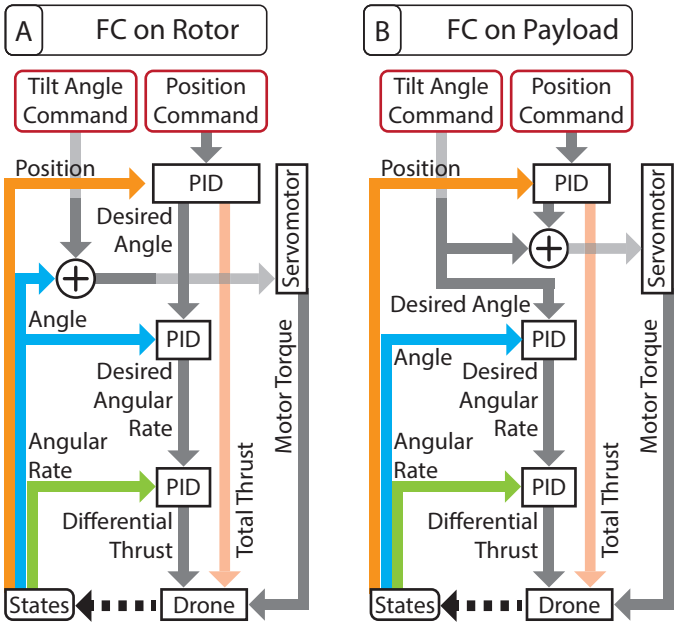


Figure 5.2: **Cascaded cascaded PID controller** diagram of the simulated tiltrotor drone with (**A**) the IMU on the rotor body and (**B**) on the payload body.

5.2.3 Simulation Scenario

In the simulation, the tiltrotor drone is tasked with a series of commands on its three controllable degrees of freedom, x, z, and the payload tilt angle θ_1 (Fig. 5.3 and 5.4). Starting at $(\theta_1, x, z) = [0.0(deg), 0.0(m), 0.0(m)]$, we command a step vertical ascend to $(0.0, 0.0, 1.0)$ at $t = 0.0s$. At $1 \leq t < 2s$, the drone follows a ramp command from $(0.0, 0.0, 1.0)$ to $(0.0, 0.5, 0.5)$. A step vertical ascend from $(0.0, 0.5, 0.5)$ to $(0.0, 0.5, 1.0)$ is commanded at $t = 2.0s$. The drone then holds at $(0.0, 0.5, 1.0)$ until $t = 3.0s$, when the drone is given a step command to $(0.0, 0.0, 1.0)$. From $5 \leq t < 6s$ the drone tracks a ramp command from $(0.0, 0.0, 1.0)$ to $(30.0, 0.0, 1.0)$. This is followed by a step command back to $(0.0, 0.0, 1.0)$ at $t = 7.0s$, where the drone remains until the end of the simulation at $t = 10.0s$. The timestep for the simulation is $dt = 5 \times 10^{-6}s$.

5.2.4 Comparison of the PID Controller Outputs

Comparing the PID controller outputs between FC-on-rotor and FC-on-payload, we can observe a significant difference between the lower-level commands. When the payload-rotor inertia ratio (R_i) is low, FC-on-payload gave more aggressive lower-level commands (Fig. 5.3). Conversely,

Algorithm 2: The Proportional Integral Derivative Controller (PID) with a loop time

```
function input: current_time, ticker, time_delay, target, input, input_rate, error_i,
 timestep, PID, offset;
if current_time - ticker ≥ time_delay then
    error_p = target - input;
    error_i = error_i + error_p · timestep;
    error_d = -input_rate;
    output = error_p · PID[0]+ error_i · PID[1] +error_d · PID[2]+ offset;
    ticker=current_time;
else
    output = input;
    ticker = ticker;
end
return output, error_i, ticker
```

when the payload-rotor inertia ratio (R_i) is high, FC-on-rotor gave more aggressive lower-level commands (Fig. 5.4). However, the aggressiveness of the lower-level commands does not directly penalise flight performance, thus I examine the total position and payload angle error of each drone setup.

5.2.5 Root Mean Squared Error Analysis

Taking the Root Mean Squared Error (RMSE) of position and angle tracking, we can observe the overall difference in performance between the two FC mounting options. The tracking performance is separated by $T < 5$ and $T \geq 5$ to reflect commanding a varying setpoint with a constant zero tilt and holding a constant position with a varying tilt command (Fig. 5.5 to 5.12). The difference between these two scenarios is that the former, in theory, does not require the servomotor to exert any torque.

Plotting RMSE against R_i, there are clear trends which are followed across the frequencies and shared between the flight conditions, $T < 5s$ and $T \geq 5s$ (Fig. 5.5 and 5.6, Fig. 5.7 and 5.8, Fig. 5.9 and 5.10, Fig. 5.11 and 5.12). However, the trend patterns for FC-on-rotor and FC-on-payload are different, and so are the trends for changes in FC and servomotor frequencies. Notably, not all performance metrics benefit from higher FC and/or servomotor frequencies

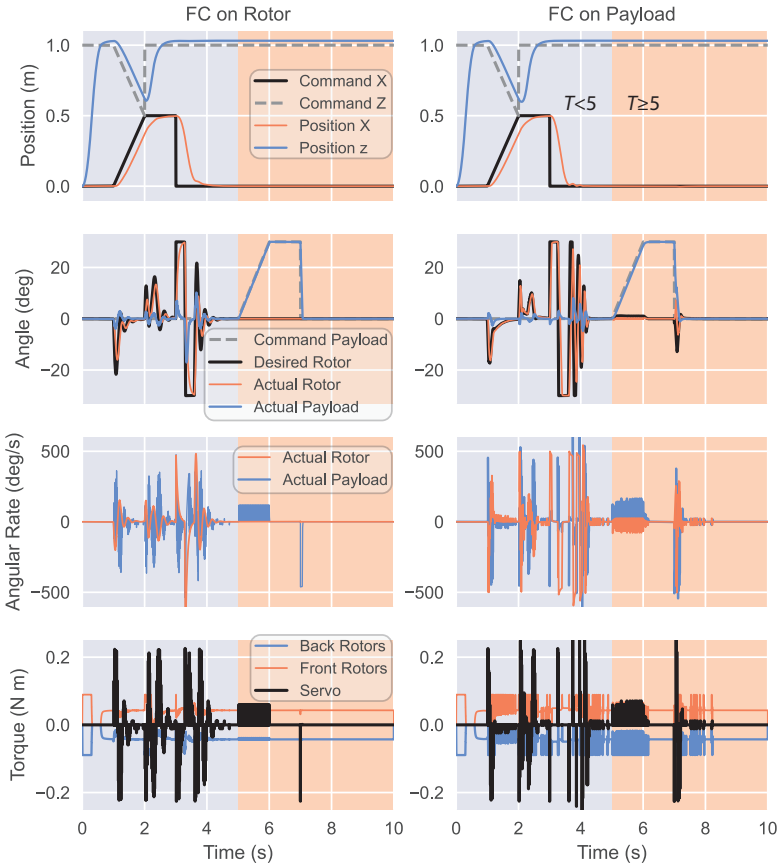


Figure 5.3: **Simulation** of the tiltrotor with a cascaded position-Proportional Integral Derivative Controller (PID). The tiltrotor has an inertia ratio of 0.01, corresponding to the rotor body having a 100 times larger inertia than the payload. The Flight Controller (FC) is running at $4000Hz$ and outputs servomotor commands at $50Hz$. The light blue background denotes $T < 5s$, where we commanded a varying position setpoint with a constant zero tilt, and orange encloses $T \geq 5s$, where we commanded a constant position with a varying tilt setpoint.

(Fig. 5.5A and 5.9A respectively). The position tracking error is higher when the servomotor frequency increases at $R_i \approx 20$, $T < 5s$, and FC frequency at $4000Hz$, albeit the error is lowest for the highest simulated servomotor frequency $500Hz$ when $R_i \approx 1$.

We can quantify the percentage improvement (P_{improve}) gained between the better and the worse mounting position using the equation

$$P_{\text{improve}} = \frac{\text{RMSE}_{\text{payload}} - \text{RMSE}_{\text{rotor}}}{\mathbf{max}(\text{RMSE}_{\text{payload}}, \text{RMSE}_{\text{rotor}})} \tag{5.11}$$

the signage indicates which mounting position has the better performance—positive means FC-on-rotor is better (Fig. 5.5C to 5.12C, and Fig. 5.13 to 5.16).

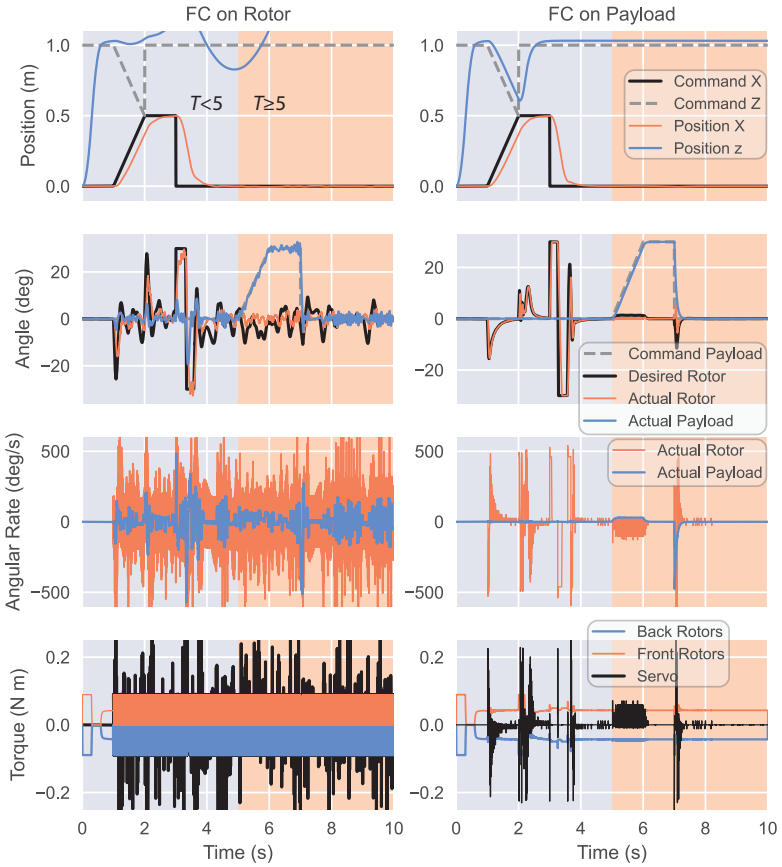


Figure 5.4: **Simulation** of the tiltrotor with a cascaded position-Proportional Integral Derivative Controller (PID). The tiltrotor has an inertia ratio of 100, corresponding to the payload body having a 100 times larger inertia than the rotor. The Flight Controller (FC) is running at $4000Hz$ and outputs servomotor commands at $50Hz$. The light blue background denotes $T < 5s$, where we commanded a varying position setpoint with a constant zero tilt, and orange encloses $T \geq 5s$, where we commanded a constant position with a varying tilt setpoint. Note that the tiltrotor becomes unstable in the vertical axis z when the FC is mounted to the rotor body.

In all conditions, we can observe non-linear trends influenced by the FC frequency, servomotor frequency, and the R_i. Interestingly, from Fig. 5.5C to 5.12C there is a general trend of FC-on-payload being more beneficial as R_i increase, and the inverse is true for FC-on-rotor. This is further corroborated by Fig. 5.13 to 5.16, where the percentage improvement is plotted as a heatmap against the FC and servomotor frequencies. As R_i increases, areas on the heatmap where FC-on-payload has higher performance (blue) also increase. This increase is most significant around the top right quadrant of the plots, where FC and servomotor frequencies are the highest.

At this point, we must revisit the original question posed in this chapter: "where should we mount the flight controller?". Having analysed position tracking and payload angle tracking separately, we must be aware of the likelihood that both performance metrics are considered when designing a tiltrotor.

The addition of the position and angle RMSE is invalid as they have different units. Nevertheless, it is possible to determine which FC mounting position is definitely preferred—I will explain this later in Subsection 5.2.6. We see that there are preferred FC mounting positions which satisfy both the position and angle tracking metrics (Fig. 5.17A, B, D, E, G, and H). With an error band of 20%, there are also areas where there is no preferential FC position, mostly occurring in high FC and servomotor frequency zones. In general, there are large zones where the FC position is highly dependent on if the position or the payload angle tracking is more important—thus, "it depends".

Another two distinct scenarios are moving without tilting the payload body and tilting the payload body without positional movement. But these scenarios might overlap in real life. A camera drone can change its camera tilt angle whiles holding a hover, it will also fly forwards whiles maintaining a constant camera angle. Combining these two scenarios, we see that in high FC and servomotor frequency zones, it is better to mount the FC on the rotor if the rotor body inertia is higher than the payload body (Fig. 5.17C, F, and I). Also in high FC and servomotor frequency zones, it is better to mount the FC on the payload if the payload body inertia is equal to or higher than the rotor body.

The final situation we can consider is if the inertia ratio shifts during flight, an example being a mid-air payload drop. In this situation, the FC would be mounted to the payload bay in the FC-on-payload case, not the payload itself. Note that this is not a perfectly accurate analysis as the simulations have not accounted for the change in payload weight. Moving with a constant payload body angle, FC-on-payload is optimal at high FC and servomotor frequencies across $10^{-2} \geq R_i \geq^2$ (Fig. 5.17J). If the payload body tilts under torque from the servomotor, there is a small zone at high servomotor frequencies and FC frequency at approximately $100Hz$ where it is optimum to mount the FC on the rotor body (Fig. 5.17K). However, is there a definite global optimal FC placement for all tiltrotors (Fig. 5.17L)? No, it all depends.

5.2.6 Combining position preference identifier logic

I categorise the FC position preference with

$$N_{\text{pref}} = \begin{cases} 1+0i, & \text{if } P_{\text{improve}} > 0 \\ 0+1i, & \text{if } P_{\text{improve}} = 0 \\ -1+0i, & \text{if } P_{\text{improve}} < 0 \\ 0+0i, & \text{otherwise } (P_{\text{improve}} \text{ not certain}) \end{cases} \tag{5.12}$$

where the FC mounting position preference identifier $N_{\text{pref}} = 1$ if FC-on-rotor is preferred, $N_{\text{pref}} = -1$ if FC-on-payload is preferred, $N_{\text{pref}} = i$ the imaginary number if the performance has no bias towards the mounting position, and $N_{\text{pref}} = 0$ if the identifier is uncertain. Using complex numbers to create 4 logic states ensures that the logic is correct when combining the FC mounting position preference identifiers.

There are important details to note when combining the FC position preferences. As an example, let us take combining the position and payload angle RMSE driven FC position preference identifiers, $N_{\text{pref,pos}} = N_{\text{pos}}$ and $N_{\text{pref,ang}} = N_{\text{ang}}$ respectively. Because $P_{\text{improve}} \in \mathbb{R}$, N_{pos} and N_{ang} separately cannot attain the uncertain state $0+0i$. However, the uncertain state can be attained once two or more identifiers are combined. Let $N_{\text{pos}} = [a_1, a_i, a_{-1}]$ and $N_{\text{ang}} = [b_1, b_i, b_{-1}]$ correspond to the attainable states FC-on-rotor, no bias, and FC-on-payload. The 4 logical possibilities are:

1. $N_{\text{pos}} + N_{\text{ang}} = [(a_1 + b_0),\ (a_0 + b_1),\ (a_1 + b_1)]$ — FC-on-rotor is preferred;

2. $N_{\text{pos}} + N_{\text{ang}} = [(a_0 + b_0)]$ — no preference bias;

3. $N_{\text{pos}} + N_{\text{ang}} = [(a_{-1} + b_0),\ (a_0 + b_{-1}),\ (a_{-1} + b_{-1})]$ — FC-on-payload is preferred;

4. $N_{\text{pos}} + N_{\text{ang}} = [(a_1 + b_{-1}),\ (a_{-1} + b_1)]$ — the uncertain state, where the position preference would depend on how the different RMSEs accumulate from the flight trajectory command and the relative significance of each RMSE.

Calculating the combinations using (5.12), we get:

1. $$N_{\text{pos}} + N_{\text{ang}} = [(a_1 + b_0), (a_0 + b_1), (a_1 + b_1)] = [(1 + i), (1 + i), (2 + 0i)] \tag{5.13}$$
2. $$N_{\text{pos}} + N_{\text{ang}} = [(a_0 + b_0)] = [0 + 2i] \tag{5.14}$$
3. $$N_{\text{pos}} + N_{\text{ang}} = [(a_{-1} + b_0), (a_0 + b_{-1}), (a_{-1} + b_{-1})] = [(-1 + i), (-1 + i), (-2 + 0i)] \tag{5.15}$$
4. $$N_{\text{pos}} + N_{\text{ang}} = [(a_1 + b_{-1}), (a_{-1} + b_1)] = [0 + 0i, 0 + 0i] \tag{5.16}$$

The real part of both (5.14) and (5.16) sum to $0 + 0 = 1 - 1 = 0$, the imaginary part of (5.14) sums to $2i$; we can differentiate the two logical possibilities using this property. The real part of (5.13) is positive while (5.15) is negative, similar to the definition in (5.12). But it is premature to end the exercise here. What if we would like to combine more than two identifiers?

Extending the combination of the logical states to any number of FC position preference identifiers would require an algorithm which returns a N_{pref} as defined in (5.12). In other words, having a function which $N_{\text{pref,sum}} = f_\sigma(N_{\text{pref,0}}, N_{\text{pref,1}}, ..., N_{\text{pref,k}})$ enables us to process the combination of identifiers recursively (Fig. 5.18). Doing so allows us to combine multiple FC position preferences without increasing the scale of the analysis.

Creating the algorithm entails finding the logical expressions to differentiate the 4 states. I first consider the properties of summing N_{pref}.

$$\begin{aligned} \textbf{Let } \sum_{k=1}^{m} N_{\text{pref,k}} &= d_1(1) + d_{-1}(-1) + d_i(1i) + d_0(0) \\ \textbf{where } & d_1 + d_{-1} + d_i + d_0 = m, \\ & d_1, d_{-1}, d_i, d_0 \in p, \quad p \geq 0,\ p \subset \mathbb{Z} \end{aligned} \tag{5.17}$$

$$\sum_{k=1}^{m} N_{\text{pref,k}} = (d_1 - d_{-1}) + d_i i \tag{5.18}$$

where d_1, d_{-1}, d_i, d_0 are arbitrary numbers of the possible FC position preferences which adds up to the total number of N_{pref}, m. From Fig. 5.18 we see that only the outer values of the

identifier sum (green and blue) give non-zero logical outcomes. These outer values are

$$\sum_{k=1}^{m} N_{\text{pref,k}} = -(m-j)+ji \ \textbf{or} \ (m-j)+ji \quad \textbf{where} \ j = 0, 2, ..., m \tag{5.19}$$

where j is a counter from 0 to m. Incidentally, if we relate the sum of non-zero logical outcomes to the total number of identifiers

$$m = (m-j)+j \tag{5.20}$$

$$\because \quad j = 0, 2, ..., m \tag{5.21}$$

$$m = |-(m-j)|+j \ \textbf{or} \ |(m-j)|+j \tag{5.22}$$

$$\therefore \quad m = \left|\text{Re}\left(\sum_{k=1}^{m} N_{\text{pref,k}}\right)\right| + \text{Im}\left(\sum_{k=1}^{m} N_{\text{pref,k}}\right) \tag{5.23}$$

Therefore, by the inverse of the logic

$$N_{\text{pref,sum}} = f_\sigma\big(\sum_{k=1}^{m} N_{\text{pref,k}}\big) \tag{5.24}$$

$$N_{\text{pref,sum}} = 0 \iff \left|\text{Re}\left(\sum_{k=1}^{m} N_{\text{pref,k}}\right)\right| + \text{Im}\left(\sum_{k=1}^{m} N_{\text{pref,k}}\right) \neq m \tag{5.25}$$

The only possibility for the no-preference case is

$$N_{\text{pref,sum}} = i \iff \text{Im}\left(\sum_{k=1}^{m} N_{\text{pref,k}}\right) = m \tag{5.26}$$

To determine $N_{\text{pref,sum}} = \pm 1$, (5.23) must hold true, and under that condition

$$N_{\text{pref,sum}} = \textbf{sgn}\left(\text{Re}\left(\sum_{k=1}^{m} N_{\text{pref,k}}\right)\right) \iff \text{Re}\left(\sum_{k=1}^{m} N_{\text{pref,k}}\right) > 0 \tag{5.27}$$

The function to combine the position preference identifiers $f_\sigma\big(\sum_{k=1}^{m} N_{\text{pref,k}}\big)$, with (5.25)-(5.27), is implemented as an algorithm (Algorithm 3). The algorithm is vectorised to increase the data

processing rate.

Algorithm 3: The algorithm to combine flight controller position preference identifiers

Input: $N_{\text{pref,0}}$,$N_{\text{pref,1}}$,...,$N_{\text{pref,m}}$
element-wise sum;
$A = \sum_{k=1}^{m} N_{pref,k}$;
if $\|\text{Re}(A)\| + \text{Im}(A) \neq m$ **then** $A = 0 + 0i$;
if $\text{Im}(A) = m$ **then** $A = 0 + 1i$;
if $\text{Re}(A) \neq 0$ **then** $A = \textbf{sgn}\big(\text{Re}(A)\big)$;
if $\text{Re}(A) < 0$ **then** $A = -1 + 0i$;
return A

5.3 Discussion

With the tiltrotor drone having two bodies, I asked the question: "where should we mount the flight controller?". I conducted numerical simulations of tiltrotors with varying servomotor frequency, Flight Controller (FC) loop frequency, and the ratio of inertia between the rotor and payload body—in this chapter, the payload body is the measuring ring.

Due to limitations in computational resources, the simulation is limited to a 1 : 100 ratio between the two inertias, higher ratios would require smaller timesteps. Another limitation is the gains tuning. The servomotor Proportional Integral Derivative Controller (PID) is tuned to mimic the performance of an MKS HV75K Servomotor; the flight controller PIDs are tuned so the platform is stable at an inertia ratio of 1. The gains are constant throughout the simulation. As we are only interested in the relative performance between the two FC mounting positions, it is assumed that suboptimal tuning affects both cases approximately equally. But as multirotor systems are non-linear, a more comprehensive study is needed to understand the conditions under which the current results are valid. Future work can also consider other control architectures The control scheme presented in this chapter is a cascaded PID controller. As this is similar to current multirotor control architectures, it is reasonable to assume that the results extend to the other control schemes. But again, a more comprehensive study is needed to confirm this assumption.

In conclusion, I am able to determine that, at high FC and servomotor frequencies, mounting the FC to the body with the higher inertia will yield more accurate position and payload angle trajectory tracking. The results and the method of analysis presented in this chapter can aid tiltrotor designers in better informing their design choice. The use of complex numbers as logic can be more broadly applied in other contexts to provide insight into multi-dimensional data analysis.

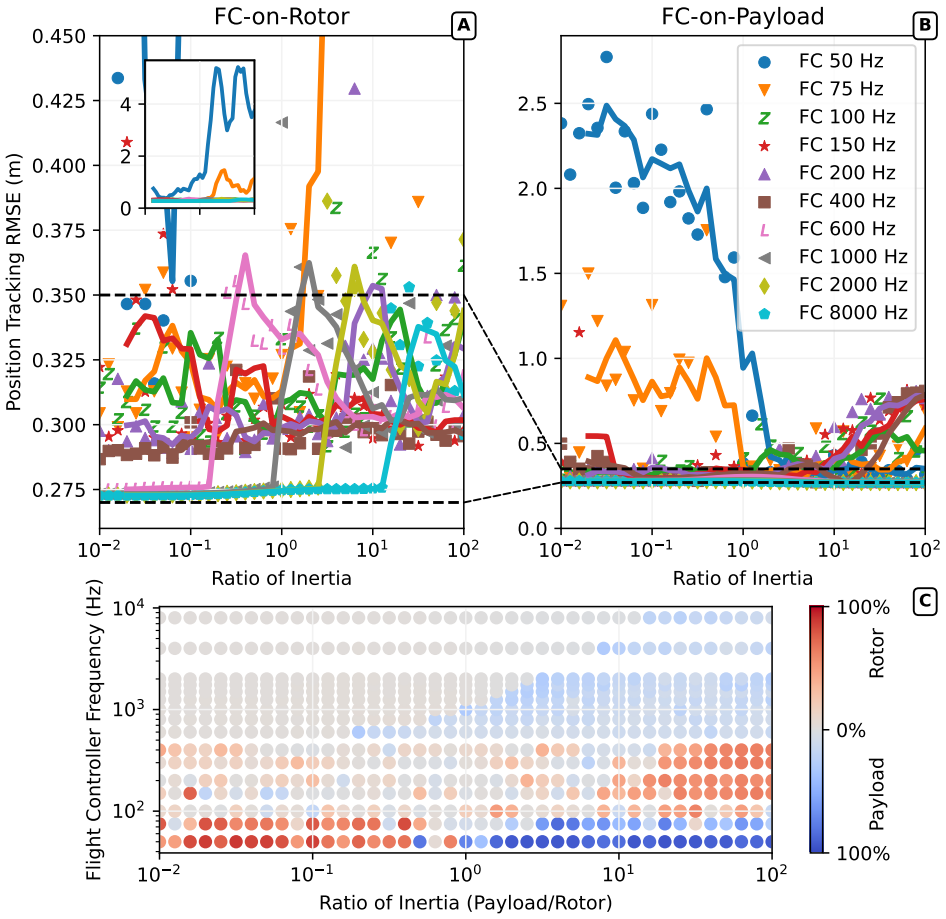


Figure 5.5: **Position root mean squared error** at $0 \leq T < 5s$, where the robot is commanded to follow a position setpoint trajectory at 0° tilt. The servomotor frequency is $50Hz$ while a range of Flight Controller (FC) frequencies was simulated. (**A**) The FC is mounted on the rotor body. The embedded plot shows the full error range when the FC runs at $50Hz$. (**B**) The FC is mounted on the payload body. (**C**) The comparison of the difference in errors as a fraction of the scenario with the larger error reviews which mounting position has a better performance. Note the clear shift in the preferred mounting position as the payload-rotor inertia change at low FC frequencies. And the shift in the preferred position as the FC frequency varies at high payload-rotor inertia ratios.

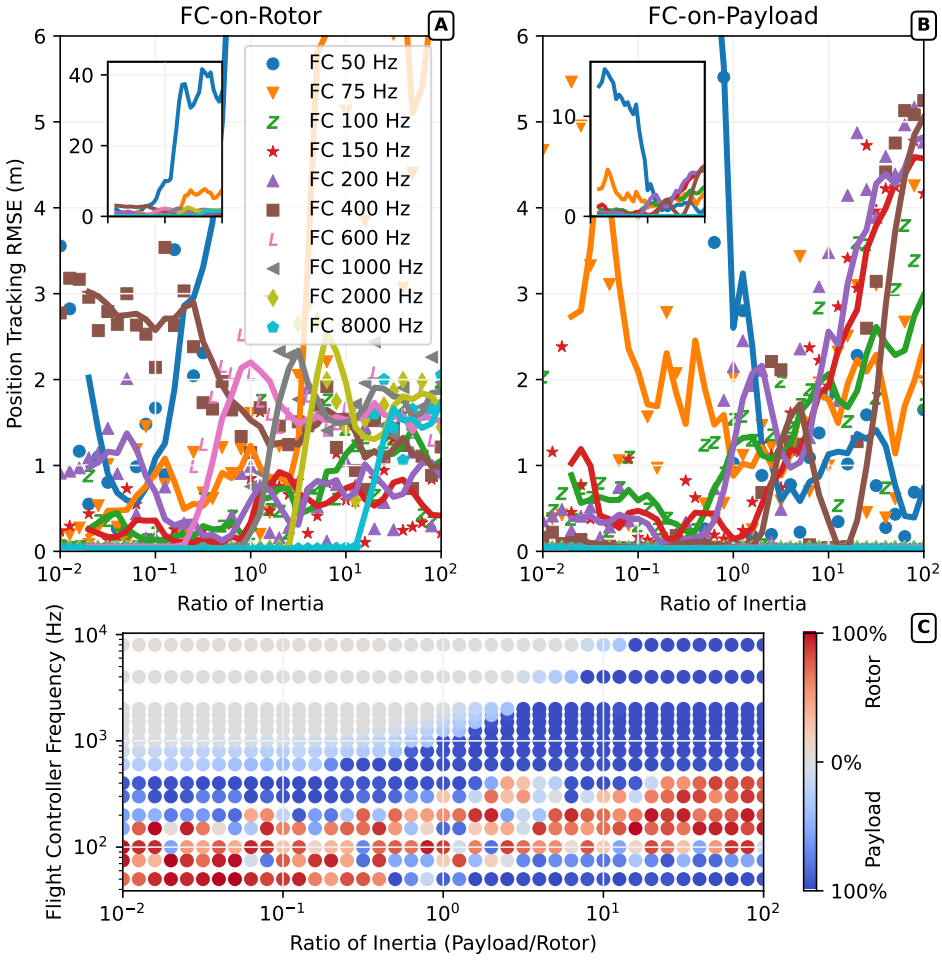


Figure 5.6: **Position root mean squared error** from $5 \leq T < 10s$ where the robot is commanded to follow a tilt setpoint trajectory at a static position. The servomotor frequency is $50Hz$ while a range of Flight Controller (FC) frequencies was simulated. (**A**) The FC is mounted on the rotor body. The embedded plot shows the full error range when the FC runs at $50Hz$. (**B**) The FC is mounted on the payload body. (**C**) The comparison between the two mounting positions shows a bifurcation of results occurring at lower FC frequencies.

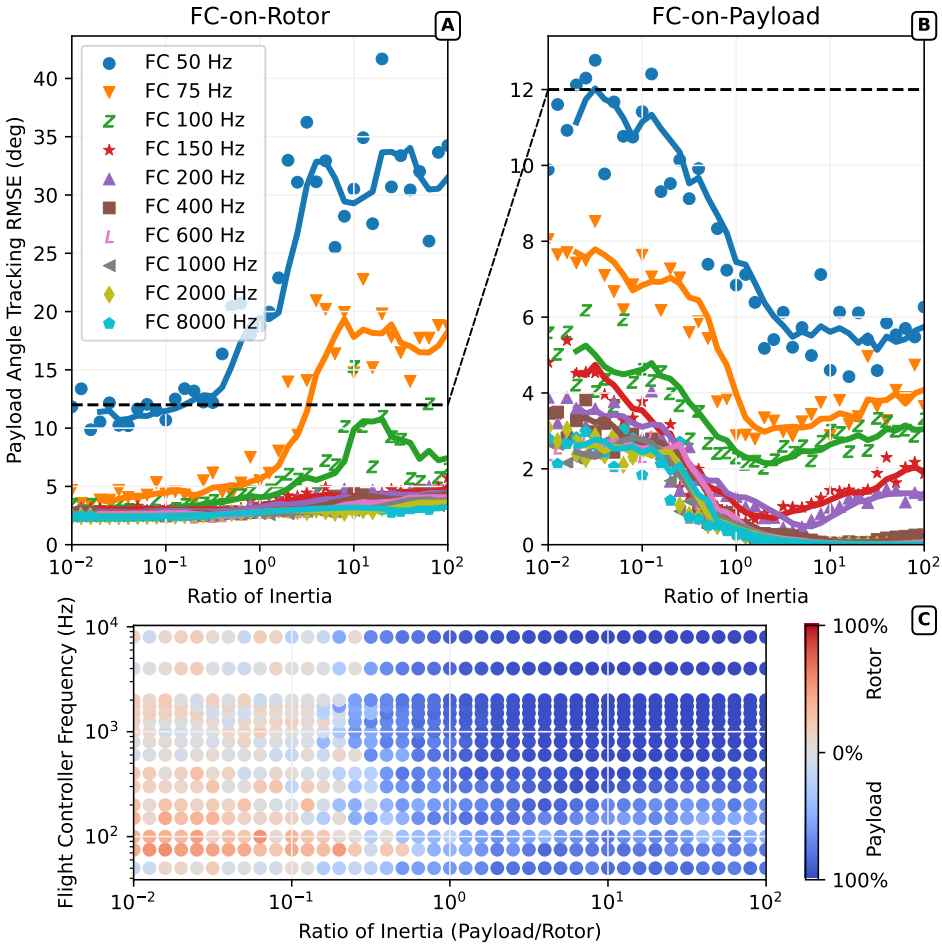


Figure 5.7: **Payload angle root mean squared error** at $0 \leq T < 5s$ where the robot is commanded to follow a position setpoint trajectory at 0° tilt. The servomotor frequency is $50Hz$ while a range of Flight Controller (FC) frequencies was simulated. (**A**) The FC is mounted on the rotor body. (**B**) The FC is mounted on the payload body. (**C**) The percentage improvement.

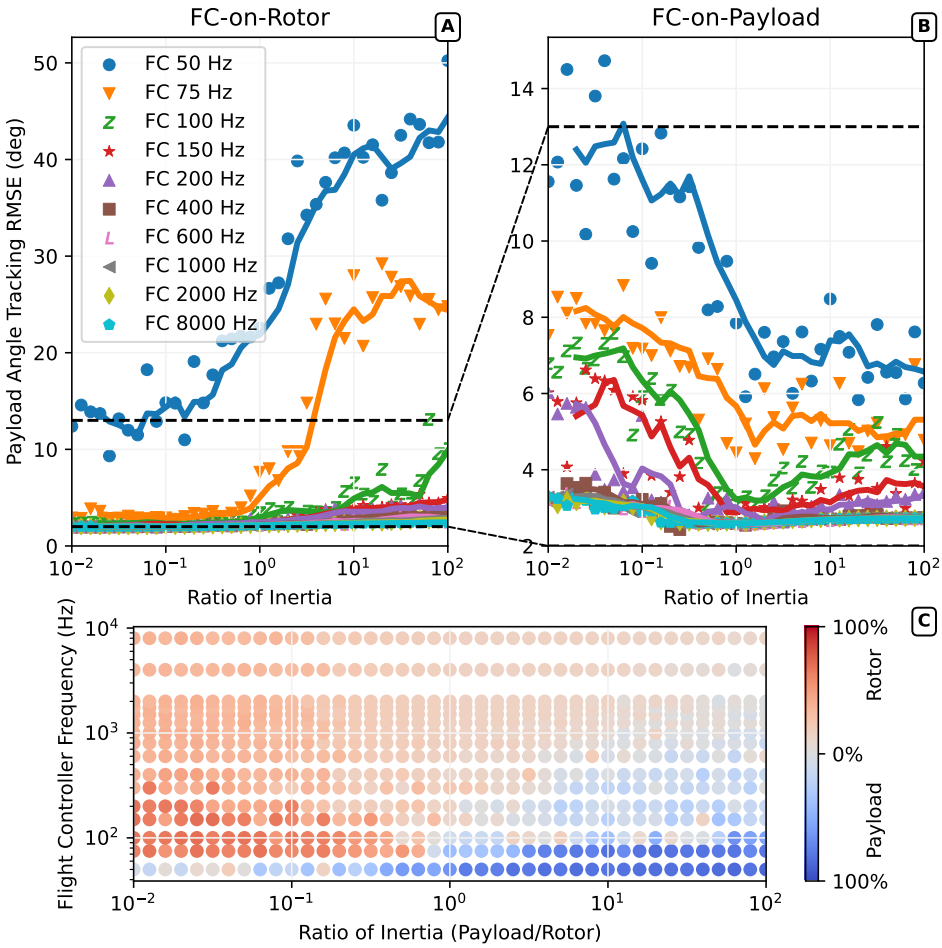


Figure 5.8: **Payload angle root mean squared error** from $5 \leq T < 10s$ where the robot is commanded to follow a tilt setpoint trajectory at a static position. Servomotor frequency is set at $50Hz$ while a range of Flight Controller (FC) frequencies was simulated. The FC is (**A**) mounted on the rotor body, and (**B**) on the payload body. (**C**) The percentage improvement.

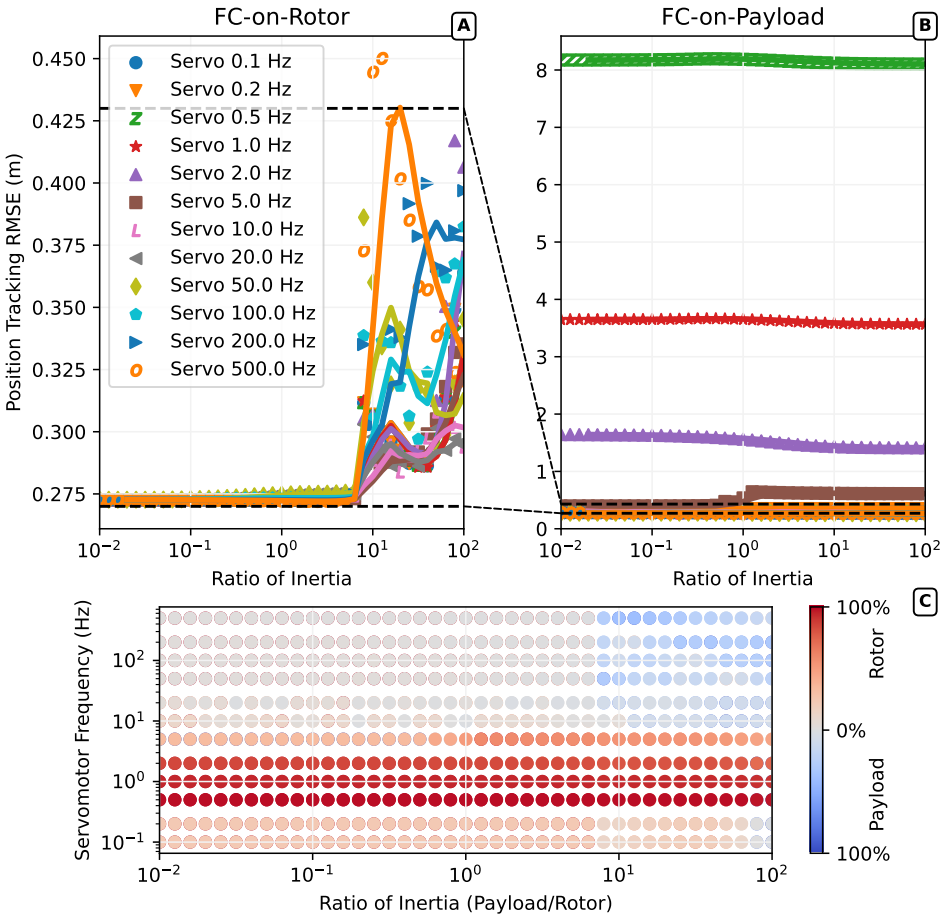


Figure 5.9: **Position root mean squared error** from $0 \leq T < 5s$ where the robot is commanded to follow a position setpoint trajectory at 0° tilt. The Flight Controller frequency is set at $4000Hz$ while a series of servomotor frequencies are tested. The FC is (**A**) mounted on the rotor body, and (**B**) on the payload body. (**C**) The percentage improvement.

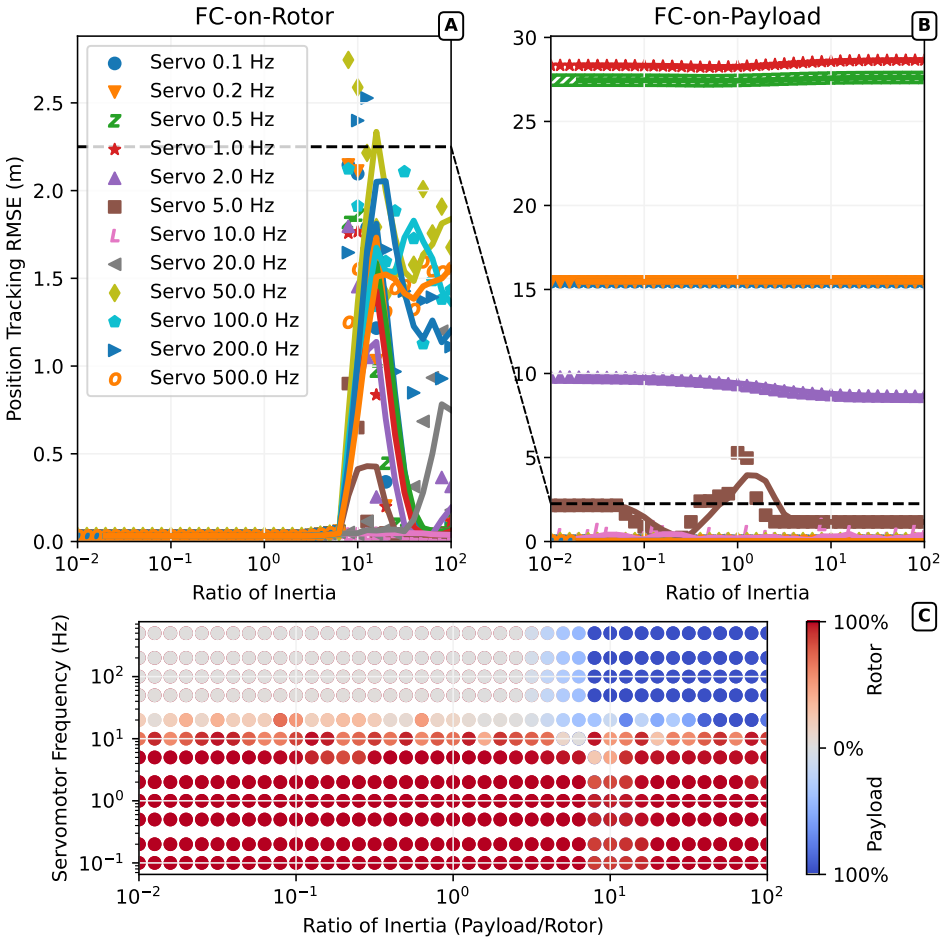


Figure 5.10: **Position root mean squared error** from $5 \leq T < 10s$ where the robot is commanded to follow a tilt setpoint trajectory at a static position. The Flight Controller frequency is set at $4000Hz$ while a series of servomotor frequencies are tested. The FC is (**A**) mounted on the rotor body, and (**B**) on the payload body. (**C**) The percentage improvement.

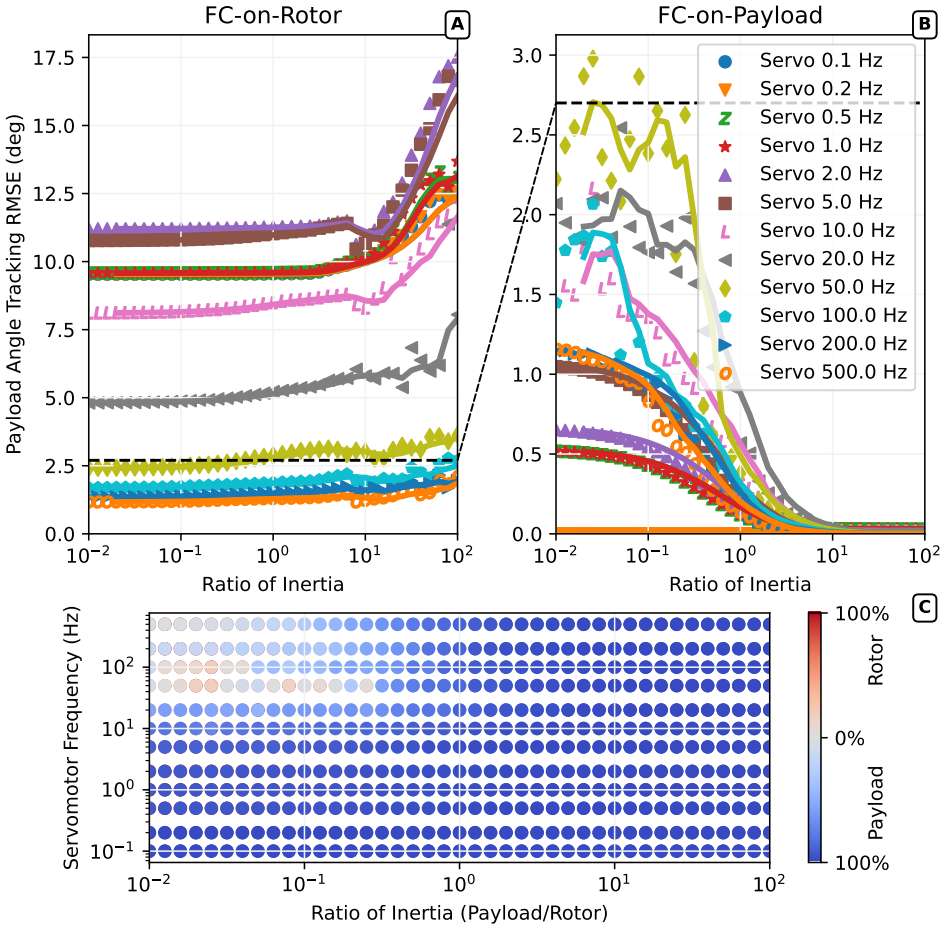


Figure 5.11: **Payload angle root mean squared error** from $0 \leq T < 5s$ where the robot is commanded to follow a position setpoint trajectory at 0° tilt. The Flight Controller frequency is set at $4000Hz$ while a series of servomotor frequencies are tested. The payload tilt angle error when the FC is (**A**) mounted on the rotor body, and (**B**) on the payload body. (**C**) The payload angle RMSE is lower when the FC is mounted to the payload body for most drone setups. But the difference in performance becomes marginal at higher servomotor frequencies and when the rotor body has significantly more inertia.

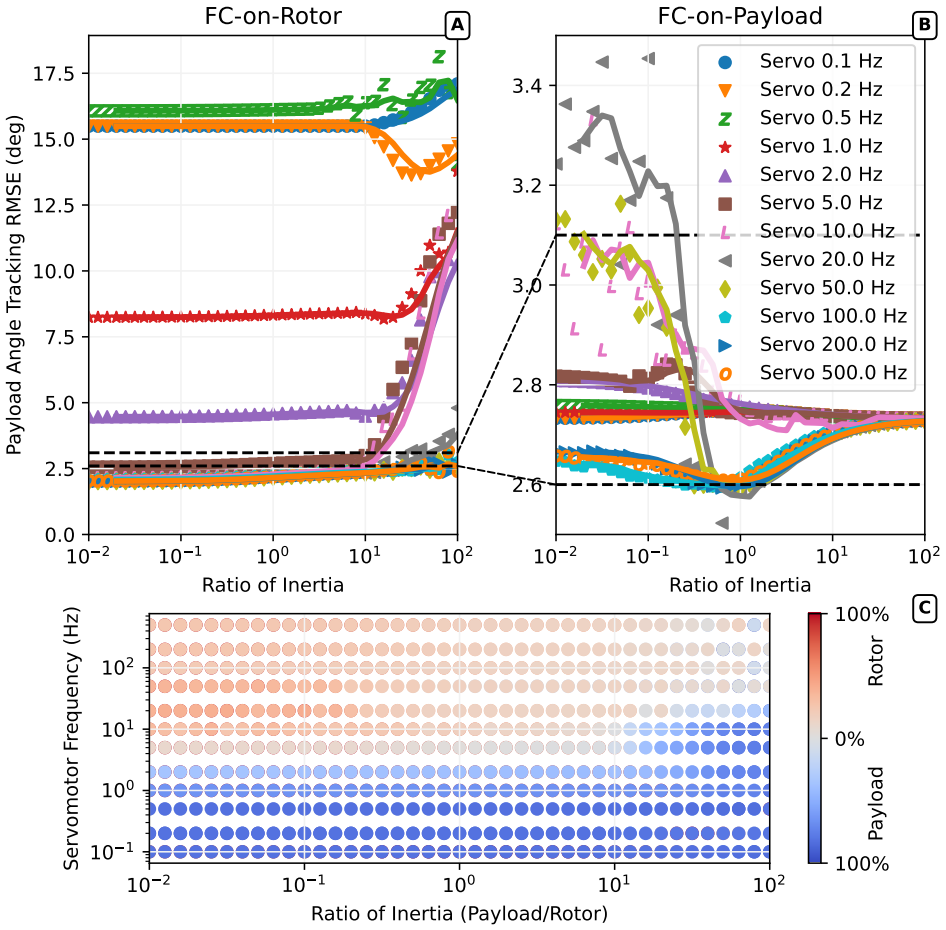


Figure 5.12: **Payload angle root mean squared error** from $5 \leq T < 10s$ where the robot is commanded to follow a tilt setpoint trajectory at a static position. The Flight Controller frequency is set at $4000Hz$ while a series of servomotor frequencies are tested. The payload tilt angle error when the FC is (**A**) mounted on the rotor body, and (**B**) on the payload body. (**C**) The percentage improvement.

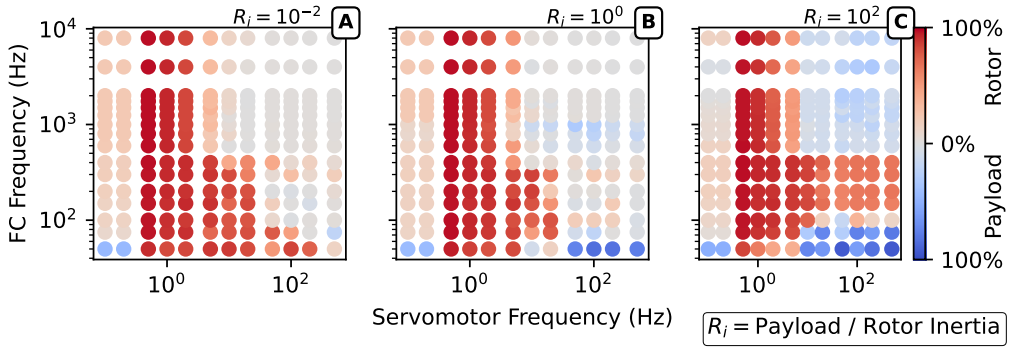


Figure 5.13: **Position root mean squared error** from $0 \leq T < 5s$. The robot is commanded to follow a position setpoint trajectory at a static payload tilt angle with the payload-rotor body inertia ratios of (**A**) $R_i = 0.01$, (**B**) $R_i = 1$, and (**C**) $R_i = 100$.

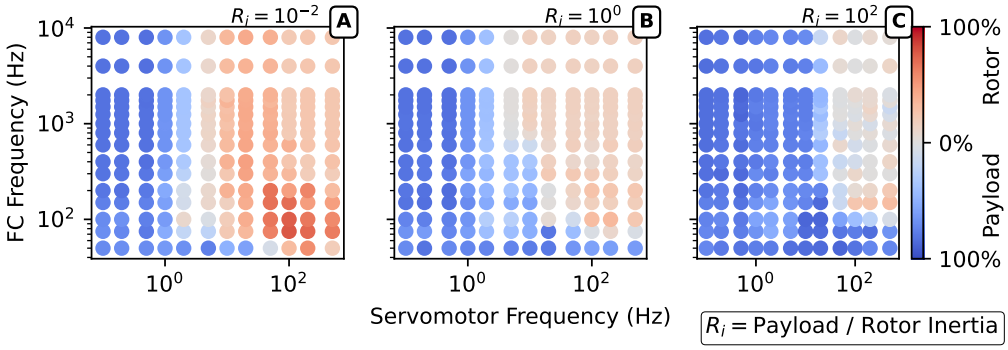


Figure 5.14: **Position root mean squared error** from $5 \leq T < 10s$. The robot is commanded to follow a tilt setpoint trajectory at a static position with the payload-rotor body inertia ratios of (**A**) $R_i = 0.01$, (**B**) $R_i = 1$, and (**C**) $R_i = 100$.

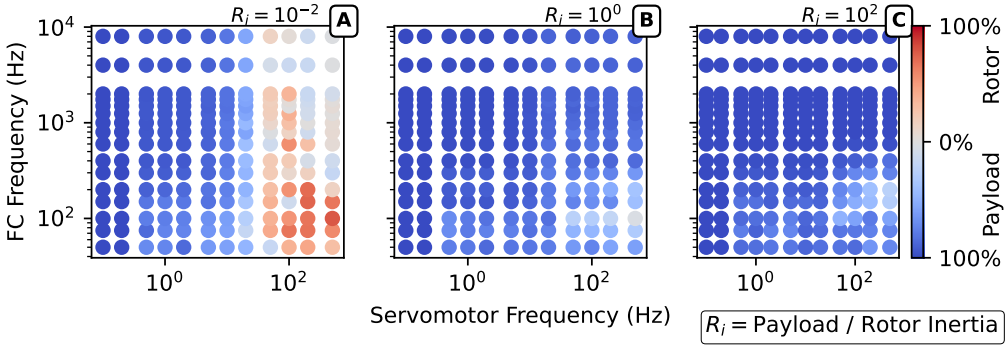


Figure 5.15: **Payload angle root mean squared error** from $0 \leq T < 5s$. The robot is commanded to follow a position setpoint trajectory at a static payload tilt angle with the payload-rotor body inertia ratios of (**A**) $R_i = 0.01$, (**B**) $R_i = 1$, and (**C**) $R_i = 100$.

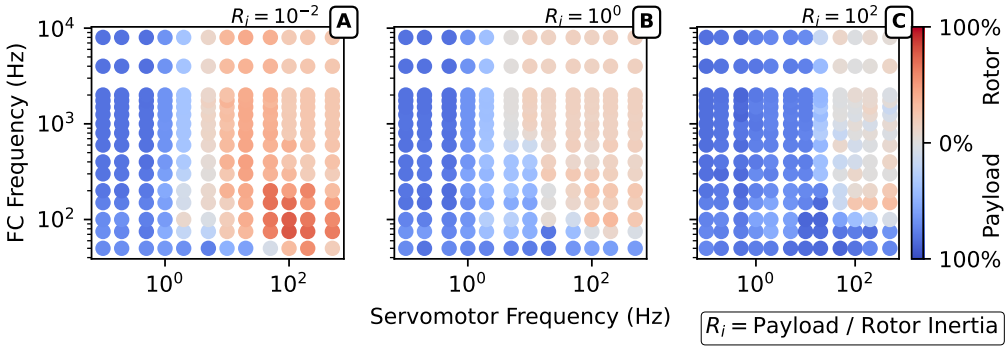


Figure 5.16: **Payload angle root mean squared error** from $5 \leq T < 10s$. The robot is commanded to follow a tilt setpoint trajectory at a static position with the payload-rotor body inertia ratios of (**A**) $R_i = 0.01$, (**B**) $R_i = 1$, and (**C**) $R_i = 100$.

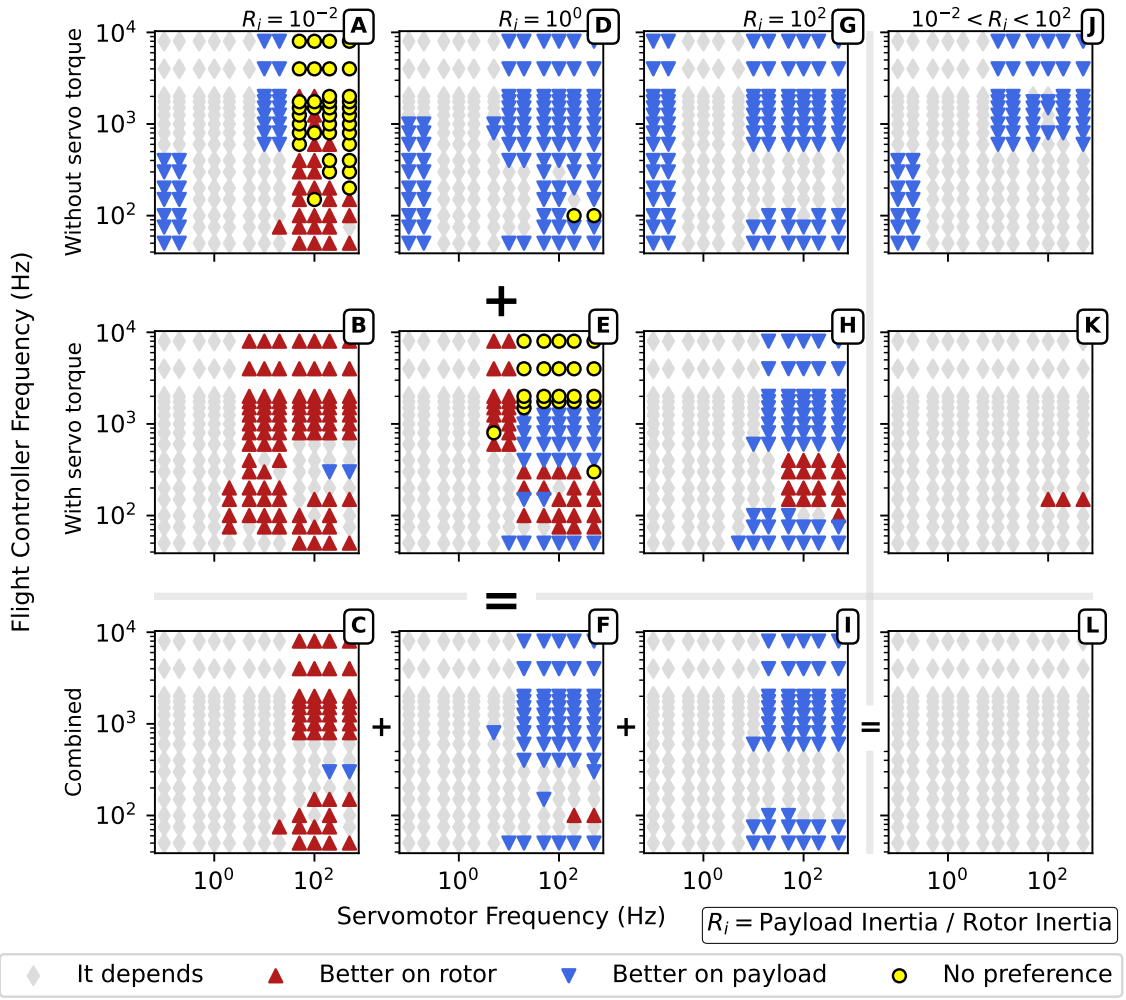


Figure 5.17: **Combined position and payload angle Root Mean Squared Error (RMSE) preferred Flight Controller (FC) mounting position indicator** with the red and blue spots showing where it is definitely preferable to mount the FC in various scenarios. The grey spots indicate that the preferred mounting position is situational. The black-and-yellow dots signifies where, within a ±20% RMSE error difference, there is no preferred mounting position. (**C**) is the combination of the identifiers from (**A**) the payload at a constant angle case and (**B**) payload rotation with no rotor tilt. Similarly (**D**)+(**E**)→(**F**),(**G**)+(**H**)→(**I**), and (**C**)+(**F**)+(**I**)→(**L**) the combination across different flight conditions and inertia ratios. (**J**) and (**K**) shows the preference from the combination of various inertia ratios, ie. (**A**)+(**D**)+(**G**)→(**J**) and (**B**)+(**E**)+(**H**)→(**K**).

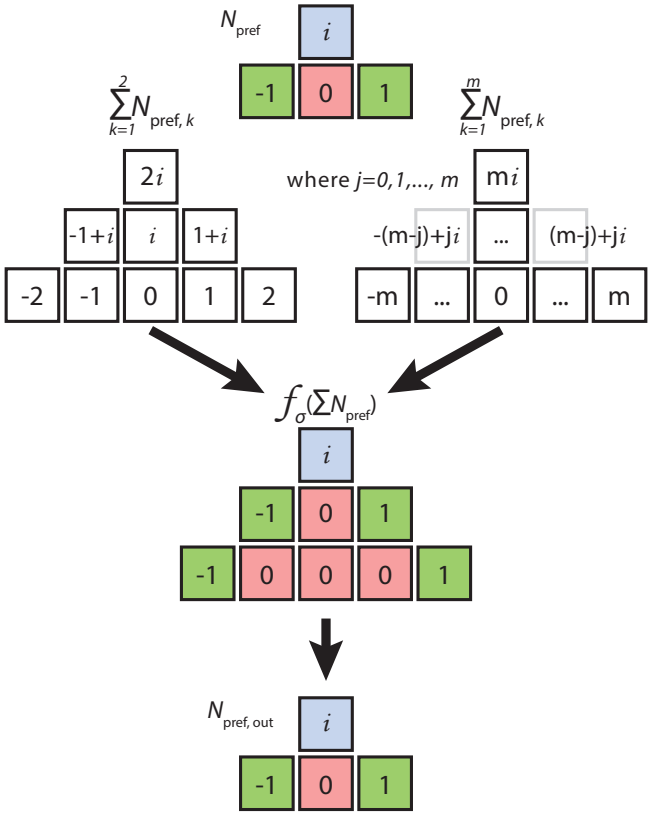


Figure 5.18: **The combination of the position preference identifiers**. The diagram visualises the algorithm or the function that combines multiple position preferences and returns an identifier that follows the same logic as the original.

Chapter 6

Design and Application of a Metamorphic Aerial Robot

Perching aerial robots have taken much inspiration from birds. However, the use of modular designs, liken to birds' wings and legs, not only increases the weight of the robot but also its size. In this paper, we take inspiration from gliding and tree-dwelling mammals such as the sugar glider and the flying squirrel. In doing so, we offer an alternative perspective on an aerial robot's functional requirements, form factor, and mobility architecture. We noted how these mammals morph their whole limb to transit between gliding flight and perch. This insight is applied to design a quadrotor robot that transitions between morphologies to fly and perch. The robot's arm is rigid in flight but will morph and conform to its target within 1 second when perching. holding its grasp with minimal energy use. The integration of the perching capability also provides a 30% platform mass reduction over the modular approach. Furthermore, the robot perches through dynamic and static manoeuvres. Our proposed design solution can fulfil the need for small perching robots in complex environments.

6.1 Introduction

The accessing and collecting of eco-physiological data in the forest understory layer are of great importance for the conservation management of endangered species and plants. In denser

forests, there are also micro-climate enclaves that can vastly differ from the macro-climate above the canopy [139]. Multirotor unmanned aerial vehicles (UAV) have shown to be well suited for imaging forest canopies and low vegetation height environments [140, 141]. However, there are limited solutions for remote sensor deployment in these confined spaces [142, 143], such as the forest understory [144].

Aerial robots need to have high endurance, be small to penetrate deep into a dense forest and be adaptable to constantly changing environments. These specifications are needed so the robot is able to access and collect data in the understory deep into the forest. Perching between intermittent movement from tree to tree has often been highlighted as a method to save energy, escape predators, and take cover from errant weather for aerial robots and their biological counterparts [145]. Perching and resting also allow these creatures to be placed in an advantageous position for surveillance [146, 145]. Animals, such as sloths and koalas, have also shown their ability to retain, recover, and maintain homeostasis while resting on trees [147].

Bioinspired principles have allowed roboticists to reimagine new strategies to approach adaptable perching robot designs [148, 149]. There are mechanically activated gecko-inspired, fibre-based dry adhesives that utilise van der Waals forces [150, 151]. Alternatively, there are mechanical interaction-based solutions that rely on surface friction and interlocking. Preloaded deployable spikes and passive microspines can perch on rough surfaces [152, 153, 154, 155]. Spider-web-inspired methods, utilizing string entanglement or magnetic anchors on ferromagnetic surfaces, are used to perch and suspend the robot in mid-air [156, 157]. Active and passive avian-inspired graspers are deployed to envelop cylindrical targets, such as tree branches and pipes, with a claw-like grip [158, 159, 160, 161, 162, 163, 155, 164].

Currently, the aforementioned perching methods add additional modules and would increase a drone's weight. Therefore, a compromise between the mission endurance, which includes the time when the robot is perched, and the flight time must be struck. An ideal aerial robotic solution would be a platform that can intelligently transform and adapt its body to perch on various sized and shaped structures without any penalties.

As well as providing bioinspired mechanisms, nature has also given robotics various strategies to integrate these mechanisms within a monolithic body. One form of such strategy is meta-

morphosis. Metamorphosis allows the organism to innately take on various forms in order to adapt to its targeted task and/or environment [165]. This transformation of an organism's body during its life cycle that allows the specie to adapt to various ecological niches [166, 167]. This improves the survival rate of species that now can depend on different food resources, habitats, and competition [168]. Dragonflies, for example, metamorphose from a larval stage to acquire the ability to fly as an adult [169]. Amphibians like frogs and salamanders also transform from tadpoles that can swim to adults that can operate on terrestrial habitats [165].

More recently, the concept of metamorphosis and metamorphic mechanisms have played a key role in the development of multi-modal robotic designs [170]. These metamorphic robots can adapt and perform different tasks and operate in varying environments, such as water, air, and land [171, 172, 173, 174, 175]. Adaptable and programmable structures can be formed from soft materials or origami folding [176, 177, 178, 179, 56, 180, 181, 182, 183, 184, 185]. Metamorphosis has also diversified and augmented the functionality of multi-modal aerial robotic platforms. Aerial robotic platforms can modify their structure during flight to go through different-sized apertures, adapt to collision, or grasp objects [186, 187, 117]. Other aerial robots use metamorphosis to enable the operation in different environments, like the transition from air to water [72, 188], or from air to terrains [189, 190].

Applying metamorphic design to perching mechanisms on aerial robots elegantly fulfils the need for compact long endurance remote sensing platforms. I propose a metamorphic perching aerial robotic system that is capable of transitioning its multirotor arms between different shape primitives to perform adaptable whole-body grasping over various sized and shaped surfaces while being resistant to wind disturbances. Therefore, the robot offers a shared functionality between flight and perching, without having the weight penalty of any additional grasping device.

I designed a robotic arm capable of adaptive morphing to enable dual characteristics of rigidity and compliance. The system incorporates shared actuation and multi-functional components to minimise weight. By employing origami-based self-locking [191] and classical structural design principles, the morphing arm is able to sustain positive and negative loads and maintain stiffness during flight. The developed platform utilizes tendon drives with tensile cables [115],

as seen in Fig. 6.1. This novel tendon-driven system occupies minimal space on the platform and can conform to the geometry of the articulated structure.

Developed in conjunction with the adaptive bi-stable metamorphic arm is the multi-modal quadrotor robot, which is named "the Sloth". The robot transitions between three distinct morphologies: a locked state for flight; an unlocked state with which the arm is fully extended but cannot sustain the forces for flight; a perched state where the robot arm conforms to its target and holds its grasp with minimal energy use. The $650g$ Sloth robot with a pair of morphing arms, weighing $48g$, demonstrated flight and perching through dynamic and static manoeuvres. The approach of robotic metamorphosis leads to a compact quadrotor design that autonomously reconfigures within a second between flying and perching.

6.2 Results

6.2.1 Morphing robot arm design

The robot arm has three morphological states: triangular, flat, and curled. In these respective states, the robot can lock its arm for flight, transition between triangular and curled configurations, and grip onto tree branches to perch. The robot arm is formed as a carbon fibre-polyimide-carbon fibre sandwich panel, a technology inspired by other lightweight articulated robots [192]. The polyimide layer acts as hinges, allowing the carbon (fibre) panels to have articulated movement. From the arm's root to its tip, it has two rows of axial hinges, enabling the arm to fold into an open-section triangular cylinder. The arm can have an arbitrary number of rows of lateral hinges across the arm. The arm rotates about its lateral hinges to grip and perch. Elastic membranes, embedded in the sandwich panel, hold the arm in the triangular state. The membranes are pre-stretched prior to layer stacking and pressing (Fig. 6.1). The pre-stretch is accounted for when the membranes are cut. The sacrificial tabs ensure a repeatable pre-stretch and are removed during final assembly. The membrane is offset from the centre of the polyimide hinges to ensure that there is a moment arm for the elastic membrane to bend the arm to its natural triangular state. Overlapping teeth are cut on the outer

carbon fibre sheet to act as mechanical endstops, restricting the arm's motion to its designed workspace. The interlocking teeth on the edge of the sandwich panel exhibit a self-locking behaviour when the arm is locked. This enables the triangular cross-section to hold its shape, thus resisting both upward and downward loads on the thrust axis (Fig. 6.2). As thrust is applied, the strain of the panels forces the teeth at the two open sides to brace on each other. Finite element analysis shows the clamping force between the teeth increasing with the thrust load (Fig. 6.3G).

6.2.2 Tendon drive design

The perching action is controlled by a servomotor-driven tri-tendon system, threaded across the arm and the robot body during assembly. The driving tendon is wound around the spool and transmits the tension to the T-tendons on both arms. The T-tendon comprises an unlocking tendon, running across the width of the arm, and the gripping tendon, threaded from the tip to the root of the arm (Fig. 6.1).

The servomotor turns the spool to actuate the arm. This retracts the driving tendon which, in turn, pulls on the T-tendons. As the arm is still in the locked state, the gripping tendon cannot move; thus, the unlocking tendon is retracted towards the spool, opening the arm. The T-tendon acts as a differential, diverting the tension from the driving tendon between the unlocking and gripping tendons. Once the unlocking tendon has reached its limit, the arm is opened. Therefore, the gripping tendon will be pulled and the arms contract, perching the robot.

I designed in a gravity-assisted self-locking feature to reduce the load on the servomotor as the arm transitions toward the curled state. When spooling in the driving tendon, the unlocking tendon is acting against the elastic membranes to open the arm. The force from the membrane is mostly exhibited as a moment about the axial joint. However, when the arm is in the flat state, the force from the membranes predominately becomes a compression perpendicular across the axial joint. There remains a bending moment due to the offset of the membrane from the hinge axis. The curling of the arm creates interference between the rows of panels; the bending moment becomes a compressive force on the subsequent row of panels. In other

words, once the arm begins the perching motion, a stable equilibrium is reached and no force from the servomotor is needed to keep the arm in the curled configuration. Furthermore, with the quadrotor rotors not producing thrust at perching, the rotors act as weights, increasing the perch speed by overcoming the bending resistance of the polyimide hinges.

When perching, the arm can be considered an underactuated gripper. The sequence of joint movement is thereby dependent on the stiffness of the joints. For perching applications, it is preferable for the gripper to cover the largest possible workspace. The largest workspace is covered by ensuring that the hinges rotate in sequence, starting from the root. In the prototype, the requirements above are met by the embedded variable stiffness mechanism.

The variable stiffness mechanism takes advantage of the thin sandwich panels. With a low cross-section polar moment of area, the panels are prone to twist. By tuning the position where the unlocking tendon attaches to the arm and the location of the elastic membrane(s), the desired moment profile along the axial hinge can be created. For the prototype robot, a low to high hinge stiffness profile, from the arm root to the tip, was chosen. Furthermore, as the lateral hinges progressively bend, it forces the subsequent rows of panels to flatten. This flattening reduces the stiffness of the subsequent hinge, thus reducing the load on the servomotor, and increasing the grip speed.

The transition from perched to locked morphology occurs as follows. The servomotor releases the tendon tension. Simultaneously, the rotors generate thrust, providing the force to recover to the flat state. Once in the state, the elastic elements return the arm to the triangular configuration as the spool further unwinds the tendon.

6.2.3 Energy usage

The energy cost of perching and flight is determined with onboard current sensors. With a 4-cell lithium-polymer battery and a takeoff weight of $872g$, a typical cruising flight draws an average current of $15A$. The same battery is used for perching. The holding current draw depends on the diameter of the branch and the perch angle (Fig. 6.3D). For smaller branches and perch angles below $60°$ off the vertical, the robot can rest on the branch, and only the $40mA$ standby

current is expended by the servomotor; the gearbox friction is sufficient to hold the perch. At steeper perch angles and with larger branches, the perch holding current increases. At higher holding currents and for extended perch duration, the servomotor will overheat and shut down. This leads to a failed perch. In this event, an onboard electronic switch can remotely reset the servomotor.

6.2.4 Vehicle mass breakdown

The integrated metamorphic design allows components on the robot to perform multiple roles, reducing the overall weight. For the aerial robot, the rotors on the perching arm are used to recover the arm when transitioning to flight. Not accounting for the battery mass but including the flight computer, the flight and perch subsystems weigh $430g$ and $383g$ respectively. As an integrated subsystem, the flight and perch subsystem weighs $541g$, giving a shared mass of $272g$. The shared mass constitutes 49% of the integrated subsystem; a 33% mass reduction from modular to integrated subsystem design.

6.2.5 Perching

The robot arm reduces its stiffness in the flat and curled state by an order of four magnitudes over its locked configuration. While this increases the compliance of the arm when perching, the arms cannot sustain the thrust load. This results in a highly erratic and uncontrollable flight when transitioning to perch. As the transition process lasts at least $0.72s$, I demonstrated two methods to mitigate the inability to fly whiles the arms are not triangular.

The first method, named "land-perch", ensures that the robot spends the minimum time in the un-powered and un-perched state, thereby reducing the likelihood of failing to perch and falling off the target. The robot can descend gently and maintain a minimal thrust to remain level in the locked configuration whiles resting on the target. The rotors the throttle down at the beginning of the transition to perch from the unlocked state. However, flying close to the target structure causes significant turbulence, resulting in substantial difficulties aligning the robot to the structure in the horizontal directions (Fig. 6.4, A and B).

Alternatively, the robot can hover high above the target and perform an un-powered drop onto it to minimise the aerodynamic disturbance. This method is called the "drop-perch". The drone will cut power to the rotors and begin the perching motion while in mid-air. The throttle cutoff is synchronised to ensure that the free-falling robot impacts the target at the perched state. This method is more demanding of the controller's positional precision. But as the robot can hover with minimal turbulence and is not at risk of collisions, drop-perch avoids the complex interactions of the land-perch. This ability can be further expanded to allow throttle cutoff when the robot launches itself onto a ballistic trajectory to enable perching on inclined structures.

Land-perching

The land-perch method is demonstrated both indoors, with motion capture, and manually outdoors. The transition from perch to flight is also validated from a static perch (Fig. 6.3A).

The land-perch method utilized a finite state machine to detect the contact with the target branch. The detection is determined by the mismatch between the throttle and the vertical acceleration. Upon detecting the contact, the robot attempts to remain balanced on the structure with minimal throttle. This gives the arm sufficient time to morph and grip before all rotors shut off in a successful perch. These three distinct behaviours are encoded with the logic presented in Fig. 6.5A.

Drop-perching

The ability of the robot to drop-perch was first tested with an electronically timed-release mechanism. At high impact speed and energy, the robot will rebound off the branch. Upon the second impact, if the branch is still within the range of the arm, the robot successfully perches (Fig. 6.3C).

The drop-perch is then demonstrated during autonomous flights in an indoor environment. Two distinct perching mechanics were observed. If the body makes initial contact with the branch at impact, the front of the drone would bounce. The morphing arm, at the back of

the robot, would remain in contact with the branch and grip. The arm grips firmly onto the branch at the rebound of the front body. Alternatively, if the arms are positioned such that they make contact first, they would deform to dampen the impact. Providing that the arms deform outwards such that it exposes the spines, the robot perches without rebounding.

However, if the arms contract too much at impact, it would cause them to deform inwards towards the body. This morphology hides the spines and results in a failed perch. Another failure mode is the arms not gripping in time to prevent the robot from sliding off the branch. This failure mode is easily remedied by increasing the height of the drop, allowing the arm the time to contract more.

There is a large scatter in the data. While this affected the drop-perch success rate, this scatter was indented purposefully to capture the breadth of perching behaviours. The data suggests that the optimum arm angle at impact is between $-45°$ and $-75°$ from the assumed ideal arm angle, where simultaneous body and arm impact would theoretically occur (Fig. 6.2C). This is logical as a slightly wider arm position would increase the robustness to off-centred impacts without causing too much detriment to the gripping speed. The statistical analysis further corroborates the findings as both the interquartile range and the extremity differs significantly between perch success and failure (Fig. 6.4).

6.3 Discussion

In utilising metamorphic designs on small multirotor UAVs, I created a robot that can fly and perch. The integration and sharing of components on the flight and perching subsystems resulted in a $208g$ mass reduction on the $650g$ robot. Using the full span of the multirotor structure to perch, the robot can grip onto tree branches of various geometries, diameters, and in various angles. In having the gripper integrated compactly and close to the centroid of the robot, the robot's centre of gravity is closer to the surface of the branch than other modular perching robots. This reduces the moment arm when the robot's centre of mass is offset from the centre of the branch, reducing the peeling moment. As a result, our robot can grip onto branches from all angles. Overall, the minimal weight penalty for gaining a robust perching

capability contributes to an increase in the robot's operational endurance.

While substantial weight is saved by using integrated metamorphosis, there are penalties to consider. Most significantly, in making the quadrotor arm articulated, the structure is weaker at the hinges. Furthermore, the metamorphic perching transition process and the use of an underactuated gripper configuration result in complex system dynamics which are difficult to control. This is mitigated by the proposed perching methods, land-perch and drop-perch, both shown to be successful. Autonomous land-perch and drop-perch were demonstrated in an indoor environment with motion capture. In addition, the land-perch was demonstrated manually in a forested environment. For the robot to function autonomously outdoors, a number of improvements must be made. When the robot slips during gripping, it would perch at an acute angle (Fig. 6.1A). While this does not affect the perching performance or its ability to transition back to the triangular configuration, taking off from this position requires the robot to fall a substantial distance when self-righting. This can be mitigated by aborting the perch when the onboard sensors measure a large angular velocity after detecting contact with the branch, thereby reducing the transition time to flight as the arm would not be fully curled.

Identification of suitable perch locations is also an intriguing challenge. As shown in Fig. 6.5B, the robot can land-perch on inclined branches. But the maximum incline, suitable geometries, and other limiting branch characteristics remain unknown. Current perch locations are determined by trial and error. Identifying suitable locations prior to perching would be a major advancement toward full automation.

Integrated metamorphosis is a design principle that can be further explored in numerous ways, some of which have already been shown in other types of robots with capabilities such as self-assembly [78]. Our design is also not limited to a metamorphic arm. Adding the bi-stable metamorphic mechanism to the body of the drone could increase its compliance to aid perching on vertical branches, similar to a gliding gecko [193]. The large surface area of the arm in its flat state can be utilized as an aerodynamic surface for gliding flight. Many situational behaviors are also left unexplored. An example of such is our current interest; a method of low-power aquatic locomotion, whereby the robot would perch on floating objects to maintain buoyancy and steer with the rotors on the rigid arms.

To conclude, the multi-modal capability gained through integrated metamorphosis, in conjunction with inspiration from tree-dwelling animals, enables us to imagine synergetic mission profiles where robots can spend a greater proportion of the operation at rest than in flight. Our results have displayed the potential wealth of capabilities that can be gained by applying metamorphic designs, producing compact robots that are suitable for the autonomous exploration of the natural world.

6.4 Materials and Methods

6.4.1 Robot Construction

The metamorphic arm is a sandwich of $0.5mm$ carbon fibre reinforced polymer panels, $0.075mm$ polyimide sheets, and elastic latex membranes bonded with acrylic glue sheets (Fig. 6.1). The carbon fibre panels are pre-cut on an Oxford laser and the others on a Universal laser. The sandwich is aligned with pins on a jig and then pressed flat to activate the pressure-sensitive glue sheet. Tabs on the carbon fibre panels are then removed to allow the arm to fold. Two arms are interlinked at manufacturing to form an arm pair. This offered increased stiffness during flight and improved the synchronization of the arms during perching. The stainless steel servomotor spool is laser sintered. The mounting brackets for the servomotor and tracking markers, and the flight computer and camera are fuse-deposition manufactured with polylactic acid and thermoplastic polyurethane respectively.

The robot body uses a twin deck $3mm$ carbon fibre plate construction with the lower deck providing the mounting for the propulsion components (rotors, electronic speed controllers, flight controller). The upper deck houses the Dynamxiel XH430-W350 smart servomotor, an AAEON Up Core computer, an Intel T265 tracking camera, and the battery.

6.4.2 Control System

Indoor flights were conducted with the robot odometry provided by a VICON motion capture system. For outdoor autonomous flights, the odometry is provided by the optional tracking

camera module (Fig. 6.5B). A PID controller was implemented to control the robot's position and yaw orientation.

6.4.3 Experimental Setup

The indoor perching test is carried out by dropping the robot on simulated tree branches, round PVC pipes covered by a layer of $10mm$ thick non-woven fibre abrasive pads were used as branches. The pipes ranged in diameter from $75mm$ to $200mm$. The wrapped pipes gave similar perch-and-hold performances to hardwood trees. The branch is marked by tracking markers so that its global position in the motion capture world frame can be obtained. The robot is controlled to fly to the branch position and hover above the pipe at a set distance. When the robot hovers stably above the pipe, the perching command can be initiated.

When initiating dynamic drop-perch, the goal current commands will be sent to the servo, and the servo will apply a constant grasping force. The arm will start to unfold. A disarm command is then sent to the flight controller after a short delay, timed to maximise control of the robot whiles reducing the duration of free fall. At disarm, the robot loses lift and starts free fall, while the arm continues to unfold and grip. When the robot hits the pipe, the arm should be fully unfolded and curled to grasp the pipe. The dropping height and the delay time are crucial for a successful drop-perch. In 33 tests With high-speed camera footage and motion tracking at $90Hz$, the robot executed the free-fall with a mean starting position of $+4.4mm$ off the centre of the branch and a standard deviation of $19.1mm$. Relative to the centre of the branch, the mean point of impact is at $+3.5mm$ with a standard deviation of $25.5mm$; the time of impact is defined as 2 timesteps prior to maximum jerk. The time offset is applied to account for the filter delay.

For the static land-perch, the robot is commanded to slowly descend. Once the robot stably lands on the pipe, the robot will be disarmed while the folding arm grip.

During the perching tests, the position, velocity, and orientation of the robot, the position of the branch, and the servo position are recorded. For outdoor tests, the robot is manually controlled. When outdoors, the perching process is commanded by a switch on the remote

control.

6.4.4 Perch strength bench test

The required servomotor's holding current at various perch angles was determined by bench tests. The servo is actuated at maximum current before ramping down until the robot detaches from the pipe.

Steel spines, embedded on the inner side of the arm, were critical to perching success. By interlocking with coarse surfaces, such as tree barks, adhesion was greatly improved over the control group, a smooth PVC tube.

Statistical analysis of arm angle at impact

The arms and the body should impact at the same time for an ideal perch. This is likely due to the gripping action of the arm allowing maximum energy transfer to the branch, thus dampening the impact and increasing the probability of a good perch. Therefore, for a given branch radius, we can find the ideal servomotor position.

Assuming the arm is only bent at the innermost joint before impact, the arm angle θ_{ext} is well defined as a function of the servo position, $\text{servo}_{\text{current}}$, and can be calculated by

$$\theta_{\text{ext}} = \theta_{a1} = \pi - 2\sin^{-1}\left(1 - \frac{0.088}{2}\frac{r_{\text{spool}}}{l_t}(\text{servo}_{\text{current}} - \text{servo}_{\text{singularity}})\frac{\pi}{180}\right) \tag{6.1}$$

where l_t is the distance from the tendon hole to the joint. The ideal arm angle is defined as the angle between the horizon and tangent to the branch, with the robot impacting perfectly level and at the centre of the branch. We place the origin of the Cartesian coordinate system at the top of the circular branch, where the body of the robot first contacts the branch. The gradient

of the tangent m_0 and its normal $m_\perp$ are related by

$$m_0 \cdot m_\perp = -1 \tag{6.2}$$

$$m_0 = \frac{y_{\text{cont}}}{x_{\text{cont}} - x_{\text{root}}} \tag{6.3}$$

$$m_\perp = \frac{x_{\text{root}} - x_{\text{cont}}}{y_{\text{cont}}} \tag{6.4}$$

$$x_{\text{cont}}^2 + (y_{\text{cont}} - (-r_b))^2 = r_b^2 \tag{6.5}$$

where $(x_{\text{root}}, y_{\text{root}}), (x_{\text{cont}}, y_{\text{cont}})$ are the root joint of the arm and the arm's point of impact respectively, r_b is the radius of the branch. As the normal also crosses the centre of the branch

$$m_\perp = \frac{y_{\text{cont}} - (-r_b)}{x_{\text{cont}}} \tag{6.6}$$

(6.3) and (6.6) are manipulated, given (6.2), to form

$$y_{\text{cont}}^2 + r_b y_{\text{cont}} - x_{\text{root}} x_{\text{cont}} + x_{\text{cont}}^2 = 0 \tag{6.7}$$

and by multiplying out (6.5)

$$y_{\text{cont}}^2 + 2r_b y_{\text{cont}} + x_{\text{cont}}^2 = 0 \tag{6.8}$$

the difference between the two equations gives

$$y_{\text{cont}} = -\frac{x_{\text{root}} x_{\text{cont}}}{r_b} \tag{6.9}$$

which by a further substitution into (6.5) yields

$$x_{\text{cont}} \left(\frac{r_b^2 + x_{\text{root}}^2}{r_b^2} x_{\text{cont}} - 2x_{\text{root}} \right) = 0 \tag{6.10}$$

$$\therefore\ x_{\text{cont}} = 0\,,\ x_{\text{cont}} = \frac{2x_{\text{root}} r_b^2}{r_b^2 + x_{\text{root}}^2} \tag{6.11}$$

where the first root $x_{\text{cont}} = 0$ is practically moot as this implies that the arm has rotated by

180° at impact. The gradient of the tangent is

$$m_0 = \frac{y_{\text{cont}}}{x_{\text{cont}} - x_{\text{root}}} = -\frac{x_{\text{root}} x_{\text{cont}}}{r_b(\frac{2x_{\text{root}} r_b^2}{r_b^2 + x_{\text{root}}^2} - x_{\text{root}})} = -\frac{2r_b x_{\text{root}}^2}{(r_b^2 + x_{\text{root}}^2)(\frac{2x_{\text{root}} r_b^2}{r^2 + x_{\text{root}}^2} - x_{\text{root}})} \tag{6.12}$$

6.5 Deflection of the morphing robotic arm

Approximating the quad-rotor arms as Euler-Bernoulli cantilever beams during flight, I derived vertical deflection z_{arm} as

$$z_{\text{arm}}(x) = \frac{Tx^2}{2(EI)_{\text{arm}}}(L - \frac{x}{3}) \tag{6.13}$$

where T is the thrust of the rotor, L is the length of the arm, and the distance from the root of the arm x. The stiffness of the arm $(EI)_{\text{arm}}$, due to the sandwich construction, is bounded by two analytical models. As the arm is comprised of a series of polyimide joints, the lower bound stiffness model assumes that the load is carried by a homogeneous polyimide structure. Further assuming that second order and higher terms of the thickness, t_k and t_{cf}, are insignificant, this gives

$$(EI)_{arm} = 2E_k \int z_{\text{arm}}^2 dA = \frac{E_k t_k w^3}{2} \tag{6.14}$$

The upper bound model assumes a homogeneous carbon fibre structure. With the neutral axis of bending imposed at the centroid of the cross-section, this gives

$$(EI)_{arm} = E_{cf} t_{cf} w^3 \left(\frac{23}{8} - \sqrt{3}\right) \tag{6.15}$$

We can further model the arm as connected homogeneous sections, alternating between polyimide and carbon fibre, giving equations in the form

$$\frac{dz}{dx}|_{i<x\leq i+1} = \frac{T}{(EI)_i}\left((x - X_i)l_i - \frac{1}{2}(x - X_i)^2\right) - \frac{T(X_i - L)}{(EI)_i}(x - X_i) + \frac{dz}{dx}|_{x=i} \tag{6.16}$$

$$z_{i<x\leq i+1} = \frac{T}{(EI)_i}\left(\frac{l_i}{2}(x - X_i)^2 - \frac{1}{6}(x - X_i)^3\right) - \frac{T(X_i - L)}{2(EI)_i}(x - X_i)^2 + \frac{dz}{dx}|_{x=i}(x - X_i) + z_i \tag{6.17}$$

with initial conditions

$$\frac{dz_{\text{arm}}}{dx}|_{x=0} = 0 \quad , \quad z_{\text{arm0}} = 0 \tag{6.18}$$

and $X_i = \sum_0^i l_i$.

6.6 Parametric numerical study of the tendon actuation

The transition dynamics from the locked to unlocked state are determined by the characteristics of the servomotor-spool, the elastic elements, the polyimide hinges, and the tendon anchor position (Fig. 6.6). The servomotor is modelled as a DC motor with a linear speed-torque curve such that

$$\tau = \tau_{\text{stall}}\left(1 - \frac{\text{RPM}}{\text{RPM}_{\text{no-load}}}\right) \tag{6.19}$$

$$\dot{\theta} = \frac{2\pi}{60}\text{RPM}_{\text{no-load}}\left(1 - \frac{\tau}{\tau_{\text{stall}}}\right) \tag{6.20}$$

The speed of the arm unfolding is estimated by a forward Euler numerical scheme with the servo angular rate ($\dot{\theta}$) determined by the torque (τ) at each time step.

Using a Mooney–Rivlin model, assuming the membrane to be incompressible (Poisson ratio= 0.5), the stress of the membrane, σ is

$$\sigma = \frac{2}{\lambda}\left(C_{10} + \frac{C_{01}}{\lambda}\right)\left(\lambda^2 - \frac{1}{\lambda}\right) \tag{6.21}$$

with the stretch ratio (λ) defined as the length ratio of the stretched and unstretched membrane length. Thus

$$\lambda = \frac{l_{\text{stretched}}}{l_{\text{unstretched}}} = \frac{l_{\text{st.}}}{l_0}\frac{l_0}{l_{\text{unst.}}} = \frac{l_{\text{st.}}}{l_0}\lambda_0 \tag{6.22}$$

which, for the geometry of the prototype,

$$\lambda = \lambda_0 \sin\frac{\alpha_s}{2} \tag{6.23}$$

The moment due to the stiffness of the polyimide hinge is modelled as an Euler-Bernoulli beam

of uniform curvature

$$\epsilon = \frac{w_k - w_{k0}}{w_{k0}} = \frac{(r+t)(\pi - \alpha_s) - r(\pi - \alpha_s)}{w_{k0}} = \frac{t(\pi - \alpha_s)}{w_{k0}} \tag{6.24}$$

$$M_{\text{joint}} = \int_{-\frac{t_k}{2}}^{\frac{t_k}{2}} E_k \epsilon t L_{\text{arm}} dt \tag{6.25}$$

$$= \frac{E_k L_{\text{arm}}(\pi - \alpha_s)}{w_{k0}} \int_{-\frac{t_k}{2}}^{\frac{t_k}{2}} t^2 dt \tag{6.26}$$

$$M_{\text{joint}} = \frac{E_k L_{\text{arm}}(\pi - \alpha_s) t_k^3}{12 w_{k0}} \tag{6.27}$$

where ϵ is the strain The moment equilibrium at the hinge gives

$$F_t a \sin\beta_s + \frac{E_k L_{\text{arm}}(\pi - \alpha_s) t_k^3}{12 w_{k0}} = F_m d \cos\frac{\alpha_s}{2} \tag{6.28}$$

$$\frac{F_t ab \sin\alpha_s}{\sqrt{a^2 + b^2 + 2ab\cos\alpha_s}} + \frac{E_k L_{\text{arm}}(\pi - \alpha_s) t_k^3}{12 w_{k0}} = F_m d \cos\frac{\alpha_s}{2} \tag{6.29}$$

assuming frictionless tendon motion. F_t denotes the tension of the tendon, the force of the membrane $F_m = \sigma w_m t_m$, β_s the angle between the tendon and the side links of the arm, and m the length of the tendon between the side links and the tendon pivot.

The angle between the sections of the arm (α_s) is formulated as a function of the servo angle (θ),

$$\alpha_s(\theta) = \cos^{-1}\left(\frac{R^2\theta^2 + ab - R\theta\sqrt{a^2 + b^2 + ab}}{2ab}\right) \tag{6.30}$$

where $\theta = 0$ is the neutral state of the arm in flight configuration.

The tension of the tendon is further multiplied eightfold by the number of actuated tendons on an arm pair and the pulley system. The torque is a function of the servo angle (Fig. 6.6)

$$\begin{aligned}\tau(\theta) = &\frac{8R\sqrt{a^2 + b^2 + 2ab\cos\alpha_s}}{ab\sin\alpha_s} \\ &\cdot \left(\sigma w_m t_m d \cos\frac{\alpha_s}{2} - \frac{E_k L_{\text{arm}}(\pi - \alpha_s) t_k^3}{12 w_{k0}}\right)\end{aligned} \tag{6.31}$$

$$\text{At } \alpha_s = \pi, \qquad T(\theta_{\alpha_s = \pi}) = \frac{RdA_m(a-b)\sigma(\pi)}{2ab} \neq 0 \tag{6.32}$$

Finally, (6.31) can be substituted into (6.20) and numerically advanced in time to determine the position of the arm.

A parametric study was conducted to determine the trade-offs between actuation speed and servomotor limits. Predictably, the opening time increased with increasing membrane thickness and stretch and decreased with increasing hinge thickness. However, the servomotor's torque-speed characteristics and spool manufacturing constraints result in an optimum spool radius limited by hardware.

6.7 Video analysis

The transition times between the three configurations on the prototype robots are determined by video analysis. During this analysis, the robots are rigidly mounted to a test frame. While the folding and unfolding speeds vary due to the variances in the manufacturing, the robots are able to achieve locked-to-unlocked times of less than $1s$. A further $0.3s$ is required for both the unlocked arms to sweep past $\pi/2$.

The flight behaviours of the robot during the perching transition were further examined with high-speed video. The platform, while in a semi-flexible state in mid-transition, was sufficiently rigid to exert some stabilizing forces. Thus, the perching transition can begin prior to motor cutoff, reducing the glide time.

6.8 Robot mass breakdown

The mass breakdown of the prototype robot is as shown in Tab.6.1.

6.9 Outdoor autonomous flight testing

The T265 camera was mounted on the platform during all perching tests. However, during outdoor testing using the camera's Visual Inertial Odometry (VIO), I noted that the VIO

Table 6.1: **Prototype robot mass breakdown**. The integrated subsystems for perching and flight are highlighted in blue and red, respectively.

Function group	Components	Mass (g)	Perching Subsystem	Flight Subsystem
Sensing & Command	Tracking Camera	55.0		
	Computer Voltage Converter	9.0		
	Cables	16.0		
	Flight Computer	54.0	■	■
	Flight Controller	9.0	■	■
Flight Suite	Battery connector cables	10.0	■	■
	2 Motor Cables	24.0		■
	2 ESC + 2 BLDC Motors + 2 Propellers	67.9		■
	2 Motor Cables	24.0	■	■
	2 ESC + 2 BLDC Motors + 2 Propellers	67.9	■	■
Perching Electronics	USB Communication Converter	9.0	■	
	Servomotor	88.0	■	
	Peripheral Electronics	12.0	■	
	Mounts	2.5	■	
Structure	Morphing Arms	48.0	■	■
	Carbon fibre Body	58.8	■	■
	Static Arms	26.0		■
	Nuts/Bolts/Standoffs	40.0		■
	TPU Computer Mount + Bumper	72.0		
	TPU Camera Mount	11.0		
	Vicon Bubble + Mounts	12.0		
Battery	4 Cell LiPo	148.0		
	Battery alarm	8.0		
Subtotal	Perching Subsystem	383.2		
	Flight Subsystem	429.5		
Total	without battery/battery alarm/camera	650.0		
	with battery	872.0		

output drifts significantly in the absence of contrasting and angular objects. This issue was confirmed qualitatively with flight tests in four settings; indoor, forest understory, grassland, and grassland with a scattering of man-made objects. During the latest test, in the summer of 2021, the robot was able to take off and hover stably when man-made objects were in view. As soon as these objects are out of the Field of View (FoV), the robot drifts away.

6.10 Summary

In this chapter, I explored the use of metamorphic design on the arm of a quadrotor. I created a bi-stable beam structure with compliant joints by embedding elastic tendons within a Carbon-Fibre-Reinforced Polymers (CFRP)-polyimide sandwich. The quadrotor arm can sustain the forces from the rotor during flight, and unfold and curl to grip onto tree branches with aid from its embedded spines.

I also proposed a novel tendon actuation system for the morphing arm. The tendon actuation is analytically studied to determine the appropriate servomotor specification and the perching rate.

The morphing arm is integrated into a prototype quadrotor robot to conduct aerial perching. Two perching methods, the land-perch and the drop-perch, were proposed and characterised. The land-perch was demonstrated autonomously in an indoor motion capture environment, and manually outdoors. The drop-perch was demonstrated autonomously indoors but with manual fine-tuning of various perching parameters. The static perching performance of the robot is also characterised by measuring the power consumed by the servomotor at various perch angles and branch diameters. I further discussed the prospects and limitations of the robot, namely how fully autonomous operation in outdoor environments can be achieved.

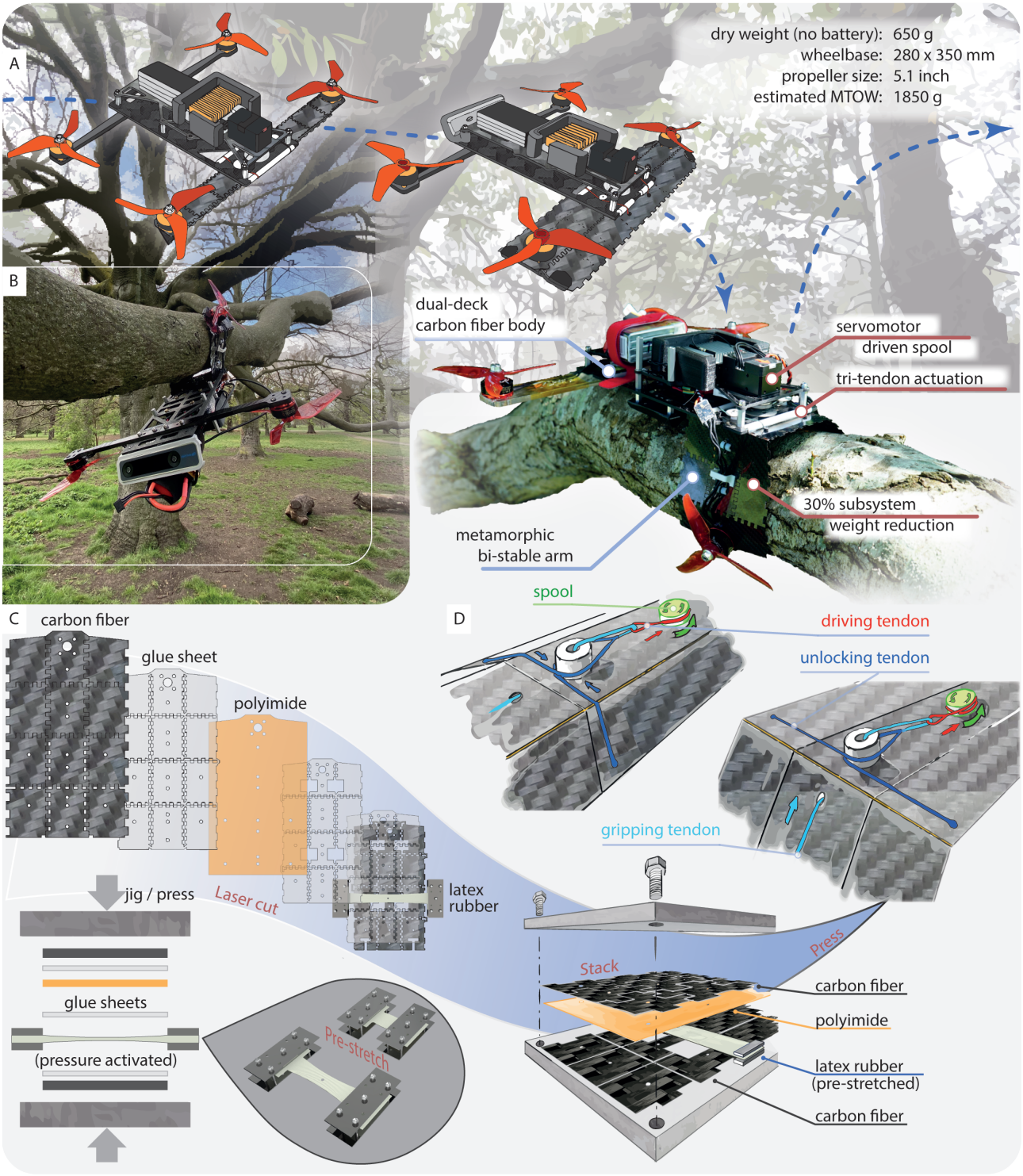


Figure 6.1: **The bioinspired perching quadrotor robot.** The top half of the figure diagrams the perching process. (**A**) A photograph of the prototype robot perching upside down on tree branches. The bottom half of the figure diagrams the manufacturing of the morphing arm. The layers are laid on jigs with the elastic membranes pre-stretched before being pressed to form a single panel. The actuation process of the tri-tendon spool mechanism to unlock the arm.

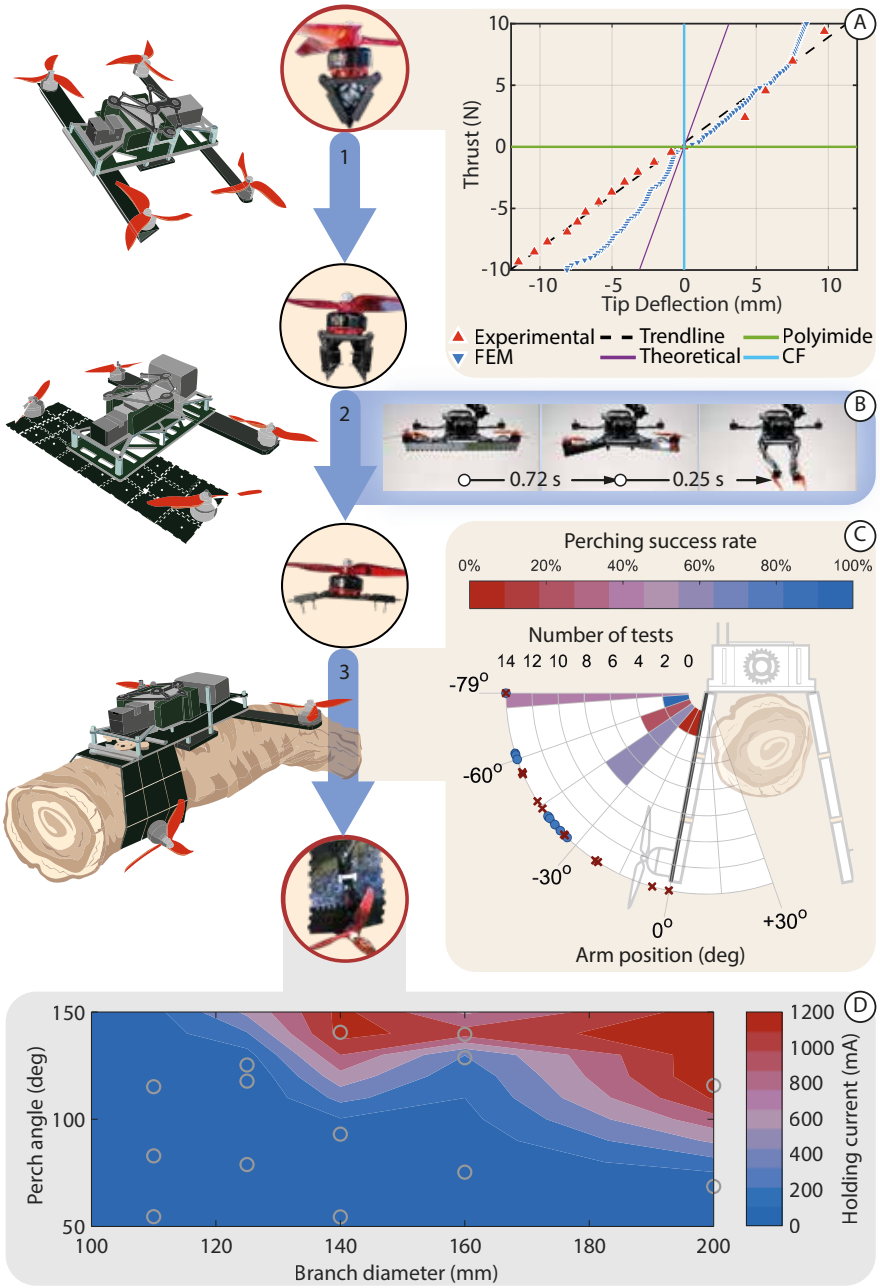


Figure 6.2: **Performance study of the prototype robot.** The arm morphing process has three stages: 1. locked for flight, 2. transition to unlocked, and 3. fully unlocked to grasp. The photographs of the arm at each stage are displayed. (**A**) The relationship between the tip deflection and thrust loading is plotted against the analytical models and finite element analysis when the arm is locked. (**B**) The time needed for the arm to open and grasp, is determined with a high-speed camera. (**C**) The drop-perch successful rate in relation to the arm position. After landing, the robot must grasp the branch (approximated by a cylindrical pipe) to remain perched. (**D**) The holding current of the servomotor with varying perching angles and branch diameters.

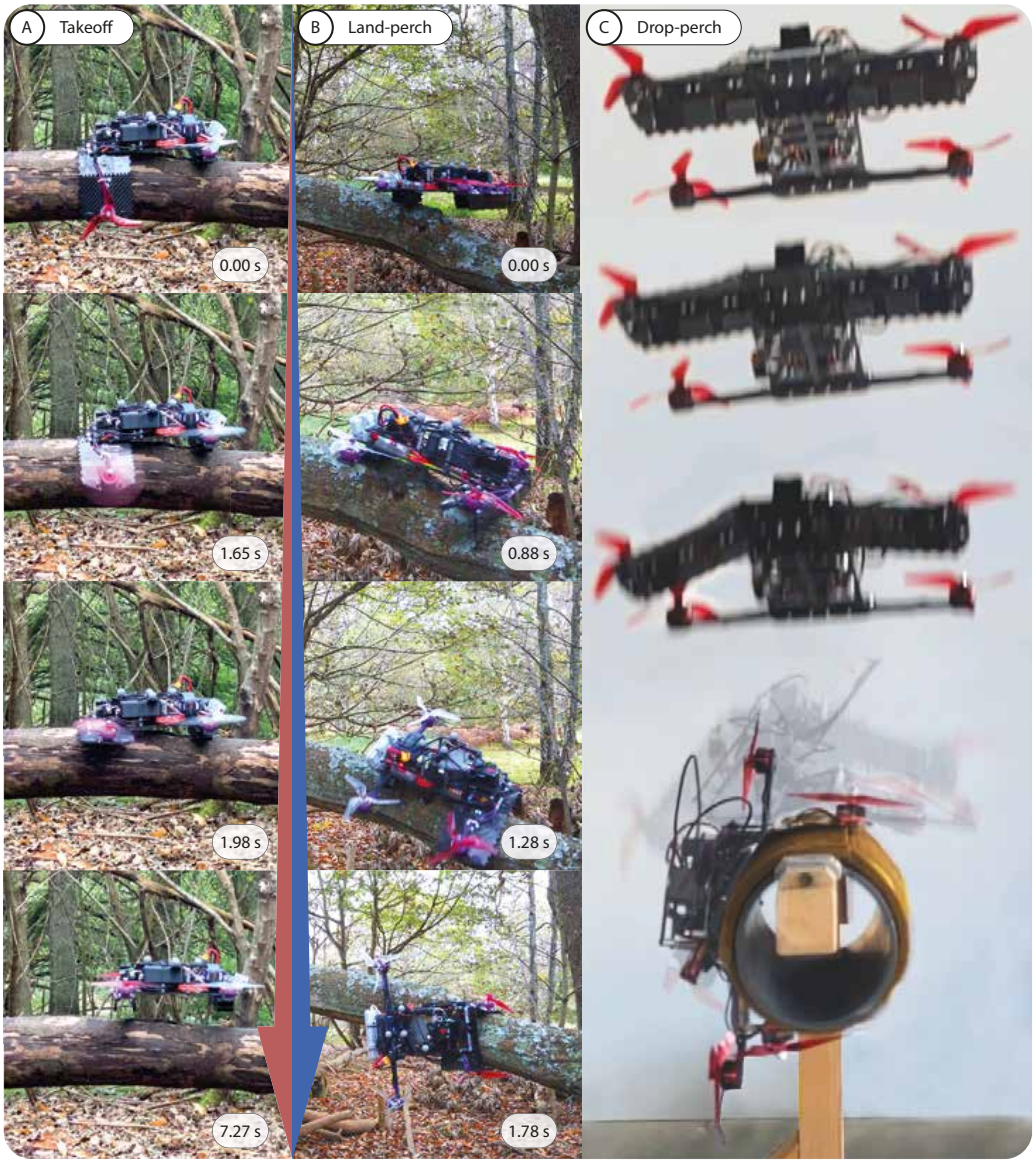


Figure 6.3: **The morphing robot perching indoors and outdoors.** (**A**) The robot taking off from a perch (bottom to top). (**B**) The robot performing a land-perch (top to bottom). (**C**) The robot performing a drop-perch.

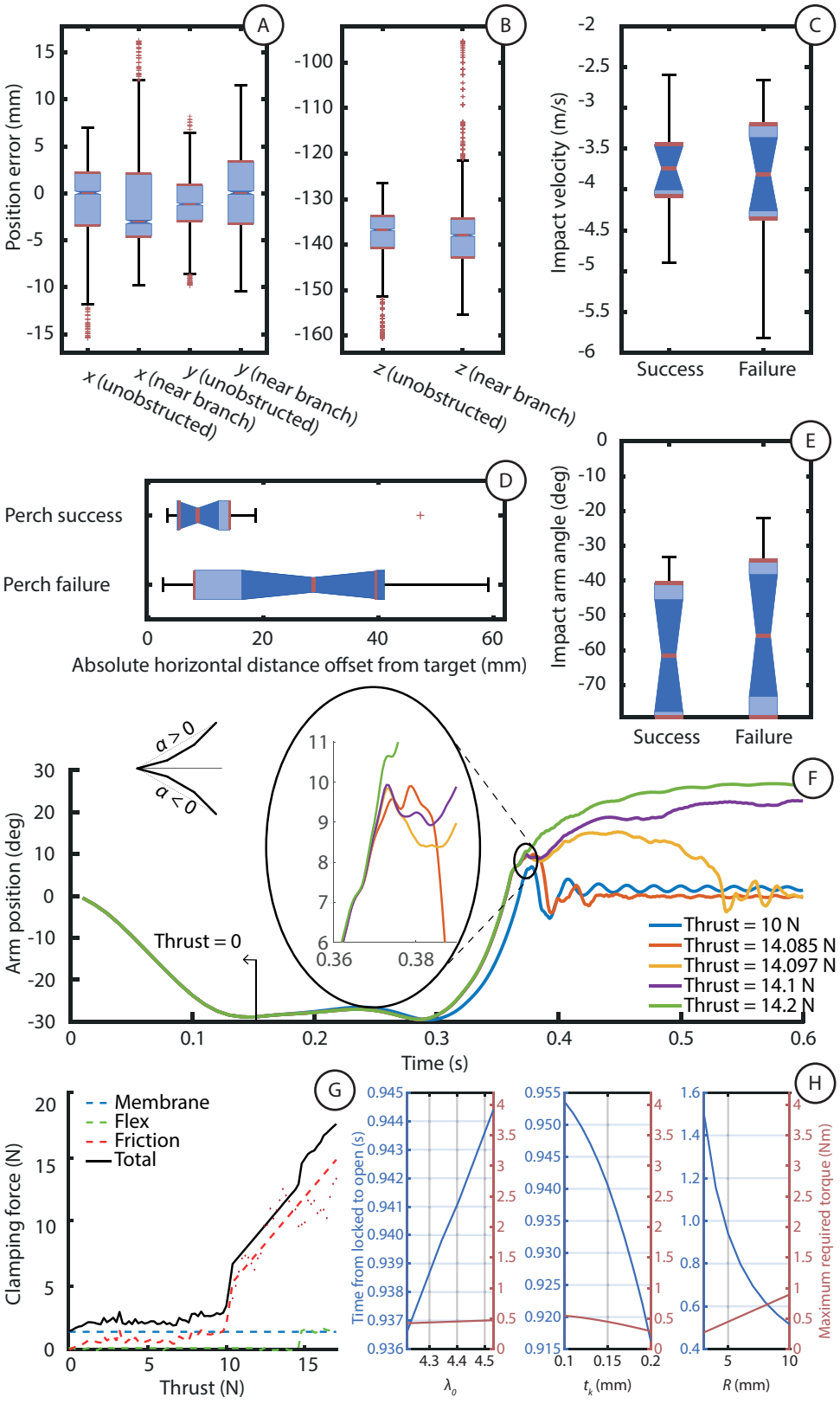


Figure 6.4: **Statistical analysis of the flight and perching data.** Dynamic finite element simulation of the effect of thrust on the morphing arm's locking behaviour.

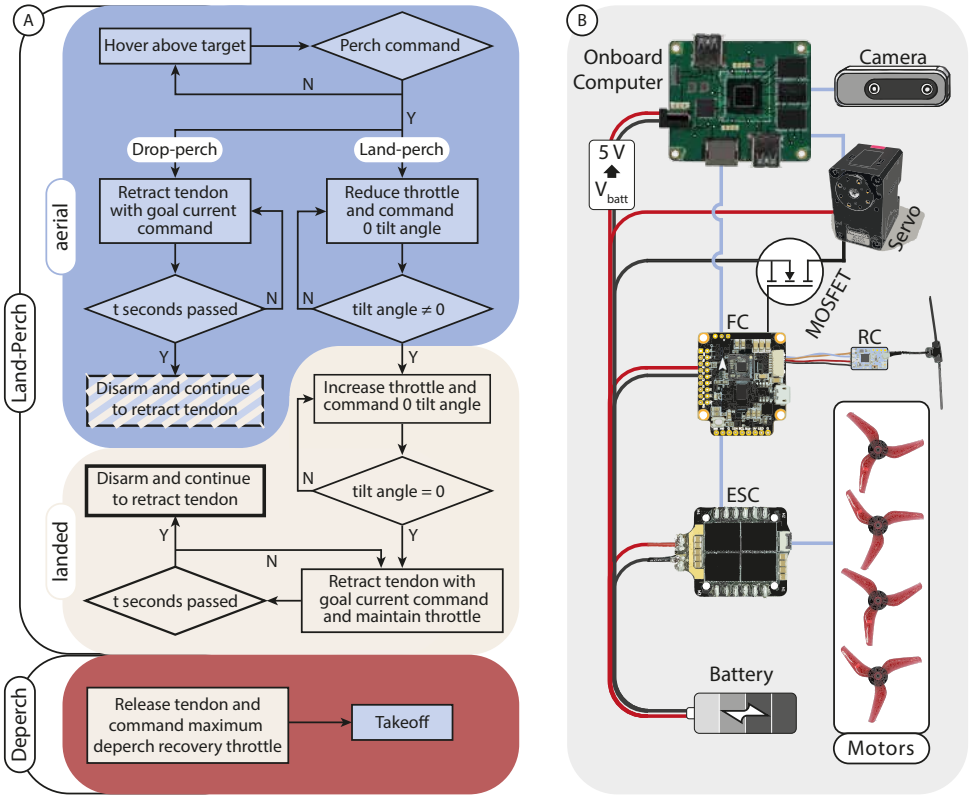


Figure 6.5: **The control flow chart and electronics system.** (**A**) The finite state machine of the land-perch procedure, the drop-perch controller, and the deperch process. (**B**) The electronics architecture of the robot with an additional N-channel MOSFET to switch on and off the servomotor.

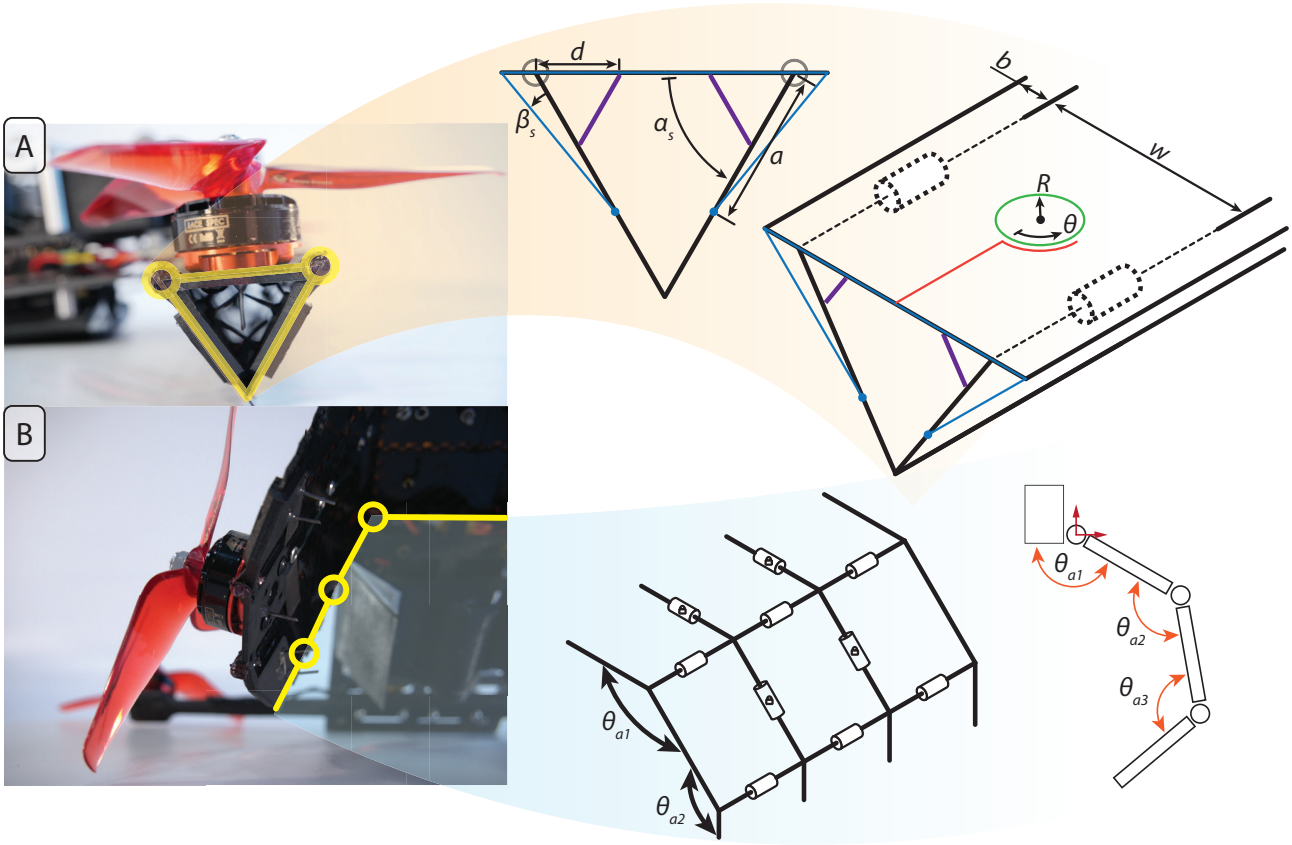


Figure 6.6: **Diagram of the morphing arm** with the dimension variables used to (**A**) model the structural stiffness and the unlocking dynamics, and (**B**) the position of the arm at perch.

Chapter 7

Robust aerial platform for long-duration acoustic sensing

7.1 Introduction

Sensor deployment in forest canopies has always been a challenging task. While various manual methods have been trialled, they are either too costly, unsafe, and/or slow to deploy. While touted as the ultimate solution, sensor-deploying aerial robots still face a number of hurdles.

The forest presents a unique challenge for aerial robots. Beyond the difficulties of noisy GPS data in cluttered areas and onboard localisation environments with shifting scenery [88, 89], the robot needs to be small enough to traverse a dense forest canopy. Being small limits the aerial robot in a number of ways. The designer must first pack the components, including the battery, into a finite design volume. This in turn limits the size, thus the capacity of the battery. The diameter of the propellers is also restricted by the design volume. The combination of factors leads to the ceiling on the payload capacity of the aerial robot. Compounding this issue, the more advanced and capable localisation sensors, such as LiDAR scanners, are generally heavier than their lesser counterparts, the conventional cameras. Thus, there is a trade-off in achieving precise localisation for automation and reserving the payload capacity for the mission, which is to deploy environmental sensors.

Sensor-deploying robots can be categorized into two groups: standoff deployment and contact deployment. Standoff deployment involves expelling sensors from the robot at a distance from the sensors' intended targets. This can be conducted passively by dropping the sensors under gravity, preferably with aerodynamic devices to reduce the impact forces [194]. For sensor deployment in forests, it is reasonable to fly the robot above the forest canopy, in open air, and drop multiple sensors in a single flight. Dropping sensors in a top-down approach avoids the limitations on the size of the robot, and by flying in open air it greatly improves the accuracy of GPS localisation. The sensors can also be dropped at set GPS locations. Depending on the density of the foliage, the sensors may be entangled within the tree leaves and branches, enabling them to remain in the canopy layer to gather data. However, there are inevitable trade-offs with top-down sensor dropping. The randomness of entangling the sensor pods within the canopy means they are difficult to track and retrieve post-deployment. To date, many environmental sensors are non-networked, so the data gathered must be manually transferred via storage devices, such as SD cards. These sensors are also not biodegradable and must be collected to prevent them from becoming a source of pollution. Therefore, the ease of retrieval must be considered when designing the sensor pods.

Actively launching the sensors could provide more control over the deployment and retrieval process. Taking off from the forest understory, the robot can traverse through the more open tree layers before launching its sensor dart into the higher and denser canopy [133]. By embedding the dart into the trees, the location of the sensor can be precisely selected and recorded to allow for convenient retrieval. However, launching sensors restricts the feasible weight of the pod. heavier sensors are more difficult to secure with indentation-based methods. Also, although the robot may compensate for the recoil from launching a heavy sensor with additional thrust, this is non-trivial and requires the launch process to be heavily automated. This, in turn, brings us back to the issue alluded to above regarding precise autonomous flight within the forest canopy.

Alternatively, the aerial robot can place sensors whiles maintaining physical contact with the target tree [92]. Bringing the robot within reach of the tree enables the use of tools onboard the robot to secure the sensor. This allows the robot to deploy larger and heavier sensors but

it too requires extensive automation.

I propose a radical perspective to sensor deployment in the forest canopy. Having considered the difficulties of flying between branches in the forest canopy, I examine the difficulties of manually flying into the said tree branches. To do so, I developed a novel morphing quadrotor robot that perches passively onto tree branches (Fig. 7.1). The perching process is initiated by the impact, upon which the folding quadrotor arms will wrap upwards onto the branch using their momentum, the thrust from the propellers, and a spring-loaded mechanism (Fig. 7.2). Spikes on a leaf spring integrated into the arm would conform to the shape of the branch. The folding arms remain wrapped around the branch by the force from the spring mechanism and secured with an integrated ratchet. By perching the whole robot, we can use the high-capacity quadrotor battery to power the onboard eco-acoustic sensor, extending the sensor's operational endurance. The eco-acoustic sensor and the sensitive electronics are housed within a protective TPU pod. To recover the sensor, the pod is remotely separated from the quadrotor structure and lowered to the forest floor via a magnetically damped tether spool, reducing the speed of descent. Having a smaller cross-sectional area than the quadrotor structure, the pod has a clearance, thus a greater likelihood to reach the forest floor unobstructed from the point of initial impact. Once the pod reaches the forest floor, the tether can be pulled to release the perched quadrotor from its branch.

The prototype platform is able to demonstrate the use of perching to deploy large acoustic sensors in the forest canopy. The use of the quadrotor battery as the power source of the sensor greatly increases the endurance, maximising the amount of data collected per flight. Overall, the proposed concept shows that we can produce affordable robots to aid ecologists in sensing difficult-to-access environments.

7.2 Results

7.2.1 Hardware design

Perching

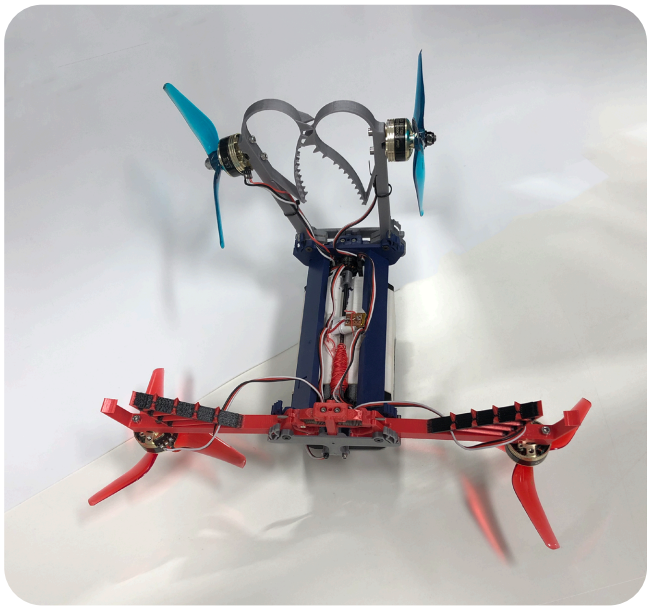


Figure 7.1: **Prototype passive perching platform**. The top view of the robot shows the front arms (teal) in a perched state, and the back arms (red) in the flying configuration.

The morphing quadrotor arms are hinged about their root. Their downward folding motion is restricted by the ratchet locking pin. In flight, the arms are held in place by the cam-follower and the spring-slider at the top of the cam tracks. In this configuration, the spring-slider's springs are fully retracted and compressed by the cam-follower to the end of the mechanism's travel. Thus the mechanism acts like a rigid bar between the two arms, holding the arms firmly in place for flight. In this section, the cam tracks have a neutral pressure angle. This ensures that the forces from the rotors and any minor contacts on the spring-slider would not dislodge it from its flight configuration, prematurely morphing the robot.

As impact pushes the spring-slider past the neutral pressure angle section, it reaches a negative pressure angle section and allows the arms to rotate. As the arms rotate by their momentum and the thrust from the rotors, the cam track, which is integrated into the arm, also rotates to create a more negative pressure angle on the follower. The spring-slider will continue downwards under the cam-followers' spring tension until a neutral point is reached and the arms grip the branch.

The geometry of the morphing arm cam track can be dimensioned to match a desired dynamic state at impact. Here I assume the mass of the spring-slider to be negligible. Initially, the resistive force along the vertical cam tracks is purely friction

$$F = \frac{\mu T L}{y} \tag{7.1}$$

where μ is the friction coefficient between the cam-track and the cam-follower, T the thrust

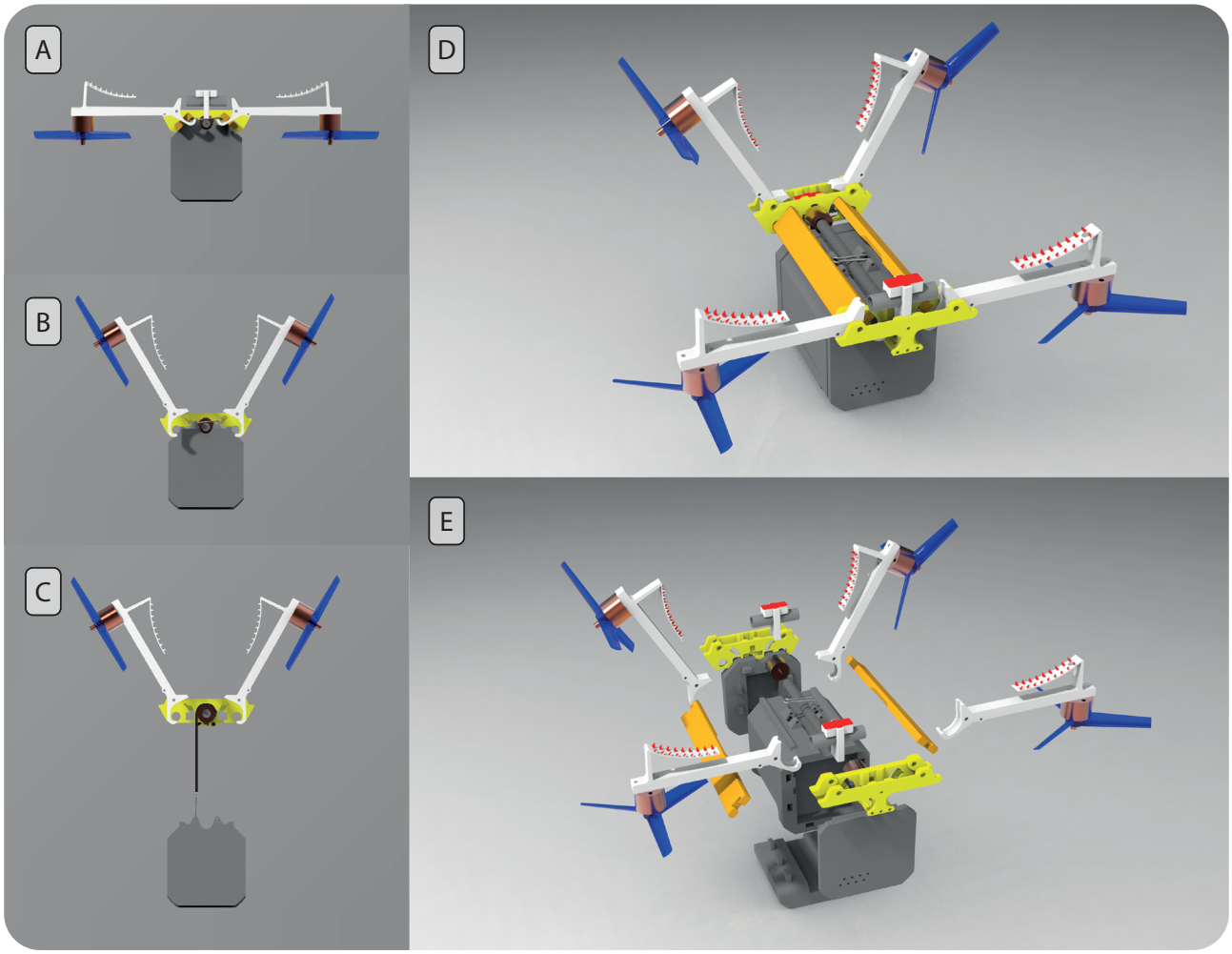


Figure 7.2: **Rendered drawings of the prototype platform**. (**A**) Side view of the robot in flight configuration. (**B**) Side view of the robot perched. (**C**) Side view of the perched robot deploying the pod. (**D**) The assembled robot with the far side set of arms in perching configuration. (**E**) Exploded view of the robot.

from the rotor, L the length of the arm from the rotor to the hinge, and y is the height of the cam-follower relative to the hinge. The work done by friction is

$$W = \int_{y_{\text{top}}}^{y_{\text{rot}}} \mu T L \frac{1}{y} dy = \mu T L \ln \frac{y_{\text{rot}}}{y_{\text{top}}} \tag{7.2}$$

with y_{top} denoting the initial height of the cam-track's vertical section and y_{rot} is the height where the arms are free to rotate. Note that the perching manoeuvre is bounded by two extremes. If the robot has sufficient kinetic energy to overcome the work done by friction, the rotors can be turned off prior to impact. On the other hand, if the quadrotor robot is in a

hover prior to impact, thrust from the rotors must overcome the friction forces and the weight of the robot in order to activate the perching mechanism. Assuming all rotors are providing equal thrust, the thrust from one rotor is

$$T \geq F + \frac{mg}{n_{\text{rotor}}} \tag{7.3}$$

$$T \geq \frac{\mu T L}{y} + \frac{mg}{n_{\text{rotor}}} \tag{7.4}$$

$$T(1 - \frac{\mu L}{y}) \geq \frac{mg}{n_{\text{rotor}}} \tag{7.5}$$

$$n_{\text{rotor}} T \geq \frac{mg}{1 - \frac{\mu L}{y}} \tag{7.6}$$

with n_{rotor} denoting the total number of rotors; for the prototype quadrotor, $n_{\text{rotor}} = 4$. As $y \to \infty$, we get $n_{\text{rotor}} T > mg$, describing that the total thrust must be more than the weight. But as the total thrust must be positive for the hovering robot to ascend and perch,

$$1 - \frac{\mu L}{y} > 0 \tag{7.7}$$

$$\mu < \frac{y}{L} \tag{7.8}$$

the material properties of the cam-track and the cam-follower are determined by the geometry of the design. And with $y_1 < y_t$,

$$\mu_{\max} < \frac{y_1}{L} \tag{7.9}$$

Pod release

The platform is designed to ensure the safe retrieval of eco-acoustic data. A sky-crane-style, passively damped wrench system is implemented, both to lock the pod onto the quadrotor and to reduce the force of the pod's eventual ground impact. The wrench system is formed of a carbon fibre rod through the front-to-back centre of the platform. The rod is mounted to a small brushless DC (BLDC) motor on each end. The motors are mounted to the quadrotor frame. The three phases of the BLDC motors are connected together to provide magnetic

damping.

7.2.2 Electronics

Idle mode circuit design

Often not considered in the design of aerial robots is the idle power draw. This is reasonable considering the power required for flight is magnitudes higher than the idle power. However, in a long-duration perching scenario, the idle power of the flight subsystem electronics is scaled by days, rather than minutes. The resulting battery consumption of the Flight Controller (FC) and the motor Electronic Speed Controller (ESC) is significant, thus they must be reduced. The mission payload, an acoustic data recorder, and the AudioMoth (Moth) also require power to function [195]. Therefore, to maximise the length of which the AudioMoth can record, I reduced the idle power draw by using a novel electronics architecture (Fig.7.3A).

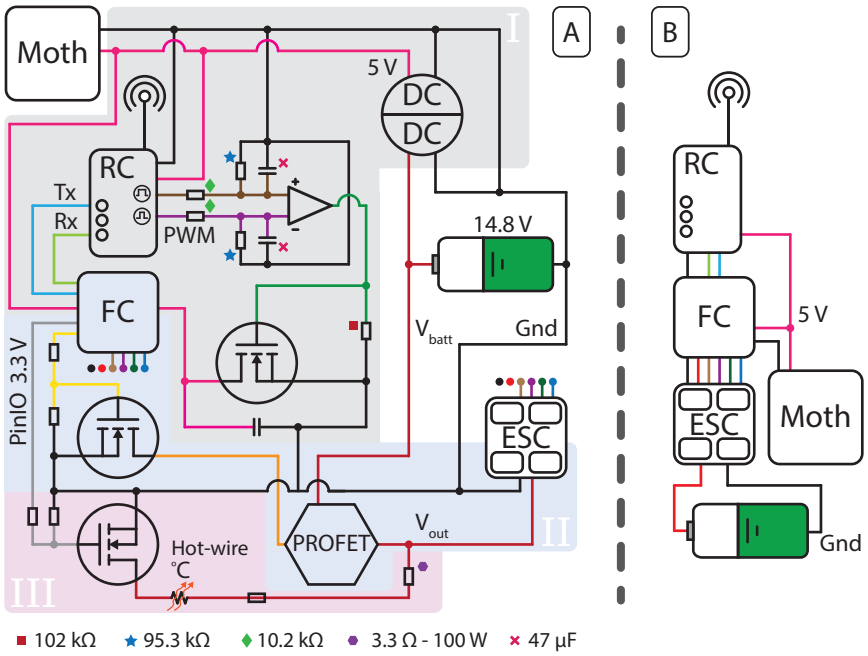


Figure 7.3: **Electronics diagrams** of (**A**) the novel 3-stage circuit compared to (**B**) a conventional approach. The proposed circuit design switches on the FC, ESC, and the pod release hot-wire in a hierarchical sequence. This design ensures that Stage III (red) cannot be triggered without Stage II (blue) and Stage I (grey) turned on, and Stage II without Stage I on. This prevents the operator from accidentally turning on increasingly more dangerous components on the robot.

Our novel electronics architecture is constructed around a Team BlackSheep (TBS) Tracer radio system. The TBS Tracer utilises a lightweight RC receiver that is able to send Pulse Width Modulation (PWM) signals from break-out ports separate from the TX/RX channels connected to the FC. A standalone DC-DC converter powers the RC receiver and the AudioMoth continuously from the battery. This setup allows the receiver PWM to operate a switch, turning on and off the FC. Once the FC is powered, we can operate its pin output signal to turn on the ESC via a BTS50055-1TMA high-current power switch.

However, the duty cycle is limited between $5\% - 10\%$ at $3.3V$ logic level. While the RC PWM is able to operate an IRLL024Z N-channel enhancement mode MOSFET like a switch to turn on and off the FC, it cannot hold the switch in a constant on/off state. A filtering circuit is used to smooth the pulsing PWM into a constant signal.

Two problems were noted for this approach. First, the smoothed signal voltage cannot exceed the PWM logic level. A simple approximation of averaging the signal voltage over time yields a smoothed voltage of $0.33V$ at high and $0.16V$ when low. This issue may be solved by selecting low threshold voltage MOSFETs. However, this leads to the second problem. Lower threshold voltage MOSFETs typically have lower maximum current. In Matlab-Simulink simulations and in physical testing, the ALD212902 MOSFET, with a gate-source threshold voltage of $0.20V$, is unable to power the FC. I suspect this to be related to having a low gate-source overdrive voltage, so the MOSFET is operating within the sub-threshold bounds. Therefore, while the MOSFET is conducting at a filtered high signal, the current flow is restricted and insufficient to power the FC.

Our design circumvents these problems by utilizing an Op-Amp comparator to boost the difference between two RC PWM channels (Fig.7.3A). Both PWM signals are smoothed, like before. But with one channel permanently at low, the comparator changes its output from $0V$ to $5V$ depending on the signal on the active PWM channel. The output from the Op-Amp provides sufficient overdrive voltage to toggle the IRLL024Z MOSFET as a simple switch. The circuit is simulated in MATLAB-Simulink to fine-tune the filtering resistors and capacitors according to the available stocks (Fig.7.4).

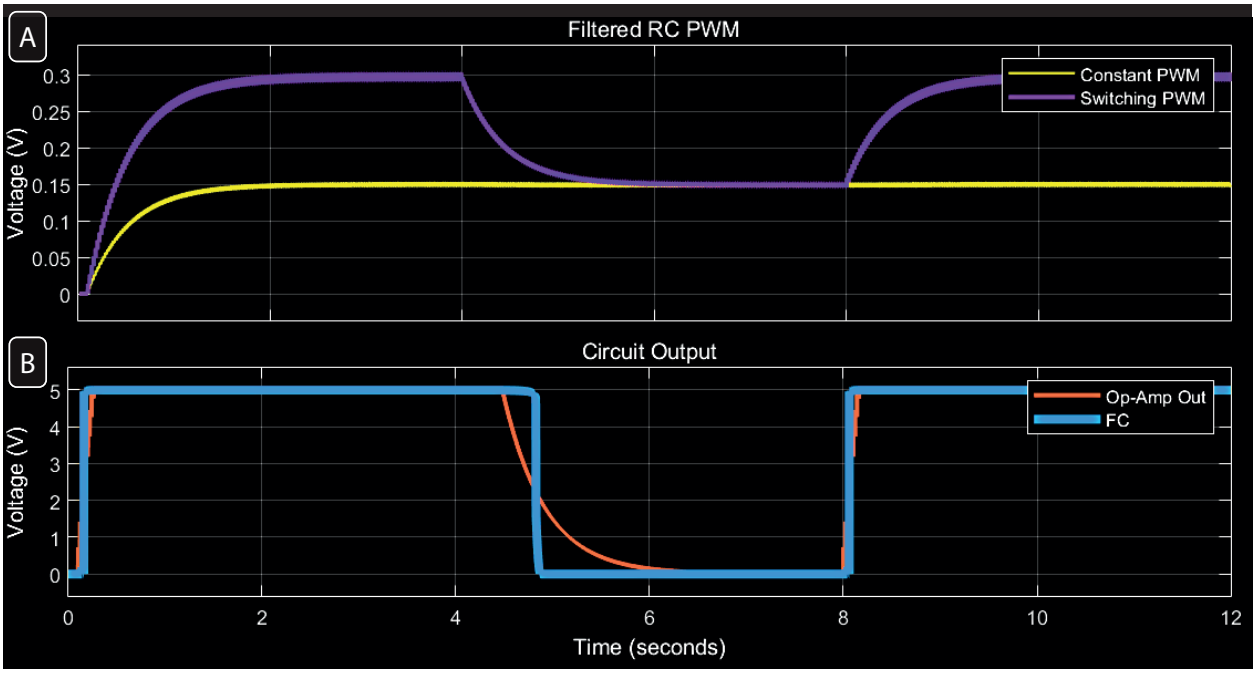


Figure 7.4: **A simulation of the Op-Amp signal comparator booster circuit in MATLAB-Simulink**. (**A**) displays the filtered PWM signals from the TBS Tracer RC receiver. The comparator compares a user-controlled channel (purple) to a constant low PWM (yellow). (**B**) shows the output from the Op-Amp (orange) successfully switching the flight controller on/off MOSFET (blue).

Pod release mechanism circuit design

The latch of the pod release mechanism is held by a thin polyethylene (PE) thread. To release the latch, the PE thread is melted by a hot wire. The hot-wire is connected to a $100W$ resistor and a IRLL024Z MOSFET in series (Fig.7.3A). The resistor limits the current draw of the hot-wire circuit below the MOSFET's maximum rating. The circuit is connected to the ESC power switch on the high side, and the MOSFET on the low side to minimize the likelihood of control errors unexpectedly releasing the latch.

To break the hot-wire circuit passively when the latch is properly released, I designed a novel latch mechanism with a mechanical fuse which is collectively named the Latch Unlock Cut-off Apparatus (LUCA). The LUCA's mechanical fuse is contained within the latch and it separates from its high-side connector when the latch is released, physically breaking the circuit.

7.2.3 Numerical assessment

Passively morphing a quadrotor has been shown to be effective in fitting it through narrow gaps [117]. To aid the design and sizing of the robot, the benefit of morphing to pass through canopy openings is statistically quantified. I approximate the canopy opening as a circle and the robot in its flying state, the arms contracted configuration, and the pod as rectangles. The test applies the simple logic as shown in Al.4 across various sizes of canopy openings.

Algorithm 4: Probability of the robot becoming stuck when coming down from a canopy opening

```
create normally distributed random radius from the centre of the canopy opening r;
create uniformly distributed random radial orientation θ;
create uniformly distributed random 3D unit vector a;
create normally distributed random rotation b;
create quaternion p = [cos(b)/2, v · sin(b)/2];
for i from 1 to 4 do
    rotate corner i by quaternion p;
    shift corner i by x and y offset [r cos θ, r sin θ];
    if corner i (x_i + y_i)^2 > R^2 then
        corner did not drop through the canopy opening, the corner is stuck;
    end
end
if more than 2 corner is stuck then
    The platform is stuck;
end
```

The variance of the normal distribution would depend on variations of the bodies' centre of gravity, winds, and minor bumps against leaves and small branches. But as shown in Fig. 7.5, it is clear that a significant margin of safety can be gained by deploying the pod. Note that the successful descent of the pod and the morphed drone are not truly independent as the user can affect the trajectory of the morphed drone by pulling on the tether from the drone to the pod at an angle to vertical.

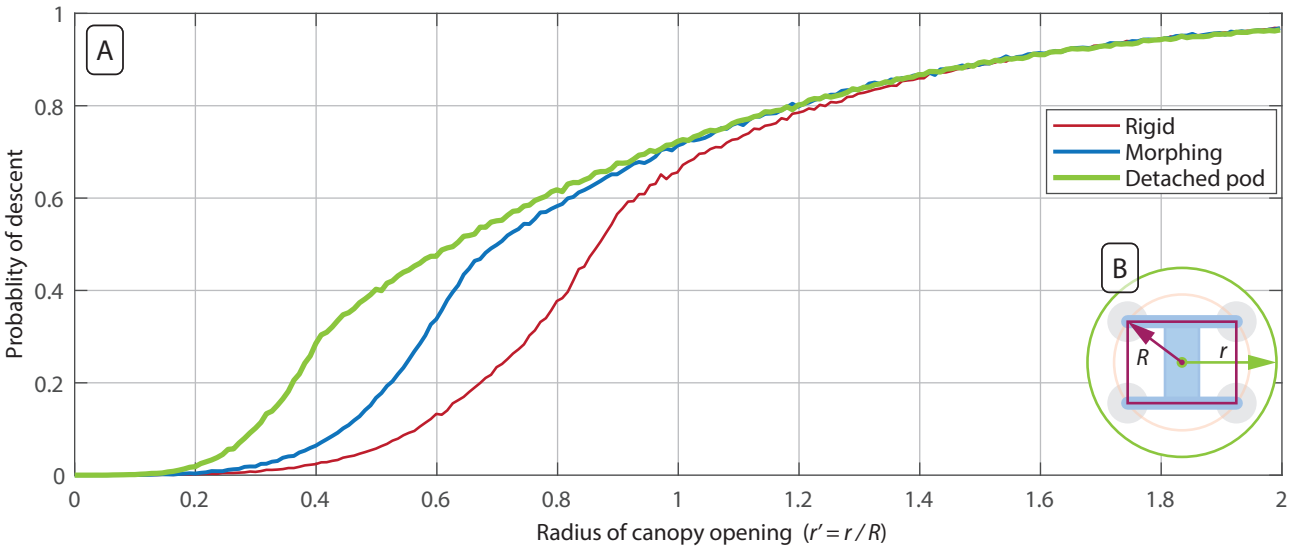


Figure 7.5: **Estimated probability of free-falling through a canopy opening**. (**A**) The most significant differences in probabilities are obtained between $0.4 < r' < 0.7$. (**B**) The radius of canopy opening is non-dimensionalised relative to the distance from the centre of the rigid platform to its rotor.

7.3 Discussion

This chapter explored the viability of using impact-driven semi-passive morphing to perch on branches within the forest canopy. The benefit of increased probabilities of the drone dropping through a canopy opening upon retrieval, as a result of body separation and arms folding, is also numerically demonstrated. To reduce the idling power draw when the drone is perched, I created a novel electronics system architecture that is capable of switching on and off the high-power quadrotor with two very low-duty cycle PWM signals. This is verified in simulation.

While the prototype is functional, its boundary of operation is not experimentally defined. There are two reasons for the need to quantify the perching performance. First, it is reasonable to presume that the perching performance is affected by factors such as the tree branch density, canopy height, branch diameter and orientation, and the surface characteristics of the tree bark. Understanding these limitations inevitably leads to better robot designs. Secondly, quantifying these variables in the field allows for the optimisation of the perch location. This avoids the needless trial-and-error to perch the robot if the conditions are not favourable.

Characterising the perching environment may take the form of 3D maps or other advanced

metrics. The canopy density, measured by over-canopy or upward-looking sensors, is a potential indicator [196]. However, to the author's knowledge, there are no studies correlating the canopy density to any tree branch properties for perching or sensor deployment. Setting up an upwards-pointing camera on the drone could allow for means of quantifying the canopy characteristics and with further advancements a method to semi-autonomously perch [159].

Results from the analytical model hints at other potential uses of the base design. (7.9) seems to indicate that, with a simple actuator to modulate the relative geometries, we can control the rigidity of passive gripping mechanisms. For example, we may be able to toggle between a rigid protective structure and a morphing structure for interactive tasks.

Chapter 8

Design and Testing of Single-Part Assembly Metamorphic Aerial Robots

Manufacturing drones in remote locations create design problems that are often overlooked. The lack of logistics means limited tooling and waste disposal, and reduced stock of commonly available parts, such as fasteners and adhesives. Compact and low-cost desktop Fused Filament Fabrication (FFF) Three dimensional (3D) printers mitigate the tooling limitation by directly manufacturing the component. FFF printers, barring limited exceptions, deposit material in layers. Depositing material in layers leads to anisotropic strength and surface finish; the part is much weaker between the layers in the Z direction. While desktop 3D printers are not able to reach the next milestone of additive manufacturing, the production of 3D isotropic unibody designs, their ability to create strong and high-fidelity parts in the XY plane is often undervalued. By utilising metamorphic design as a method to simplify assembly, I present a pop-up unibody quadrotor frame design which generates minimal waste during fabrication while maximising the structural strength. The resulting $100g$ prototype is tested indoors with an offboard autonomous flight system, and shown to be robust in outdoor environments.

8.1 Introduction

Multirotor Unmanned Aerial Vehicles (UAV) operation in remote locations, such as monitoring rainforests, brings extreme challenges not faced by current robots. Often cited problems are flight endurance, flight safety, and spatial constraints.

Endurance can be improved with direct means to increase flight time, such as weight-saving designs, the use of structural power materials [197], or energy harvesting [198]. Flight safety, similarly, can be both improved and mitigated. From full-body encasing cages to impact resilient quadrotor frames, designs of protective frames are wide-ranging [199].

However, these are solely problems associated with the robot during operation, few have addressed the issue with logistics of operating in remote locations. These problems are the repair, acquisition of replacement parts, and the overall cost of maintenance. More specifically, the cost of maintenance includes the need for expertise, man-hour, as well as transport costs.

3D printing on-site has shown promise in its adaptability. In combination with a lack of need for specialised tooling, 3D printable designs can be rapidly modified and manufactured. This is highly beneficial for low-volume, high-variability production runs, such as building drones in remote locations.

Fused Filament Fabrication (FFF), although widely marketed as "3D printing", while true in geometric terms, is somewhat misguiding. With FFF, the most popular form of additive manufacturing, the need to "print" in layers creates highly anisotropic parts, in strength, geometric fidelity, and finishing [200]. There is significant interest in improving the layer adhesion by additional material processes, such as the post-build crosslinking of embedded particles or localised preheating of the deposited layer [201, 202]. Printing with limited depth gradient to create 3D layers also partially mitigates the anisotropy [203, 204]. Thus, FFF may be referred to as 2.5D in reference to the resultant part's anisotropic characteristics. With the research into true 3D additive manufacturing ongoing, one could also take exploit the unique properties of current 2.5D FFF capabilities [205].

In this chapter, I explore 2.5D manufacturing by extending 2D design ideas, such as metal sheet bending, origami, and kirigami [206]. Unconstrained from uniform depth, we can create Single-

Part Assembly (SPA) with both greater complexity in design and simplicity in geometry [207, 208]. This, coupled with a shorter build time in the horizontal directions and minimal post-processing of SPA, makes this approach of interest for application on Nano- to Micro-scaled Aerial Vehicles (NAV/MAV).

8.2 The Structural Forces of Rotation

Following the calculations and notation established in Chapter 3 The total angular momentum of the rotor is

$$\hat{L}_r = \hat{L}_{\text{tilt}} + \hat{L}_{\text{spin}} \tag{8.1}$$

$$= (I + M_r h_r^2)\Omega_t \hat{t} + I_r \omega \hat{r} \tag{8.2}$$

where $[\hat{r}, \hat{t}, \hat{p}]$ are the Cartesian unit vectors with $\hat{r}$ denoting the rotor spin axis thus it varies over time. $\hat{t}$ represents the unit vector in the opposite direction of the force applied on the rotor and is therefore stationary. The third unit vector $\hat{p}$ lies on the plane of precession and is orthogonal to $\hat{r}$ and $\hat{p}$.

Assuming constant ω and initial $\Omega_t = 0$, a torque τ applied to the system will yield

$$\tau = \frac{dL_r}{dt} \tag{8.3}$$

$$= (I + M_r h_r^2)(\frac{d\Omega_t}{t}\hat{t} + \Omega_t \frac{d\hat{t}}{dt}) + I_r(\frac{d\omega}{dt}\hat{r} + \omega \frac{d\hat{r}}{dt}) \tag{8.4}$$

and as $\hat{t}$ is held constant by the torque, thus $\frac{d\hat{t}}{dt} = 0$. The change of spin axis orientation $d\hat{r}$ is equal to the change of tilt angle about $\hat{t}$ but in the direction of $\hat{p}$ such that $\frac{d\hat{r}}{dt} = \frac{d\theta_t}{dt}\hat{p} = \Omega_t \hat{p}$. (8.4) simplifies to

$$\hat{\tau} = (I + M_r h_r^2)\dot{\Omega}_t \hat{t} + I_r \omega \Omega_t \hat{p} \tag{8.5}$$

Noting that the quadrotor is an unconstrained free body when in flight, to derive the forces of rigid body motion on the quadrotor arm, we take the rotor frame of reference (Fig.8.1). To

convert the angular rate to the rate of precession

$$\tan\alpha = -\arctan(\cos\gamma\tan\phi) \tag{8.6}$$

$$\tan\beta = \arctan(\sin\gamma\tan\phi) \tag{8.7}$$

$$\gamma = -\arctan\frac{\tan\beta}{\tan\alpha} \tag{8.8}$$

$$\phi = -\arctan\left(\tan\alpha\sqrt{\frac{\tan^2\beta}{\tan^2\alpha}+1}\right) \tag{8.9}$$

$$\tag{8.10}$$

Alternatively, we can derive the angular rate

$$\dot{\alpha} = \frac{\dot{\gamma}\sin\gamma\tan\phi - \cos\gamma\dot{\phi}\sec^2\phi}{\cos^2\gamma\tan^2\phi+1} \tag{8.11}$$

$$\dot{\beta} = \frac{\dot{\gamma}\cos\gamma\tan\phi + \sin\gamma\dot{\phi}\sec^2\phi}{\sin^2\gamma\tan^2\phi+1} \tag{8.12}$$

and as the coordinate system rotates with the rotor, $\phi \equiv 0$, thus

$$\dot{\alpha} = -\dot{\phi}\cos\gamma \tag{8.13}$$

$$\dot{\beta} = \dot{\phi}\sin\gamma \tag{8.14}$$

$$\dot{\phi} = \sqrt{\dot{\alpha}^2+\dot{\beta}^2} \tag{8.15}$$

$$\dot{\phi}\ddot{\phi} = \dot{\alpha}\ddot{\alpha} + \dot{\beta}\ddot{\beta} \tag{8.16}$$

$$\ddot{\phi} = \ddot{\beta}\sin\gamma - \ddot{\alpha}\cos\gamma \tag{8.17}$$

With the rotation matrix

$$\mathbf{R} = \begin{bmatrix} \cos\gamma & \sin\gamma & 0 \\ -\sin\gamma & \cos\gamma & 0 \\ 0 & 0 & 1 \end{bmatrix} \tag{8.18}$$

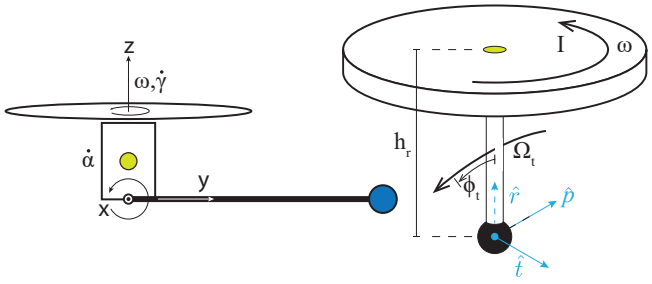


Figure 8.1: **Rotor frame of reference** with the rotor centre of mass in yellow, the multirotor centre of mass in blue.

we can map $\hat{\tau}$ to quadrotor arm coordinates x, y, z

$$\begin{bmatrix} \tau_x \\ \tau_y \\ \tau_z \end{bmatrix} = \mathbf{R} \begin{bmatrix} (I + mh_r^2)\dot{\Omega}_t \\ I_r \omega \Omega_t \\ I_r(\dot{\omega} + \ddot{\gamma}) + k_D(\omega + \dot{\gamma})^2 \end{bmatrix} \tag{8.19}$$

where k_D is the rotor drag coefficient. As $\Omega_t = \dot{\phi}$

$$\begin{bmatrix} \tau_x \\ \tau_y \\ \tau_z \end{bmatrix} = \mathbf{R} \begin{bmatrix} (I + mh_r^2)(\ddot{\beta}\sin\gamma - \ddot{\alpha}\cos\gamma) \\ I_r \omega(\sqrt{\dot{\alpha}^2 + \dot{\beta}^2}) \\ I_r(\dot{\omega} + \ddot{\gamma}) + k_D(\omega + \dot{\gamma})^2 \end{bmatrix} \tag{8.20}$$

Further accounting for the linear forces

$$\begin{bmatrix} F_x \\ F_y \\ F_z \end{bmatrix} = \begin{bmatrix} m\ddot{x} \\ m\ddot{y} \\ m\ddot{z} + k_L\omega^2 \end{bmatrix} \tag{8.21}$$

$$\begin{bmatrix} \ddot{x} \\ \ddot{y} \\ \ddot{z} \end{bmatrix} = \begin{bmatrix} \ddot{X} + l\ddot{\gamma}_B \\ \ddot{Y} \\ \ddot{Z} - \ddot{\alpha}_B \end{bmatrix} \tag{8.22}$$

and the torque due to the offset rotor CG in the z-axis

$$\tau_y' = -mh_r\ddot{x} = -mh_r(\ddot{X} + l\ddot{\gamma}_B) \tag{8.23}$$

F denotes the forces applied on the structure at the tip of the quadrotor arm where the rotor is joint, $\ddot{X}, \ddot{Y}, \ddot{Z}$ are the linear accelerations of the platform measured at its CG, l the length of the arm, and k_L the rotor coefficient of lift. To minimise the forces on the arm, we should aim to place the rotor as close to the length-wise centroid axis as possible whiles minimising the arm length.

8.3 Design

8.3.1 Materials

The selection of material is critical to the properties and the design of the flexure joints. Both the elastic and plastic phases of the material are harnessed to form temporary and permanent morphologies respectively. There are also scenarios where a slight resistive force is desired to pre-load the structure. Thus a combination of design for elastic and plastic deformation is required. The various joints used on the prototype quadrotor are described in Tab. 8.1.

Table 8.1: The role of elastic and plastic deformation in the design of the prototype quadrotor

Item	Elastic	Plastic	Role
FC retention springs	✓	✗	Must ensure the material does not deform plastically during the operation of the spring
Core structure folds	✗	✓	To maintain the natural deformed shape without other constraints
Motor clamp	✓	✗	Fully actuated within the elastic regime to allow repeated swapping of motors
Battery bay	✓	✓	Need to retain folded shape but also apply tension to restrain the battery

8.3.2 Methodology

To create folds in the structure, I utilised compliant mechanisms [209]. The compliant mechanism's flexure joints are simple to manufacture and mitigate the need for part clearance, unlike

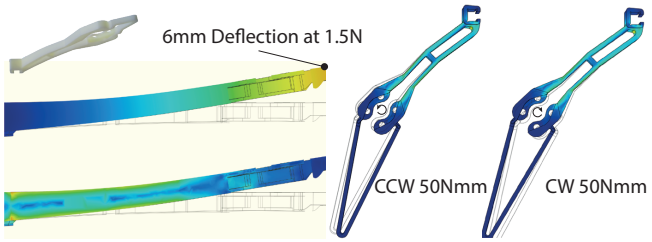


Figure 8.2: **Finite element analysis of the quadrotor arm** when under maximum thrust (left) and torque (right). Common PETG properties were used. This shows that the motor will be secure under all flight conditions. The finalised prototype used a chopped carbon-fibre-filled nylon composite which is stiffer and stronger.

conventional revolute joints. To fully realise a single-part assembly quadrotor structure, a number of static and dynamic mechanisms were used. Finite element analysis is used to ensure the final structure can withstand the forces of drone flight (Fig. 8.2).

Out-of-plane flexure

To fold the structure away from the printer plane, a simple flexure joint is formed from a thin strip of material. This is akin to a "mountain" or "valley" fold in origami. For optimal quality, these joints are printed directly on the print bed. The walls of the "valley" fold are chamfered to ensure clearance.

In-plane flexure

Folding within the printer plane To enable folding within the printer plane, a thin line of material is used to create a simple compliant joint.

Fasteners

Standard quadrotor power train components conventionally necessitate the use of fasteners. To mitigate the need for separate fasteners, the component interfaces were replaced with single-part mechanisms, designed to harness the compliance/elasticity of the material.

Due to the limited capabilities of Brushless DC motors (BLDC) to generate torque, the stiffness of the structure in the printer plane can be minimal. Thus, a "clamp-on" rotor mounting system

was implemented. A twin-boom quadrotor arm acts as a compressive leaf spring in the planar direction, locking the rotor in place. However, it was noted that opening in a non-parallel "V" configuration resulted in difficulty when mounting the rotor. By adding another "V" shaped spring, the rotor clamps opened evenly, allowing secure fastening and easier assembly (Fig. 8.2).

The mini-quadrotor community is currently standardised on a $30.5 \times 30.5mm$ M3 screw mounting pattern for some onboard electronics, namely the Flight Controller (FC). To ensure a safe and stable flight, the FC must be securely mounted to the platform. A spring-loaded design was conceived to replace the M3 screw mount (Fig. 8.3D), the friction and the slight spring pressure angle were tested to be sufficient to resist vibrations during flight.

Compound folds

For more complex geometries, a few simple folds can be combined to form the desired end morphology. This is required for the prototype quadrotor. The interference of the upper payload attachment pylons dictates that the core substructure must be offset to achieve the FC mounting pattern when folded (Fig. 8.3B and C).

The resulting compound fold features a single 90° valley fold and two parallel in-plane folds. This forms a four-bar linkage that resists any in-plane torsion. The stiffness of the valley fold and the FC board post-assembly, likewise, resist the out-of-plane torsion but also in-plane shear. Regardless, the shear force is insignificant for these lightweight quadrotors during free flight.

Bridging and underpasses

The unique ability of FFF to allow limited fabrication of overhangs without support differentiates 2.5D design from sheet material manufacturing. Overpasses and underpasses can be created without additional joining processes.

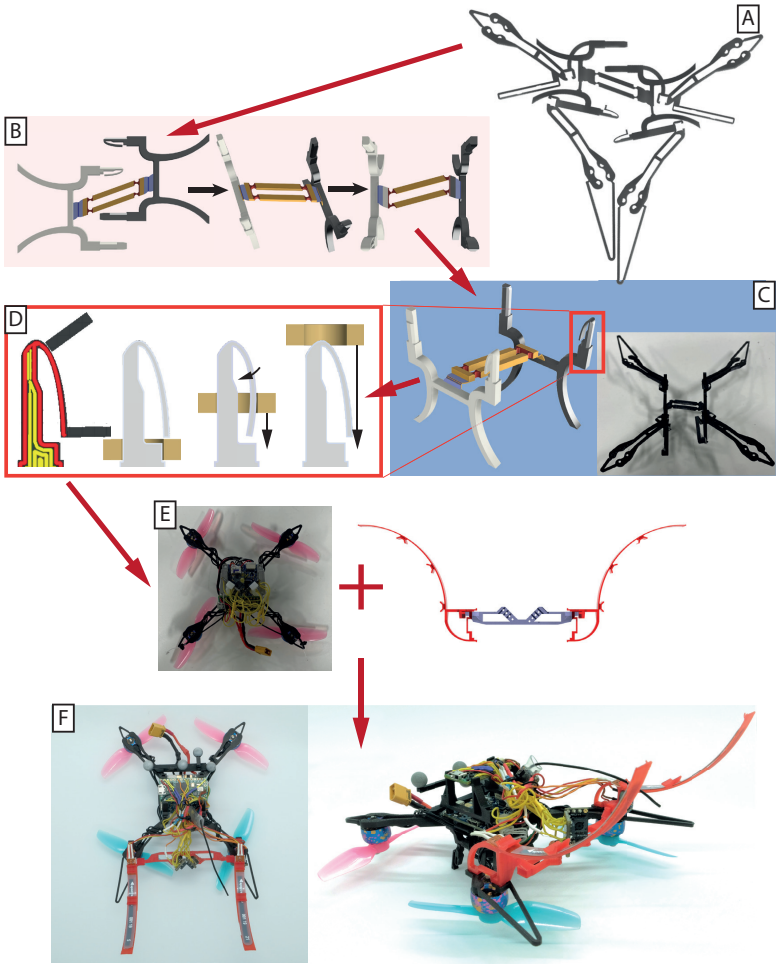


Figure 8.3: **The assembly drawings of the single-part assembly metamorphic quadrotor**. (**A**) The flat-pack 3D printed drone frame. (**B**) The parallel cross beams are bent into their final positions with plastic deformation. (**C**) The arms are then slotted into the vertical posts. (**D**) the Flight Controller (FC) is pressed into the posts, the springs will index and keep the FC secure. (**E**) The frame with the rotors clipped onto the arms, and the surface interaction antenna module. (**F**) Photographs of the assembled drone.

Out-of-plane four bar linkage

The battery bay is constructed with two out-of-plane four-bar linkages, one on each rear arm. The mechanism features a valley fold and a suspended mountain fold on each of the two parallel members. The two members are rigidly linked at both ends. During assembly, the mechanism is folded into a rectangle. The combination of elastic and plastic deformation will allow the mechanism to restrain the battery adequately during violent flight manoeuvres.

Therefore, the interior dimensions must be properly sized to fit the battery (Fig.8.4). The

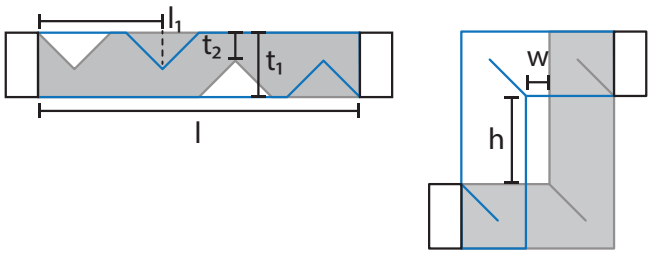


Figure 8.4: Side view diagrams of the four-bar linkage compliant mechanism as printed (left) and folded (right). The two parallel members are blue and shaded grey.

design dimensions of the printed parts, length of the member l and the distance, corresponding to the width, from the edge of the folding member to the middle of the fold l_1, are approximately

$$l = w + h + 4t_1 - t_2 \tag{8.24}$$

$$l_1 = w + 2t_1 - t_2 \tag{8.25}$$

where w and h are the width and the height of the battery respectively, t_1 is the thickness of the members, and t_2 is the thickness of the compliant joint. This approximation assumes that the material can deform plastically about a singular point. For the construction of the prototype, due to the variability of the battery dimension, trial and error determined the final battery bay geometry.

8.4 Testing of Lightweight Prototype Robots

With all novel robotic designs, live testing is often the hardest hurdle in the developmental process to overcome. While novel software can be implemented with a more established control architecture that can intervene and prevent accidents [210], prototype hardware is not afforded such luxuries. Structural and aerodynamic models and simulations can, to an extent, infer the airworthiness of the robot. However, this is not guaranteed, and most analytical and numerical models need real data to calibrate their parameters to give accurate results. Therefore, live testing of an unverified, uncertified robot is a necessary step.

For aerial robots, the velocities that an uncontrolled prototype can reach during live testing

means there is a significant amount of risk of damage to itself and its surroundings. Therefore, it is beneficial for the prototype robot at initial flight testing to have a minimal cost loadout—a configuration that does not contain costly components such as onboard computers and sensor arrays. As the onboard computer is used for onboard autonomous flight, and manual flight testing for non-convention aerial robots is not possible, a method of offboard autonomous flight must be used. And as the finalised prototype robot would have the onboard computer mounted, it is helpful to be able to transfer the controller created and tuned offboard to the onboard computer for onboard autonomous flight.

I devised an offboard control experimental environment for aerial robots to the requirements above. As all multirotor platforms mandate the use of RC control, I used the RC radio to broadcast the command signals. Aerial robots are mostly controlled by the roll and pitch angle or angular rate, yaw angular rate, and thrust, but they can also contain other commands mapped to the available RC channels. By using RC to send roll and pitch angles, yaw rate, and thrust level, the offboard controller should be no different to a manual pilot. The high-level controllers, which are controlling the robot's position and/or velocity, are integrated within the Robot Operating System (ROS-I) [211, 212]; the odometry is feedback through VICON™ motion capture. This control architecture, appropriately named "ROS-RC", enables the testing of the robot at the minimum specification for flight, without needing to integrate onboard computing or robot-to-ground station communication (Fig. 8.5).

The ROS-RC, being fully off-board, can be run independently alongside the onboard control system. This independent dual-control architecture adds a layer of redundancy. The offboard controller would overrule the onboard controller should the robot's behaviour exceed any boundary thresholds, such as a geofence. Offboarding the controller also helps to debug errors and harness the increased computing power to compile the code faster, increasing the rate of software prototyping. Overall, the ROS-RC architecture provides a minimalistic "first step" indoor autonomous flight solution to test experimental aerial platforms.

8.4.1 Autonomous control system architecture

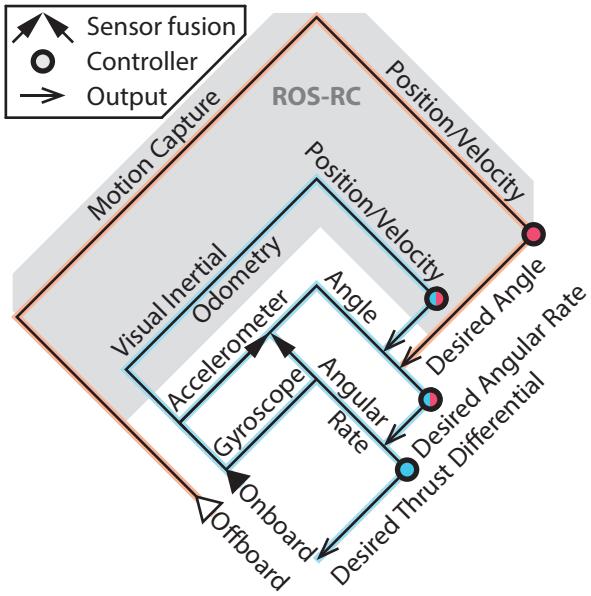


Figure 8.5: **The ROS-RC control architecture**. The blue paths denote onboard sensors and onboard computed odometry. The blue-filled circles are onboard controllers, and red denotes offboard. The grey block indicates the ROS-RC system—angle and angular rate control are handled by the Flight Controller (FC). The user can choose between using motion capture or onboard Visual Inertial Odometry (VIO) for position/velocity control. The user can also send the position odometry to an offboard controller. Note that the total thrust is controlled by the ROS-RC but it is not shown in this figure.

The ROS-RC has a cascaded controller architecture—each level of control, from angular rate to position, is handled by a nested feedback controller (Fig. 8.5). Much like a human pilot flying a quadrotor drone, the angular rate and angle controllers—which in this thesis are considered the low-level controllers—require high sampling frequencies with minimal delay and are therefore implemented on the onboard Flight Controller (FC). While other types of controllers have been tried [20], all current open-sourced FC firmwares use the Proportional Integral Derivative Controller (PID) controller for its lightweight computation and simple tuning process.

The high-level controllers, for velocity and position, can be sampled and controlled at lower frequencies as they do not affect the drone's flight stability. Thus, the high-level controllers can be implemented offboard. Having the high-level controllers offboard offers a range of benefits. The computation for the controller can be done on more powerful ground computers, affording the use of more complex control and path-planning algorithms. The Wi-Fi on single-board computers, commonly used on small aerial robots to transmit odometry data, can be low. This adds design considerations such as adding antennas and/or component placement to avoid signal blockage. RC radio has a longer wavelength, thus it is more penetrative and more reliable. Using ROS-RC is therefore safer for a prototype drone.

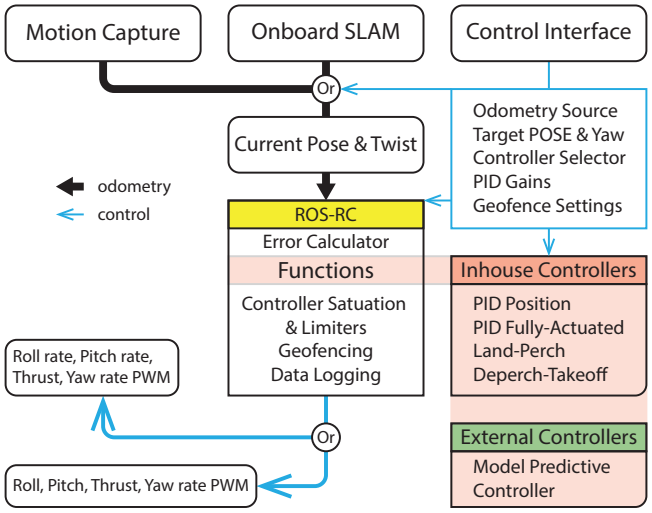


Figure 8.6: **The internal architecture of the ROS-RC** offboard autonomous flight system. The Functions block is free for the user to modify without hindering safety as the Geofence can shut down the robot or take over control.

The ROS-RC takes the odometry data from motion capture or the VIO/SLAM camera onboard (Fig. 8.6). From the user input, the ROS-RC will calculate the associated error and pass this to the user-selected controller. The various controllers are coded as functions within the ROS-RC node; they are selected via a switch function. Given the error and gain inputs, the controllers output the RC value to be transmitted—the output commands are quantised to integers within the controller. The RC commands are then processed through limiters to ensure that they are within the upper and lower bounds of the sensible values. The processed RC commands are sent to a microcontroller via a serial link. The microcontroller converts the commands into Combined Pulse Position Modulation (CPPM) and feeds them to the RC transmitter.

The system can also adapt to other open-sourced controllers. For example, when running a Model Predictive Controller (MPC) which requires both position and velocity commands, the high-level commands are broadcasted to the MPC node which will output the RC commands. The ROS-RC has been shown to be simple to adopt and highly adaptive; the ROS-RC was implemented on aerial robots featured in Chapter 2, 6, 8, and further demonstrated in [133] and [206].

8.5 Discussion

Using metamorphic design, I created a fastener-less single-part quadrotor that is additively manufactured using desktop 3D Fused Filament Fabrication (FFF) printers (Fig.8.3). By leveraging compliant mechanisms with both elastically and plastically deformable elements, the $100g$ quadrotor can be manufactured in under 3 hours. With no support structure, no waste material is generated during the fabrication of the structure. The printed structure weighs $7.2g$ and is shown to be sufficiently rigid for stable flight (Fig. 8.7). I further demonstrate indoor autonomous flight using an offboard control system.

The low setup cost of manufacturing also allows efficient customisation of the airframe, exemplified by the integration of flex sensor whiskers. The attachment port on the quadrotor arms allows additional modules, with the module also designed to add to the overall stiffness of the structure.

However, larger aerial robots require greater rigidity. Thus, they must use carbon fibre composites and metallic fasteners. This can be partially mitigated by the use of composite printers with continuous fibre layup capability. The size of the build plate is also a constraint on the size of the platform.

For future work, I aim to investigate the role of elastomeric filament types in the design for additive manufacturing. Multi-material extrusion also brings another dimension for further advancements. Overall, the work in this chapter contributes to faster and lower-cost flight testing of prototype aerial robots in motion capture environments, and demonstrates the potential to construct micro aerial robots during fieldwork.



Figure 8.7: **The prototype "BeeMAV" quadrotor platform flying** close to the forest floor with the whisker attachment to allow safe and stable contact with trees.

Chapter 9

Conclusion

9.1 Contributions

The contributions made in this thesis are outlined in Tab. 9.1 I explored the current challenges of building aerial robots for ecological fieldwork. These challenges cumulate into the need for robots to have more capabilities. I further review the available design solutions, concluding that integrated morphing designs can offer quadrotors more inherent capability, extending them from hover-capable payload-carrying platforms to robots with diverse skill sets.

Applying morphing to quadrotor robots, I demonstrated that fully-actuated bi-axial tiltrotor robots can shrink their cross-section in flight, thus obtaining improved agility when flying through narrow openings. I analytically quantify the extent of the ability to shrink and the effects of moving the rotors' mass. Applying morphing towards surface interaction with trees, I designed a tiltrotor measuring ring to measure the tree circumference. The prototype platform demonstrated stable flight when interacting with vertical surfaces whiles keeping the measuring ring level. Noting that tiltrotor-quadrotor designs, in principle, involve two rotating bodies, I studied the effects of the flight controller placement using a numerical model. I showed that pose tracking performance is optimal if the flight controller is placed on the body with the higher moment of inertia.

Expanding the possible morphologies, I trialled the use of metamorphic design. Using a novel

bi-stable active morphing arm, I created a compact robot which can perch within the forest canopy. I also show that the robot can execute a perch by dropping onto the tree branch, demonstrating the possibility of high-speed ballistic perching manoeuvres. I mirrored this mission profile using passive perching mechanisms. Extending the use of perching to increase a robot's endurance, I designed a novel electronic architecture to reduce the energy cost of idling. With this robot, I also assessed the viability of recovering the expensive components of the robot safely. The main body detaches from the arms and is lowered to the forest floor via an onboard crane mechanism. To provide a solution to the limited logistical support during fieldwork, I applied the metamorphic concept to design for manufacturing. I developed a quadrotor robot which can be 3D printed without any waste material and assembled without any fasteners. I also developed an offboard autonomous flight system for motion capture environments. By passing commands to the robots via RC radio, this system allowed me to test the robots without the need to integrate onboard computers.

Overall, I expanded our understanding of tiltrotor-quadrotors, both demonstrating novel designs and providing insights into the optimal placement of the flight controller. I also realised a novel design concept through a new class of aerial robots, the metamorphic quadrotor.

9.2 Conclusions

The robots presented in this thesis explored a number of facets of integrated morphing design, with the consideration of applying aerial robotics to remote sensing. Through the development of these platforms, I noted that there exists an ideal relative design size for morphing quadrotor. Larger platforms would suffer from lower relative structural stiffness, resulting in performance penalties, such as increased weight or reduced agility. Smaller platforms are often limited by available components, material properties, and the need for highly specialised manufacturing equipment. The ideal relative design size is not an absolute measurement, but a need for awareness for the designers that the morphing robots designed for a certain specification cannot be easily enlarged or miniaturised.

Due to imperfections in manufacturing, morphing structures inevitably reduce the overall rigid-

ity of the quadrotor. Compliant mechanisms, by their nature of being a single part, have less play and thus are more rigid. Nevertheless, insufficient rigidity leads to severe aeroelastic behaviours which need modifications on the conventional flight control scheme to keep the robot controllable. These mechanical inaccuracies can also dictate the placement of the Inertial Measurement Unit (IMU), and by extension the Flight Controller (FC). The prototype robots presented in this thesis are airworthy without flight control software modifications. Thus they validate the hardware design approaches taken to mitigate any significant aeroelastic behaviours.

Naturally, future morphing designs will increase in complexity and functionality. The broadening of the robot's hardware capabilities must also be matched by the robot's ability to utilise these skills. With the increased functionality and the complexity of the outdoor world, the designer-specified state machine will inevitably become a bottleneck to the robot's performance. In such a case, a reinforcement learning-driven, behaviour-based state machine would be an appropriate next step.

Regarding when to apply morphing design, while morphing can mitigate the weight increase of added functionality, it cannot fully eliminate the added weight. Therefore, the best practice is first to seek to conduct the mission with a conventional quadrotor, then turn to morphing designs when the added functionality is necessary.

Beyond its application to remote sensing, integrated morphing can be applied more broadly as a design strategy to enhance and increase any robot's functions. By embedding multifunctionality within the hardware and adaptability within the software, morphing robots will ultimately accomplish more tasks and a greater variety of tasks, taking us closer towards general-purpose robotics.

Table 9.1: Summary of Contributions - Chapter 1 to 8

Introduction (Chapter 1)	TiltDrone (Chapter 2 and 3)	Ring-Beatle (Chapter 4 and 5)
Contributions		
Review of state-of-the-art morphing aerial robots Study of the state of aerial robot use in ecology The scaling of morphing aerial robots Flight controller placement of tiltrotor-quadrotors in practice	Fully-actuated quadrotor robot Study of the tilting mechanism's spatial benefits The kinematics and dynamics of synchronised rotor tilting	Active tilting flying measuring ring Demonstration of stable free flight and flights in contact with vertical surfaces Studied flight controller placement of tiltrotor-quadrotors using numerical simulation
The Sloth (Chapter 6)	**BreaDe (Chapter 7)**	**BeeMAV (Chapter 8)**
Contributions		
Metamorphic quadrotor robot Bi-stable arm with tensile actuation Demonstration of autonomous land-perching and drop-perching	Passive morphing robot with a breakaway body Studied the use of thrust from the rotors as a perching aid Analytical modelling of morphing/perching trigger subsystem RC toggled low-power idle electronics	The use of metamorphic design to improve the ease of assembly for micro aerial robots The use of 3D printed compliant structures to create single-part assembly lightweight quadrotor Offboard indoor autonomous flight system for quadrotor robots from sub-100g to 2000g

Bibliography

[1] D. C. Marvin, L. P. Koh, A. J. Lynam, S. Wich, A. B. Davies, R. Krishnamurthy, E. Stokes, R. Starkey, and G. P. Asner, "Integrating technologies for scalable ecology and conservation," *Global Ecology and Conservation*, vol. 7, pp. 262–275, 2016.

[2] S. Baena, D. S. Boyd, and J. Moat, "UAVs in pursuit of plant conservation - Real world experiences," *Ecological Informatics*, vol. 47, no. October 2017, pp. 2–9, 2018.

[3] L. P. Koh and S. A. Wich, "Dawn of drone ecology: Low-cost autonomous aerial vehicles for conservation," *Tropical Conservation Science*, vol. 5, no. 2, pp. 121–132, 2012.

[4] M. A. Boon, A. P. Drijfhout, and S. Tesfamichael, "Comparison of a fixed-wing and multi-rotor UAV for environmental mapping applications: A case study," *International Archives of the Photogrammetry, Remote Sensing and Spatial Information Sciences - ISPRS Archives*, vol. 42, no. 2W6, pp. 47–54, 2017.

[5] B. T. Walkenhorst, G. F. Miner, and D. V. Arnold, "Low cost, radio controlled blimp as a platform for remote sensing," *International Geoscience and Remote Sensing Symposium (IGARSS)*, vol. 5, no. 801, pp. 2308–2309, 2000.

[6] J. Forsmoo, K. Anderson, C. J. Macleod, M. E. Wilkinson, L. DeBell, and R. E. Brazier, "Structure from motion photogrammetry in ecology: Does the choice of software matter?," *Ecology and Evolution*, vol. 9, no. 23, pp. 12964–12979, 2019.

[7] J. Garforth and B. Webb, "Lost in the Woods? Place Recognition for Navigation in Difficult Forest Environments," *Frontiers in Robotics and AI*, vol. 7, no. November, pp. 1–9, 2020.

[8] F. Kayitakire, C. Hamel, and P. Defourny, "Retrieving forest structure variables based on image texture analysis and IKONOS-2 imagery," *Remote Sensing of Environment*, vol. 102, no. 3-4, pp. 390–401, 2006.

[9] C. S. Neigh, J. G. Masek, P. Bourget, B. Cook, C. Huang, K. Rishmawi, and F. Zhao, "Deciphering the precision of stereo IKONOS canopy height Models for US forests with G-LiHT airborne LiDAR," *Remote Sensing*, vol. 6, no. 3, pp. 1762–1782, 2014.

[10] J. Tomaštík, M. Mokroš, P. Surový, A. Grznárová, and J. Merganič, "UAV RTK/PPK method-An optimal solution for mapping inaccessible forested areas?," *Remote Sensing*, vol. 11, no. 6, 2019.

[11] E. Gregolinska, R. Khanam, F. Lefort, and P. Parthasarathy, "Capturing the true value of Industry 4.0," Tech. Rep. April, McKinsey & Company, 2022.

[12] "What robots do (and don't do) at Amazon fulfilment centres."

[13] Hairobotics, "Hairobotics Products."

[14] M. Chui, J. Manyika, M. Miremadi, and K. George, "Human + machine: A new era of automation in manufacturing," *McKinsey*, pp. 1–8, 2017.

[15] J. Hawksworth, R. Berriman, and S. Goe, "Will robots really steal our jobs ? An international analysis of the potential long term impact of automation Key findings : impact of automation," *PwC*, 2018.

[16] G. Loianno, C. Brunner, G. McGrath, and V. Kumar, "Estimation, Control, and Planning for Aggressive Flight With a Small Quadrotor With a Single Camera and IMU," *IEEE Robotics and Automation Letters*, 2017.

[17] B. B. Kocer, M. A. Hady, H. Kandath, M. Pratama, and M. Kovac, "Deep Neuromorphic Controller with Dynamic Topology for Aerial Robots," in *2021 IEEE International Conference on Robotics and Automation*, pp. 110–116, IEEE, 2021.

[18] A. Loquercio, E. Kaufmann, R. Ranftl, M. Müller, V. Koltun, and D. Scaramuzza, "Learning high-speed flight in the wild," *Science Robotics*, vol. 6, no. 59, 2021.

[19] W. Koch, R. Mancuso, R. West, and A. Bestavros, "Reinforcement Learning for UAV Attitude Control," *ACM Transactions on Cyber-Physical Systems*, vol. 3, no. 2, 2019.

[20] W. Koch, R. Mancuso, and A. Bestavros, "Neuroflight: Next Generation Flight Control Firmware," tech. rep., Boston University, 2019.

[21] J. Ma, Y. Li, N. S. Grundish, J. B. Goodenough, Y. Chen, L. Guo, Z. Peng, X. Qi, F. Yang, L. Qie, C. A. Wang, B. Huang, Z. Huang, L. Chen, D. Su, G. Wang, X. Peng, Z. Chen, J. Yang, S. He, X. Zhang, H. Yu, C. Fu, M. Jiang, W. Deng, C. F. Sun, Q. Pan, Y. Tang, X. Li, X. Ji, F. Wan, Z. Niu, F. Lian, C. Wang, G. G. Wallace, M. Fan, Q. Meng, S. Xin, Y. G. Guo, and L. J. Wan, "The 2021 battery technology roadmap," *Journal of Physics D: Applied Physics*, vol. 54, no. 18, 2021.

[22] J. P. Duffy, A. M. Cunliffe, L. DeBell, C. Sandbrook, S. A. Wich, J. D. Shutler, I. H. Myers-Smith, M. R. Varela, and K. Anderson, "Location, location, location: considerations when using lightweight drones in challenging environments," *Remote Sensing in Ecology and Conservation*, vol. 4, no. 1, pp. 7–19, 2018.

[23] Z. Bian, B. Cao, H. Li, Y. Du, W. Fan, Q. Xiao, and Q. Liu, "The Effects of Tree Trunks on the Directional Emissivity and Brightness Temperatures of a Leaf-Off Forest Using a Geometric Optical Model," *IEEE Transactions on Geoscience and Remote Sensing*, vol. 59, no. 6, pp. 5370–5386, 2021.

[24] D. Floreano and R. J. Wood, "Science, technology and the future of small autonomous drones," *Nature*, vol. 521, no. 7553, pp. 460–466, 2015.

[25] "Consultation Paper 3: A regulatory framework for automated vehicles - OVERVIEW," tech. rep., Law Commision and Scottish Law Commission, 2021.

[26] J. Winslow, M. Benedict, V. Hrishikeshavan, and I. Chopra, "Design, development, and flight testing of a high endurance micro quadrotor helicopter," *International Journal of Micro Air Vehicles*, vol. 8, no. 3, pp. 155–169, 2016.

[27] DJI, "Mavic Series Comparison: Which Drone Should You Get?," 2021.

[28] S. Derammelaere, M. Haemers, J. De Viaene, F. Verbelen, and K. Stockman, "A quantitative comparison between BLDC, PMSM, brushed DC and stepping motor technologies," in *19th International Conference on Electrical Machines and Systems, ICEMS 2016*, pp. 1–5, The Institute of Electrical Engineers of Japan, 2016.

[29] Avartek, "Avartek Boxer – Advanced Hybrid Power Technology," 2019.

[30] Foxtech, "GAIA 160HY-Hybrid Pixhawk 2.1 - User Manual V1.1," tech. rep., Foxtech, 2019.

[31] P. Debitetto, "Hybrid VTOL : Increased Energy Density for Increased Payload and Endurance," tech. rep., Top Flight Technologies, Inc., 2019.

[32] Quaternium, "Hybrix Long-Endurance Drone," 2021.

[33] Skyfront, "Perimeter 4," 2021.

[34] Intelligent Energy, "Fuel Cell UAV Introduction," tech. rep., Intelligent Energy Limited, 2019.

[35] FliteTest, "Stingray 500 - Review."

[36] Merriam-Webster.com, "robot."

[37] R. Siddall and M. Kovač, "Launching the AquaMAV: Bioinspired design for aerial-aquatic robotic platforms," *Bioinspiration and Biomimetics*, vol. 9, no. 3, 2014.

[38] H. Alzu'bi, I. Mansour, and O. Rawashdeh, "Loon Copter : Implementation of a hybrid unmanned aquatic – aerial quadcopter with active buoyancy control," *Journal of Field Robotics*, no. February 2017, pp. 764–778, 2018.

[39] R. Zufferey, A. Ortega Ancel, A. Farinha, R. Siddall, S. F. Armanini, M. Nasr, R. V. Brahmal, G. Kennedy, and M. Kovac, "Consecutive aquatic jump-gliding with water-reactive fuel," *Science Robotics*, vol. 4, no. 34, 2019.

[40] N. B. David and D. Zarrouk, "Design and Analysis of FCSTAR, a Hybrid Flying and Climbing Sprawl Tuned Robot," *IEEE Robotics and Automation Letters*, vol. 6, no. 4, pp. 6188–6195, 2021.

[41] V. A. Tucker, "Energetic cost of locomotion in animals," *Comparative Biochemistry And Physiology*, vol. 34, no. 4, pp. 841–846, 1970.

[42] V. A. Tucker, "The Energetic Cost of Moving About," *American Scientist*, vol. 63, no. 4, pp. 413–419, 1975.

[43] S. M. O'Connor, T. J. Dawson, R. Kram, and J. Maxwell Donelan, "The kangaroo's tail propels and powers pentapedal locomotion," *Biology Letters*, vol. 10, no. 7, pp. 1–4, 2014.

[44] Guinness World Records, "Fastest bird (diving)."

[45] A. M. Berg and A. A. Biewener, "Wing and body kinematics of takeoff and landing flight in the pigeon (Columba livia)," *Journal of Experimental Biology*, vol. 213, no. 10, pp. 1651–1658, 2010.

[46] M. Hildebrand, "The Quadrupedal Gaits of Vertebrates: The timing of leg movements relates to balance, body shape, agility, speed, and energy expenditure," *BioScience*, vol. 39, pp. 766–775, 12 1989.

[47] J. Blaszczyk and G. E. Loeb, "Why Cats Pace on the Treadmill," *Physiology and Behaviour*, vol. 53, pp. 501–507, 1993.

[48] F. E. Fish, N. K. DiNenno, and J. Trail, "The "dog paddle": Stereotypic swimming gait pattern in different dog breeds," *Anatomical Record*, vol. 304, no. 1, pp. 90–100, 2021.

[49] V. Galindo-Zamora, V. von Babo, N. Eberle, D. Betz, I. Nolte, and P. Wefstaedt, "Kinetic, kinematic, magnetic resonance and owner evaluation of dogs before and after the amputation of a hind limb," *BMC Veterinary Research*, vol. 12, no. 1, pp. 1–14, 2016.

[50] N. T. Roach, M. Venkadesan, M. J. Rainbow, and D. E. Lieberman, "Elastic energy storage in the shoulder and the evolution of high-speed throwing in Homo," *Nature*, vol. 498, no. 7455, pp. 483–486, 2013.

[51] P. Lemelin, "Comparative and functional myology of the prehensile tail in new world monkeys," *Journal of Morphology*, vol. 224, no. 3, pp. 351–368, 1995.

[52] L. L. Bergey and J. S. Weis, "Molting as a mechanism of depuration of metals in the fiddler crab, Uca pugnax," *Marine Environmental Research*, vol. 64, no. 5, pp. 556–562, 2007.

[53] B. Ebenman, "Evolution in Organisms that Change Their Niches during the Life Cycle," *American Society of Naturalists*, vol. 139, no. 5, pp. 990–1021, 1992.

[54] J. Rolff, P. R. Johnston, and S. Reynolds, "Complete metamorphosis of insects," *Philosophical Transactions of the Royal Society B: Biological Sciences*, vol. 374, no. 1783, 2019.

[55] F. Yin, A. Tang, L. Xu, Y. Cao, Y. Zheng, Z. Zhang, and X. Chen, "Run Like a Dog : Learning Based Whole-Body Control Framework for Quadruped Gait Style Transfer," *IEEE/RSJ International Conference on Intelligent Robots and Systems*, pp. 8485–8491, 2021.

[56] X. Liang, M. Xu, L. Xu, P. Liu, X. Ren, Z. Kong, J. Yang, and S. Zhang, "The AmphiHex: A novel amphibious robot with transformable leg-flipper composite propulsion mechanism," *IEEE International Conference on Intelligent Robots and Systems*, pp. 3667–3672, 2012.

[57] M. Bjelonic, P. K. Sankar, C. D. Bellicoso, H. Vallery, and M. Hutter, "Rolling in the Deep - Hybrid Locomotion for Wheeled-Legged Robots Using Online Trajectory Optimization," *IEEE Robotics and Automation Letters*, vol. 5, no. 2, pp. 3626–3633, 2020.

[58] Y. S. Kim, G. P. Jung, H. Kim, K. J. Cho, and C. N. Chu, "Wheel Transformer: A wheel-leg hybrid robot with passive transformable wheels," *IEEE Transactions on Robotics*, vol. 30, no. 6, pp. 1487–1498, 2014.

[59] D. Y. Lee, J. K. Kim, C. Y. Sohn, J. M. Heo, and K. J. Cho, "High-load capacity origami transformable wheel," *Science Robotics*, vol. 6, no. 53, 2021.

[60] D. N. Beal, F. S. Hover, M. S. Triantafyllou, J. C. Liao, and G. V. Lauder, "Passive propulsion in vortex wakes," *Journal of Fluid Mechanics*, vol. 549, pp. 385–402, 2006.

[61] Autel Robotics, "Dragonfish: A Revolutionary eVTOL Fixed-Wing sUAS," tech. rep., Autel Robotics, Bothell, Washington USA, 2022.

[62] M. Kamel, S. Verling, O. Elkhatib, C. Sprecher, P. Wulkop, Z. Taylor, R. Siegwart, and I. Gilitschenski, "The Voliro Omniorientational Hexacopter: An Agile and Maneuverable Tiltable-Rotor Aerial Vehicle," *IEEE Robotics and Automation Magazine*, vol. 25, no. 4, pp. 34–44, 2018.

[63] K. Bodie, M. Brunner, M. Pantic, S. Walser, P. Pfndler, U. Angst, R. Siegwart, and J. Nieto, "An Omnidirectional Aerial Manipulation Platform for Contact-Based Inspection," in *Robotics: Science and Systems 2019*, 2019.

[64] Voliro, "Voliro: Technology."

[65] P. Zheng, X. Tan, B. B. Kocer, E. Yang, and M. Kovac, "TiltDrone: a Fully-Actuated Tilting Quadrotor Platform," *IEEE Robotics and Automation Letters*, vol. 5, no. 4, pp. 6845–6852, 2020.

[66] K. Y. Ma, P. Chirarattananon, S. B. Fuller, and R. J. Wood, "Controlled Flight of a Biologically Inspired, Insect-Scale Robot," *Science*, vol. 340, no. May, pp. 603–607, 2013.

[67] Y. Chen, H. Zhao, J. Mao, P. Chirarattananon, E. F. Helbling, N. s. P. Hyun, D. R. Clarke, and R. J. Wood, "Controlled flight of a microrobot powered by soft artificial muscles," *Nature*, vol. 575, no. 7782, pp. 324–329, 2019.

[68] G. A. Folkertsma, W. Straatman, N. Nijenhuis, C. H. Venner, and S. Stramigioli, "Robird: A Robotic Bird of Prey," *IEEE Robotics and Automation Magazine*, no. september, 2017.

[69] R. Zufferey, J. Tormo-Barbero, M. Mar Guzman, F. J. Maldonado, E. Sanchez-Laulhe, P. Grau, M. Perez, J. A. Acosta, and A. Ollero, "Design of the High-Payload Flapping Wing Robot E-Flap," *IEEE Robotics and Automation Letters*, vol. 6, no. 2, pp. 3097–3104, 2021.

[70] R. Zufferey, A. O. Ancel, C. Raposo, S. F. Armanini, A. Farinha, R. Siddall, I. Berasaluce, H. Zhu, and M. Kovac, "SailMAV: Design and Implementation of a Novel Multi-Modal Flying Sailing Robot," *IEEE Robotics and Automation Letters*, vol. 4, no. 3, pp. 2894–2901, 2019.

[71] F. Rockenbauer, S. Jeger, L. Beltran, M. Berger, M. Harms, N. Kaufmann, M. Rauch, M. Reinders, N. Lawrance, T. Stastny, and R. Siegwart, "Dipper: A Dynamically Transitioning Aerial-Aquatic Unmanned Vehicle," in *Robotics: Science and Systems*, 2021.

[72] R. Siddall, A. Ortega Ancel, and M. Kovač, "Wind and water tunnel testing of a morphing aquatic micro air vehicle," *Interface focus*, vol. 7, no. 1, p. 20160085, 2017.

[73] Y. H. Tan and B. M. Chen, "Thruster Allocation and Mapping of Aerial and Aquatic Modes for a Morphable Multimodal Quadrotor," *IEEE/ASME Transactions on Mechatronics*, vol. 25, no. 4, pp. 2065–2074, 2020.

[74] A. Sadeghi, A. Mondini, and B. Mazzolai, "Toward self-growing soft robots inspired by plant roots and based on additive manufacturing technologies," *Soft Robotics*, vol. 4, no. 3, pp. 211–223, 2017.

[75] A. Fabris, S. Kirchgeorg, and S. Mintchev, "A Soft Drone with Multi-modal Mobility for the Exploration of Confined Spaces," *IEEE International Symposium on Safety, Security, and Rescue Robotics*, 2021.

[76] D. Hwang, E. J. Barron, A. B. Haque, and M. D. Bartlett, "Shape morphing mechanical metamaterials through reversible plasticity," *Science robotics*, vol. 7, no. 63, p. eabg2171, 2022.

[77] L. Daler, *Adaptive Morphology for Multi-Modal Locomotion*. PhD thesis, École polytechnique fédérale de Lausanne, 2015.

[78] S. Felton, M. Tolley, E. Demaine, D. Rus, and R. Wood, "A method for building self-folding machines," *Science*, vol. 345, no. 6197, pp. 644–646, 2014.

[79] S. Miyashita, S. Guitron, S. Li, and D. Rus, "Robotic metamorphosis by origami exoskeletons," *Science Robotics*, vol. 2, no. 10, p. eaao4369, 2017.

[80] H. W. Park, P. M. Wensing, and S. Kim, "High-speed bounding with the MIT Cheetah 2: Control design and experiments," *International Journal of Robotics Research*, vol. 36, no. 2, pp. 167–192, 2017.

[81] H. Kim and A. T. Asbeck, "An elbow exoskeleton for haptic feedback made with a direct drive hobby motor," *HardwareX*, vol. 8, p. e00153, 2020.

[82] A. Spröwitz, A. Tuleu, M. Vespignani, M. Ajallooeian, E. Badri, and A. J. Ijspeert, "Towards dynamic trot gait locomotion: Design, control, and experiments with Cheetah-cub, a compliant quadruped robot," *International Journal of Robotics Research*, vol. 32, no. 8, pp. 932–950, 2013.

[83] R. Sato, E. Kazama, A. Ming, M. Shimojo, F. Meng, H. Liu, X. Fan, X. Chen, Z. Yu, and Q. Huang, "Design and control of robot legs with bi-articular muscle-tendon complex," *2017 IEEE International Conference on Robotics and Biomimetics, ROBIO 2017*, vol. 2018-Janua, pp. 2605–2610, 2018.

[84] T. J. Zenzal and F. R. Moore, "Stopover biology of Ruby-throated Hummingbirds (Archilochus colubris) during autumn migration," *The Auk*, vol. 133, no. 2, pp. 237–250, 2016.

[85] "albatross — bird — Britannica," 1 2022.

[86] Cornell Lab Bird Cams, "Albatross Attempts Landing, Fails Spectacularly! #RoyalCam — NZ DOC — Cornell Lab [Video]," 2021.

[87] B. Theys, G. Dimitriadis, P. Hendrick, and J. De Schutter, "Influence of propeller configuration on propulsion system efficiency of multi-rotor Unmanned Aerial Vehicles," *2016 International Conference on Unmanned Aircraft Systems, ICUAS 2016*, no. 3, pp. 195–201, 2016.

[88] P. Sigrist, P. Coppin, and M. Hermy, "Impact of forest canopy on quality and accuracy of GPS measurements," *International Journal of Remote Sensing*, vol. 20, no. 18, pp. 3595–3610, 1999.

[89] J. Garforth and B. Webb, "Visual appearance analysis of forest scenes for monocular SLAM," *Proceedings - IEEE International Conference on Robotics and Automation*, vol. 2019-May, pp. 1794–1800, 2019.

[90] C. F. Liew, D. DeLatte, N. Takeishi, and T. Yairi, "Recent Developments in Aerial Robotics: A Survey and Prototypes Overview," *arXiv*, 2017.

[91] P. Chermprayong, K. Zhang, F. Xiao, and M. Kovac, "An Integrated Delta Manipulator for Aerial Repair: A New Aerial Robotic System," *IEEE Robotics and Automation Magazine*, vol. 26, no. 1, pp. 54–66, 2019.

[92] S. Hamaza, I. Georgilas, M. Fernandez, P. Sanchez, T. Richardson, G. Heredia, and A. Ollero, "Sensor Installation and Retrieval Operations Using an Unmanned Aerial Manipulator," *IEEE Robotics and Automation Letters*, vol. 4, no. 3, pp. 2793–2800, 2019.

[93] K. Kawasaki, Y. Motegi, M. Zhao, K. Okada, and M. Inaba, "Dual connected Bi-Copter with new wall trace locomotion feasibility that can fly at arbitrary tilt angle," *IEEE International Conference on Intelligent Robots and Systems*, vol. 2015-Decem, pp. 524–531, 2015.

[94] B. B. Kocer, T. Tjahjowidodo, M. Pratama, and G. G. L. Seet, "Inspection-while-flying: An autonomous contact-based nondestructive test using UAV-tools," *Automation in Construction*, vol. 106, no. June, p. 102895, 2019.

[95] J. Paneque-Gálvez, M. K. McCall, B. M. Napoletano, S. A. Wich, and L. P. Koh, "Small drones for community-based forest monitoring: An assessment of their feasibility and potential in tropical areas," *Forests*, vol. 5, no. 6, pp. 1481–1507, 2014.

[96] R. Hashem, J. Goerres, R. G. Aarts, J. B. C. Engelen, and S. Stramigioli, "Fully Actuated Multirotor UAVs: A Literature Review," *IEEE Robotics and Automation Magazine*, 2020.

[97] A. Franchi, R. Carli, D. Bicego, and M. Ryll, "Full-Pose Tracking Control for Aerial Robotic Systems with Laterally Bounded Input Force," *IEEE Transactions on Robotics*, vol. 34, no. 2, pp. 534–541, 2018.

[98] G. Jiang and R. M. Voyles, "Hexrotor UAV Platform Enabling Dextrous Aerial Mobile Manipulation," *Proceedings of the International Micro Air Vehicle Conference and Flight Competition IMAV 2013*, pp. 122–131, 2013.

[99] D. Brescianini and R. D'Andrea, "Design , Modeling and Control of an Omni-Directional Aerial Vehicle," *2016 IEEE International Conference on Robotics and Automation (ICRA)*, pp. 3261–3266, 2016.

[100] P. Boyle, C. Liu, D. Shanks, and A. Weinstein, "Team Volonomic," Tech. Rep. April, University of Pennsylvania, 2017.

[101] S. Park, J. Lee, J. Ahn, M. Kim, J. Her, G.-h. Yang, and D. Lee, "ODAR : Aerial Manipulation Platform Enabling Omnidirectional Wrench Generation," *IEEE/ASME Transactions on Mechatronics*, vol. 23, no. 4, pp. 1907–1918, 2018.

[102] J. Y. S. Lee, K. K. Leang, and W. Yim, "Design and control of a fully- actuated hexrotor for aerial manipulation applications," *Journal of Mechanisms and Robotics*, vol. 10, no. 4, pp. 1–10, 2018.

[103] D. Kastelan, M. Konz, and J. Rudolph, "Fully actuated tricopter with pilot-supporting control," *IFAC-PapersOnLine*, vol. 28, no. 9, pp. 79–84, 2015.

[104] A. Nemati, *Designing, Modeling and Control of a Tilting Rotor Quadcopter*. PhD thesis, University of Cincinnati, 2016.

[105] Y. Long and D. J. Cappelleri, "Linear control design, allocation, and implementation for the Omnicopter MAV," *IEEE International Conference on Robotics and Automation*, pp. 289–294, 2013.

[106] M. Ryll, H. H. Bülthoff, and P. R. Giordano, "A Novel Overactuated Quadrotor Unmanned Aerial Vehicle: Modeling, Control, and Experimental Validation," *IEEE TRANSACTIONS ON CONTROL SYSTEMS TECHNOLOGY*, vol. 23, no. 2, 2015.

[107] M. Ryll, D. Bicego, M. Giurato, M. Lovera, and A. Franchi, "FAST-Hex – A Morphing Hexarotor: Design, Mechanical Implementation, Control and Experimental Validation," *arXiv*, pp. 1–11, 2020.

[108] A. F. \cSenkul and E. Altu\ug, "System Design of a Novel Tilt-Roll Rotor Quadrotor UAV," *Journal of Intelligent and Robotic Systems: Theory and Applications*, vol. 84, no. 1-4, pp. 575–599, 2016.

[109] A. B. Junaid, A. D. D. C. Sanchez, J. B. Bosch, N. Vitzilaios, and Y. Zweiri, "Design and implementation of a dual-axis tilting quadcopter," *Robotics*, vol. 7, no. 4, pp. 1–20, 2018.

[110] M. Odelga, P. Stegagno, and H. H. Bülthoff, "A Fully Actuated Quadrotor UAV with a Propeller Tilting Mechanism : Modeling and Control," *IEEE International Conference on Advanced Intelligent Mechatronics (AIM)*, pp. 1–6, 2016.

[111] J. Paulos, B. Caraher, and M. Yim, "Emulating a Fully Actuated Aerial Vehicle using Two Actuators," *International Conference on Robotics and Automation*, pp. 7011–7016, 2018.

[112] J. Paulos and M. Yim, "Cyclic blade pitch control without a swashplate for small helicopters," *Journal of Guidance, Control, and Dynamics*, vol. 41, no. 3, pp. 689–700, 2018.

[113] R. Ji, J. Ma, and S. S. Ge, "Modeling and Control of a Tilting Quadcopter," *IEEE Transactions on Aerospace and Electronic Systems*, vol. 14, no. 8, p. 1, 2019.

[114] A. Desbiez, F. Expert, M. Boyron, J. Diperi, S. Viollet, and F. Ruffier, "X-Morf: A crash-separable quadrotor that morfs its X-geometry in flight," *2017 Workshop on Research, Education and Development of Unmanned Aerial Systems, RED-UAS 2017*, pp. 222–227, 2017.

[115] V. Riviere, A. Manecy, and S. Viollet, "Agile Robotic Fliers: A Morphing-Based Approach," *Soft Robotics*, vol. 00, no. 00, p. soro.2017.0120, 2018.

[116] D. Falanga, K. Kleber, S. Mintchev, D. Floreano, and D. Scaramuzza, "The Foldable Drone: A Morphing Quadrotor That Can Squeeze and Fly," *IEEE Robotics and Automation Letters*, vol. 4, no. 2, pp. 209–216, 2019.

[117] N. Bucki and M. W. Mueller, "Design and control of a passively morphing quadcopter," in *IEEE International Conference on Robotics and Automation*, vol. 2019-May, pp. 9116–9122, 2019.

[118] D. Nixon, A. Mironov, M. A. M. Martinez, J. Blackman, Codecae, B. Luckcuck, A. J. Christensen, D. Clifton, M. Keller, R. Coeffic, and S. Windoffer, "Betaflight."

[119] Markforged, "Material Datasheet Composites."

[120] EasyComposites, "EasyComposites - Single Sided High Strength Carbon Fibre Sheet - Specification."

[121] P. Seidel and Tbs-trappy, "Open Source FPV Drone Frame - SOURCE ONE."

[122] M. Gatti and F. Giulietti, "Preliminary design analysis methodology for electric multirotor," in *2nd IFAC Workshop on Research, Education and Development of Unmanned Aerial Systems*, vol. 2, pp. 58–63, IFAC, 2013.

[123] C. Ampatis and E. Papadopoulos, "Parametric Design and Optimization of Multi-Rotor Aerial Vehicles," in *Applications of Mathematics and Informatics in Science and Engineering*, vol. 91, pp. 1–25, Springer International Publishing Switzerland, 2014.

[124] O. Magnussen, M. Ottestad, and G. Hovland, "Multicopter design optimization and validation," *Modeling, Identification and Control*, vol. 36, no. 2, pp. 67–79, 2015.

[125] J. Winslow, V. Hrishikeshavan, and I. Chopra, "Design Methodology for Small Scale Unmanned Quadrotors," in *AIAA Aerospace Sciences Meeting*, no. January, pp. 1–15, 2017.

[126] P. Dourmashkin, "Classical Mechanics: MIT 8.01 Course Notes," 2016.

[127] J. P. Snyder, "Map projections: A working manual," tech. rep., U.S. Government Printing Office, Washington, D.C., 1987.

[128] The Organisation for Economic Cooperation and Development (OECD), "A Comprehensive Overview of Global Biodiversity Finance A Comprehensive Overview of Global Biodiversity Finance," tech. rep., 2020.

[129] United Nations Environment Programme, "State of Finance for Nature Tripling investments in nature-based solutions by 2030," tech. rep., Nairobi, 2021.

[130] D. Fawcett, B. Azlan, T. C. Hill, L. K. Kho, J. Bennie, and K. Anderson, "Unmanned aerial vehicle (UAV) derived structure-from-motion photogrammetry point clouds for oil palm (Elaeis guineensis) canopy segmentation and height estimation," *International Journal of Remote Sensing*, vol. 40, no. 19, pp. 7538–7560, 2019.

[131] L. Tang and G. Shao, "Drone remote sensing for forestry research and practices," *Journal of Forestry Research*, vol. 26, no. 4, pp. 791–797, 2015.

[132] Y. Xie, Z. Sha, and M. Yu, "Remote sensing imagery in vegetation mapping: a review," *Journal of Plant Ecology*, vol. 1, no. 1, pp. 9–23, 2008.

[133] A. Farinha, R. Zufferey, P. Zheng, S. F. Armanini, and M. Kovac, "Unmanned Aerial Sensor Placement for Cluttered Environments," *IEEE Robotics and Automation Letters*, vol. 5, no. 4, pp. 6623–6630, 2020.

[134] F. Xiao, P. Zheng, J. D. Tria, B. B. Kocer, and M. Kovac, "Optic Flow-Based Reactive Collision Prevention for MAVs Using the Fictitious Obstacle Hypothesis," *IEEE Robotics and Automation Letters*, vol. 6, no. 2, pp. 3144–3151, 2021.

[135] P. Sareh, P. Chermprayong, M. Emmanuelli, H. Nadeem, and M. Kovac, "Rotorigami: A rotary origami protective system for robotic rotorcraft," *Science Robotics*, vol. 3, no. 22, p. eaah5228, 2018.

[136] M. Ryll, H. H. Bülthoff, and P. R. Giordano, "Modeling and Control of a Quadrotor UAV with Tilting Propellers," *2012 IEEE International Conference on Robotics and Automation (ICRA)*, pp. 4606–4613, 2012.

[137] A. Sakaguchi and K. Yamamoto, "A Novel Quadrotor with a 3-axis Deformable Frame using Tilting Motions of Parallel Link Modules without Thrust Loss," *IEEE Robotics and Automation Letters*, pp. 1–8, 2022.

[138] S. Hamaza and M. Kovac, "Omni-Drone: On the Design of a Novel Aerial Manipulator with Omni-directional Workspace," *2020 17th International Conference on Ubiquitous Robots, UR 2020*, pp. 153–158, 2020.

[139] F. Zellweger, P. De Frenne, J. Lenoir, D. Rocchini, and D. Coomes, "Advances in Microclimate Ecology Arising from Remote Sensing," *Trends in Ecology and Evolution*, vol. 34, no. 4, pp. 327–341, 2019.

[140] M. Mohan, C. A. Silva, C. Klauberg, P. Jat, G. Catts, A. Cardil, A. T. Hudak, and M. Dia, "Individual tree detection from unmanned aerial vehicle (UAV) derived canopy height model in an open canopy mixed conifer forest," *Forests*, vol. 8, no. 9, 2017.

[141] I. Dronova, C. Kislik, Z. Dinh, and M. Kelly, "A review of unoccupied aerial vehicle use in wetland applications: Emerging opportunities in approach, technology, and data," *Drones*, vol. 5, no. 2, 2021.

[142] A. Farinha and P. U. Lima, "A Novel Underactuated Hand Suitable for Human-Oriented Domestic Environments," *Proceedings - 2016 International Conference on Autonomous Robot Systems and Competitions, ICARSC 2016*, pp. 106–111, 2016.

[143] S. Hamaza, I. Georgilas, G. Heredia, A. Ollero, and T. Richardson, "Design, modeling, and control of an aerial manipulator for placement and retrieval of sensors in the environment," *Journal of Field Robotics*, vol. 37, no. 7, pp. 1224–1245, 2020.

[144] A. Nakamura, R. L. Kitching, M. Cao, T. J. Creedy, T. M. Fayle, M. Freiberg, C. N. Hewitt, T. Itioka, L. P. Koh, K. Ma, Y. Malhi, A. Mitchell, V. Novotny, C. M. P. Ozanne,

L. Song, H. Wang, and L. A. Ashton, "Forests and Their Canopies: Achievements and Horizons in Canopy Science," *Trends in Ecology and Evolution*, vol. 32, no. 6, pp. 438–451, 2017.

[145] K. Hang, X. Lyu, H. Song, J. A. Stork, A. M. Dollar, D. Kragic, and F. Zhang, "Perching and resting - A paradigm for UAV maneuvering with modularized landing gears," *Science Robotics*, vol. 4, no. 28, p. eaau6637, 2019.

[146] T. W. Danko, A. Kellas, and P. Y. Oh, "Robotic rotorcraft and perch-and-stare: sensing landing zones and handling obscurants," in *ICAR '05. Proceedings., 12th International Conference on Advanced Robotics, 2005.*, pp. 296–302, 2005.

[147] J. N. Pauli, M. Zachariah Peery, E. D. Fountain, and W. H. Karasov, "Arboreal folivores limit their energetic output, all the way to slothfulness," *American Naturalist*, vol. 188, no. 2, pp. 196–204, 2016.

[148] M. Kovač, J. Germann, C. Hürzeler, R. Y. Siegwart, and D. Floreano, "A perching mechanism for micro aerial vehicles," *Journal of Micro-Nano Mechatronics*, vol. 5, no. 3, pp. 77–91, 2009.

[149] J. Toon, "'SlothBot in the Garden' Demonstrates Hyper-Efficient Conservation Robot."

[150] J. Thomas, M. Pope, G. Loianno, E. W. Hawkes, M. A. Estrada, H. Jiang, M. R. Cutkosky, and V. Kumar, "Aggressive Flight With Quadrotors for Perching on Inclined Surfaces," *Journal of Mechanisms and Robotics*, vol. 8, no. 5, p. 51007, 2016.

[151] L. Daler, A. Klaptocz, A. Briod, M. Sitti, and D. Floreano, "A perching mechanism for flying robots using a fibre-based adhesive," in *2013 IEEE International Conference on Robotics and Automation*, pp. 4433–4438, IEEE, 2013.

[152] M. Kovač, J. Germann, C. Hürzeler, R. Y. Siegwart, and D. Floreano, "A perching mechanism for micro aerial vehicles," *Journal of Micro-Nano Mechatronics*, vol. 5, no. 3-4, pp. 77–91, 2009.

[153] M. T. Pope, C. W. Kimes, H. Jiang, E. W. Hawkes, M. A. Estrada, C. F. Kerst, W. R. T. Roderick, A. K. Han, D. L. Christensen, and M. R. Cutkosky, "A Multimodal Robot for Perching and Climbing on Vertical Outdoor Surfaces," *IEEE Transactions on Robotics*, vol. 33, no. 1, pp. 38–48, 2017.

[154] A. Lussier Desbiens, A. T. Asbeck, and M. R. Cutkosky, "Landing, perching and taking off from vertical surfaces," *The International Journal of Robotics Research*, vol. 30, no. 3, pp. 355–370, 2011.

[155] H.-N. Nguyen, R. Siddall, B. Stephens, A. Navarro-Rubio, and M. Kovač, "A Passively Adaptive Microspine Grapple for Robust, Controllable Perching," in *2019 2nd IEEE International Conference on Soft Robotics (RoboSoft)*, pp. 80–87, IEEE, 2019.

[156] A. Braithwaite, T. Al Hinai, M. Haas-Heger, E. McFarlane, and M. Kovač, "Tensile Web Construction and Perching with Nano Aerial Vehicles," in *Robotics Research: Volume 1* (A. Bicchi and W. Burgard, eds.), pp. 71–88, Cham: Springer International Publishing, 2018.

[157] K. Zhang, P. Chermprayong, T. M. Alhinai, R. Siddall, and M. Kovac, "SpiderMAV: Perching and Stabilizing Micro Aerial Vehicles with Bio-inspired Tensile Anchoring Systems," in *International Conference on Intelligent Robots and Systems*, 2017.

[158] W. R. T. Roderick, H. Jiang, S. Wang, D. Lentink, and M. R. Cutkosky, "Bioinspired grippers for natural curved surface perching," in *Conference on Biomimetic and Biohybrid Systems*, pp. 604–610, Springer, 2017.

[159] J. Thomas, G. Loianno, K. Daniilidis, and V. Kumar, "Visual Servoing of Quadrotors for Perching by Hanging From Cylindrical Objects," *IEEE Robotics and Automation Letters*, 2016.

[160] A. McLaren, Z. Fitzgerald, G. Gao, and M. Liarokapis, "A Passive Closing, Tendon Driven, Adaptive Robot Hand for Ultra-Fast, Aerial Grasping and Perching," *IEEE International Conference on Intelligent Robots and Systems*, pp. 5602–5607, 2019.

[161] Z. Zhang, P. Xie, and O. Ma, "Bio-inspired trajectory generation for UAV perching," in *2013 IEEE/ASME International Conference on Advanced Intelligent Mechatronics*, pp. 997–1002, IEEE, 2013.

[162] C. E. Doyle, J. J. Bird, T. A. Isom, J. C. Kallman, D. F. Bareiss, D. J. Dunlop, R. J. King, J. J. Abbott, and M. A. Minor, "An Avian-Inspired Passive Mechanism for Quadrotor Perching," *IEEE/ASME Transactions on Mechatronics*, vol. 18, no. 2, pp. 506–517, 2013.

[163] M. A. Erbil, S. D. Prior, and A. J. Keane, "Design optimisation of a reconfigurable perching element for vertical take-off and landing unmanned aerial vehicles," *International Journal of Micro Air Vehicles*, vol. 5, no. 3, pp. 207–228, 2013.

[164] W. Chi, K. H. Low, K. H. Hoon, and J. Tang, "An optimized perching mechanism for autonomous perching with a quadrotor," in *IEEE International Conference on Robotics and Automation*, pp. 3109–3115, 2014.

[165] MichałJoachimczak, R. Suzuki, and T. Arita, "Artificial Metamorphosis: Evolutionary Design of Transforming, Soft-Bodied Robots," *Artificial Life*, vol. 22, pp. 271–298, 8 2016.

[166] K. Sims, "Evolving Virtual Creatures," in *Proceedings of the 21st Annual Conference on Computer Graphics and Interactive Techniques*, SIGGRAPH '94, (New York, NY, USA), p. 15–22, Association for Computing Machinery, 1994.

[167] J. Bongard, "Morphological change in machines accelerates the evolution of robust behavior," *Proceedings of the National Academy of Sciences*, vol. 108, pp. 1234–1239, 1 2011.

[168] J. W. Truman and L. M. Riddiford, "The origins of insect metamorphosis," *Nature*, vol. 401, pp. 447–452, 9 1999.

[169] N. A. Campbell, J. B. Reece, L. A. Urry, M. L. Cain, S. A. Wasserman, P. V. Minorsky, and R. B. Jackson, *Biology: a global approach*. Pearson New Your, NY, 2018.

[170] J. S. Dai and J. Rees Jones, "Mobility in Metamorphic Mechanisms of Foldable/Erectable Kinds," *Journal of Mechanical Design*, vol. 121, no. 3, p. 375, 1999.

[171] S. Mintchev and D. Floreano, "Adaptive morphology: A design principle for multimodal and multifunctional robots," *IEEE Robotics and Automation Magazine*, vol. 23, no. 3, pp. 42–54, 2016.

[172] D. Shah, B. Yang, S. Kriegman, M. Levin, J. Bongard, and R. Kramer-Bottiglio, "Shape changing robots: bioinspiration, simulation, and physical realization," *Advanced Materials*, vol. 33, no. 19, p. 2002882, 2021.

[173] S. Sareh, R. Siddall, T. Alhinai, and M. Kovac, "Bio-inspired soft aerial robots: adaptive morphology for high-performance flight," in *Soft Robotics: Trends, Applications and Challenges*, pp. 65–74, Springer, 2017.

[174] S. H. Derrouaoui, Y. Bouzid, M. Guiatni, and I. Dib, "A Comprehensive Review on Reconfigurable Drones: Classification, Characteristics, Design and Control Technologies," *Unmanned Systems*, pp. 1–27, 2021.

[175] D. Floreano and R. J. Wood, "Science, technology and the future of small autonomous drones," *Nature*, vol. 521, no. 7553, pp. 460–466, 2015.

[176] I. Shimoyama, H. Miura, K. Suzuki, and Y. Ezura, "Insect-like microrobots with external skeletons," *IEEE Control Systems Magazine*, vol. 13, no. 1, pp. 37–41, 1993.

[177] M. Noh, S.-W. Kim, S. An, J.-S. Koh, and K.-J. Cho, "Flea-Inspired Catapult Mechanism for Miniature Jumping Robots," *IEEE Transactions on Robotics*, vol. 28, pp. 1007–1018, 10 2012.

[178] S. Miyashita, S. Guitron, M. Ludersdorfer, C. R. Sung, and D. Rus, "An untethered miniature origami robot that self-folds, walks, swims, and degrades," *Proceedings - IEEE International Conference on Robotics and Automation*, vol. 2015-June, no. June, pp. 1490–1496, 2015.

[179] J. Morgan, S. P. Magleby, and L. L. Howell, "An Approach to Designing Origami-Adapted Aerospace Mechanisms," *Journal of Mechanical Design*, vol. 138, 3 2016.

[180] P. Polygerinos, N. Correll, S. A. Morin, B. Mosadegh, C. D. Onal, K. Petersen, M. Cianchetti, M. T. Tolley, and R. F. Shepherd, "Soft Robotics: Review of Fluid-Driven Intrinsically Soft Devices; Manufacturing, Sensing, Control, and Applications in Human-Robot Interaction," *Advanced Engineering Materials*, vol. 19, no. 12, 2017.

[181] S. Coyle, C. Majidi, P. LeDuc, and K. J. Hsia, "Bio-inspired soft robotics: Material selection, actuation, and design," *Extreme Mechanics Letters*, vol. 22, pp. 51–59, 2018.

[182] D. Rus and M. T. Tolley, "Design, fabrication and control of soft robots," *Nature*, vol. 521, no. 7553, pp. 467–475, 2015.

[183] C. Laschi, B. Mazzolai, and M. Cianchetti, "Soft robotics: Technologies and systems pushing the boundaries of robot abilities," *Science Robotics*, vol. 1, no. 1, p. eaah3690, 2016.

[184] P. Boyraz, G. Runge, and A. Raatz, "An overview of novel actuators for soft robotics," *High-Throughput*, vol. 7, no. 3, pp. 1–21, 2018.

[185] A. Miriyev, K. Stack, and H. Lipson, "Soft material for soft actuators," *Nature Communications*, vol. 8, no. 1, pp. 1–8, 2017.

[186] S. Mintchev, L. Daler, G. L. Eplattenier, D. Floreano, and S. Member, "Foldable and Self - Deployable Pocket Sized Quadrotor," *Proc. of the IEEE Conference on Robotics and Automation*, pp. 2190–2195, 2015.

[187] S. Mintchev, J. Shintake, and D. Floreano, "Bioinspired dual-stiffness origami," *Science Robotics*, vol. 0275, no. July, pp. 1–8, 2018.

[188] Y. Chen, H. Wang, E. Farrell Helbling, N. T. Jafferis, R. Zufferey, A. Ong, K. Ma, N. Gravish, P. Chirarattananon, M. Kovac, and R. J. Wood, "A biologically inspired, flapping-wing, hybrid aerial-aquatic microrobot," *Science Robotics*, vol. 2, no. 11, 2017.

[189] L. Daler, S. Mintchev, C. Stefanini, and D. Floreano, "A bioinspired multi-modal flying and walking robot," *Bioinspiration and Biomimetics*, vol. 10, no. 1, 2015.

[190] M. Kovač, Wassim-Hraiz, O. Fauria, J. C. Zufferey, and D. Floreano, "The EPFL jumpglider: A hybrid jumping and gliding robot with rigid or folding wings," *2011 IEEE International Conference on Robotics and Biomimetics, ROBIO 2011*, pp. 1503–1508, 2011.

[191] S.-J. Kim, D.-Y. Lee, G.-P. Jung, and K.-J. Cho, "An origami-inspired, self-locking robotic arm that can be folded flat," *Science Robotics*, vol. 3, no. 16, p. eaar2915, 2018.

[192] N. Doshi, B. Goldberg, R. Sahai, N. Jafferis, D. Aukes, R. J. Wood, and J. A. Paulson, "Model driven design for flexure-based Microrobots," *IEEE International Conference on Intelligent Robots and Systems*, vol. 2015-Decem, pp. 4119–4126, 2015.

[193] R. Siddall, G. Byrnes, R. J. Full, and A. Jusufi, "Tails stabilize landing of gliding geckos crashing head-first into tree trunks," *Communications Biology*, vol. 4, no. 1, pp. 1–12, 2021.

[194] P. E. Pounds and S. P. Singh, "Integrated electro-aeromechanical structures for low-cost, self-deploying environment sensors and disposable UAVs," *Proceedings - IEEE International Conference on Robotics and Automation*, pp. 4459–4466, 2013.

[195] A. P. Hill, P. Prince, E. Piña Covarrubias, C. P. Doncaster, J. L. Snaddon, and A. Rogers, "AudioMoth: Evaluation of a smart open acoustic device for monitoring biodiversity and the environment," *Methods in Ecology and Evolution*, vol. 9, no. 5, pp. 1199–1211, 2018.

[196] D. A. Umarhadi and P. Danoedoro, "Comparing canopy density measurement from UAV and hemispherical photography: An evaluation for medium resolution of remote sensing-based mapping," *International Journal of Electrical and Computer Engineering*, vol. 11, no. 1, pp. 356–364, 2021.

[197] J. P. Thomas, M. T. Keennon, A. DuPasquier, M. A. Qidwai, and P. Matic, "Multifunctional Structure-Battery Materials for Enhanced Performance in Small Unmanned Air Vehicles," in *ASME International Mechanical engineering Congress*, (Washington, D.C.), 2003.

[198] R. A. Sowah, M. A. Acquah, A. R. Ofoli, G. A. Mills, and K. M. Koumadi, "Rotational Energy Harvesting to Prolong Flight Duration of Quadcopters," *IEEE Transactions on Industry Applications*, vol. 53, no. 5, pp. 4965–4972, 2017.

[199] S. Kirchgeorg and S. Mintchev, "HEDGEHOG : Drone Perching on Tree Branches with High-Friction Origami Spines," *IEEE Robotics and Automation Letters*, vol. XX, no. c, pp. 1–9, 2021.

[200] O. S. Es-Said, J. Foyos, R. Noorani, M. Mendelson, R. Marloth, and B. A. Pregger, "Effect of layer orientation on mechanical properties of rapid prototyped samples," *Materials and Manufacturing Processes*, vol. 15, no. 1, pp. 107–122, 2000.

[201] S. Shaffer, K. Yang, J. Vargas, M. A. Di Prima, and W. Voit, "On reducing anisotropy in 3D printed polymers via ionizing radiation," *Polymer*, vol. 55, no. 23, pp. 5969–5979, 2014.

[202] P. Han, A. Tofangchi, A. Deshpande, S. Zhang, and K. Hsu, "An approach to improve interface healing in FFF-3D printed Ultem 1010 using laser pre-deposition heating," *Procedia Manufacturing*, vol. 34, pp. 672–677, 2019.

[203] S. Singamneni, A. Roychoudhury, O. Diegel, and B. Huang, "Modeling and evaluation of curved layer fused deposition," *Journal of Materials Processing Technology*, vol. 212, no. 1, pp. 27–35, 2012.

[204] R. J. A. Allen and R. S. Trask, "An experimental demonstration of effective Curved Layer Fused Filament Fabrication utilising a parallel deposition robot," *Additive Manufacturing*, vol. 8, pp. 78–87, 2015.

[205] J. W. Booth, J. Alperovich, P. Chawla, J. Ma, T. N. Reid, and K. Ramani, "The design for additive manufacturing worksheet," *Journal of Mechanical Design, Transactions of the ASME*, vol. 139, no. 10, pp. 1–9, 2017.

[206] K. Zhang, Y. Zhu, C. Lou, P. Zheng, and M. Kovac, "A design and fabrication approach for pneumatic soft robotic arms using 3D printed origami skeletons," *RoboSoft 2019 - 2019 IEEE International Conference on Soft Robotics*, pp. 821–827, 2019.

[207] Z. Zhao, X. Kuang, J. Wu, Q. Zhang, G. H. Paulino, H. J. Qi, and D. Fang, "3D printing of complex origami assemblages for reconfigurable structures," *Soft Matter*, vol. 14, no. 39, pp. 8051–8059, 2018.

[208] W. Gao, Y. Zhang, D. Ramanujan, K. Ramani, Y. Chen, C. B. Williams, C. C. L. Wang, Y. C. Shin, S. Zhang, and P. D. Zavattieri, "The status, challenges, and future of additive manufacturing in engineering," *CAD Computer Aided Design*, vol. 69, pp. 65–89, 2015.

[209] L. L. Howell, S. P. Magleby, and B. M. Olsen, eds., *Handbook of Compliant Mechanisms*. John Wiley {\&} Sons Ltd, 2013 ed., 2008.

[210] S. Mayya and G. Notomista, "The Robotarium," *IEEE Control Systems Magazine*, no. February, 2020.

[211] M. Quigley, B. Gerkey, K. Conley, J. Faust, T. Foote, J. Leibs, E. Berger, R. Wheeler, and A. Ng, "ROS: an open-source Robot Operating System," *IEEE International Conference on Robotics and Automation workshop on open source software*, vol. 3, no. 3.2, p. 5, 2009.

[212] L. Zhang, R. Merrifield, A. Deguet, and G.-Z. Yang, "Powering the world's robots—10 years of ROS," *Science Robotics*, vol. 2, 2017.

Appendix A

Design of a single-actuator multi-launch variable-velocity sensor launcher

Ecosystem and climate monitoring are crucial for understanding the processes that drive changes in our planet. The use of wireless sensor networks greatly aids scientists during the data gathering process, collecting data over large spacial and temporal scales at low cost. Their deployment, however, is problematic in dangerous or hard to access locations. Unmanned aerial vehicles have been shown to be useful in the installation of wireless sensors in those cases. However, the rate and precision of placement limits the practicality of current drone technologies. Current sensor launching systems idealize the payload as an orientation-less point mass. However, sensors are often directional and can only attach front-on to the monitored structure. Therefore, this assumption results in unfeasible flight-paths which reduces the likelihood of successful attachment. This paper presents a novel multirotor robot, equipped with an integrated multi-launch sensor placement system, rotor tilting capability to stabilize in windy conditions, and a lightweight collision avoidance sensor suite. By fully actuating the robot in 6 degrees of freedom, the orientation of the sensor at impact can be controlled.

A.1 Introduction

Sensor networks often consist of a large cluster of individual units. To be cost efficient, sensor units must be standardised, and cost effective to produce. Actively guided sensor units, while precise, is not cost efficient due to the need for control surfaces and onboard guidance electronics. Therefore, a precise un-guided sensor launching method must be found.

In unpredictable environment, where direct contact placement poses very high risks of collisions, launching at a standoff is highly preferable. There are broadly two approaches for launching at distance, free-fall and propelled. Free-fall deployment involves minimal requirements on the launch platform. Sensors can be stored in downward facing pods which open to deploy at set locations. Once dropped from the UAV, the sensor follows an almost vertical ballistic trajectory to its target location. This is very efficient when deploying vast WSNs with loose restrictions on the precision of individual sensors. Free-fall deployment is also limited to downwards launching; this may not be applicable to vertical or top-covered surfaces. The sensors could be propelled to their target by the platform. The more energetic approach increases the precision of deployment and enables sideways and/or upwards attachment.

Due to the limited flight time, it is highly preferable for the UAV to travel to the area of deployment and with a number of the sensor pods onboard and deploy in batches before returning to replenish. This implies that a means to launch multiple sensors is required.

A.2 Ballistic computation

Sensor launching undoubtedly draws comparisons to modern small arms and archery. Upon further investigation, while similarities are noted, the distinctions in the objective and the operating regime result in unique requirements. Two distinct ballistic solutions often exist for a given point target. Such distinction are made in classical artillery. A "gun" launches in a flat direct trajectory, with an angle smaller than the optimum for maximum range. On the other hand, a "howitzer" launches above the optimum angle in an indirect trajectory. Thus, within the maximum range of the system, the launch solution is non-unique.

Here the requirements of sensor launching diverge. Unlike current targets for gunnery, sensors are non-destructive. Thus the maximum impact energy, and by extension the impact speed, is limited. The sensor pods could also require placement in a certain orientation to ensure attachment. For example, attaching a magnetic sensor to a surface requires the sensor to be normal to the surface. Therefore the ballistic computation must account for both the target position, orientation and the impact speed of the sensor.

The following ballistic equations were first derived disregarding aerodynamics (ie. drag). With gravity providing the sole constant acceleration term, the equation of motion are given as

$$u = u_0 \tag{A.1}$$

$$v = v_0 - gt \tag{A.2}$$

$$x = x_0 + u_0 t \tag{A.3}$$

$$y = y_0 + v_0 t - \frac{1}{2} g t^2 \tag{A.4}$$

where x_0, y_0 are the launch distance and height respectively, and u_0, v_0 the initial velocities. As we are solely concerned with the terminal properties of the trajectory, we further define

$$u_0 = -S \cos \alpha \tag{A.5}$$

$$u_1 = \quad S_f \cos \theta \tag{A.6}$$

$$v_0 = \quad S \sin \alpha \tag{A.7}$$

$$v_1 = -S_f \sin \theta \tag{A.8}$$

$$t = \quad \frac{x - x_0}{u_0} \tag{A.9}$$

with S, S_f denoting launch and terminal speed, α, θ launch and terminal impact angle of elevation, and u_1, v_1 the terminal velocities respectively. The gradient of the trajectory is given

by

$$y = y_0 + \frac{v_0(x - x_0)}{u_0} - \frac{1}{2}\frac{g(x - x_0)^2}{u_0^2} \tag{A.10}$$

$$\frac{dy}{dx} = \frac{v_0}{u_0} - \frac{g(x - x_0)}{u_0^2} \tag{A.11}$$

$$\frac{dy}{dx} = \tan\alpha - \frac{g(x - x_0)}{S^2\cos^2\alpha} \tag{A.12}$$

Assuming the target is located at (0,0)

$$\frac{dy}{dx}|_{(0,0)} = \tan\theta = \tan\alpha + \frac{gx_0}{S^2\cos^2\alpha} \tag{A.13}$$

Given 7 variables $(x_0, y_0, S, S_f, \alpha, \theta, t)$ and 4 equations of motion, 3 boundary conditions are required to solve the system of equations. In other words, the firing solution is not limited by the impact speed and angle alone.

A.2.1 Adjustable launch speed

As noted above, higher exit velocity is not always beneficial when launching non-destructive objects. The terminal behaviour of the sensor unit sets an ideal launch velocity. For example, a spike style sensor attachment to tree trunks require higher impact energy, whereas a magnetic style attachment with the same launch condition would result in the sensor bouncing off the metallic surface upon contact. The ability to autonomously adjust the launch speed would enable wider use of a single system.

A.2.2 Adjustable launch angle

As shown above, enabling adjustable launch angles increases the flexibility of the platform. This is evident when deployed near/in cluttered environment where the operation volume is limited.

Tilt enabled launchers are commonly pivoted on mounts. This limits the compactness of the overall system as one must account for the clearance of both positive and negative elevation

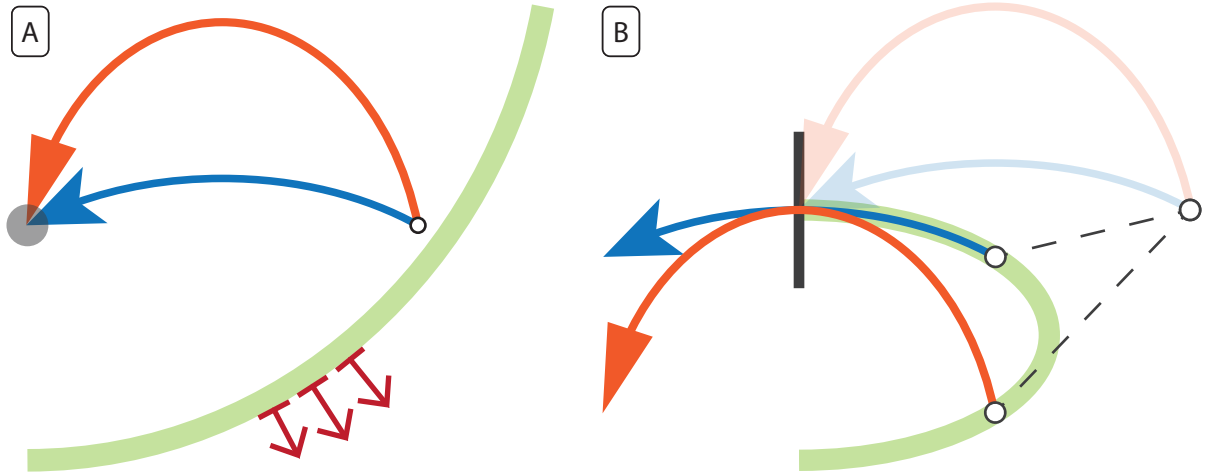


Figure A.1: **The available flight paths for a constant exit speed launcher**. (**A**) The firing solutions for a point target are bounded by a parabola, within which there are two available firing solution. On the parabola there is only one solution, beyond the boundary parabola, as indicated by the red arrow, there are no solutions. (**B**) If the impact angle is specified, the firing solutions are further limited to an ellipse.

launches. Therefore we propose tilting the rotors and pitching the body to achieve the required launch angles.

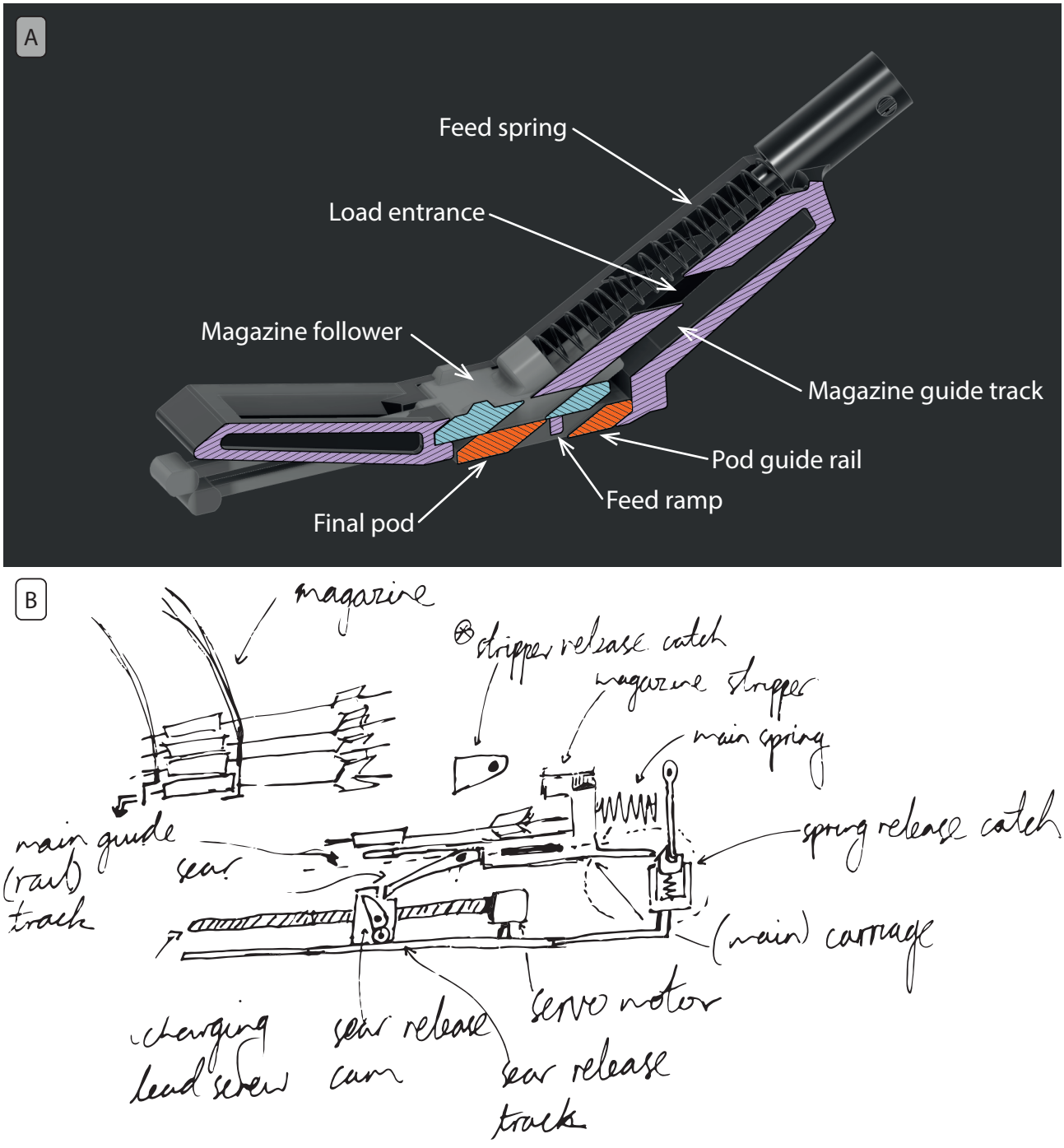


Figure A.2: **Design of the multi-launch launcher**. (**A**) A sectioned view of the sensor pod magazine and feed system. (**B**) Outline sketch of the single-actuator variable launch speed mechanism.

Appendix B

Design of the Armadillo: an omni-orientation protective ball cage for miniature multirotors

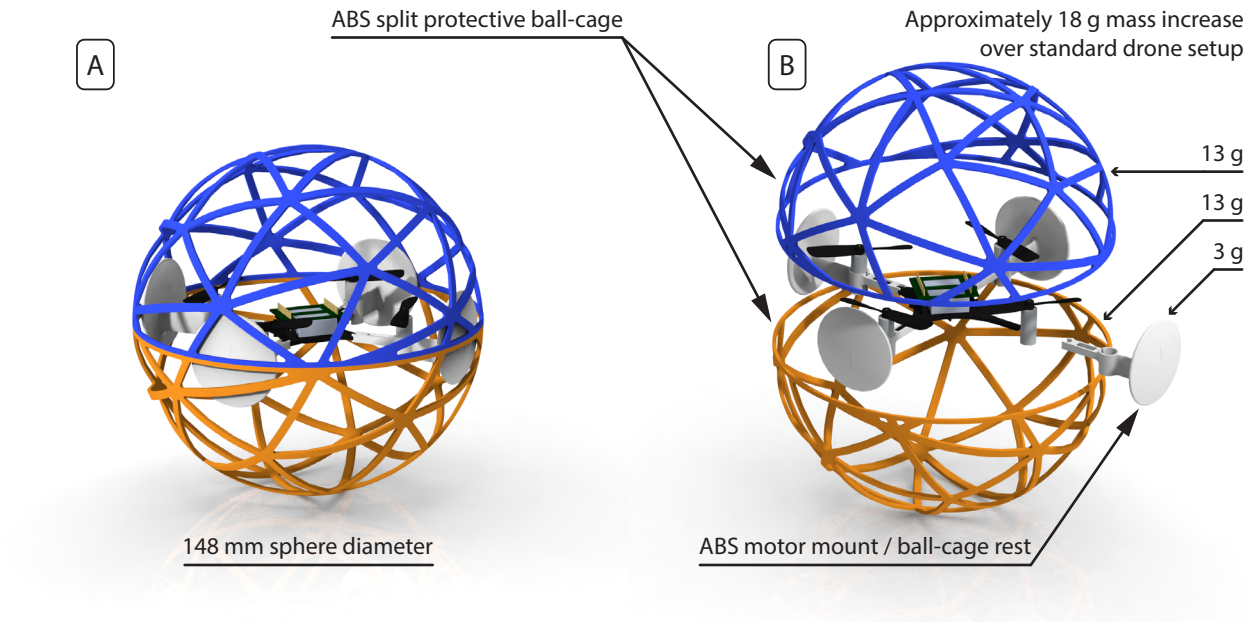


Figure B.1: **Rendered picture of the Armadillo drone** (**A**) assembled and (**B**) in exploded view.